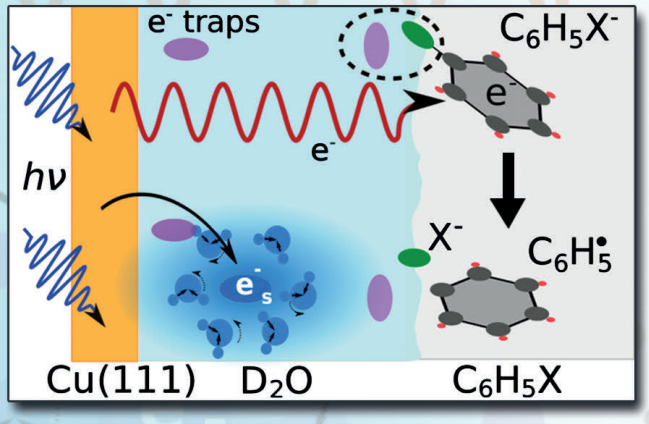

FAU Studies Mathematics & Physics 17

Philipp Auburger

Ab-initio investigation of dissociative electron attachment to halogenated hydrocarbons on the ice surface

FAU UNIVERSITY PRESS

Philipp Auburger

Ab-initio investigation of dissociative electron attachment to halogenated hydrocarbons on the ice surface

FAU Studies Mathematics & Physics

Band 17

Herausgeber der Reihe:
Prof. Dr. Karl-Hermann Neeb und Prof. Dr. Klaus Mecke

Philipp Auburger

Ab-initio investigation of dissociative electron attachment to halogenated hydrocarbons on the ice surface

Erlangen
FAU University Press
2020

Bibliografische Information der Deutschen Nationalbibliothek:
Die Deutsche Nationalbibliothek verzeichnet diese Publikation in der Deutschen Nationalbibliografie; detaillierte bibliografische Daten sind im Internet über http://dnb.d-nb.de abrufbar.

Autoren-Kontaktinformation: Philipp Auburger, Lehrstuhl für Theoretische Festkörperphysik (Friedrich-Alexander-Universität Erlangen-Nürnberg), Philipp-Auburger@t-online.de, ORCID: 0000-0002-5994-5426

Der vollständige Inhalt des Buchs ist als PDF über den OPUS Server der Friedrich-Alexander-Universität Erlangen-Nürnberg abrufbar:
https://opus4.kobv.de/opus4-fau/home

Bitte zitieren als
Auburger, Philipp. 2020. *Ab-initio investigation of dissociative electron attachment to halogenated hydrocarbons on the ice surface*. FAU Studies Mathematics & Physics Band 17. Erlangen: FAU University Press.
DOI: 10.25593/978-3-96147-2963.

Umschlag:
Bildmotiv: Dr. Ishita Kemeny, Duisburg

Verlag und Auslieferung:
FAU University Press, Universitätsstraße 4, 91054 Erlangen

Druck: docupoint GmbH

ISBN: 978-3-96147-295-6 (Druckausgabe)
eISBN: 978-3-96147-296-3 (Online-Ausgabe)
ISSN: 2196-7482
DOI: 10.25593/978-3-96147-296-3

Ab-initio investigation of dissociative electron attachment to halogenated hydrocarbons on the ice surface

Den Naturwissenschaftlichen Fakultäten
der Friedrich-Alexander-Universität
Erlangen-Nürnberg

zur
Erlangung des Doktorgrades
der Naturwissenschaften (Dr. rer. nat.)

vorgelegt von

Philipp Auburger

aus Bamberg, Bayern, Deutschland

Als Dissertation genehmigt
von der Naturwissenschaftlichen Fakultät
der Friedrich-Alexander-Universität Erlangen-Nürnberg

Tag der mündlichen Prüfung: 02.07.2019

Vorsitzender des Promotionsorgans: Prof. Dr. Georg Kreimer

Gutachter: Prof. Dr. Michel Bockstedte
Gutachter: Prof. Dr. Bernd Meyer

Zusammenfassung

Atmosphärische Chemie ist heutzutage von besonderem Interesse, weil anthropogene Einflüsse das Erdklima wesentlich verändern. Beispielsweise führt die Emission industriell produzierter Fluorchlorkohlenwasserstoffe (FCKW) zu umweltgefährdenden ozonabbauenden Reaktionen. Die Freisetzung von Halogenen und Radikalen als Folge der Dissoziation von FCKW auf Eispartikeln in der Erdatmosphäre ist ein wichtiger Zwischenschritt, welcher sich bis jetzt einer gründlichen theoretischen Beschreibung entzogen hat. Verunreinigungen der katalytisch wirkenden Eispartikel mit Metallatomen ermöglichen das Einsetzen dieser Prozesse durch photoinduzierte dissoziative Elektronenanlagerung (DEA) an die Moleküle. Elektronensolvatation auf der Eisoberfläche ist ebenfalls ein aktuelles Thema, weil die entstehende Spezies Reaktionen von Adsorbaten auf vielen Energie- und Zeitskalen induzieren kann.

Gegenwärtige theoretische Beschreibungen befassen sich nur mit DEA an halogenierte Kohlenwasserstoffe in der Gasphase. Sie benötigen empirische Parameter, um unphysikalische Resultate für die molekulare elektronische Struktur zu vermeiden.

Die vorliegende Studie verfolgt einen systematischen *ab-initio* Ansatz, um DEA auch für die Moleküle auf Eis zu beschreiben. Dazu werden GW-Rechnungen und die vorausgehende Dichtefunktionaltheorie (DFT) verwendet. Der Zugang verwendet ebene Wellen und periodische Superzellen. Nachfolgende BSE-Rechnungen geben Einblick in die direkte neutrale Photodissoziation.

Die neue Modellierung der DEA an die Adsorbate liefert ein umfassendes Bild der elektronischen Strukturen und trägt wesentlich zur Erklärung der experimentellen Beobachtungen bei. Das betrifft auch die kryogenen Experimente aus den Bereichen der Rastertunnelmikroskopie und Zwei-Photonen-Photoemissions-Spektroskopie, welche von zwei anderen Gruppen im Rahmen eines gemeinsamen Projekts durchgeführt wurden. Die Betrachtung niederenergetischer DEA an die prototypischen Phenylhalogenide evidenziert ein charakteristisches Szenario für den mikroskopischen Mechanismus. Die Reaktion beginnt mit Elektroneneinfang in eine π^*-Resonanz und ist ein aktivierter Prozess, in dem das Exzesselektron in einen dissoziativen σ^*-Zustand übergehen muss. Sie wird durch die Beteiligung eines weniger elektronega-

tiven Halogens begünstigt. Adsorption ist insofern auch günstig, weil sie den Elektroneneinfang rotverschiebt und katalytisch wirkt. Eine systematische Analyse zeigt, dass Ansammlungen von Protonen ohne Wasserstoffbrückenbindung an der Eisoberfläche Elektronensolvatation ermöglichen und Zentren der Adsorption der Moleküle sind. Beide Eigenschaften korrelieren in hinreichend starker Ausprägung miteinander. DEA wird jedoch von heißen Elektronen induziert. Direkte neutrale Photodissoziation wird als Konkurrenzprozess ausgeschlossen. Auch ein Zusammenhang zwischen Elektronensolvatation und Umorientierungen von Eisoberflächenmolekülen erscheint plausibel.

Abstract

Nowadays atmospheric chemistry is of particular interest, since anthropogenic effects have a substantial influence on the global climate. For example, the emission of industrially produced chlorofluorocarbons (CFCs) leads to environmentally hazardous ozone depleting reactions. The release of halogens and radicals, upon the dissociation of CFCs on catalytically active icy grains in the atmosphere of the earth, is an important intermediate step, that has eluded thorough theoretical description until today. Metal dopants enable the onset of these processes via photoinduced dissociative electron attachment (DEA) to the molecules. Electron solvation at the ice surface is also an essential topic, because the nascent species is able to induce reactions of adsorbates spanning a wide range of transferred energy and time scales.

Current theoretical descriptions of DEA to halogenated hydrocarbons treat only the reactions in the gas phase. They require empirical parameters to avoid unphysical results for the molecular electronic structure.

The present study follows a systematic *ab-initio* approach to describe DEA also for the molecules adsorbed on ice. For this purpose GW calculations and the underlying plane wave periodic supercell density functional theory (DFT) are employed. Subsequent BSE calculations give insight into direct neutral photodissociation.

The new modelling of DEA to the adsorbates provides a comprehensive picture of the relevant electronic structures. Its results are entirely consistent with the experimental observations and contribute significantly to their explanation. This concerns also the cryogenic scanning tunnelling microscopy and two-photon photoemission spectroscopy experiments performed by two other groups as part of a joint project. The investigation of low-energy DEA to the prototypical phenyl halogenides suggests a characteristic scenario for the microscopic mechanism. The reaction starts with electron capture by a π^* resonance and proceeds with an activated transfer of the excess electron into a dissociative σ^* state via internal conversion at a conical intersection. It is favoured by the involvement of a less electronegative halogen. Adsorption also promotes dissociation via these channels by redshift of the electron capturing molecular resonances and catalysis. A systematic analysis of surface defects and the positioning of the molecules at them reveals that agglomeration of surface dangling protons is the key aspect for both electron solvation

and adsorption. Ice surface defects are the electron solvation sites, as well as the preferential adsorption sites, and both features correlate with each other for sufficient strength. However, DEA is induced by hot electrons. Direct neutral photodissociation is excluded as a competitive process. Apart from that results pointing towards a connection between electron solvation and reorientations of ice surface molecules were obtained.

Index of abbreviations

ε_{QP}	**QP** energy with respect to Φ_{vac}
ε_{XC}	**XC** density
Γ	**gamma** point (center of the first Brillouin zone) or vertex function or higher Green's function (according to context)
λ	photon wavelength
ω	screening parameter (HSE XC-functionals)
Φ_{vac}	**vac**uum potential
Σ	self-energy
$\sigma(E_{DEA})$	cross section at **DEA** peak **e**nergy
θ	temperature in degrees Celsius
d	C-X bond **d**istance/length or supercell edge length (according to context)
d_0	equilibrium C-X bond **d**istance/length
d_{cross}	C-X bond **d**istance/length at conical intersection
d_{vac}	C-X bond **d**istance/length at which the excess electron becomes stable
E	potential **e**nergy
E^0	electronic ground state potential **e**nergy
E_γ	photon **e**nergy
$E_{A,add}$	**add**itional **a**ctivation **e**nergy
E_{ads}	**ads**orption **e**nergy
E_A	**a**ctivation **e**nergy

E_{BF}	C-X **b**ond **f**ission **e**nergy
E_{B}	**b**inding **e**nergy
$E_{\text{cut-GW}}$	response function **e**nergy **cut**off for **GW** calculations (VASP parameter)
E_{cut}	**e**nergy **cut**off for plane wave basis set (VASP parameter)
E_{DEA}	**DEA** peak **e**nergy
$E_{\mathrm{EXO}}^{\mathrm{DEA}}$	**DEA exo**thermicity
$E_{\mathrm{EXO}}^{\mathrm{TNID}}$	**TNID exo**thermicity
E_{he}	**h**ole-**e**lectron state **e**nergy (required for vertical optical excitation)
E_{XC}	**XC e**nergy
EA	**e**lectron **a**ffinity
$G_{\mathbf{k}\sigma}^{\mathrm{ret/av/c}}$	**ret**arded/**a**d**v**anced/**c**ausal one-electron **G**reen's function
IP	**i**onisation **p**otential
P	irreducible **p**olarisability
p	local fraction of an electronic state
r_{S}	electron density parameter
v	bare Coulomb interaction
V_{XC}	**XC** potential
W	screened Coulomb interaction
(n+m) REMPI	**r**esonance-**e**nhanced **m**ulti**p**hoton **i**onisation (**n** photons are absorbed to reach the intermediate state, **m** further photons for the final state)
(tr-)2PPE	(**t**ime-**r**esolved) **two**-**p**hoton **p**hotoelectron spectroscopy
(X-)(*L*)*DOS*	(**X**-projected) (**l**ocal) **d**ensity **o**f **s**tates (X ≡ halogen)
AD	**a**uto**d**etachment
ADMP	**a**tom-centered **d**ensity **m**atrix **p**ropagation method

AE	**a**ll-**e**lectron
B3LYP	hybrid **B**ecke-**L**ee-**Y**ang-**P**arr XC-functional (hybrid DFT)
BL	**bi**layer
BLYP	**B**ecke-**L**ee-**Y**ang-**P**arr XC-functional (gradient DFT)
BOA	**B**orn-**O**ppenheimer **a**pproximation
BSE	**B**ethe-**S**alpeter **e**quation
C	**c**arbon or **c**orrelation (quantum mechanical part of the Coulomb interaction between electrons of opposite spin) (according to context)
CB(M)	**c**onduction **b**and (**m**inimum)
CFCs	**c**hloro**f**luoro**c**arbons (german: FCKW)
CI	**c**onfiguration **i**nteraction technique
CSHIFT	**c**omplex **shift** (VASP parameter)
DEA(S)	**d**issociative **e**lectron **a**ttachment (**s**pectroscopy)
DFG	**D**eutsche **F**orschungs**g**emeinschaft (english: German Research Foundation)
DFT	**d**ensity **f**unctional **t**heory
DRC	**d**ynamic **r**eaction **c**oordinate
ETS	**e**lectron **t**ransmission **s**pectroscopy
EXC	**Ex**zellenz**c**luster (english: Cluster of Excellence)
FAU	**F**riedrich-**A**lexander-**U**niversity Erlangen-Nuremberg
FCKW	**F**luor**c**hlor**k**ohlen**w**asserstoffe (english: CFCs)
FDM	**f**inite **d**ifference **m**ethod
FTIR	**F**ourier-**t**ransform **i**nfra**r**ed spectroscopy
G_0W_0	fully non-selfconsistent GW
GAP	band **gap** (usually at Γ)

GEA	**g**radient **e**xpansion **a**pproximation
GGA	**g**eneralised **g**radient **a**pproximation XC-functionals (gradient DFT)
GW	partially selfconsistent GW (QP energies in G and W updated)
GW_0	partially selfconsistent GW (QP energies in G updated)
GW(A)	Hedin's **GW a**pproximation
HF SCF	**H**artree-**F**ock **s**elf-**c**onsistent **f**ield method
HF(A)	**H**artree-**F**ock (**a**pproximation)
HF-X	**H**artree-**F**ock e**x**change
HFT	**H**ellmann-**F**eynman **t**heorem
HKT	**H**ohenberg-**K**ohn **t**heorem
HOMO	**h**ighest **o**ccupied **m**olecular **o**rbital
HSE03	**H**eyd-**S**cuseria-**E**rnzerhof-**03** XC-functional (hybrid DFT)
HSE06	**H**eyd-**S**cuseria-**E**rnzerhof-**06** XC-functional (hybrid DFT)
I_h	**h**exagonal ice of type **I**
IC	**i**nternal **c**onversion
IR	**i**nfra**r**ed radiation
KS	**K**ohn-**S**ham
LAPW	**l**inear **a**ugmented **p**lane **w**ave method
LDA	**l**ocal **d**ensity **a**pproximation XC-functional (DFT)
LPEAD	VASP tag to employ the FDM for deriving the cell-periodic part of the orbitals w.r.t. **k** (required for $scGW_{(0)}$ calculations underlying beyond-TDA BSE calculations)
LR	**l**ong **r**ange
LUMO	**l**owest **u**noccupied **m**olecular **o**rbital
MBPT	**m**any **b**ody **p**erturbation **t**heory

MC	**M**onte **C**arlo
ML	**m**ono**l**ayer
MO(s)	**m**olecular **o**rbital(s)
MP	**M**øller-**P**lesset perturbation theory
NBANDS	**n**umber of **bands** (VASP parameter)
NL	**n**on-**l**ocal
OS	**o**scillator **s**trength
PAW	**p**rojector **a**ugmented **w**ave method (Blöchl)
PBC	**p**eriodic **b**oundary **c**onditions
PBE	**P**erdew-**B**urke-**E**rnzerhof XC-functional (gradient DFT)
PBEo	hybrid **P**erdew-**B**urke-**E**rnzerhof XC-functional (hybrid DFT)
PES	**p**hoto**e**lectron **s**pectroscopy
pho.	direct neutral **pho**todissociation
PIES	**P**enning **i**onisation **e**lectron **s**pectroscopy
PP	**p**seudo**p**otential
PS	**ps**eudised
PSCs	**p**olar **s**tratospheric **c**louds
QP	**q**uasi**p**article
REC	**rec**ombination
RESOLV	**R**UHR **E**XPLORES **SOLV**ATION
RPA	**r**andom **p**hase **a**pproximation
RWIGS	“Wigner-Seitz” radius (VASP parameter)
S_{AD}	orientational defect (pair) of $I_h(0001)$
scGW	fully selfconsistent GW

$scGW_0$	partially selfconsistent GW (QP energies in G and orbital wave functions updated)
SFG	**s**um **f**requency **g**eneration
SIE	**s**elf-**i**nteraction **e**rror
SOMO	**s**ingly **o**ccupied **m**olecular **o**rbital
SR	**s**hort **r**ange
STM	**s**canning **t**unnelling **m**icroscopy
STS	**s**canning **t**unnelling **s**pectroscopy
TDA	**T**amm-**D**ancoff **a**pproximation
TNI(D)	**t**ransient **n**egative **i**on (**d**issociation)
TOFMS	**t**ime-**o**f-**f**light **m**ass **s**pectrometry
UPS	**u**ltraviolet **p**hotoelectron **s**pectroscopy
UV	**u**ltra**v**iolet radiation
V_A	molecular **v**acancy of $I_h(0001)$ (first BL, molecule able to **a**ccept a hydrogen bond removed)
V_D	molecular **v**acancy of $I_h(0001)$ (first BL, molecule able to **d**onate a hydrogen bond removed)
VAE	**v**ertical **a**ttachment **e**nergy
VASP	**V**ienna **a**b-initio **s**imulation **p**ackage
VB(M)	**v**alence **b**and (**m**aximum)
vdW	**v**an **d**er **W**aals
VMI	**v**elocity **m**ap(ped) (ion) **i**maging
VUV	**v**acuum **u**ltra**v**iolet spectroscopy
X	halogen or e**x**change (quantum mechanical part of the Coulomb interaction between electrons of parallel spin) (according to context)
XC	e**x**change-**c**orrelation (quantum mechanical part of the electron-electron Coulomb interaction)
XPS	**X**-ray **p**hotoelectron **s**pectroscopy

Contents

1. Introduction

Water is the foundation of life. Examples for its ubiquity are given by the facts that it constitutes $\approx 70\%$ of the mature human body and covers 71% of the surface of the earth, where it occurs naturally in all three basic aggregate phases. Human health is affected by countless internal and external factors. For example, hormonal imbalances evoke diseases such as adiposity and depression. Electrons solvated in liquid water are exceptionally reactive [1–10] and crucial in avoiding these as they enable the communication of biological systems in humans via the brain [11]. Pollutants are toxic substances, or responsible for their production, or bad for the global climate resp. the atmosphere of the earth. Industrially produced chlorofluorocarbons (CFCs) are an example as their emission leads to a lack of ozone in the stratosphere, which in turn becomes more transparent for carcinogenic UV radiation [12]. Interestingly, ice is capable of both solvating electrons and catalysing the decomposition of CFCs.

In 1995 the nobel prize in chemistry was awarded to Crutzen, Molina and Rowland for their research on the atmospheric chemistry of the earth, especially formation and depletion of ozone (O_3). The stratospheric ozone layer is an essential regulator of global climate, because it protects the terrestrial surface from an overdose of solar UV radiation (100-380nm), that leads to global warming and has an adverse effect on photosynthesis [12]. Moreover, this radiation weakens the immune system and acts carcinogenically [12]. Life on earth, e.g. phytoplankton, is most sensitive to UV-B (280-320nm) [12]. The stratosphere, in contrast to the troposphere, has a positive temperature gradient with respect to altitude. This gradient is due to the absorption of solar UV radiation by stratospheric ozone and limits vertical air movements. Therefore the stratosphere has an additional impact on the terrestial climate system [12]. Global warming means not only that the temperature of the terrestrial surface is higher than usual, as it absorbs an enhanced amount of solar UV radiation. Global warming also relates to the absorption of the concomitant additional terrestrial IR emission by tropospheric molecules, i.e. the rise of their average temperature due to a stronger greenhouse effect. Since the industrial revolution, which began primarily in Great Britain during the second half of the 18th century, the, originally natural, greenhouse effect has an additional anthropogenic component, i.e. production and emission of so-

called "greenhouse gases" responsible for ozone depletion are intensified. The most drastic consequence is the creation of the antarctic ozone hole discovered in 1985 [13]. The total amount of stratospheric ozone in this region decreases by up to 70% during the spring months september and october [12, 14]. This has been attributed to the emission of industrially manufactured halocarbons, whose dissociation is favoured by special meteorological conditions [15]. More specifically, UV radiation and cosmic rays induce the dissociation of halocarbons[1], in particular industrially produced chlorofluorocarbons (CFCs) adsorbed on polar stratospheric clouds (PSCs), whereby halogens and radicals are released (cf. Fig. 1.4). These, above all chlorine (Cl) and also bromine (Br), are of large environmental relevance [16, 17], especially as they cause ozone depleting reactions [12, 18, 19]. The important role of halocarbon dissociations in atmospheric chemistry is also based on the significant effect on their concentrations [17] and the abundance of clouds [17].

Compared to the gas phase the photoinduced dissociation of various halogenated organic compounds, including pollutants, is catalysed and proceeds with increased reaction rate, if they are adsorbed (solvated) at naturally frequently available H_2O ice particles [18]. It has been demonstrated that the adsorption of these species occurs due to their interaction with dangling protons at the ice surface [20, 21]. Essential modifications of their optical absorption spectra were observed in diverse cases [17]. While direct neutral photodissociation [22–37] is still possible, the relevant spectral range can not be covered without taking dissociative electron attachment (DEA) of photoexcited excess electrons [18, 19, 35, 36, 38–49] into account.

DEA to halogenated hydrocarbons is the central theme of this work, because on atmospheric ice particles it can proceed at lower incident photon energies E_γ than direct neutral photodissociation. This is enabled by the presence of dopants, such as metals like sodium (Na), since it allows electrons to be photoinjected into the ice conduction band at E_γ far below the width of the band gap [51–53]. This might be accomplished by absorption of sunlight [51–53] and excess electrons also originate from the impact of high energy particles (cosmic radiation) [18]. Furthermore, adsorption at the ice surface catalyses DEA to halogenated hydrocarbons to a much larger extent than their direct neutral photodissociation (see chapters 5 and 6). While excess electrons in the conduction band (hot electrons) are delocalised, they are localised by solvation at defects (cf. Fig. 1.1) [1, 2]. Since its discovery by Hart and Boag (1962) [1], the solvated excess electron is subject to intense research for chemical physicists. This highly reactive transient species is one of the

[1] This work assumes the former without loss of generality for the microscopic reaction mechanisms.

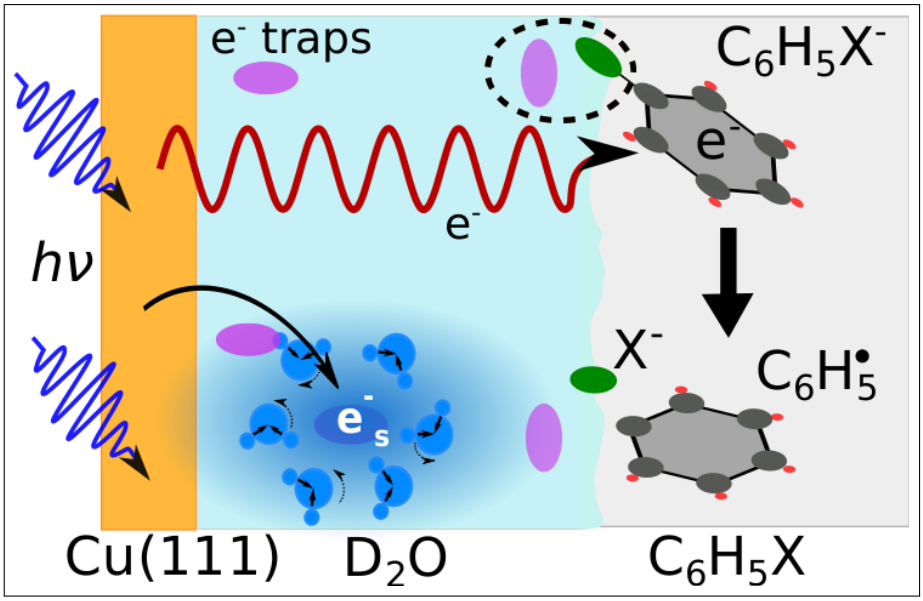

Figure 1.1.: $C_6H_5X/D_2O/Cu(111)$: An excess electron is photoexcited from the Cu(111) metal substrate. It either attaches to one of the adsorbed C_6H_5X molecules (top), or solvates at an electron trap of the D_2O film (bottom). The former process can lead to dissociation (DEA), while the latter may induce molecular reorientations. The dashed ellipse indicates the preference of (strong) electron traps as adsorption sites. Kemeny (2017) [50] (X=F,Cl,Br)

most potent reducing agents in chemistry [1–10]. It has been demonstrated experimentally that the DEA is induced by hot, instead of solvated, excess electrons [18, 47], but this did not reveal the underlying reaction mechanism. Hence an explicit model of DEA, in particular the electronic structures and interaction of adsorbate and substrate, is desirable. Unfortunately a qualitatively correct reproduction of the experimental results could not be achieved without empirical assumptions. Therefore the predictive capability of the models is considerably limited, and the influence of the ice substrate has not been taken into account [39, 42, 54, 55]. An ab-initio model shedding more light on the microscopic reaction mechanisms, among others by aiming to remedy both these issues, is presented here. Apart from that, defects facilitate excess electron solvation at the ice surface. The conditions for their formation, and the key motifs determining their adequacy as electron traps, are investigated during preliminary considerations.

Since ice is a polar medium it solvates both excess electrons and polar adsorbates, e.g. halogenated hydrocarbons. More specifically, these solvation processes are (energetically) favoured at adequate defect structures. The

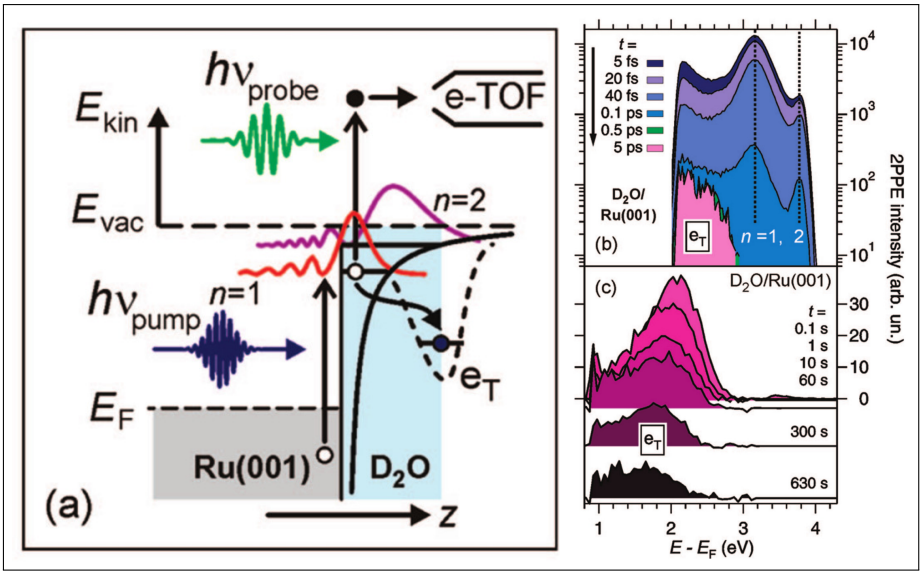

Figure 1.2.: (a) scheme of time-resolved two-photon photoelectron spectroscopy (tr-2PPE); 2BL crystalline D_2O on Ru(001): (b) $h\nu_{pump}$=3.9eV, $h\nu_{probe}$=1.95eV (c) $h\nu_{pump}$=3.9eV, $h\nu_{probe}$=3.1eV; Bovensiepen et al. (2009) [3]

lifetimes of excess electrons in bulk liquid water are of the order of microseconds [4], while no values beyond the picosecond range have been measured for surface species [4, 5, 56]. However, ice exhibits a more rigid hydrogen bonded molecular network, which facilitates localisation, stabilisation and charge screening of excess electrons on top of surface defects in vacuum due to dipole reorientation. There the lifetimes are drastically increased reaching up to minutes for crystalline ice [3]. A general interest is justified as their interaction with reactants initiates, e.g. catalytical, processes spanning a wide range of transferred energy and time scales [3, 57]. Bovensiepen et al. (2009) [3] employed time-resolved two-photon photoelectron spectroscopy (tr-2PPE) (cf. Fig. 1.2) to demonstrate that the solvation of excess electrons proceeds through several conformational substates and leads to their trapping. Based on results obtained with a combination of the technique and xenon (Xe) titration it was concluded that this takes place at the ice surface. Bertram (2017) [58] substantiated this further by observing electron solvation induced molecular reorientations such as annealing of defects, which are supposedly mediated by high vibronic excitations, with scanning tunnelling microscopy (STM) (see also section 7.1).

Hence describing nuclear geometry and electronic structure of ice poses challenges that can be interconnected to an unusually high degree. The

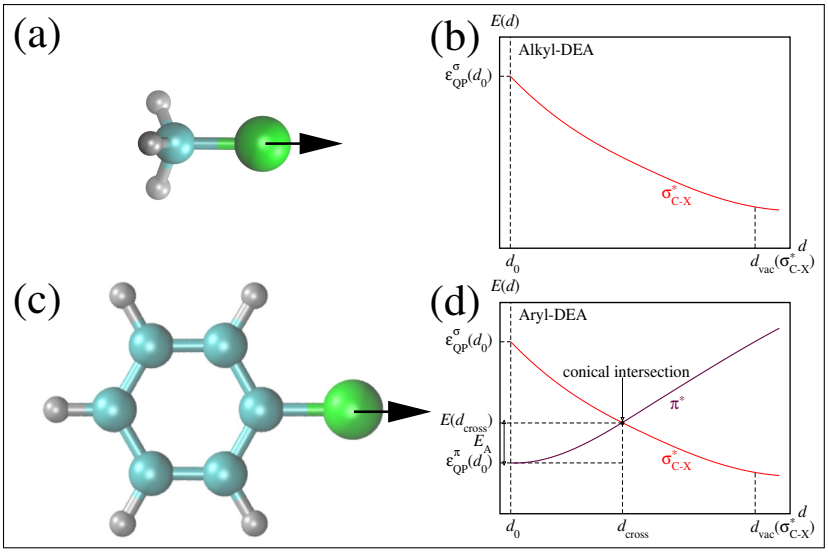

Figure 1.3.: Scheme of the anionic potential energy curves involved in low-energy DEA to hydrogenated halocarbons: (a,b) alkyls, most simply methyl halogenides CH_3X (c,d) aryls, most simply phenyl halogenides C_6H_5X

archetypal geometrical frustration is a major aspect of the enormously complicated physics of ice. The protonic subsystem is naturally disordered as it exhibits a plethora of almost isoenergetic configurations [59]. While transitions between these can easily be thermally induced in the bulk, there are much larger energy barriers at the surface due to lack of screening between the positive partial charges of surface dangling protons [60]. Furthermore, the molecular termination of the ice surface, as well as the relation to its ability of surface electron trapping [3], is also a subject of debate [61]. The electronic structure of ice is generally regarded as not well understood [59, 62–65].

To reveal the microscopic mechanism of DEA to halogenated hydrocarbons a preferably simple series of molecules, involving all crucial aspects, is analysed. In the low-energy range it generally requires the excess electron to undergo internal conversion, i.e. a transition between its initial (π^*) and final (σ^*) state at the conical intersection (see section 2.8) between them. This feature is exhibited by most of the aryl type compounds [66]. Hence DEA to them can not proceed without sufficient activation energy E_A (cf. Fig. 1.3). In contrast to these, the alkyl type compounds possess no aromatic rings. Therefore the directly dissociative lowest $\sigma^*_{C\text{-}X}$ (cf. Fig. 1.3) is often the most stable molecular orbital able to harbour an excess electron throughout the reaction [48, 67]. Hence, and to clarify the influence of the halogen electronegativity, phenyl halogenides C_6H_5X (with X=F,Cl,Br), the simplest aromatic halocarbons, were

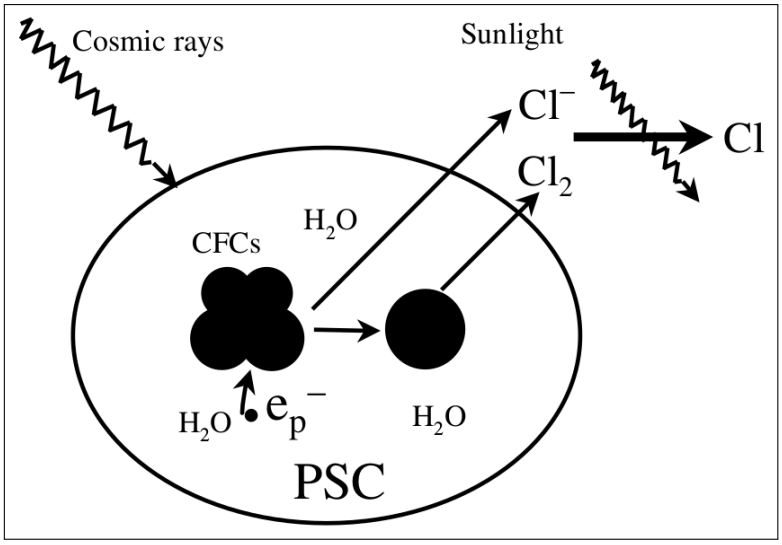

Figure 1.4.: Mechanism of chlorine atom (Cl) release responsible for ozone (O_3) depletion in the atmosphere of the earth as suggested by Lu and Sanche (2001) [18]: Incident cosmic rays produce excess electrons in icy grains in dense polar stratospheric clouds (PSCs) consisting primarily of water (H_2O) and also of nitric acid (HNO_3). They can undergo dissociative electron attachment (DEA) to adsorbed chlorofluorocarbon (CFC) molecules while being presolvated (hot). This yields chlorine anions (Cl^-), which desorb either immediately or after forming molecular chlorine (Cl_2) by reacting with other species adsorbed on PSCs. Sunlight creates chlorine atoms (Cl) either by photodetaching the excess electron from the former or photodissociating the latter emission.

chosen as prototypical molecules. They are neither too small to be observed via scanning tunnelling microscopy (STM) nor too large to be treated with reasonable computational effort.

The present study aims to reveal the underlying microscopic reaction mechanism responsible for the following picture emerging from the ab-initio calculations as well as the experiments performed in collaboration. Adsorption of phenyl halogenide molecules at the ice surface leads to catalysis and enhanced reaction probability of low-energy DEA to them. These effects are particularly strong at defects, which are the main adsorption and electron trapping sites. The reactions are induced by excess electrons from the ice conduction band and the involvement of a heavier halogen favours them. The dissociative reactions of the free and adsorbed molecules are described with an ab-initio model developed employing the GW+BSE approach based on plane wave periodic supercell DFT. This method was chosen, because atomic wave function based techniques, like configuration interaction (CI), are not suited, i.e. too

expensive, to describe delocalised scattering states relevant for excess electron capture and dissociation upon it. DFT serves to calculate the ionic positions and the total energy of each system in its (electronic) ground state, and to provide the starting points for subsequent GW calculations. For the molecules in vacuum hybrid DFT is applied throughout. This is also done to relax the adsorbate-substrate systems electronically after the treatment of their geometry, which computational expense restricts to gradient DFT. It turns out that a sufficiently adequate characterisation of the electronic structures, especially charged and excited states, is only enabled upon continuing with many body perturbation theory (MBPT) revolving around the quasiparticle (QP) concept. GW produces the QP electronic energy levels, including their characters, so that DEA can be analysed accurately. Furthermore it yields the (local) density of states and its components, dielectric properties, photoemission spectra and finally the starting points for subsequent BSE calculations. These allow to gain insight into energies, and dominant characters, of electron-hole pairs, which is used to investigate photodissociation, as well as spectra of UV absorption possibly responsible for their creation. In close connection with this theoretical study collaborators Ishita Kemeny[2] (formerly Agarwal) and Cord Bertram[3] performed complementing surface experiments and wrote their PhD theses about them (2017) [50, 58]. They systematically investigated modifications upon illumination for C_6H_5X with X=F,Cl,Br adsorbed on a Cu(111) transition metal substrate also with amorphous ultrathin films or crystalline nanoislands of D_2O. The low-temperature (7.5-11K) scanning tunnelling microscopy (STM) images of Cord Bertram contain characteristic apparent height profiles being indicative of the crystalline quality of the ice and the metal substrate, molecular reorientations and the occurrence of dissociative reactions. In particular they permit to distinguish between the phenyl halogenide adsorbates and substrate structures. Ishita Kemeny employed time- and angle-resolved two-photon photoelectron spectroscopy (2PPE) to measure photoelectron kinetic energy spectra depending on the time delay between both photon pulses. These allow to identify not only the positions of the lower ice conduction band edge and solvated electron states, but also the Fermi edge of the metal substrate and image potential states appearing due to it. The upper ice conduction band edge was measured previously [68]. She focussed on determining the evolution of the work function with illumination time for various systems and fluences. Thereby evidences for electron trapping, photoinduced ionisation or dissociation (DEA) of adsorbed molecules and contingent back or secondary reactions, as well as charge screening effects, were gathered. The

[2] University Duisburg-Essen, supervisors Prof. U. Bovensiepen and Dr. M. Ligges
[3] Ruhr-University Bochum, supervisor Prof. K. Morgenstern

gradually disappearing slope of the work function indicates the attainment of a photostationary state.

Outline

Chapter 2 elucidates the theoretical methods and instruments, whose functionality and hierarchy has to be understood so that the quantum mechanics of the dissociative molecular reactions (in the low-energy range) can be revealed and described precisely. It starts with density functional theory (DFT), in particular the appropriate use of the periodic supercell approach and the various relevant exchange-correlation (XC) functionals approximating the quantum mechanical part of the electron-electron interaction. Then the more sophisticated electronic structure methods GW, giving the energy levels a direct physical interpretation, and BSE, required for the description of collective excitations (here: electron-hole pairs), are discussed. Finally fundamental properties of conical intersections are mentioned, because it was discovered that under the most relevant initial conditions the dissociations can generally not proceed without internal conversion at them. Chapters 3 to 6 are the core part of this investigation. They verify that it has developed a feasible model incorporating all essential aspects by systematically elaborating on the ab-initio calculations, their results and the consequently made predictions. Chapter 3 is concerned with basic features and the electronic structure of mere ice systems. Analysing the pristine bulk state also serves to examine the adequacy of various approaches with different degrees of sophistication and to determine convenient simulation parameters for the investigation of more complex cases. Simple representative defect structures at the bilayer-terminated ice surface are employed to recognise how surface electron trapping becomes possible. Chapter 4 focuses on electronic structure trends exhibited by the prototypical phenyl halogenide molecules and emerging upon their adsorption at the ice surface. The favourability of adsorption sites and geometries is determined by successively considering exemplary defects, of various types and sizes, interacting with the molecules. This allows to understand the importance of the different bonding motifs and their relation to the concomitant electronic structure modifications is clarified. The microscopic mechanism of DEA is addressed in chapter 5. Modelling reveals e.g. the necessity of internal conversion ($\pi^*_{a,s} \rightarrow \sigma^*_s$), the catalytic effect of the ice substrate and its ability to make dissociation following resonant electron capture more likely. The, widely analogous, investigation of photodissociation is discussed in chapter 6. For these processes internal conversion ($\pi_s - \pi^*_a \rightarrow \pi_s - \sigma^*_s$) is also mandatory, yet the influence of the ice substrate is much weaker in the present context. Both kinds of dissociative reactions are found to be favoured by a higher row of the halogen. Chapter 7 draws a comparison between the present study and

the experiments performed in collaboration. Coinciding trends in computational and measurement results are revealed. All aspects are summarised in chapter 8. It assesses how the theoretical picture, developed together with the experimental collaborators, advances the microscopic understanding of the dissociative mechanisms. Open questions, like the development of a general dissociation pathway finding algorithm, and options for future research, like measuring the gas phase reaction rates, are discussed.

2. Ab-initio approach: GW+BSE based on DFT

As molecular dissociation processes – dissociative electron attachment (DEA) and neutral photodissociation – shall be quantified, a thorough description of potential landscapes and electronic structures is paramount. Geometry and (non-degenerate) ground state total energy of the systems are determined applying density functional theory (DFT, see section 2.1 for the basics). This yields the basis for more sophisticated approaches, namely Hedin's GW approximation (GWA, section 2.7) and the Bethe-Salpeter equation (BSE, subsection 2.7.4), which are required for an adequate treatment of the electronic structures. The present study is "ab-initio", which, from a physical point of view, means that the corresponding approximations can be expressed solely by constants of nature. As will be seen, the low-energy range of the molecular dissociations is governed by conical intersections (section 2.8) between potential energy surfaces of different quantum mechanical states. Hence their properties, especially the conditions for their occurrence and their positions, have to be understood.

This chapter serves to explain the methodical aspects of the investigation. The task is to find suitable approximations, which scale down the computational effort to a feasible extent, but still capture the essential physics. Exact analytical solutions for realistic problems concerning the electronic structure of molecules or solids (bulk or surface) are practically unattainable, because the many electron Hamiltonian would have to be diagonalised.

DFT, which is a mean field theory, is based on the Born-Oppenheimer approximation (BOA, subsection 2.1.1), the Hohenberg-Kohn theorem (HKT, subsection 2.1.2) and the Kohn-Sham (KS) scheme (subsection 2.1.3). The BOA uses a product ansatz and neglects non-adiabatic coupling to separate ionic and electronic wave function of the system, which is justified by the mass ratio between electrons and atomic nuclei. The electron density of a quantum mechanical system can be mapped bijectively onto each stationary external potential applied to it as stated by the HKT for non-degenerate ground states. This leads to a problem of variational calculus as the electronic energy is a functional of the ground state density. The KS scheme, which is the reason for DFT being a mean field theory, addresses this by projecting the physical system onto a fictitious one with non-interacting electrons described by an orbital picture and an external potential making up for the lack of interaction.

It demonstrates that the problem basically consists in finding an appropriate functional for the energy contribution made by the exchange-correlation, which is the quantum mechanical part of the electron-electron interaction. Different approximations will be discussed (section 2.5).

Many body perturbation theory (MBPT) is required particularly since the molecular dissociations of course proceed through charged resp. excited states. The approach GW+BSE serves to overcome the insufficiency of independent-particle methods, like DFT, caused by many body effects such as self-energy resp. charge screening and collective excitations (here: electron-hole pairs). Hedin's GWA is obtained by neglecting vertex corrections. It makes use of the quasiparticle (QP) concept (section 2.7) to describe an excess electron and its polarisation cloud equivalently to a system of non-interacting electrons with modified masses and possibly finite lifetimes in free space. The role of GW selfconsistency has to be considered not only to estimate the error margin of non-selfconsistent calculations, but also to understand the importance of the underlying physical assumptions. As Hedin's GWA works "only" with a (causal) one-electron Green's function, it lacks to include interactions specific to collective excitations, here the Coulomb interaction between the components of an electron-hole pair. This deficiency is overcome by performing Bethe-Salpeter equation (BSE) calculations on top of it.

2.1. Basics of density functional theory

2.1.1. Adiabaticity: The Born-Oppenheimer approximation

An atomic ensemble (molecule or solid) consisting of cores (index c) and electrons (e) is treated. According to Schrödinger-picture quantum mechanics, its Hamilton operator $\hat{H}$ has the following shape.

$$\hat{H} = \hat{T}_\mathrm{c} + \hat{T}_\mathrm{e} + \hat{V}_\mathrm{cc} + \hat{V}_\mathrm{ee} + \hat{V}_\mathrm{ec} \tag{2.1}$$

$\hat{T}_\mathrm{c}$ and $\hat{T}_\mathrm{e}$ are the kinetic energy operators of the cores (indices I, spatial coordinates $\mathbf{R}_\mathrm{I}$) resp. electrons (i, $\mathbf{r}_\mathrm{i}$).

$$\hat{T}_\mathrm{c} = -\sum_\mathrm{I} \frac{\hbar^2}{2M_\mathrm{I}} \frac{\partial^2}{\partial \mathbf{R}_\mathrm{I}^2} \quad \wedge \quad \hat{T}_\mathrm{e} = -\frac{\hbar^2}{2m_\mathrm{e}} \sum_\mathrm{i} \frac{\partial^2}{\partial \mathbf{r}_\mathrm{i}^2} \tag{2.2}$$

The core masses are denoted as M_I, while m_e is the electron mass. The coulombic interaction potentials are already known from classical mechanics.

$$\hat{V}_\mathrm{cc} = \frac{1}{2} \frac{e^2}{4\pi\varepsilon_0} \sum_{\mathrm{I}\neq\mathrm{J}} \frac{Z_\mathrm{I} Z_\mathrm{J}}{\left|\mathbf{R}_\mathrm{I} - \mathbf{R}_\mathrm{J}\right|} \quad \wedge \quad \hat{V}_\mathrm{ee} = \frac{1}{2} \frac{e^2}{4\pi\varepsilon_0} \sum_{\mathrm{i}\neq\mathrm{j}} \frac{1}{\left|\mathbf{r}_\mathrm{i} - \mathbf{r}_\mathrm{j}\right|} \tag{2.3}$$

Z stands for the proton number. The coefficient $\frac{1}{2}$ is necessary to avoid double counting.

$$\hat{V}_{\mathrm{ec}} = -\frac{e^2}{4\pi\varepsilon_0}\sum_{\mathrm{I,i}}\frac{Z_{\mathrm{I}}}{|\mathbf{R}_{\mathrm{I}}-\mathbf{r}_{\mathrm{i}}|} \tag{2.4}$$

The Born-Oppenheimer approximation (BOA) applies a product ansatz (2.5) to split up the wave function Ψ of the system into core (χ) and electronic (Φ) part[1]. It assumes that the electrons adiabatically follow the cores, hence χ depends only on $\mathbf{Q}$ and the $\mathbf{Q}$-dependence of Φ is only parametric.

$$\Psi(\mathbf{q},\mathbf{Q}) = \chi(\mathbf{Q})\Phi(\mathbf{q};\mathbf{Q}) \tag{2.5}$$

The quotient of proton and electron mass is $\frac{m_{\mathrm{p}}}{m_{\mathrm{e}}} = 1836$, while for a typical semiconductor M_{I} is about four orders of magnitude larger than m_{e}. Hence the electrons follow the cores almost instantaneously, showing that the BOA makes sense.

$\hat{H}$ is the sum of core part $\hat{H}_{\mathrm{c}}$ and electronic part $\hat{H}_{\mathrm{e}}$, as defined by equations (2.6)-(2.8).

$$\hat{H} = \hat{H}_{\mathrm{c}} + \hat{H}_{\mathrm{e}} \tag{2.6}$$

$$\hat{H}_{\mathrm{c}} = \hat{T}_{\mathrm{c}} + \hat{V}_{\mathrm{cc}} \tag{2.7}$$

$$\hat{H}_{\mathrm{e}} = \hat{T}_{\mathrm{e}} + \hat{V}_{\mathrm{ee}} + \hat{V}_{\mathrm{ec}} \tag{2.8}$$

Thereby the stationary Schrödinger equation (2.9) for the system can be transformed as follows yielding (2.11).

$$\hat{H}\Psi(\mathbf{q},\mathbf{Q}) = E\Psi(\mathbf{q},\mathbf{Q}) \tag{2.9}$$

$$\begin{aligned}
&\hat{H}\Psi(\mathbf{q},\mathbf{Q}) \\
&\overset{(2.6)}{=} \chi(\mathbf{Q})\hat{H}_{\mathrm{e}}\Phi(\mathbf{q};\mathbf{Q}) + \hat{H}_{\mathrm{c}}\chi(\mathbf{Q})\Phi(\mathbf{q};\mathbf{Q}) \\
&\overset{(2.7),(2.8)}{=} \chi(\mathbf{Q})\hat{H}_{\mathrm{e}}\Phi(\mathbf{q};\mathbf{Q}) + \Phi(\mathbf{q};\mathbf{Q})\hat{H}_{\mathrm{c}}\chi(\mathbf{Q}) + \hat{T}_{\mathrm{c}}\chi(\mathbf{Q})\Phi(\mathbf{q};\mathbf{Q}) - \Phi(\mathbf{q};\mathbf{Q})\hat{T}_{\mathrm{c}}\chi(\mathbf{Q}) \\
&\overset{BOA}{\approx} \chi(\mathbf{Q})\hat{H}_{\mathrm{e}}\Phi(\mathbf{q};\mathbf{Q}) + \Phi(\mathbf{q};\mathbf{Q})\hat{H}_{\mathrm{c}}\chi(\mathbf{Q})
\end{aligned} \tag{2.10}$$

$$\overset{(2.9),(2.10)}{\Rightarrow} \chi(\mathbf{Q})\hat{H}_{\mathrm{e}}\Phi(\mathbf{q};\mathbf{Q}) + \Phi(\mathbf{q};\mathbf{Q})\hat{H}_{\mathrm{c}}\chi(\mathbf{Q}) = E\chi(\mathbf{Q})\Phi(\mathbf{q};\mathbf{Q}) \tag{2.11}$$

Non-adiabatic coupling between χ and Φ occurs as $\hat{T}_{\mathrm{c}}$ contains the second partial derivatives with respect to the core coordinates $\mathbf{Q}$ and Φ also exhibits a dependence on them. As previously explained, and displayed in (2.10), this is neglected by the BOA.

[1] The set $\{\mathbf{R}_{\mathrm{I}}\}$ of core coordinates is denoted as $\mathbf{Q}$, while $\mathbf{q}$ stands for the electronic set $\{\mathbf{r}_{\mathrm{i}}\}$.

(2.11) can be reformulated as one Schrödinger equation for each subsystem (see (2.13)), as $\mathbf{q}$ and $\mathbf{Q}$ are generally independent of each other allowing a comparison of coefficients. Furthermore the normalisation (2.12) of the wave functions is taken into account. The $\mathbf{Q}$-dependence of the energy eigenvalues $E^{\mathrm{e}}_{\mu}(\mathbf{Q})$ of the electronic system is again considered to be only parametric, since it comes solely from its wave function Φ. DFT treats the ground state, which is indicated by $\mu = 0$.

$$\langle\chi|\chi\rangle = \int \chi^*(\mathbf{Q})\chi(\mathbf{Q})d\mathbf{Q} = 1 \quad \wedge \quad \langle\Phi|\Phi\rangle = \int \Phi^*(\mathbf{q};\mathbf{Q})\Phi(\mathbf{q};\mathbf{Q})d\mathbf{q} = 1$$
$$\Rightarrow \langle\Psi|\Psi\rangle = \langle\chi|\chi\rangle\,\langle\Phi|\Phi\rangle = 1 \tag{2.12}$$

$$\hat{H}_{\mathrm{e}}\Phi(\mathbf{q};\mathbf{Q}) = E^{\mathrm{e}}(\mathbf{Q})\Phi(\mathbf{q};\mathbf{Q}) \quad \wedge \quad \hat{H}_{\mathrm{c}}\chi(\mathbf{Q}) = (E - E^{\mathrm{e}}_{\mu}(\mathbf{Q}))\chi(\mathbf{Q}) \tag{2.13}$$

The exact solution of the BOA could in principle be obtained by solving (2.13) analytically starting from the core equation, because the parametric $\mathbf{Q}$ is the expectancy value of the general $\mathbf{Q}$. Yet, this is too expensive for realistic problems. Hence further approximations are needed. The electrons are relaxed in a stationary structure of cores, which are treated classically. The cores are moved for a certain time step according to the resulting forces on them. This approach is iterated until energy differences and/or forces fulfill an arbitrary convergence criterion. See subsection 2.6.2 for the reduction of the forces.

The BOA links thermodynamics and quantum mechanics by being an application of the quantum mechanical adiabatic theorem, whose original form was presented by Max Born and Vladimir Fock in 1928 [69]. Any change of occupation numbers (heat transport, which can happen as energetic crossing of occupied and empty states might occur during electronic relaxation) is considered quasi-instantaneously, so that a change of energy eigenvalues (work, due to modifications of the core structure) is not possible during it. This decoupling of work and heat transport ensures the exclusion of non-adiabatic effects.

At this point the electron coordinates are the variables required to describe the quantum mechanical part of the problem. The Hohenberg-Kohn theorem (HKT) for non-degenerate ground states, which is proven in subsection 2.1.2, shows that it is sufficient to know the electronic charge density. Hence only three coordinates, instead of three for each electron, are needed. The restatement leads to a problem of variational calculus.

2.1.2. The Hohenberg-Kohn theorem: Electronic ground state density and variational principle

Each ground state density $n(\mathbf{r})$ of a quantum mechanical electronic system can only be related to one specific external potential $V_{\text{ext}}(\mathbf{r})$ applied to it and vice versa. This original version of the Hohenberg-Kohn theorem (HKT) was first formulated by Pierre Hohenberg and Walter Kohn in 1964 [70]. It is valid for all $V_{\text{ext}}(\mathbf{r})$, which lead to a non-degenerate electronic ground state. External potentials which differ by only a constant are of course equivalent. V_{cc} also becomes an external potential, but is merely a constant already determined by the parametric $\mathbf{Q}$ (see subsection 2.1.1).

The calculation of the electronic system eigenstates, which depend on all electron coordinates according to (2.13), is avoided by the HKT, because it shows that the electronic energy has to be a functional of $n(\mathbf{r})$.

Be $\{\mathbf{V_{ext}}\}$ the set of all external potentials and $\{\psi\}$ resp. $\{\mathbf{n}\}$ the set of all electronic ground state wave functions resp. densities, which result from them. A,B,BA are their mappings onto each other.

$$\begin{aligned} A &: \{\mathbf{V_{ext}}\} \to \{\psi\} \\ B &: \{\psi\} \to \{\mathbf{n}\} \\ BA &: \{\mathbf{V_{ext}}\} \to \{\mathbf{n}\} \end{aligned} \tag{2.14}$$

The HKT is true exactly if BA is bijective, i.e. surjective as well as injective, in any case. It will be demonstrated, that this is indeed the case, because A,B are also bijective $[(BA)^{-1} = A^{-1}B^{-1}]$.

A is surjective by construction. A reductio ad absurdum shows the injectivity of A. Assume there were two equal wave functions $|\psi_1\rangle$,$|\psi_2\rangle$ generated by the corresponding non-equivalent external potentials $V_{\text{ext},1}$,$V_{\text{ext},2}$.

$$\psi_1, \psi_2 \in \{\psi\} \quad \wedge \quad \psi_1 = \psi_2 \tag{2.15}$$

$$V_{\text{ext},1}, V_{\text{ext},2} \in \{\mathbf{V_{ext}}\} \quad \wedge \quad V_{\text{ext},1} \neq V_{\text{ext},2} + C \;\forall\, C \in \mathbb{R} \tag{2.16}$$

The definition of the Hamilton operators gives the following relations.

$$\begin{aligned} \hat{H}_1 = \hat{T} + \hat{U} + \hat{V}_{\text{ext},1} \quad \wedge \quad \hat{H}_2 = \hat{T} + \hat{U} + \hat{V}_{\text{ext},2} \\ \Rightarrow\; \hat{H}_1 - \hat{H}_2 = \hat{V}_{\text{ext},1} - \hat{V}_{\text{ext},2} \neq C \;\forall\, C \in \mathbb{R} \end{aligned} \tag{2.17}$$

This allows to create a contradiction.

$$\begin{aligned} \hat{H}_1 |\psi_1\rangle = E_1 |\psi_1\rangle \quad \wedge \quad \hat{H}_2 |\psi_2\rangle = E_2 |\psi_2\rangle \quad \wedge \quad \psi_1 = \psi_2 \\ \Rightarrow (\hat{H}_1 - \hat{H}_2) |\psi_1\rangle = (E_1 - E_2) |\psi_1\rangle \neq C |\psi_1\rangle \;\forall\, C \in \mathbb{R} \;\lightning \end{aligned} \tag{2.18}$$

Hence A has to be bijective.

B is also surjective by construction and the same method is applied to prove the injectivity. Consider two different wave functions ψ_1, ψ_2 leading to an identic ground state density $n(\mathbf{r})$.

$$\psi_1, \psi_2 \in \{\psi\} \quad \wedge \quad \psi_1 \neq \psi_2 \tag{2.19}$$

Proceed as previously.

$$\begin{gathered} \hat{H}_1 = \hat{T} + \hat{U} + \hat{V}_{\text{ext},1} \quad \wedge \quad \hat{H}_2 = \hat{T} + \hat{U} + \hat{V}_{\text{ext},2} \\ \Rightarrow \; \hat{H}_1 - \hat{H}_2 = \hat{V}_{\text{ext},1} - \hat{V}_{\text{ext},2} \end{gathered} \tag{2.20}$$

An upper boundary for the electronic energy E_1 resp. E_2 is calculated with the aid of the Rayleigh-Ritz variational principle (originally by John William Strutt 3rd baron Rayleigh in 1877 [71] and as a mathematical procedure by Walter Ritz in 1909 [72]). The case of equality is excluded due to the ground state non-degeneracy.

$$\begin{aligned} E_1 &= \left\langle \psi_1 \middle| \hat{H}_1 \middle| \psi_1 \right\rangle \\ &< \left\langle \psi_2 \middle| \hat{H}_1 \middle| \psi_2 \right\rangle \\ &= \left\langle \psi_2 \middle| \hat{H}_2 \middle| \psi_2 \right\rangle + \left\langle \psi_2 \middle| \hat{V}_{\text{ext},1} - \hat{V}_{\text{ext},2} \middle| \psi_2 \right\rangle \\ &= E_2 + \int_{\mathbb{R}^3} [V_{\text{ext},1}(\mathbf{r}) - V_{\text{ext},2}(\mathbf{r})] n(\mathbf{r}) d^3 r \end{aligned} \tag{2.21}$$

$$\begin{aligned} E_2 &= \left\langle \psi_2 \middle| \hat{H}_2 \middle| \psi_2 \right\rangle \\ &< \left\langle \psi_1 \middle| \hat{H}_2 \middle| \psi_1 \right\rangle \\ &= \left\langle \psi_1 \middle| \hat{H}_1 \middle| \psi_1 \right\rangle - \left\langle \psi_1 \middle| \hat{V}_{\text{ext},1} - \hat{V}_{\text{ext},2} \middle| \psi_1 \right\rangle \\ &= E_1 - \int_{\mathbb{R}^3} [V_{\text{ext},1}(\mathbf{r}) - V_{\text{ext},2}(\mathbf{r})] n(\mathbf{r}) d^3 r \end{aligned} \tag{2.22}$$

An impossible inequation is obtained.

$$\overset{(2.21)+(2.22)}{\Rightarrow} E_1 + E_2 < E_1 + E_2 \; \lightning \tag{2.23}$$

So B is also bijective. Therewith the proof of the HKT is completed.

Every element of $\{\psi\}$ is a function of 3N (spatial) coordinates ($\mathrm{N} \in \mathbb{N}$ being the number of electrons), while the elements of $\{\mathbf{V_{ext}}\}$ resp. $\{\mathbf{n}\}$ depend on only three. The electronic energy E, which results from ψ, has to be a functional of n, because the mapping

$$BA : \{\mathbf{V_{ext}}\} \to \{\mathbf{n}\} \tag{2.24}$$

is bijective according to the HKT. The ground state density n_0 leads to the ground state energy E_0, which is the minimum of all E obtainable from an arbitrary element of $\{\mathbf{n}\}$. The reformulated problem is of variational calculus and requires only three (spatial) coordinates.

$$E = E[n] \quad \wedge \quad E_0 = E[n_0] = \min_{n\in\{\mathbf{n}\}} \{E[n]\} \quad \text{with} \quad \int_{\mathbb{R}^3} n(\mathbf{r}) d^3r = \mathrm{N} \in \mathbb{N} \tag{2.25}$$

$$\left.\frac{\delta E[n]}{\delta n(\mathbf{r})}\right|_{n(\mathbf{r})=n_0(\mathbf{r})} = 0 \tag{2.26}$$

Like the Rayleigh-Ritz variational principle, the HKT enables approximations of ground state energies. Yet the latter approach is more sophisticated, since it is a functional, not a function, which has to be constructed.

2.1.3. The Kohn-Sham scheme

To construct the electronic energy functional $E[n]$ (proof of existence in subsection 2.1.2 (HKT)), Kohn and Sham came up with the scheme named after them in 1965 [73]. The basic idea of the Kohn-Sham (KS) scheme is to solve a fictitious system of non-interacting electrons, whose ground state density $n_\mathrm{s}(\mathbf{r})$ coincides with the one of the real system $n(\mathbf{r})$. This distribution not a priori known, but will result with the aid of a variational distribution $\rho(\mathbf{r})$ arising from the set of occupied variational orbitals $\{\tilde{\phi}_\mathrm{i}^\mathrm{occ}\}$.

$$n_\mathrm{s}(\mathbf{r}) = n(\mathbf{r}) \tag{2.27}$$

A new potential $V_\mathrm{s}(\mathbf{r})$ is applied to the fictitious system to make up for the neglect of electron-electron interaction. The problem can be reduced to a set of single particle equations (2.32), because $V_\mathrm{s}(\mathbf{r})$ is a single particle potential. Yet these have to be solved selfconsistently (iteratively in practice), as $V_\mathrm{s}(\mathbf{r})$ depends on $n(\mathbf{r})$. Like for the real system, ground state non-degeneracy of the fictitious system is also assumed. Hence $V_\mathrm{s}(\mathbf{r})$ exists (proof to be found in [74]) and is unique as already shown during the discussion of the HKT (bijectivity of mapping A from subsection 2.1.2).

The KS scheme employs an orbital picture to describe the non-interacting electrons. Each of them possesses an orbital wave function $\phi_\mathrm{i}(\mathbf{r})$. The fictitious ground state wave function $\psi_\mathrm{s}(\mathbf{r}_1, ..., \mathbf{r}_\mathrm{N})$ is obtained by applying the antisymmetriser $\mathscr{A}$ to the set $\{\phi_\mathrm{i}^\mathrm{occ}\}$ of correspondingly occupied orbitals. This leads to a Slater determinant, as it would e.g. also be used within the

Hartree-Fock approximation (HFA, subsection 2.5.1). Yet by incorporating correlation effects (section 2.5), the KS scheme goes beyond the HFA.

$$n(\mathbf{r}) = \sum_{i=1}^{N} |\phi_i(\mathbf{r})|^2 \tag{2.28}$$

$$\{\phi_i^{occ}\} = \{\phi_i | i = 1, ..., N\} \tag{2.29}$$

$$\begin{aligned} \psi_s(\mathbf{r}_1, ..., \mathbf{r}_N) &= \mathscr{A}(\{\phi_i^{occ}\}) = \frac{1}{\sqrt{N!}} \det\{\phi_i^{occ}(\mathbf{r}_j)\} \\ &= \frac{1}{\sqrt{N!}} \begin{vmatrix} \phi_1(\mathbf{r}_1) & \dots & \phi_1(\mathbf{r}_N) \\ \vdots & \ddots & \vdots \\ \phi_N(\mathbf{r}_1) & \dots & \phi_N(\mathbf{r}_N) \end{vmatrix} \end{aligned} \tag{2.30}$$

The orbital eigenfunctions constitute the set $\{\phi_i\}$ of solutions to the KS equations (2.32), which are single particle pseudo-Schrödinger equations, with the KS Hamiltonian defined in (2.31). They are numbered in ascending order of the corresponding eigenenergies ε_i, which are also called "KS energies".

$$\hat{H}_s = -\frac{\hbar^2}{2m_e}\nabla^2 + V_s(\mathbf{r}) \quad \text{with} \quad V_s(\mathbf{r}) = V_s([n], \mathbf{r}) \tag{2.31}$$

$$\hat{H}_s \phi_i(\mathbf{r}) = \varepsilon_i \phi_i(\mathbf{r}) \ \wedge \ \varepsilon_1 \leq \varepsilon_2 \leq ... \tag{2.32}$$

$\varepsilon_N < \varepsilon_{N+1}$ is necessary and sufficient for the non-degeneracy of the KS ground state.

Exploiting that the HKT applies to both systems, it is found that $n(\mathbf{r})$ must obey the condition (2.33).

$$\left.\frac{\delta E_s[\rho]}{\delta \rho(\mathbf{r})}\right|_{\rho(\mathbf{r})=n(\mathbf{r})} \overset{HKT}{=} 0 \tag{2.33}$$

$$\rho(\mathbf{r}) = \sum_{i=1}^{N} \left|\tilde{\phi}_i(\mathbf{r})\right|^2 \tag{2.34}$$

Hence solving the KS equations (2.32) can be reduced to mere calculation by appropriately constructing the energy functionals which add up to $E_s[\rho]$.

$E_s[\rho]$ is the sum of the Hohenberg-Kohn functional $F_{HK}[\rho]$, which is the intrinsic contribution of the real system, and $U_{ext}[\rho]$, which comes from the – stationary and local – external potential $V_{ext}(\mathbf{r})$ applied to it. $F_{HK}[\rho]$ incorporates kinetic, coulombic and exchange-correlation (XC) effects.

$$E_s[\rho] = F_{HK}[\rho] + U_{ext}[\rho] \quad \wedge \quad F_{HK}[\rho] = T_s[\rho] + E_H[\rho] + E_{XC}[\rho] \tag{2.35}$$

Constructing the functionals for potential energy $U_{\text{ext}}[\rho]$ and kinetic energy $T_{\text{s}}[\rho]$ is superficial. In principle this is also the case for the Hartree functional $E_{\text{H}}[\rho]$, which deals with the classical part of the electron-electron (two particle) interaction. Yet as $\rho(\mathbf{r})$ is quantum mechanical in itself, $E_{\text{H}}[\rho]$ is affected by a self-interaction error (SIE [75, 76]). The SIE is negligible in the given context.

$$U_{\text{ext}}[\rho] = \int_{\mathbb{R}^3} V_{\text{ext}}(\mathbf{r})\rho(\mathbf{r})d^3r \tag{2.36}$$

$$T_{\text{s}}[\rho] = \sum_{\tilde{\phi}_{\text{i}} \in \{\tilde{\phi}_{\text{i}}^{\text{occ}}\}} \left\langle \tilde{\phi}_{\text{i}} \middle| \hat{T}_{\text{e}} \middle| \tilde{\phi}_{\text{i}} \right\rangle = \sum_{\text{i}=1}^{\text{N}} \int_{\mathbb{R}^3} \tilde{\phi}_{\text{i}}^{*}(\mathbf{r}) \frac{-\hbar^2}{2m_{\text{e}}} \nabla^2 \tilde{\phi}_{\text{i}}(\mathbf{r}) d^3r \tag{2.37}$$

$$E_{\text{H}}[\rho] = \frac{1}{2}\int_{\mathbb{R}^3} \rho(\mathbf{r}) V_{\text{H}}([\rho], \mathbf{r}) d^3r = \frac{1}{2}\frac{e^2}{4\pi\varepsilon_0} \int_{\mathbb{R}^3}\int_{\mathbb{R}^3} \frac{\rho(\mathbf{r})\rho(\mathbf{r}')}{|\mathbf{r}-\mathbf{r}'|} d^3r' d^3r \tag{2.38}$$

Only the XC-functional $E_{\text{XC}}[\rho]$, which treats the quantum mechanical part of the electron-electron interaction, remains to be constructed. Solving this problem exactly is prohibited by computational effort, but section 2.5 discusses workable approximations speaking for the importance of the KS scheme. With that $V_{\text{s}}([\rho], \mathbf{r})$ and $E_{\text{s}}[\rho]$ are given according to (2.39) and (2.40).

$$V_{\text{s}}([\rho], \mathbf{r}) = \frac{\delta(U_{\text{ext}}[\rho] + E_{\text{H}}[\rho] + E_{\text{XC}}[\rho])}{\delta\rho(\mathbf{r})} = V_{\text{ext}}(\mathbf{r}) + V_{\text{H}}([\rho], \mathbf{r}) + \frac{\delta E_{\text{XC}}[\rho]}{\delta\rho(\mathbf{r})} \tag{2.39}$$

$$E_{\text{s}}[\rho] = T_{\text{s}}[\rho] + \int_{\mathbb{R}^3} V_{\text{s}}([\rho], \mathbf{r})\rho(\mathbf{r}) d^3r \tag{2.40}$$

2.2. Bloch theorem: Periodic boundary conditions and plane wave basis set

A thorough description of electronic structures requires a convenient wave function basis set. To investigate strongly bound electrons ("core electrons"), atom centered functions, e.g. spherical harmonics (paradigmatic hydrogen orbitals), are usually chosen. However this is not always a feasible approach if chemical bonding – in a molecule or solid – is considered. The valence electrons, which are responsible for it, delocalise and extend into the interstitial regions. This effect is particularly strong in metals, whose electronic structure is hence not well captured by a, chemically motivated, ansatz of covalent bonds between nearest neighbours. Since the valence electrons can then no longer be assigned to single atoms, untenably many of the aforementioned functions would be needed to represent their orbitals (as linear combinations

of them). The usage of periodic boundary conditions (PBC) is especially motivated by crystal structures. Hereunder a basis set of plane waves, which are delocalised and more suited to approach the problem, can be employed. This is ensured by the Bloch theorem[2], which was first deduced by Felix Bloch in 1929 [78], as will be elucidated in this section.

May $\mathbf{a}_1, \mathbf{a}_2, \mathbf{a}_3$ generate the primitive unit cell. The Bravais lattice is the set of all their integral linear combinations $n_1\mathbf{a}_1 + n_2\mathbf{a}_2 + n_3\mathbf{a}_3 = \sum_i n_i\mathbf{a}_i$ with $\mathbf{n} = (n_1, n_2, n_3)^T \in \mathbb{Z}^3$. The defining property of the primitive reciprocal lattice vectors $\mathbf{b}_1, \mathbf{b}_2, \mathbf{b}_3$ is $\langle \mathbf{a}_i.\mathbf{b}_j \rangle = 2\pi\delta_{ij} \forall i,j = 1,2,3$. Any reciprocal lattice vector $\mathbf{K}$ can be written as $\mathbf{K} = \sum_i m_i\mathbf{b}_i = m_1\mathbf{b}_1 + m_2\mathbf{b}_2 + m_3\mathbf{b}_3$ with $\mathbf{m} = (m_1, m_2, m_3)^T \in \mathbb{Z}^3$, whereby the reciprocal lattice is defined analogously to the Bravais lattice. The translation operator $\hat{T}_\mathbf{n}$ serves to shift the wave function $\phi(\mathbf{r})$ of an electron by the lattice vector $-\sum_i n_i\mathbf{a}_i$.

$$\hat{T}_\mathbf{n}\phi(\mathbf{r}) = \phi(\mathbf{r} + \sum_i n_i\mathbf{a}_i) \quad \forall \quad \mathbf{n} \in \mathbb{Z}^3 \tag{2.41}$$

If the interaction of electrons with each other is neglected, like e.g. in a fictitious Kohn-Sham system (subsection 2.1.3), they are sometimes called "Bloch electrons". Their eigenenergies are then called "Bloch energies". The Bloch theorem states, that a wave function basis set with properties 1 and 2 exists for Bloch electrons in any perfect crystal.

1. Each of the basis functions ϕ_i is a Bloch energy eigenstate, i.e. $\hat{H}(\mathbf{r})\phi_i(\mathbf{r}) = \varepsilon_i\phi_i(\mathbf{r})$.

2. Every basis function ϕ is a Bloch wave, i.e. it can be displayed as $\phi(\mathbf{r}) = e^{i\langle \mathbf{k}.\mathbf{r} \rangle}u(\mathbf{r})$, where $\mathbf{k}$ lies within the first Brillouin zone and $u(\mathbf{r})$ exhibits the periodicity of the crystal lattice[3].

Since the unit cell is primitive, it should even be the same periodicity. Then the Bloch waves must be plane waves, because planes of equal phase angle $\langle \mathbf{k}.\mathbf{r} \rangle$ are always orthogonal to the fixed vector $\mathbf{k}$. Hence their direction of propagation is spatially constant.

This lemma regarding the eigenstates of the translation operators $\hat{T}_\mathbf{n}$ helps to prove the Bloch theorem.

[2] The Bloch theorem is a physical application of the Floquet theorem (Gaston Floquet 1883 [77]), which is a mathematical proposition about the structure of the fundamental matrices of a homogeneous linear ordinary differential equation system with a periodic coefficient matrix.

[3] It would be possible to write $\mathbf{k} + \mathbf{K}$ instead of $\mathbf{k}$, where $\mathbf{K}$ could be any reciprocal lattice vector. Yet then $u(\mathbf{r})$ would have to be replaced with $e^{-i\langle \mathbf{K}.\mathbf{r} \rangle}u(\mathbf{r})$, such that $\phi(\mathbf{r})$, which captures the quantum state of the electron, is reproduced. To avoid this redundancy $\mathbf{k}$ is restricted to the first Brillouin zone, which is the Wigner-Seitz cell of the reciprocal lattice.

- If a wave function ϕ is a simultaneous eigenstate of all translation operators $\hat{T}_{\mathbf{n}\in\mathbb{Z}^3}$, then ϕ is a Bloch wave.

The crystal symmetry compels the translation eigenvalues to be phase factors, i.e. their absolute value has to be 1. Considering this, the lemma can be proven straightforwardly.

$$\hat{T}_{\mathbf{n}}\phi(\mathbf{r}) = \phi(\mathbf{r}+\sum_{\mathrm{i}} n_{\mathrm{i}}\mathbf{a}_{\mathrm{i}}) = C_{\mathbf{n}}\phi(\mathbf{r}) \quad \wedge \quad |C_{\mathbf{n}}| = 1 \quad \forall \quad \mathbf{n}\in\mathbb{Z}^3 \tag{2.42}$$

$$\hat{T}_{\mathbf{n}} = \prod_{\mathrm{i}} \hat{T}_{\mathbf{e}_{\mathrm{i}}}^{n_{\mathrm{i}}} \tag{2.43}$$

$$C_{\mathrm{j}} \coloneqq C_{\mathbf{e}_{\mathrm{j}}} \quad \forall \quad \mathrm{j} = 1,2,3 \tag{2.44}$$

$$\Rightarrow \hat{T}_{\mathbf{n}}\phi(\mathbf{r}) = (\prod_{\mathrm{i}} \hat{T}_{\mathbf{e}_{\mathrm{i}}}^{n_{\mathrm{i}}})\phi(\mathbf{r}) = (\prod_{\mathrm{j}} C_{\mathrm{j}}^{n_{\mathrm{j}}})\phi(\mathbf{r}) \tag{2.45}$$

$$\Rightarrow C_{\mathbf{n}} = \prod_{\mathrm{j}} C_{\mathrm{j}}^{n_{\mathrm{j}}} \tag{2.46}$$

$$C_{\mathrm{j}} = e^{2\pi i\theta_{\mathrm{j}}} \quad \text{with} \quad \theta_{\mathrm{j}} \in [-\frac{1}{2};+\frac{1}{2}) \tag{2.47}$$

$$u(\mathbf{r}) \coloneqq e^{-i\langle\mathbf{k}.\mathbf{r}\rangle}\phi(\mathbf{r}) \quad \wedge \quad \mathbf{k} = \sum_{\mathrm{j}} \theta_{\mathrm{j}}\mathbf{b}_{\mathrm{j}} \tag{2.48}$$

$$\begin{aligned} \Rightarrow u(\mathbf{r}+\mathbf{a}_{\mathrm{j}}) &= e^{-i\langle\mathbf{k}.(\mathbf{r}+\mathbf{a}_{\mathrm{j}})\rangle}\phi(\mathbf{r}+\mathbf{a}_{\mathrm{j}}) = e^{-i\langle\mathbf{k}.\mathbf{r}\rangle}e^{-i\langle\mathbf{k}.\mathbf{a}_{\mathrm{j}}\rangle}\hat{T}_{\mathbf{e}_{\mathrm{j}}}\phi(\mathbf{r}) \\ &= e^{-2\pi i\theta_{\mathrm{j}}}e^{2\pi i\theta_{\mathrm{j}}}e^{-i\langle\mathbf{k}.\mathbf{r}\rangle}\phi(\mathbf{r}) = u(\mathbf{r}) \end{aligned} \tag{2.49}$$

$$\Rightarrow u(\mathbf{r}+\sum_{\mathrm{i}} n_{\mathrm{i}}\mathbf{a}_{\mathrm{i}}) = u(\mathbf{r}) \tag{2.50}$$

Hence ϕ is indeed always a Bloch wave.

Every $\hat{T}_{\mathbf{n}}$ commutes with the Hamiltonian $\hat{H}$, which can be written as $\hat{H}(\mathbf{r})$ since merely Bloch electrons in a fixed core geometry are treated. $\hat{H}(\mathbf{r}+\sum_{\mathrm{i}} n_{\mathrm{i}}\mathbf{a}_{\mathrm{i}}) = \hat{H}(\mathbf{r})$ is valid due to symmetry reasons. Assume ϕ is an arbitrary element of the energy eigenbasis, i.e. $\hat{H}\phi = \varepsilon\phi$.

$$\begin{aligned} \hat{H}(\mathbf{r})\hat{T}_{\mathbf{n}}\phi(\mathbf{r}) &= \hat{H}(\mathbf{r})\phi(\mathbf{r}+\sum_{\mathrm{i}} n_{\mathrm{i}}\mathbf{a}_{\mathrm{i}}) = \hat{H}(\mathbf{r}+\sum_{\mathrm{i}} n_{\mathrm{i}}\mathbf{a}_{\mathrm{i}})\phi(\mathbf{r}+\sum_{\mathrm{i}} n_{\mathrm{i}}\mathbf{a}_{\mathrm{i}}) \\ &= \varepsilon\phi(\mathbf{r}+\sum_{\mathrm{i}} n_{\mathrm{i}}\mathbf{a}_{\mathrm{i}}) = \varepsilon\hat{T}_{\mathbf{n}}\phi(\mathbf{r}) = \hat{T}_{\mathbf{n}}\varepsilon\phi(\mathbf{r}) = \hat{T}_{\mathbf{n}}\hat{H}(\mathbf{r})\phi(\mathbf{r}) \end{aligned} \tag{2.51}$$

$$\Rightarrow [\hat{H}(\mathbf{r}), \hat{T}_{\mathbf{n}}]_- = 0 \tag{2.52}$$

Because they commute, a simultaneous eigenbasis of $\hat{H}$ and $\hat{T}_{\mathbf{n}\in\mathbb{Z}^3}$ exists. This is exactly the one searched for in order to prove the Bloch theorem.

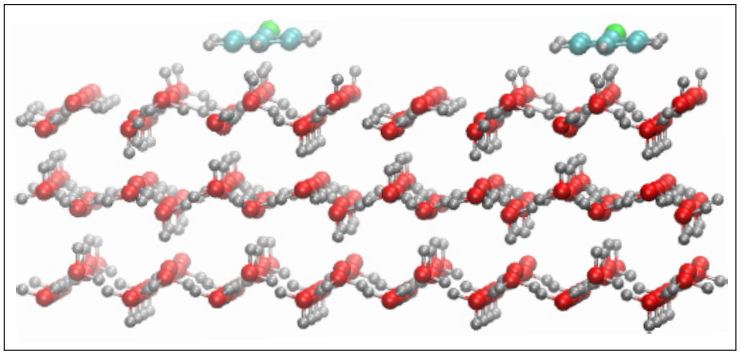

Figure 2.1.: $I_h(0001)$ surface supercell with phenyl bromide (C_6H_5Br) molecule adsorbed at a $4S_{AD}$ orientational defect complex repeated along the surface orthogonal to the Fletcher stripes due to PBC (parallel repetition and vacuum region left out for reasons of clarity); (O in red, H in silver, C in cyan, Br in green)

Crystals are regular periodic arrangements of atoms by definition. Hence it is natural to describe a perfect crystal by a unit cell containing a subset of atoms, which is irreducible regarding translational symmetry operations and repeated as permitted by any integral linear combination of the lattice vectors. However the main interest here lies on crystal surfaces with defects and adsorbed molecules (cf. Fig. 2.1). These break all three discrete translational invariances given by the basis vectors of the pristine bulk unit cell. The strategy is to build a supercell composed of a slab and a vacuum region. Spurious interactions occur inside the supercell as well as between its periodic images. A suitable geometry reduces them to a tolerable degree. If the slab possesses a sufficiently large number of crystal planes, its surfaces are effectively decoupled and the bulk properties are recreated in its center. The two surface parallel basis vectors often have to be elongated (integral multiples), such that defects resp. adsorbed molecules are practically isolated from their periodic images on the same surface. The remaining basis vector serves to modify the vacuum distance, which is vital as the supercell also interacts with its periodic images in the corresponding direction.

For a fictitious Kohn-Sham system (subsection 2.1.3) PBC make the Bloch theorem applicable[4]. Though a real solid exhibits irregularly occurring defects and in a certain manner finite size effects, which can not be accounted for by a periodic model. There are two edge cases: a pristine bulk state (such as in Fig. 2.2) and a single atom or molecule (such as in Fig. 2.3). The former is ideal as perfect crystallisation and infinite volume avoid the aforementioned sources

[4] A Fourier expansion of the solutions to the Kohn-Sham equations is often helpful as they exhibit the periodicity of the external potential (except for a phase factor, which is also periodical).

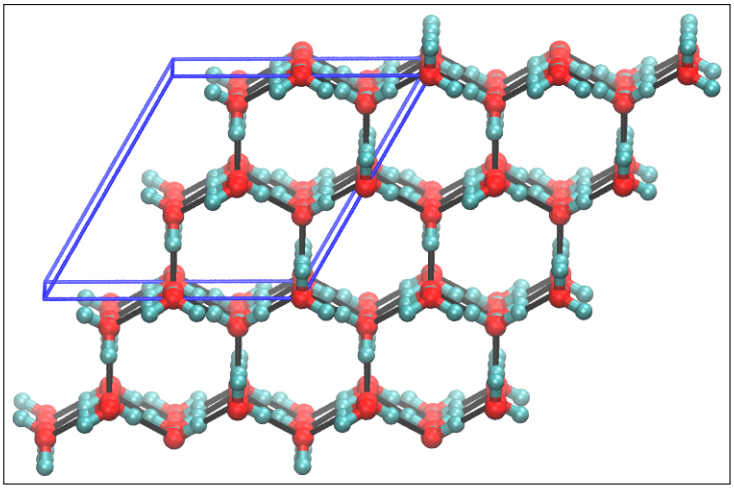

Figure 2.2.: Bulk structure of pristine antiferroelectric ice I_h (16 H_2O molecules supercell marked and repeated), exemplifying the application of PBC to simulate a solid; (H in cyan, O in red)

of errors, which is why the periodic supercell and the primitive unit cell of the crystal lattice are identical. Unlike a crystal lattice, a single atom or molecule has no translational periodicity by itself. Therefore any interaction between the structure within the supercell and its periodic images is spurious. The introduction of vacuum regions in all three independent spatial directions is hence necessitated. This leads to a huge supercell size and a consequently huge plane wave basis set. Then the worst case in terms of relative computational cost is present.

Section 2.3 includes a discussion of the fact that the plane wave basis set also has to be restricted in terms of energy.

2.3. Pseudopotential formalism

The wave functions of more strongly bound electrons exhibit higher Fourier components and hence their treatment requires an inflated plane wave basis set. Yet as core electrons are largely irresponsible for the chemical bonding, including them might just make the investigation unnecessarily cumbersome. This problem is addressed by the pseudopotential (PP) formalism [79–81], whose key concept is to replace nucleus and core electrons of an atom by an effective potential (the PP, scheme Fig. 2.4), so that only the valence electrons are treated explicitly. This allows to keep the plane wave basis set at a reasonable size, but quite some conditions must be respected to obtain a workable PP,

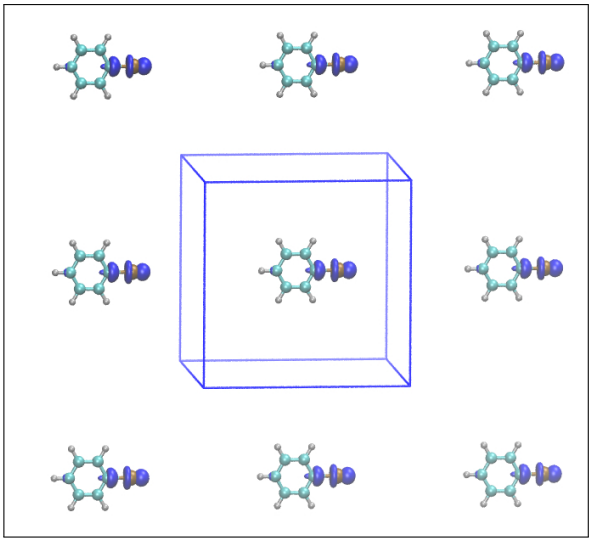

Figure 2.3.: Phenyl chloride (C_6H_5Cl) with σ_s^* orbital and marked, repeated supercell, demonstrating the use of PBC in simulating a single molecule; (C in cyan, H in silver, Cl in ochre)

which is an iterative process (flowchart Fig. 2.5). An explanation of underlying physics, construction and basic features is given.

Any electronic wave function could be expanded employing a plane wave basis set as stated by the Bloch theorem (section 2.2). However electrons in the vicinity of an atomic nucleus have larger momentum and correspondingly smaller matter wavelength, because the centrifugal force has to compensate for the attractive coulombic force. Hence their wave functions oscillate more rapidly involving higher Fourier components. Albeit the valence region corresponds to the lower kinetic energy range and the main interest lies on this part of the electronic structure, as it is most specific to the chemical bonding in a molecule or solid, which does not occur for a single atom. Furthermore as non-valence electrons are largely unaffected by the chemical bonding, their wave functions resemble their single atom equivalents. It turns out that the aforementioned approach is needlessly complicated and might not be feasible due to computational effort.

The PP for a single atom resp. one of its ions (cf. Fig. 2.4) is located in the core region ($r < r_c$) defined by the cutoff radius r_c, which is the upper limit of the distance r from the nucleus. There it must be weak compared to the real potential in order to avoid rapid oscillations of the valence wave functions, whose description would necessitate an inflated plane wave basis set. The asymptotics of the real potential is $-\frac{Z}{r}$ for $r \searrow 0$, because the screening of the

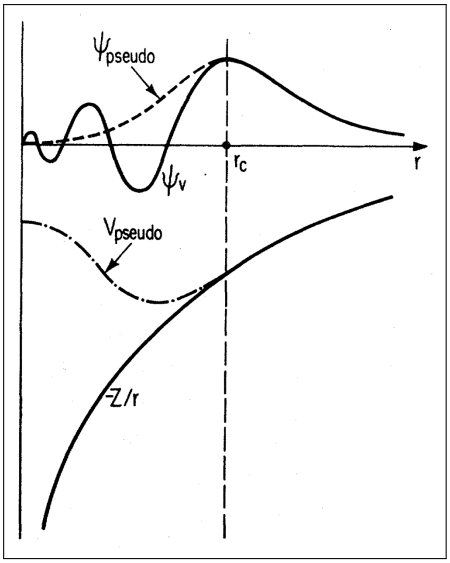

Figure 2.4.: Schematic comparison between all-electron (AE) and pseudised (PS) valence wave functions and potentials, matching of AE and PS values from the cutoff radius r_c on [82]

nucleus due to electrons vanishes. Outside there is no change of the potential. The valence all-electron (AE) wave function shall be extended from the valence region ($r \geq r_c$) to the core region without having to introduce additional plane waves. Hence the PP is tailored in such a way that it leads to a radially nodeless wave function there. Note that despite the reduction of computational effort, r_c needs to be limited as capturing the chemical bonding accurately must be enabled. Otherwise the transferability of the PP, i.e. its applicability in a preferably large variety of different chemical environments, would diminish. The following points are crucial to the construction of a workable PP.

- It must possess the same scattering properties as the real core region. In particular its phase shifts need to have the same effect as those of the real core region.
- The resulting "pseudised" (PS) wave function is forced to coincide with the valence AE wave function in the valence region.

In the core region, the AE valence wave functions are smoothened by subtracting their projections on the core states. The PS states created thereby obey a new stationary Schrödinger equation, where the Hamilton operator is modified by an additional potential operator $\hat{V}_{\mathrm{NL}}$. Due to the aforementioned

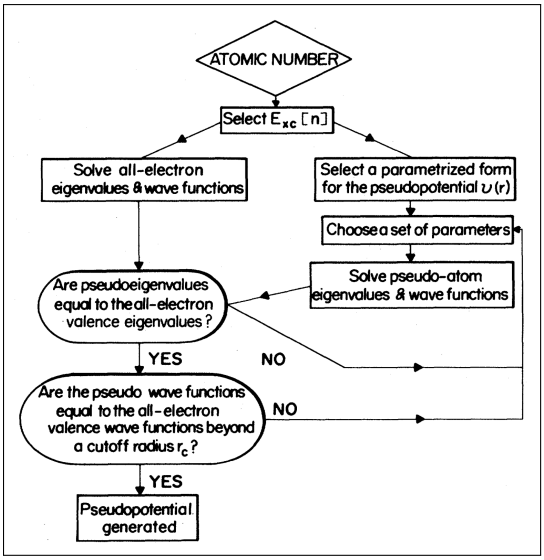

Figure 2.5.: Flowchart displaying the iterative calculation of an ionic pseudopotential (PP) for an atom of a specific chemical element (taken from [82])

involvement of the core states, which the PP formalism does not treat explicitly, in the construction of $\hat{V}_{\mathrm{NL}}$, it depends not only on the local coordinates, but also on angular momenta and eigenenergies. To calculate the scattering of a valence wave function by an alien core potential, the spherical symmetry of the latter is exploited. The incoming plane wave is decomposed into a sum over spherical partial waves, which are products of a radial and an angular wave part. Their elastic scattering introduces phase shifts related to their angular momenta and the eigenenergy of the incoming plane wave. Due to the periodicity of the scattering amplitude reduced phase shifts, which lead to radially nodeless scattered waves, can be used. The total scattered wave results from recombining the phase shifted partial waves. The PP is the potential whose complete phase shifts are the reduced phase shifts.

The most general form of a PP is given by the operator $\hat{V}_{\mathrm{NL}}$.

$$\hat{V}_{\mathrm{NL}} = \sum_{\mathrm{lm}} |\mathrm{lm}\rangle \, V_{\mathrm{l}} \, \langle \mathrm{lm}| \tag{2.53}$$

$|\mathrm{lm}\rangle$ are the spherical harmonics and V_{l} is the PP for angular momentum (quantum number) l. Acting on an electronic wave function $|\phi\rangle$ with $\hat{V}_{\mathrm{NL}}$ projects it onto the spherical harmonics (coefficient $\langle \mathrm{lm}|\phi\rangle$), each of which is then multiplied by the respective PP V_{l}. Generally a PP is "non-local" (NL), i.e. it acts differently on electrons with different l. If this is not the case, the PP is practically only a function of r and is hence called "local".

The construction of an ionic PP for an atom of a specific chemical element is an iterative process. The flowchart Fig. 2.5 displays the standard generation procedure. AE calculations with an underlying exchange-correlation (XC) functional (see section 2.5), which has to be chosen in order to approximate the quantum mechanical part of the electron-electron interaction, are performed for the ground state and some excited states of the isolated atom, whereby AE eigenvalues and wave functions are provided. A parametrised form of the PP is selected in order to adjust it iteratively. After matching the valence AE and PS eigenvalues, the parameter values are again iteratively adjusted until the valence wave functions in the valence region also match. Finally the PP is generated fulfilling both conditions. It is used without further modifications in different chemical environments. Note that this requires a certain scope of PP transferability, which tends to widen as the cutoff radius r_c is lowered.

For the PP transferability, it is important that the energy dependence of the phase shifts is correct in first order. This is ensured by a property called "norm-conservation", which states that the integrals over the squared amplitude (particle number density) of PS and valence AE wave function in the core region must be identical. Norm-conservation is also required to guarantee the coincidence of the aforementioned wave functions in the valence region, which is vital as the total energy is not only influenced by the spatial shape of the charge density but also its absolute value.

To keep the plane wave basis set at a reasonable size, an "energy cutoff" E_{cut} is introduced. Wave functions calculated according to the PP formalism can not exhibit Fourier components corresponding to higher kinetic eigenenergies. A PP is called "smooth", if it requires only a small plane wave basis set. While this is obviously desirable, E_{cut} must not be too low as an adequate modelling of the wave functions has to be enabled. Furthermore this value is not incorporated in the standard PP generation procedure (cf. Fig. 2.5). As the convergence properties are affected, it is not a priori clear if this is justifiable. On the other hand fixing E_{cut} would be questionable as the system under consideration is generally composed of several different chemical elements. Furthermore it might also depend on practical aspects like the computational power available or the accuracy required. There are different approaches to the problem like producing a more rapidly convergent potential [83], applying a separate optimisation procedure afterwards [84] or even relaxing the norm conservation of the PP [85, 86].

A further advantage of the PP formalism is the much smaller relative accuracy required to calculate energy differences between ionic configurations. The total energy of the valence electron system ($\sim$eV) is typically three orders of magnitude smaller than that of the AE system ($\sim$keV). Yet for realistic prob-

lems it is almost exclusively the valence system which may exhibit significant changes of the electronic eigenenergies.

Scattering experiments provide PP quality tests. Historically PPs were initially constructed empirically from the spectra of solids and ions. Yet over the course of time it turned out that ab-initio PPs are preferable, because the deep-lying core states can be accessed more easily by calculation than by measurement.

The unphysical core part can be remedied by reconstructing the complete valence AE wave function from the PS wave function if the PP fulfills the aforementioned conditions. This process, by which the valence AE charge density is acquired, is outlined in section 2.4.

2.4. Blöchl's projector augmented wave method

In 1994 Blöchl published his projector augmented wave (PAW) method [87] (later modified by Kresse and Joubert [88]), which combines the pseudopotential formalism (see section 2.3) and the linear augmented plane wave (LAPW, [89–91]) method to enable a more efficient treatment of electronic structures. Augmented wave methods are based on the "frozen core approximation", which assumes that the all-electron wave function in the core region, which is barely affected by the chemical bonding, is identical to its single atom equivalent. The PAW method starts from the pseudised wave function and improves over it by making the core part exact in terms of the frozen core approximation.

In the PAW method equation 2.54 serves to reconstruct the valence all-electron wave function ψ from the pseudised wave function $\tilde{\psi}$.

$$|\psi_n\rangle = |\tilde{\psi_n}\rangle + \sum_i (|\phi_i\rangle - |\tilde{\phi_i}\rangle)\langle\tilde{p_i}|\tilde{\psi_n}\rangle \tag{2.54}$$

The electronic state is denoted by the index "n", which also includes the wave vector $\mathbf{k}$ and spin. The index "i" is an abbreviation for $\mathbf{R}$ (atomic nucleus and core region), orbital angular momentum quantum number l, magnetic quantum number m and wave vector $\mathbf{k}$ respective to the reference energy $\varepsilon_{\mathbf{k}l}$. Blöchl defined the projector functions $\tilde{p}_i$, with whose aid the pseudised partial waves $\tilde{\phi}_i$ are replaced by their all-electron equivalents ϕ_i obtained from single atom calculations.

The $\tilde{p}_i$ act only in the core region, where the frozen core approximation applies, and vanish outside. This is ensured by including a radial cutoff function $f(r)$ in their definition. $\Theta(r)$ is Heaviside's unit step function.

$$f = f(r) = 1 - \Theta(r - r_c) = \Theta(r_c - r) \tag{2.55}$$

Note that the core radius r_c can in general depend on l, if the pseudopotential is non-local. Where they act, the $\tilde{p}_i$ are linear combinations of the $\tilde{\phi}_i$ with the expansion coefficients α_{ij}.

$$|\tilde{p}_i\rangle = \sum_j f\left|\tilde{\phi}_j\right\rangle \alpha_{ij} \tag{2.56}$$

If the set $\{\tilde{p}_i\}$ of all projector functions is complete, they allow to decompose the core part of the pseudised wave function into pseudised partial waves.

$$|\tilde{\psi}\rangle = \sum_i |\tilde{\phi}_i\rangle\langle\tilde{p}_i|\tilde{\psi}\rangle \;\forall\; r < r_c \tag{2.57}$$

Together with the linear independency of the elements of $\{\tilde{\phi}_i\}$, this is also the reason for the following "mixed orthonormality" relation.

$$\langle\tilde{p}_i|\tilde{\phi}_j\rangle = \sum_k \alpha_{ki}\langle\tilde{\phi}_k|f\left|\tilde{\phi}_j\right\rangle = \delta_{ij} \tag{2.58}$$

By defining the expansion coefficients α_{ki} in such a way as to fulfill this relation, it is guaranteed that the $\langle\tilde{p}_i|$ indeed project $|\tilde{\psi}\rangle$ on the pseudised partial waves $|\tilde{\phi}_i\rangle$. That is proven by a simple calculation (β_j are again expansion coefficients).

$$\begin{aligned} &|\tilde{\psi}\rangle = \sum_j \beta_j \left|\tilde{\phi}_j\right\rangle \\ &\Rightarrow \langle\tilde{p}_i|\tilde{\psi}\rangle = \sum_j \beta_j \langle\tilde{p}_i|\tilde{\phi}_j\rangle = \sum_j \beta_j \delta_{ij} = \beta_i \\ &\Rightarrow |\tilde{\psi}\rangle = \sum_i |\tilde{\phi}_i\rangle\langle\tilde{p}_i|\tilde{\psi}\rangle \;\forall\; r < r_c \end{aligned} \tag{2.59}$$

Equation (2.58) shows that the expansion coefficients are simply the elements of the matrix obtained by inverting the matrix defined by the $\langle\tilde{\phi}_k|f\left|\tilde{\phi}_j\right\rangle$. The order of line and column index does not even matter here, because the matrices are symmetrical (inverting a symmetrical matrix gives a symmetrical matrix if possible).

The PAW method is advantageous since the pseudised wave function can be expanded in a basis of plane waves, while the (valence) charge density $n(\mathbf{r})$ underlying the total energy calculation has the quality of an all-electron wave function. $n(\mathbf{r})$ is split up into three contributions according to equations (2.60)-(2.62) proven by (2.63). Apart from the "pseudo charge density" $\tilde{n}(\mathbf{r})$ calculated directly from the pseudised wave functions on a plane wave grid, there are the one-center contributions called "onsite charge densities" $n^1(\mathbf{r})$, $\tilde{n}^1(\mathbf{r})$ treated on a radial support grid, which extends up to radius r_{rad} around

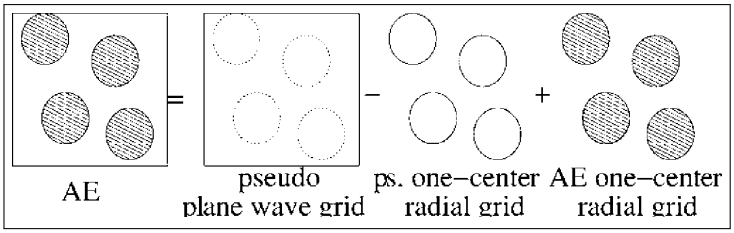

Figure 2.6.: Illustration of additive augmentation in the PAW method [92]

the centers of the core regions (for simplicity first imagine a system with only one chemical element, pseudopotential locality and $r_{rad} = r_c$). To avoid creating errors, the partial wave expansions of pseudised and all-electron wave functions have to be truncated in a fully analogous way. This principle of "additive augmentation" is depicted in Fig. 2.6. Its major importance will become more evident in the remainder of this section, because it increases the feasibility of the calculations.

$$n(\mathbf{r}) = \sum_n f_n \langle \psi_n | \mathbf{r} \rangle \langle \mathbf{r} | \psi_n \rangle = \tilde{n}(\mathbf{r}) + n^1(\mathbf{r}) - \tilde{n}^1(\mathbf{r}) \tag{2.60}$$

$$\tilde{n}(\mathbf{r}) = \sum_n f_n \langle \tilde{\psi}_n | \mathbf{r} \rangle \langle \mathbf{r} | \tilde{\psi}_n \rangle \tag{2.61}$$

$$\begin{gathered} n^1(\mathbf{r}) = \sum_{i,j} \rho_{ij} \langle \phi_i | \mathbf{r} \rangle \langle \mathbf{r} | \phi_j \rangle \quad \wedge \quad \tilde{n}^1(\mathbf{r}) = \sum_{i,j} \rho_{ij} \langle \tilde{\phi}_i | \mathbf{r} \rangle \langle \mathbf{r} | \tilde{\phi}_j \rangle \\ \text{with} \quad \rho_{ij} = \sum_n f_n \langle \tilde{\psi}_n | \tilde{p}_i \rangle \langle \tilde{p}_j | \tilde{\psi}_n \rangle \end{gathered} \tag{2.62}$$

$$
\begin{aligned}
n(\mathbf{r}) &= \sum_n f_n \langle \psi_n | \mathbf{r} \rangle \langle \mathbf{r} | \psi_n \rangle \\
&= \sum_n f_n \left[\langle \tilde{\psi}_n | + \sum_i \langle \tilde{\psi}_n | \tilde{p}_i \rangle (\langle \phi_i | - \langle \tilde{\phi}_i |) \right] | \mathbf{r} \rangle \langle \mathbf{r} | \bullet \\
&\qquad \bullet \left[| \tilde{\psi}_n \rangle + \sum_j (| \phi_j \rangle - | \tilde{\phi}_j \rangle) \langle \tilde{p}_j | \tilde{\psi}_n \rangle \right] \\
&= \sum_n f_n \langle \tilde{\psi}_n | \mathbf{r} \rangle \langle \mathbf{r} | \tilde{\psi}_n \rangle \\
&\quad + \sum_n f_n \sum_{i,j} \langle \tilde{\psi}_n | \tilde{p}_i \rangle (\langle \phi_i | - \langle \tilde{\phi}_i |) | \mathbf{r} \rangle \langle \mathbf{r} | (| \phi_j \rangle - | \tilde{\phi}_j \rangle) \langle \tilde{p}_j | \tilde{\psi}_n \rangle \\
&\quad + \sum_n f_n \langle \tilde{\psi}_n | \mathbf{r} \rangle \langle \mathbf{r} | \sum_j (| \phi_j \rangle - | \tilde{\phi}_j \rangle) \langle \tilde{p}_j | \tilde{\psi}_n \rangle \\
&\quad + \sum_n f_n \sum_i \langle \tilde{\psi}_n | \tilde{p}_i \rangle (\langle \phi_i | - \langle \tilde{\phi}_i |) | \mathbf{r} \rangle \langle \mathbf{r} | \tilde{\psi}_n \rangle \\
&= \sum_n f_n \langle \tilde{\psi}_n | \mathbf{r} \rangle \langle \mathbf{r} | \tilde{\psi}_n \rangle + \sum_{i,j} \rho_{ij} (\langle \phi_i | - \langle \tilde{\phi}_i |) | \mathbf{r} \rangle \langle \mathbf{r} | (| \phi_j \rangle - | \tilde{\phi}_j \rangle) \\
&\quad + \sum_{i,j} \rho_{ij} \langle \tilde{\phi}_i | \mathbf{r} \rangle \langle \mathbf{r} | (| \phi_j \rangle - | \tilde{\phi}_j \rangle) + \sum_{i,j} \rho_{ij} (\langle \phi_i | - \langle \tilde{\phi}_i |) | \mathbf{r} \rangle \langle \mathbf{r} | \tilde{\phi}_j \rangle \\
&= \sum_n f_n \langle \tilde{\psi}_n | \mathbf{r} \rangle \langle \mathbf{r} | \tilde{\psi}_n \rangle + \sum_{i,j} \rho_{ij} \langle \phi_i | \mathbf{r} \rangle \langle \mathbf{r} | \phi_j \rangle - \sum_{i,j} \rho_{ij} \langle \tilde{\phi}_i | \mathbf{r} \rangle \langle \mathbf{r} | \tilde{\phi}_j \rangle \\
&= \tilde{n}(\mathbf{r}) + n^1(\mathbf{r}) - \tilde{n}^1(\mathbf{r})
\end{aligned}
\tag{2.63}
$$

In the interstitial region (intersection of valence regions) the charge density is equal to the pseudo charge density ($n(\mathbf{r}) = \tilde{n}(\mathbf{r})$) as no projector function acts there. Hence the one-center contributions must cancel each other ($n^1(\mathbf{r}) = \tilde{n}^1(\mathbf{r})$). For a complete $\{\tilde{p}_i\}$ the pseudised contributions cancel each other in the augmentation (core) regions as proven by (2.64) ($\tilde{n}(\mathbf{r}) = \tilde{n}^1(\mathbf{r})$). Therefore the charge density is equal to the all-electron contribution ($n(\mathbf{r}) = n^1(\mathbf{r})$).

$$
\begin{aligned}
\tilde{n}^1(\mathbf{r}) &= \sum_{i,j} \rho_{ij} \langle \tilde{\phi}_i | \mathbf{r} \rangle \langle \mathbf{r} | \tilde{\phi}_j \rangle = \sum_n f_n \sum_{i,j} \langle \tilde{\psi}_n | \tilde{p}_i \rangle \langle \tilde{\phi}_i | \mathbf{r} \rangle \langle \mathbf{r} | \tilde{\phi}_j \rangle \langle \tilde{p}_j | \tilde{\psi}_n \rangle \\
&= \sum_n f_n \langle \tilde{\psi}_n | (\sum_i | \tilde{p}_i \rangle \langle \tilde{\phi}_i |) | \mathbf{r} \rangle \langle \mathbf{r} | (\sum_j | \tilde{\phi}_j \rangle \langle \tilde{p}_j |) | \tilde{\psi}_n \rangle \\
&= \sum_n f_n \langle \tilde{\psi}_n | \hat{1} | \mathbf{r} \rangle \langle \mathbf{r} | \hat{1} | \tilde{\psi}_n \rangle = \sum_n f_n \langle \tilde{\psi}_n | \mathbf{r} \rangle \langle \mathbf{r} | \tilde{\psi}_n \rangle \\
&= \tilde{n}(\mathbf{r}) \; \forall \; r < r_{rad}
\end{aligned}
\tag{2.64}
$$

To calculate the total energy of the system, its charge density acquired with the aid of the PAW method together with equation (2.35) from the Kohn-

Sham scheme could be applied. Assuming that the real system experiences no external potential it yields (2.65).

$$E_s[n] = F_{HK}[n] = T_s[n] + E_H[n] + E_{XC}[n] \tag{2.65}$$

However Blöchl found the analogue (2.66) to (2.60) [87].

$$E_{tot} = \tilde{E} + E^1 - \tilde{E}^1 \tag{2.66}$$

Since E_{tot} is decomposed exactly like $n(\mathbf{r})$, the contributions are evaluated on the same grids (cf. Fig. 2.6) improving the convergence properties. Exact expressions for them can be found in [88].

For the following reasons practical calculations can only yield approximate solutions.

- There is a finite energy cutoff E_{cut} for the plane wave basis set (see section 2.3).
- The exchange-correlation functional $E_{XC}[n]$ has to be approximated (see section 2.5).
- The overlap between the different core regions is neglected for all terms although it can occur in general.

The implementation in the program VASP (Vienna ab-initio simulation package) is described in [88, 93].

2.5. Electronic exchange-correlation functionals

From a physical point of view there is a hierarchy of approaches to the quantum mechanical part of the electron-electron interaction in DFT. This refers to the degree of sophistication at constructing the exchange-correlation (XC) functional $E_{XC}[\rho]$ judged by underlying fundamental assumptions. Albeit the electronic structure results provided by DFT are not final, it turns out that several XC-functionals (regular and hybrid) have to be considered, because they substantially affect those of subsequent calculations. Furthermore a compromise between precision and computational effort has to be found in order to enable a feasible investigation. This can not be achieved by a strategy incorporating only a single XC-functional. A comparison of adequacies provides insight concerning the levels on which the properties of the systems have to be modelled. To this end the inclusion of edge cases is also helpful.

Gradient (GGA) DFT [94], which takes electron gas inhomogeneities into account beyond a purely local treatment, in the shape of the PBE XC-functional

[95] is applied to determine lattice parameters, ionic positions and ground state total energies. Halocarbon adsorption at the ice surface is essentially influenced by London dispersion interaction [96–98]. Thus van der Waals (vdW) corrections (Grimme-D2 scheme) [99–102] have to be added in this case. Contrary to the simpler local density approximation (LDA) [75, 103] and Hartree-Fock (HF) approaches, GGA-DFT can be expected to yield workable values for the bulk quantities of ice [104, 105]. The main deficiency lies in an underestimation of the hydrogen bond length, leading to a slight overbinding [105]. It was demonstrated that hybrid DFT, which includes a fraction of exact (HF) exchange, can largely remedy the issue [105] due to a more elaborate description of hydrogen bonding, yet this study also involves system sizes which would then lead to unreasonable computational expense. The analysis of bulk ice (see section 3.1) systematically demonstrates that electronic relaxation with hybrid XC-functionals (here: PBE0 [106] and screened HSE06 [107, 108]) is indispensable for arriving at an intermediate stage from which it makes sense to go beyond DFT.

2.5.1. The Hartree-Fock approximation

The Hartree-Fock approximation (HFA) is the basis of molecular orbital (MO) theory. While being a mean field theory, it is not a form of DFT, since correlation effects (see subsection 2.5.2) are neglected. The method was introduced by V. A. Fock in 1930 [109] and reformulated by D. R. Hartree in 1935 [110] to make it more feasible for practical applications. The wave function $|\Psi\rangle$ of the electronic subsystem (in its ground state) is approximated as the Slater determinant of the occupied one-electron (spin) orbitals $\left|\Phi_{\gamma=1,\dots,N}\right\rangle$ to apply the Rayleigh-Ritz variational principle.

$$\begin{gathered}\hat{F}\left|\Phi_m\right\rangle = \varepsilon_m \left|\Phi_m\right\rangle \\ \hat{F} := \hat{h} + \sum_{\gamma}^{N} (\left\langle \Phi_\gamma \right| \hat{w} \left| \Phi_\gamma \right\rangle - \left|\Phi_\gamma\right\rangle \left\langle \Phi_\gamma \right| \hat{w}) \\ \hat{h} := -\frac{\hbar^2}{2m_e}\frac{\partial^2}{\partial \mathbf{r}^2} - \frac{e^2}{4\pi\varepsilon_0}\sum_I \frac{Z_I}{|\mathbf{r}-\mathbf{R}_I|} \quad \wedge \quad \hat{w} := \frac{e^2}{4\pi\varepsilon_0}\frac{1}{|\mathbf{r}-\mathbf{r}'|}\end{gathered} \tag{2.67}$$

$$\begin{aligned}\left|\Phi_m\right\rangle = \sum_i^{n=|\{\phi_i\}|} c_{im}\left|\phi_i\right\rangle &\overset{(2.67)}{\Rightarrow} \sum_i \hat{F} c_{im}\left|\phi_i\right\rangle = \varepsilon_m \sum_i c_{im}\left|\phi_i\right\rangle \\ \Rightarrow \sum_i \underbrace{\left\langle \phi_j \right| \hat{F} \left| \phi_i \right\rangle}_{=:F_{ji}} c_{im} &= \varepsilon_m \sum_i \underbrace{\left\langle \phi_j | \phi_i \right\rangle}_{=:S_{ji}} c_{im} \Rightarrow \mathrm{F}\mathbf{c}_m = \varepsilon_m \mathrm{S}\mathbf{c}_m\end{aligned} \tag{2.68}$$

$$\mathrm{F}\mathbf{c}_m = \varepsilon_m \mathrm{S}\mathbf{c}_m \tag{2.69}$$

Solving the Hartree-Fock equation (2.67) to determine the one-electron resp. molecular orbital wave functions $|\Phi_m\rangle$ and energy levels ε_m is a nonlinear eigenvalue problem. The Fock operator $\hat{F}$ is a nonlocal integro-differential operator that depends on the $|\Phi_\gamma\rangle$. The one-particle Hamilton operator $\hat{h}$ represents the kinetic energy of the respective electron and its attractive Coulomb interaction with the cores. The two-particle Coulomb operator $\hat{w}$ serves to take the classical (Hartree, minuend) and exchange [X (see subsection 2.5.2), subtrahend] part of the repulsive electron-electron Coulomb interaction into account. To solve the Hartree-Fock equation (2.67) in practice, it is transformed into the matrix representation, which is known as the Roothaan-Hall equation (2.69) (1951) [111, 112]. Using the basis set $\{\phi_i\}$, the transformation (2.68) is straightforward. While the overlap matrix S is constituted by $\{\phi_i\}$, the Fock matrix F also depends on the coefficient vectors $\mathbf{c}_{\gamma=1,\ldots,N}$ for the occupied states. Hence solving the Roothaan-Hall equation (2.69) is a generalised eigenvalue problem. It can be transformed into a regular one via Löwdin's symmetric orthogonalisation (1950) [113].

The HFA normally overestimates lattice constants and bulk moduli [114]. While the extent of these deviations might be tolerable, binding energies tend to be considerably smaller than their experimental values [114]. While being a fundamental electronic structure method, the HFA produces unacceptably inaccurate results, which require subsequent improvement by other methods such as DFT [subsections 2.5.2 (regular), 2.5.3 (hybrid), 2.5.4 (screened hybrid)] or GW (section 2.7). Typically, the band gaps of semiconductors are too large by a factor of two to three [114, 115]. In view of these deficiencies, the present study includes the HFA only as an exemplary edge case.

The Hartree-Fock (2.67) resp. Roothaan-Hall equation (2.69) is solved with an iterative approach, because the Fock operator/matrix (see equations (2.67), (2.68)) depends on the occupied orbitals $|\Phi_\gamma\rangle$. Fig. 2.7 displays a simplified algorithmic flowchart of the HF SCF (Hartree-Fock self-consistent field) method [116]. This method is usually chosen although it is not a part of the HFA itself. The initial orbitals for a specific nuclear geometry are used to calculate the Fock matrix. Its diagonalisation yields the new orbitals. These replace the initial orbitals to repeat the process until the convergence criterion – most often a sufficiently small change of the total electronic energy E – is reached. Sometimes refining the Fock matrix with a (linear) combination of old and new orbitals is more appropriate. In particular, this is one of several strategies employed to avoid numerical instabilities [116].

To derive the Hartree-Fock equation for fermionic (here: electronic) ensembles (2.67), the normalised wave function of the electronic subsystem $|\Psi\rangle$ is approximated as the Slater determinant of the orthonormalised occupied one-

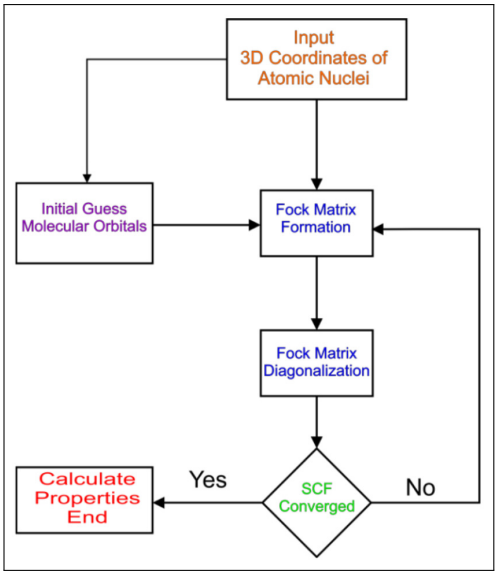

Figure 2.7.: Simplified algorithmic flowchart for the HF SCF (Hartree-Fock self-consistent field) method (taken from [117])

electron orbitals $|\Phi_\beta\rangle$. The exact expression would be a linear combination of all Slater determinants constructible based on the $|\Phi_i\rangle$. The total electronic energy E of the ground state follows from the stationary Schrödinger equation and is written with the aid of the one-particle Hamilton operators and the two-particle Coulomb operators (see equations (2.70), (2.71)). The Rayleigh-Ritz variational principle yields an upper bound for E (see equations (2.73), (2.74) for the Hartree-Fock energy E_{HF} of the non-spin-polarised homogeneous electron gas[5] [118, 119]). The orthogonality condition for the $|\Phi_\beta\rangle$ can be cancelled temporarily, since a subsequent reorthogonalisation does not affect E. However, they have to stay normalised due to the shape of the Fock operator $\hat{F}$ (equation (2.67)). The remaining Lagrange multipliers turn out to be the electronic energy levels ε_m (equation (2.72)). For $m > N$ the derivation additionally assumes this energy level to be occupied, since ε_m would not be physically meaningful otherwise.

[5] A jellium background is needed to ensure charge neutrality, because the Coulomb energy would be infinite otherwise. This cancels the classical (Hartree) part of the electron-electron Coulomb interaction due to the homogeneity of the electron gas, but not the exchange-correlation.

$$
\begin{aligned}
\hat{H}\left|\Psi\right\rangle &= E\left|\Psi\right\rangle \\
\left\langle\Psi|\Psi\right\rangle = 1 \quad \wedge \quad \left\langle\Phi_i|\Phi_j\right\rangle &= \delta_{ij} \\
\Psi(1,...,N) \approx \frac{1}{\sqrt{N!}} &\begin{vmatrix} \Phi_1(1) & \dots & \Phi_1(N) \\ \vdots & \ddots & \vdots \\ \Phi_N(1) & \dots & \Phi_N(N) \end{vmatrix} \\
\hat{H} &:= \sum_i^N \hat{h}_i + \frac{1}{2}\sum_i^N\sum_{j\neq i}^N \hat{w}_{ij} \\
\hat{h}_i := -\frac{\hbar^2}{2m_e}\frac{\partial^2}{\partial \mathbf{r}_i^2} - \frac{e^2}{4\pi\varepsilon_0}\sum_I \frac{Z_I}{|\mathbf{r}_i - \mathbf{R}_I|} \quad \wedge \quad \hat{w}_{ij} &:= \frac{e^2}{4\pi\varepsilon_0}\frac{1}{|\mathbf{r}_i - \mathbf{r}_j|}
\end{aligned}
\tag{2.70}
$$

$$
\begin{aligned}
E = \left\langle\Psi\left|\hat{H}\right|\Psi\right\rangle &= \sum_i^N \left\langle\Psi\left|\hat{h}_i\right|\Psi\right\rangle + \frac{1}{2}\sum_i^N\sum_{j\neq i}^N \left\langle\Psi\left|\hat{w}_{ij}\right|\Psi\right\rangle \\
&\approx \sum_i^N \left\langle\Phi_i\left|\hat{h}_i\right|\Phi_i\right\rangle + \frac{1}{2}\sum_i^N\sum_{j\neq i}^N \left\langle\Phi_i\Phi_j\right|\hat{w}_{ij}\left(\left|\Phi_j\Phi_i\right\rangle - \left|\Phi_i\Phi_j\right\rangle\right)
\end{aligned}
\tag{2.71}
$$

$$
\begin{aligned}
E[\{\Phi_\beta\}] &= \sum_\alpha^N \left\langle\Phi_\alpha\left|\hat{h}\right|\Phi_\alpha\right\rangle + \frac{1}{2}\sum_\alpha^N\sum_{\gamma\neq\alpha}^N \left\langle\Phi_\alpha\Phi_\gamma\right|\hat{w}\left(\left|\Phi_\gamma\Phi_\alpha\right\rangle - \left|\Phi_\alpha\Phi_\gamma\right\rangle\right) \\
\mathscr{L} &\overset{\langle\Phi_\alpha|\Phi_\gamma\rangle\overset{!}{=}\delta_{\alpha\gamma}}{=} E[\{\Phi_\beta\}] - \sum_{\alpha,\gamma}^N \varepsilon_{\alpha\gamma}(\delta_{\alpha\gamma} - \left\langle\Phi_\alpha|\Phi_\gamma\right\rangle) \\
&\overset{\varepsilon_{\alpha\gamma}[\{\tilde{\Phi}_\beta\}]=\varepsilon_\gamma\delta_{\alpha\gamma}}{=} E[\{\tilde{\Phi}_\beta\}] - \sum_\gamma^N \varepsilon_\gamma(1 - \left\langle\tilde{\Phi}_\gamma|\tilde{\Phi}_\gamma\right\rangle) \\
\frac{\delta\mathscr{L}}{\delta\left\langle\Phi_m\right|} &= \hat{h}\left|\Phi_m\right\rangle + \sum_{\gamma\neq m}^N \Big(\underbrace{\left\langle\Phi_\gamma|\hat{w}|\Phi_\gamma\right\rangle\left|\Phi_m\right\rangle}_{\text{Hartree}} - \underbrace{\left\langle\Phi_\gamma|\hat{w}|\Phi_m\right\rangle\left|\Phi_\gamma\right\rangle}_{\text{X}}\Big) - \varepsilon_m\left|\Phi_m\right\rangle \\
&= \hat{h}\left|\Phi_m\right\rangle + \sum_\gamma^N \left(\left\langle\Phi_\gamma|\hat{w}|\Phi_\gamma\right\rangle - \left|\Phi_\gamma\right\rangle\left\langle\Phi_\gamma\right|\hat{w}\right)\left|\Phi_m\right\rangle - \varepsilon_m\left|\Phi_m\right\rangle \\
&\overset{!}{=} 0 \Rightarrow \hat{F}\left|\Phi_m\right\rangle = \varepsilon_m\left|\Phi_m\right\rangle
\end{aligned}
\tag{2.72}
$$

Taking correlation effects into account, like in DFT (see subsection 2.5.2), is beyond the HFA. It reduces E for the non-spin-polarised homogeneous electron gas[5] (equation (2.73)) [118, 119]. The electron density parameter r_S is defined according to equations (2.74) [118, 119].

$$
\frac{1}{N}E_{HF}[\text{ryd}] = \underbrace{\frac{3}{5}\left(\frac{9\pi}{4}\right)^{\frac{2}{3}}\frac{1}{r_S^2}}_{\text{kinetic}} \underbrace{-\frac{3}{2\pi}\left(\frac{9\pi}{4}\right)^{\frac{1}{3}}\frac{1}{r_S}}_{\text{X}} \approx \frac{2.21}{r_S^2} - \frac{0.916}{r_S} \tag{2.73}
$$

$$n_e = \frac{N}{V} \quad \wedge \quad v_e = \frac{1}{n_e} = \frac{4\pi}{3}(a_B r_S)^3 \quad \text{with} \quad a_B = \frac{4\pi\varepsilon_0\hbar^2}{m_e e^2} \approx 0.529\text{Å} \tag{2.74}$$

2.5.2. Regular XC-functionals

$$E_{XC}[\rho] = \int_{\mathbb{R}^3} \varepsilon_{XC}([\rho],\mathbf{r})\rho(\mathbf{r})d^3r \quad \wedge \quad V_{XC}([\rho],\mathbf{r}) = \frac{\delta E_{XC}[\rho]}{\delta\rho(\mathbf{r})} \tag{2.75}$$

$$\varepsilon_{XC} = \varepsilon_X + \varepsilon_C \tag{2.76}$$

The exchange-correlation (XC) is the quantum mechanical part of the electron-electron Coulomb interaction. Its contribution to the total energy resp. Kohn-Sham potential of the system (see subsection 2.1.3) follows from the exchange-correlation density functional $\varepsilon_{XC}([\rho],\mathbf{r})$ (equations (2.75)). According to the orientation of the electron spins relative to each other ε_{XC} is decomposed into the addends ε_X [exchange (X), parallel] and ε_C [correlation (C), opposite] (equation (2.76)).

2.5.2.1. Local density approximation

$$E_{XC}^{LDA}[\rho] = \int_{\mathbb{R}^3} \varepsilon_{XC}^{LDA}(\rho(\mathbf{r}))\rho(\mathbf{r})d^3r \tag{2.77}$$

The simplest approach to XC in DFT is the local density approximation (LDA). It is assumed that the charge density $\rho(\mathbf{r})$ at each point $\mathbf{r}$ contributes to $E_{XC}[\rho]$ as if the electron gas was homogeneous (see equation (2.77)).

Empiricism demonstrates that the LDA yields surprisingly good results for a wide variety of systems, even if large electron gas inhomogeneities occur [120]. It exhibits a tendency to overbinding, e.g. the underestimation of lattice constants as well as the overestimation of elastic constants [121–123].

$$\begin{aligned}\frac{1}{N}E_{\min}[\text{ryd}] &= \underbrace{\frac{3}{5}\left(\frac{9\pi}{4}\right)^{\frac{2}{3}}\frac{1}{r_S^2}}_{\text{kinetic}} \underbrace{-\frac{3}{2\pi}\left(\frac{9\pi}{4}\right)^{\frac{1}{3}}\frac{1}{r_S}}_{\text{X}} \underbrace{+\varepsilon_{\text{corr}}[\text{ryd}]}_{\text{C}} \\ &\approx \frac{2.21}{r_S^2} - \frac{0.916}{r_S} + \varepsilon_{\text{corr}}[\text{ryd}] \text{ for low } r_S \\ \varepsilon_{\text{corr}}[\text{ryd}] &\approx \frac{2}{\pi^2}(1-\ln(2))\ln(r_S) - 0.094 + \mathcal{O}(r_S\ln(r_S)) \text{ for low } r_S \\ \frac{2}{\pi^2}(1-\ln(2)) &\approx 0.0622\end{aligned} \tag{2.78}$$

The leading orders in the energy of the non-spin-polarised homogeneous electron gas[5] for high electron densities, i.e. low r_S, are given by equations (2.78) (see equations (2.74) for the definition of the electron density parameter r_S). Correlation (C) contributions reduce the energy as compared to the Hartree-Fock result (equation (2.73)). If the electron gas is more dilute, higher terms become dominant.

In 1980 quantum Monte Carlo simulations performed by Ceperley and Alder yielded numerical values for the ground state energy per particle of a homogeneous electron gas, with either vanishing (paramagnetic) or total (ferromagnetic) spin-polarisation, at specific charge densities [103]. In limiting cases the asymptotics and some further leading orders are exactly known from many body perturbation theory [119, 124][6]. Perdew and Zunger exploited this in 1981 to parametrise the correlation density based on the aforementioned results [75]. For dilute electron gases ($r_S \geq 1$) they stuck to a former parametrisation method by Ceperley [127], which also respects the considerations of Carr, Jr. for $r_S \nearrow \infty$ [124]. Denser electron gases ($r_S \leq 1$) are described by a four order term. For vanishing spin-polarisation the first two orders are those deduced by Gell-Mann and Brueckner [119] applying Feynman graph techniques. Those for the totally spin-polarised case are provided by adding Misawa's RPA scaling relation [128], which is strictly valid only within the random phase approximation (RPA, sometimes called dynamical Hartree-Fock approximation). The two remaining coefficients were chosen such that matching at $r_S = 1$ is achieved. The spin-polarisation-dependence of exchange-correlation was investigated by von Barth and Hedin [129]. They were the first to propose a standard interpolation formula [again strictly valid only within (a generalised) RPA], which assumes that exchange and correlation density depend on spin-polarisation in the same way and produces the results for the general case from the limiting cases. Adding this Perdew and Zunger provided an approximation of ε_{XC}^{LDA} for arbitrary charge densities and spin-polarisations [75].

Any shortcomings of the LDA arise since the real $\varepsilon_{XC}([\rho], \mathbf{r})$ is not purely local. Albeit XC is (predominantly) a short-range effect, a sufficiently large slope of the electron gas might still query $\varepsilon_{XC}^{LDA}(\rho(\mathbf{r}))$ due to the neglect of inhomogeneities around $\mathbf{r}$. Indeed the LDA would be an oversimplification in the scope of the present study. It can not satisfy the demands imposed by the DFT objectives. More specifically, this relates mainly to the need of viable intermediate electronic structure descriptions for subsequent calculations and

[6] For charge density towards infinity a non-perturbative deduction also exists [125]. Furthermore a transformation has been found to establish the connection between the correlation contributions made by zero-point plasma oscillations within both ways of proceeding [126].

partly to the reproduction of potential landscapes along chemical reaction pathways. The LDA yields a severe band gap underestimation for most typical semiconductors and insulators ([130] and references therein). Furthermore reaction and activation energies for a variety of chemical reactions exhibit strong deviations from experimental values [123].

On a side note, the LDA does not always predict the ground state of the respective system correctly. E.g. a spin-polarised treatment of crystalline iron leads to paramagnetic fcc instead of ferromagnetic bcc [131]. It can also be inaccurate for the determination of the relative stability of structural phases of solids (calculation of coexistence pressures at phase boundaries) [132, 133].

2.5.2.2. PBE gradient XC-functional

Generalised gradient approximation (GGA) DFT incorporates the (length of the) charge density gradient to facilitate a not purely local – more exactly: semilocal – treatment of electron gas inhomogeneities (see equation (2.79)). Its foundations were partly laid by a preceding work of Perdew and Wang from 1986 [94]. They proposed a first-order gradient approximation of the exchange (X) hole with real-space cutoffs, which retains exact relations. Those are also fulfilled by the LDA, but sum rule and negative semidefiniteness are violated by the gradient expansion approximation (GEA) [70, 73] – which additionally includes second-order spatial derivatives – as demonstrated by Perdew [134]. Perdew and Wang recommended to apply their approximation in concert with the Langreth-Mehl approximation for correlation (C) ([135], precursor [136]).

$$E_{\mathrm{XC}}^{\mathrm{GGA}}[\rho] = \int_{\mathbb{R}^3} \varepsilon_{\mathrm{XC}}^{\mathrm{GGA}}(\rho(\mathbf{r}), |\nabla\rho(\mathbf{r})|)\rho(\mathbf{r})d^3r \tag{2.79}$$

This work makes use of the PBE XC-functional, which was presented by Perdew, Burke and Ernzerhof in 1996 [95]. It is an ab-initio GGA invoking general features of and improving over the PW91 GEA suggested by Perdew and Wang in 1991 [137]. The refined strategy is to simplify by fulfilling only those exact relations, which are energetically significant. It allows to reduce the computational effort without loss of precision, e.g. the atomisation energies of molecules are very similar. Thereby an XC-functional feasible for practical calculations is constructed despite the restrictions enforced by the semilocal form. Further advantages are an accurate description of the linear response of the uniform electron gas, correct behaviour under uniform scaling and the ability to produce a smoother pseudopotential.

$$\varepsilon_{\mathrm{XC}}^{\mathrm{GGA}}(\rho(\mathbf{r}), |\nabla\rho(\mathbf{r})| = 0) = \varepsilon_{\mathrm{XC}}^{\mathrm{LDA}}(\rho(\mathbf{r})) \tag{2.80}$$

Even compared to the LDA, the PBE is only moderately more expensive. Reaction and activation energies for a variety of chemical reactions are in distinctly better accordance with experiment [123]. Gradient corrections usually more than compensate the overbinding tendency of the LDA, yet the arising underbinding tendency is weaker and supposedly caused by overscreening [122]. Elastic constants are much better but lattice constants only slightly [122, 123] whereas cohesive energies are also improved [122].

Analogously to the LDA, any inherent limitations of GGA-DFT are due to the structure of the function serving to approximate the functional $\varepsilon_{XC}([\rho], \mathbf{r})$ (equations (2.79), (2.80) [95]). In the given context the semilocal form, realised as PBE, together with vdW corrections (see subsubsection 2.5.2.3) added under the aforementioned circumstances (see beginning of this section 2.5) suffices to provide ionic geometries and ground state total energies (of which only differences have meaning). Hence material parameters, like e.g. bulk moduli, as well as potential landscapes required for the assessment of chemical reaction barriers are available too. For semiconductors and insulators transitioning from LDA to PBE typically yields only a minor change of the band gaps sizes, so that these are still mostly essentially smaller than their experimental values [138–140]. Thus, as this section previously discussed, hybrid electronic relaxation has to be performed on top of the – possibly vdW-corrected – PBE results. Both hybrid XC-functionals applied here and their relation to each other are explained in the consecutive subsections 2.5.3 (PBE0) and 2.5.4 (HSE06).

On a side note GGA-DFT yields reliable ground state predictions throughout contrary to LDA. E.g. crystalline iron is now correctly found to be ferromagnetic bcc instead of paramagnetic fcc [141]. Furthermore coexistence pressures at phase boundaries are in much better agreement with experiment [132].

2.5.2.3. Van der Waals corrections to PBE: The Grimme-D2 scheme

London dispersion forces, sometimes called "van der Waals (vdW) forces in the narrower sense" are a merely quantum mechanical effect [96–98] originating from the Coulomb interaction between dipoles induced due to Heisenberg's uncertainty principle. They usually constitute the largest part of the vdW forces among which permanent dipoles are regarded too. Albeit dipole-dipole interaction causes only the weakest type of bonding, it is nevertheless essential if the other types are absent or confined to certain spatial directions by anisotropy. Furthermore it becomes more important on long range as the always attractive London dispersion potential decays only with the sixth power

of the interatomic distance[7] R, while the Yukawa potential of a screened charge is directly proportional to $R^{-1}e^{-\lambda_{\mathrm{TF}}R}$ (λ_{TF} is the Thomas-Fermi wavelength).

Dispersion corrections to gradient and hybrid DFT were realised according to Grimme's semiempirical DFT-D2 method ([100–102], precursor [99]). It introduces an additional atom-pairwise potential field composed of damped $-s_6 C_{6ij} r_{ij,\mathbf{L}}^{-6}$ terms (cf. equations (2.81-2.84)), where only the global scaling factor s_6 is specific to the respective XC-functional (here: GGA-DFT PBE(-D2), $s_6 = 0.75$ [100]). Note that simultaneous optimisation of all (geometrical) degrees of a freedom is permitted since this scheme may address not only the forces on the atoms, but also the stresses on the unit cell [102].

PBE-D2 has been tested in a plethora of chemically different cases like noble gas crystals, vdW complexes and layered materials as well as covalently bonded and partially ionic systems [101, 102]. The dispersion corrections brought geometry, bulk moduli and cohesive energies for weakly bonded materials, such as solid methane, which is a vdW complex, or the heterodesmic graphite and vanadium pentoxide, in close agreement with experimental values [101]. It was found that dispersion interaction might provide the major part of the binding of molecules to surfaces [101]. One example is the adsorption and chemisorption (alkoxide formation) of isobutene on acidic sites in the micropores of zeolite ferrierite [101]. In general, PBE-D2 leads to more realistic predictions when the standard PBE fails [101, 102]. It also performs very well if vdW interactions are not supposed to play an important role [102]. As this scheme is computationally inexpensive, it provides a convenient tool for structural optimisations of arbitrary systems. Moreover its accuracy demonstrates that the underlying parameters determined before for molecules allow to fashion an appropriate assessment of dispersion interaction in more complex systems.

$$E_{\text{DFT-disp}} = E_{\text{KS-DFT}} + E_{\text{disp}} \tag{2.81}$$

$$E_{\text{disp}} = -\frac{1}{2} \sum_{i,j=1}^{N} {\sum_{\mathbf{L}}}' \frac{C_{6ij}}{r_{ij,\mathbf{L}}^6} f_{d,6}(r_{ij,\mathbf{L}}) \tag{2.82}$$

$$f_{d,6}(r_{ij,\mathbf{L}}) = s_6 \left(1 + e^{-d\left(\frac{r_{ij,\mathbf{L}}}{s_{\mathrm{R}} R_{0ij}} - 1\right)} \right)^{-1} \tag{2.83}$$

$$C_{6ij} = \sqrt{C_{6ii} C_{6jj}} \quad \wedge \quad R_{0ij} = R_{0i} + R_{0j} \tag{2.84}$$

[7] The electrical far-field of a dipole decreases like R^{-3} and is capable of inducing another dipole with the same asymptotic behaviour. Therefore their interaction potential is directly proportional to R^{-6}.

Physical quantities and parameters (defaults in brackets):

- N: number of atoms in the unit cell
- $\mathbf{L}$: all possible translations of the unit cell ($'$ indicates $i \neq j$ for $\mathbf{L} = \mathbf{0}$)
- $r_{ij,\mathbf{L}}$: distance between atoms i and j for translation $\mathbf{L}$ between their unit cells
- C_{6ij}: London coupling constant for pair of atoms i and j
- R_{0i} resp. R_{0ij}: vdW radius of atom i resp. pair of atoms i and j
- $f_{d,6}(...)$: Fermi-type damping function with damping parameter d (20.0)
- s_6 resp. s_R: global scaling factor (0.75 for PBE) resp. scaling factor (1.00)

The standard Kohn-Sham ground state energy $E_{\text{KS-DFT}}$ is lowered by adding the correction E_{disp} (equation (2.81)) yielding $E_{\text{DFT-disp}}$. For each pair of atoms the attractive term of a Lennard-Jones potential is evaluated in a scaled Fermi-type damped version (equations (2.82), (2.83)). E_{disp} is the sum of all these contributions. London coupling constants C_6 and vdW radii R_0 are initially calculated for single chemical elements. Those for pairs of atoms are approximated directly from these according to the combination rules (equation (2.84)). Calculating E_{disp} is done either by introducing an appropriate interatomic distance cutoff [102] or by applying Ewald summation [101]. Despite containing truncation errors the former surprisingly outperforms the latter, which tends to overbinding [102]. A possible explanation for this would be that Grimme carried out his original investigations [99,100] with non-periodic models. Note that the damping is mandatory as near-singularities at small interatomic distances, where in reality repulsion becomes dominant due to the like charges of the electrons and the Pauli principle, have to be avoided [99].

2.5.3. PBE0 hybrid XC-functional

Replacing a part a of the approximated exchange from density functional theory (here: GGA PBE) by exact Hartree-Fock (HF) exchange, which is possible as the Kohn-Sham formalism provides the orbitals, is justified if the error in $E_{\text{XC}}^{\text{DFT}}$ arises mainly from the exchange limit ($0 \leq \lambda \ll 1$, note that $E_{\text{XC},\lambda=0} = E_\text{X}$ ("exchange end")) of the coupling-constant integral as given by

the adiabatic connection formula (cf. equation (2.85), [106] and references therein).

$$E_{\mathrm{XC}}^{(\mathrm{DFT})} = \int_0^1 E_{\mathrm{XC},\lambda}^{(\mathrm{DFT})} d\lambda \qquad (2.85)$$
$$\text{with} \quad E_{\mathrm{XC},\lambda} = \left\langle \Psi_\lambda \left| \hat{V}_{\mathrm{ee}} \right| \Psi_\lambda \right\rangle - \frac{e^2}{2} \int\int \frac{\rho(\mathbf{r})\rho(\mathbf{r}')}{|\mathbf{r}-\mathbf{r}'|} d^3r' d^3r \;\forall\; \lambda \in [0;1]$$

According to a rationale for this mixing designed by Perdew, Burke and Ernzerhof in 1996 [106], the optimum integer $n := a^{-1}$ is approximately the lowest order of Görling-Levy perturbation theory, that leads to a realistic description of $E_{\mathrm{XC},\lambda}$ in the range from $\lambda = 0$ (exchange only) to $\lambda = 1$ (physical value). Judging from earlier work, they reasoned that $n = 4$ should be adequate. A hybrid based on this and the GGA PW91 XC-functional yielded atomisation energies of typical small molecules in much better agreement with experiment than the previously discussed types of approaches [106].

PBE serves analogously to construct the PBE0 hybrid XC-functional, whereby the electronic structure results are drastically improved. The band gaps sizes for III–V semiconductors (a bit too large [142, 143]) and metal oxides (a bit too small [144]) are close to experimental values.

$$E_{\mathrm{XC}}^{\mathrm{PBE0}} = E_{\mathrm{X}}^{\mathrm{PBE0}} + E_{\mathrm{C}}^{\mathrm{PBE}} \quad \wedge \quad E_{\mathrm{X}}^{\mathrm{PBE0}} = aE_{\mathrm{X}}^{\mathrm{HF}} + (1-a)E_{\mathrm{X}}^{\mathrm{PBE}} \quad \wedge \quad a = \frac{1}{4} \qquad (2.86)$$

$$E_{\mathrm{XC}}^{\mathrm{PBE0}} = \frac{1}{4}\left(E_{\mathrm{X}}^{\mathrm{HF}} - E_{\mathrm{X}}^{\mathrm{PBE}}\right) + E_{\mathrm{XC}}^{\mathrm{PBE}} \qquad (2.87)$$

Applying PBE0 instead of LDA or PBE(-D2) to treat the same problem with the same capabilities increases the duration of the calculations by up to two orders of magnitude. PBE(-D2) can serve to prevent PBE0 [or HSE06 (see subsection 2.5.4)] from starting a merely electronic relaxation with a random electronic wave function. Thereby the computational effort gets about halved without deteriorating the results. LDA might also enable this timesaving artifice, yet PBE(-D2) seems to be a bit more suited since its PAW projectors (see section 2.4) are not different from those of the hybrids used here.

2.5.4. HSE06 screened hybrid XC-functional

The vast expense of exact exchange originates de facto from slow convergence of and rapidly increasing computational effort for $E_{\mathrm{X}}^{\mathrm{HF}}$ with distance, particularly for systems with small band resp. HOMO-LUMO gaps or metallic characteristics ([107] and references therein). Based on the insight that the

long-range (LR) part of E_X is very similar for both HF and PBE, the screened hybrid HSE XC-functional $E_{XC}^{HSE}(\omega)$, whose idea is to use exact exchange in essence merely on short range (SR), was proposed by Heyd, Scuseria and Ernzerhof in 2003 ([107], erratum [108]). Among others they performed PBC calculations in which apart from significant interactions within the supercell only those between it and its nearest neighbours enter in the exact exchange part. This truncation becomes admissible via a convenient screening of the exact exchange. Thereby the aforementioned bottleneck is circumvented.

The Coulomb operator for the exchange interaction is split up according to equation (2.88). This is possible, because the potential of a point charge is directly proportional to the reciprocal distance $\frac{1}{r}$ as already known from classical mechanics.

$$\frac{1}{r} = \underbrace{\frac{erfc(\omega r)}{r}}_{\text{SR term}} + \underbrace{\frac{erf(\omega r)}{r}}_{\text{LR term}} \tag{2.88}$$

The adjustable parameter ω controls the strength of the screening since it scales the distance in the arguments of Gauss's error function $erf(\omega r)$ and complementary error function $erfc(\omega r)$. For $\omega = 0$ the LR term vanishes, while the SR term corresponds to the full Coulomb operator. The opposite is true in the limit of $\omega \to \infty$.

Performing this decomposition on E_X^{PBE0} (see subsection 2.5.3) results in equation (2.89).

$$E_X^{PBE0} = \frac{1}{4}E_X^{HF,SR}(\omega) + \frac{1}{4}E_X^{HF,LR}(\omega) + \frac{3}{4}E_X^{PBE,SR}(\omega) + \frac{3}{4}E_X^{PBE,LR}(\omega) \tag{2.89}$$

According to [107] $\frac{1}{4}E_X^{HF,LR}(\omega)$ is a relatively small contribution (a few per cent) and tends to cancel with the analogous negative fraction of LR PBE exchange for "realistic" values of the screening parameter ω (e.g. those in equations (2.93)). It is hence justified to eliminate the expensive LR exact exchange from the PBE0 XC-functional with the aid of approximation (2.90), whereby the HSE XC-functional (equation (2.91)) is created.

$$E_X^{HF,LR}(\omega) \overset{\text{realistic } \omega}{\approx} E_X^{PBE,LR}(\omega) \tag{2.90}$$

$$\begin{aligned} E_{XC}^{HSE}(\omega) &= E_X^{HSE}(\omega) + E_C^{PBE} \\ &= \frac{1}{4}E_X^{HF,SR}(\omega) + \frac{3}{4}E_X^{PBE,SR}(\omega) + E_X^{PBE,LR}(\omega) + E_C^{PBE} \\ &= \frac{1}{4}\left(E_X^{PBE,LR}(\omega) - E_X^{HF,LR}(\omega)\right) + E_{XC}^{PBE0} \\ &= \frac{1}{4}\left(E_X^{HF,SR}(\omega) - E_X^{PBE,SR}(\omega)\right) + E_{XC}^{PBE} \end{aligned} \tag{2.91}$$

The screening defines the inclusion of exact exchange on short range as well as its compensation on long range. In that sense the HSE XC-functional lies in a transition area between PBE and PBE0, where the ideal compromise between accuracy and computational effort can be reached by optimising ω. A sufficiently high value of ω is mandatory, because the exact exchange calculations for periodic systems could not fully neglect interactions between the supercell and more distant neighbours otherwise. Equations (2.91) and (2.92) take no account of this intrinsic error.

$$E_{\mathrm{XC}}^{\mathrm{HSE}}(\omega \to \infty) = E_{\mathrm{XC}}^{\mathrm{PBE}} \quad \wedge \quad E_{\mathrm{XC}}^{\mathrm{HSE}}(\omega = 0) = E_{\mathrm{XC}}^{\mathrm{PBE0}} \tag{2.92}$$

Originally the standard enthalpies of formation for a quantum chemical test set of small molecules were considered to find an appropriate ω-range [107]. From there ω^{HSE03} was chosen since stronger screening would lead to unreliable band gap underestimation for semiconducting solids. With this value the bond lengths of the diatomic molecules from the initial set and the aforementioned enthalpies for an enlarged set are on par with the PBE0 results. Moreover PBC calculations for semiconducting and metallic single-walled carbon nanotubes demonstrate the spatially faster and smoother total energy convergence as compared to PBE0, while the density of states changes only slightly. The present study employs HSE06 instead of HSE03, but the differences are very minor.

$$\begin{aligned} \omega^{\mathrm{HSE03}} &= 0.300\text{Å}^{-1} = 0.159\mathrm{a_B^{-1}} \\ \omega^{\mathrm{HSE06}} &= 0.200\text{Å}^{-1} = 0.106\mathrm{a_B^{-1}} \end{aligned} \tag{2.93}$$

In HSE03 the band gaps of semiconductors and insulators are usually a bit underestimated but reasonable, while overestimations are mostly even smaller and occur less frequently [138, 145]. For semiconductors HSE06 either preserves this tendency or produces slightly increased values [146, 147].

2.6. Ionic relaxation

Relaxing a system serves to make it most stable, which is desirable since this is also the state it aims to obtain in nature. As justified by the Born-Oppenheimer approximation resp. its adiabaticity (see subsection 2.1.1) electronic and ionic relaxation are performed alternately, until specific convergence criteria, usually upper limits for energy differences or forces, are met. The ions are moved to reach the minimum of their potential energy hypersurface alias the "Born-Oppenheimer surface". Several methods, primarily the reduction of the forces

on individual atomic nuclei (see subsection 2.6.2), are employed to achieve this goal.

For pristine bulk cells crystal symmetry might cause the forces to vanish. In this simplest case explicit ionic relaxation is avoided by regression analysis with a fit function given by the Murnaghan equation of state (see subsection 2.6.1). However the present study treats more complicated systems, whose symmetries can not stay unbroken throughout. Two different algorithms for the reduction of the arising forces are discussed in subsection 2.6.2. At least one of them always had to be applied to determine the geometry of the molecules in vacuum (see sections 4.1, 5.1[8]) and surface systems (see sections 3.2, 4.2, 5.2). An investigation of additional cell shape and volume changes (see subsection 2.6.3) was included for the ice bulk to demonstrate the validity of a simplified model (see section 3.1).

2.6.1. Total (free) energy minimisation for force-free bulk cells

Classical thermodynamics states that thermal equilibrium minimises the free energy $F := E - TS$ of isothermal closed systems. The simulations also postulate these conditions. The equilibrium volume resp. the lattice constant leads to the lowest F. The strategy is to calculate F for some suitable lattice constants chosen around the experimental value. Regression analysis with a fit function given by an equation of state is then performed to obtain the theoretical geometry.

It is sufficient to consider E, since the zero point of the Kelvin scale is assumed in the present context. To be more exact an artificial electronic temperature was introduced to stabilise and speed up convergence, yet this is of no further meaning when the calculation is completed.

In 1944 Francis Murnaghan proposed an equation of the state named after him [148], which is applicable in a much wider range than the well-known Hooke's law. It was developed from a continuum mechanical model with the aid of thermodynamic relations and describes the isothermal volume dependency of the total energy E of a solid. The index 0 stands for thermal equilibrium. The bulk modulus B is defined in the following.

$$\begin{aligned} B &:= -V \left(\frac{\partial p}{\partial V} \right)_T \Rightarrow B_0 = -V_0 \left(\frac{\partial p}{\partial V} \right)_T \Big|_{V=V_0} \\ B' &:= \left(\frac{\partial B}{\partial p} \right)_T \Rightarrow B'_0 = \left(\frac{\partial B}{\partial p} \right)_T \Big|_{V=V_0} \end{aligned} \tag{2.94}$$

[8] Here it could have been neglected.

$$\overset{(2.94),\ \textit{Taylor expansion}}{\Rightarrow} B \approx B_0 + B_0' p \tag{2.95}$$

$$\overset{(2.94),(2.95)}{\Rightarrow} -V dp = (B_0 + B_0' p) dV \Rightarrow -\frac{dV}{V} = \frac{dp}{B_0 + B_0' p}$$

$$\Rightarrow -\int_{V_0}^{V} \frac{dV'}{V'} = \int_{0}^{p} \frac{dp'}{B_0 + B_0' p'} \Rightarrow p = \frac{B_0}{B_0'} \left[\left(\frac{V_0}{V} \right)^{B_0'} - 1 \right] \tag{2.96}$$

A canonical ensemble is present, since the system can change its total energy, but is not able to exchange matter with the environment. Hence the first law of thermodynamics – expressed solely by state variables – is valid.

$$dE = TdS - pdV \tag{2.97}$$

$$\Rightarrow p = -\left(\frac{\partial E}{\partial V} \right)_S \tag{2.98}$$

Murnaghan used a separation of variables on equation (2.98). Equation (2.96) enables solving the integral.

$$\overset{(2.98)}{\Rightarrow} E(V) = E_0 - \int_{V_0}^{V} p dV' \tag{2.99}$$

$$\overset{(2.96),(2.99)}{\Rightarrow} E(V) = E_0 - \frac{B_0}{B_0'} \int_{V_0}^{V} \left[\left(\frac{V_0}{V'} \right)^{B_0'} - 1 \right] dV' \tag{2.100}$$

This yields the Murnaghan equation of state.

$$E(V) = E_0 + B_0 \left\{ \frac{V}{B_0'} \left[\frac{\left(\frac{V_0}{V} \right)^{B_0'}}{B_0' - 1} + 1 \right] - \frac{V_0}{B_0' - 1} \right\} \tag{2.101}$$

2.6.2. Reduction of the forces on individual atomic nuclei

Experimental bond lengths or relaxed bulk structures help to construct an initial guess for the geometry of the more complex surface systems and molecules in vacuum. Starting from there an iterative optimisation is performed based on the Born-Oppenheimer approximation (see subsection 2.1.1). As already discussed in subsection 2.1.1, it is reasonable, and of course a convenient simplification, to treat the ions classically as point particles (with associated pseudopotential (see section 2.3)) due to the mass ratio between electrons and atomic nuclei as well as the Ehrenfest theorem.

Within a single ionic relaxation step the total energy of the supercell depends merely on the coordinates $\{\mathbf{R}_\mathrm{I}\} =: \mathbf{Q}$ of the atomic nuclei. These are moved on the Born-Oppenheimer surface $E_0(\mathbf{Q})$, which also determines their dynamics, to reach their equilibrium positions around which they vibrate at finite temperatures.

$$E_0(\mathbf{Q}) = E_0^\mathrm{e}(\mathbf{Q}) + V_\mathrm{cc}(\mathbf{Q}) \tag{2.102}$$

$$\mathbf{F}_\mathrm{I}(\mathbf{Q}) = M_\mathrm{I}\frac{d^2}{dt^2}\mathbf{R}_\mathrm{I} = -\frac{d}{d\mathbf{R}_\mathrm{I}}E_0(\mathbf{Q}) \tag{2.103}$$

The forces $\mathbf{F}_\mathrm{I}(\mathbf{Q})$ acting upon the atomic nuclei are essentially the Hellmann-Feynman forces $\mathbf{F}_\mathrm{I}^\mathrm{HF}(\mathbf{Q})$. Deviations (Pulay forces $\mathbf{F}_\mathrm{I}^\mathrm{P}(\mathbf{Q})$ [149]) may appear since the conditions for the Hellmann-Feynman theorem (HFT, proven independently by several authors, e.g. Feynman [150]) are only approximately fulfilled due to technical issues. For a finite basis set the electronic wave function $\Phi(\mathbf{q};\mathbf{Q})$ is generally not an exact eigenstate of the electronic Hamiltonian $\hat{H}_\mathrm{e}$. The emerging Pulay forces do not vanish a priori, since ionic relaxation also influences $\Phi(\mathbf{q};\mathbf{Q})$. Yet it could be demonstrated that each of these terms indeed gives the null vector if a plane wave basis set (see section 2.2) is employed, because these basis functions are independent of $\mathbf{Q}$ [151].

$$\begin{aligned}
\mathbf{F}_\mathrm{I}^\mathrm{HK}(\mathbf{Q}) &= -\frac{\partial}{\partial\mathbf{R}_\mathrm{I}}E_0(\mathbf{Q}) \\
\mathbf{F}_\mathrm{I}^\mathrm{P}(\mathbf{Q}) &= -\left(\left\langle\frac{d\phi}{d\mathbf{R}_\mathrm{I}}\middle|\hat{H}_\mathrm{e}\middle|\phi\right\rangle + \left\langle\phi\middle|\hat{H}_\mathrm{e}\middle|\frac{d\phi}{d\mathbf{R}_\mathrm{I}}\right\rangle\right) \approx 0
\end{aligned} \tag{2.104}$$

$$\begin{aligned}
\mathbf{F}_\mathrm{I}(\mathbf{Q}) &= -\frac{d}{d\mathbf{R}_\mathrm{I}}E_0(\mathbf{Q}) = -\frac{d}{d\mathbf{R}_\mathrm{I}}\left\langle\phi\middle|\hat{H}_\mathrm{e}\middle|\phi\right\rangle - \frac{\partial}{\partial\mathbf{R}_\mathrm{I}}V_\mathrm{cc}(\mathbf{Q}) \\
&= -\left\langle\phi\middle|\frac{\partial}{\partial\mathbf{R}_\mathrm{I}}E_0(\mathbf{Q})\middle|\phi\right\rangle - \left(\left\langle\frac{d\phi}{d\mathbf{R}_\mathrm{I}}\middle|\hat{H}_\mathrm{e}\middle|\phi\right\rangle + \left\langle\phi\middle|\hat{H}_\mathrm{e}\middle|\frac{d\phi}{d\mathbf{R}_\mathrm{I}}\right\rangle\right) \\
&= -\frac{\partial}{\partial\mathbf{R}_\mathrm{I}}E_0(\mathbf{Q}) - \left(\left\langle\frac{d\phi}{d\mathbf{R}_\mathrm{I}}\middle|\hat{H}_\mathrm{e}\middle|\phi\right\rangle + \left\langle\phi\middle|\hat{H}_\mathrm{e}\middle|\frac{d\phi}{d\mathbf{R}_\mathrm{I}}\right\rangle\right) \\
&= \mathbf{F}_\mathrm{I}^\mathrm{HK}(\mathbf{Q}) + \mathbf{F}_\mathrm{I}^\mathrm{P}(\mathbf{Q}) \approx \mathbf{F}_\mathrm{I}^\mathrm{HK}(\mathbf{Q})
\end{aligned} \tag{2.105}$$

If an artificial electronic temperature T (see subsection 2.6.1) is used, it is strictly speaking not $E_0(\mathbf{Q})$, but $F_0(\mathbf{Q}) = E_0(\mathbf{Q}) - TS_0(\mathbf{Q})$, which is the quantity to be minimised. This is not only accounted for by the influence of the occupation numbers on $E_0(\mathbf{Q})$, but also by their dependence on the electronic eigenenergies which in turn causes the atomic positions $\mathbf{Q}$ to have an effect on the entropy $S_0(\mathbf{Q})$. Nevertheless in the present context any artificial electronic temperature could be kept low enough such that it made virtually no difference.

If a good initial guess is ensured, the forces are reduced by an accelerated quasi-Newton-Raphson algorithm (VASP command: IBRION = 1), which Peter Pulay invented in 1980 [152]. It calculates the forces, the stress tensor and implicitly an approximate inverse Hessian matrix. Hence it requires very accurate forces to converge. Based thereon the search directions and relative step lengths for finding the equilibrium positions are determined, whereby the iteration history is generally also taken into account. This algorithm is most efficient close to local minima.

Intensely complicated structures, like (agglomerations of) defects or surfaces with an adsorbate or even combinations of both, may not permit such a reliable guess. Then a slower, yet more stable, conjugate gradient algorithm [153], which belongs to the predictor-corrector algorithms [153], is applied. It begins with a steepest descent from the initial positions and continues with line minimisation alternating between trial (predictor) and corrector steps. In the trial steps search directions and relative translation lengths are given by scaled gradients. After it total energy and forces are recalculated. The corrector steps refine the values of these quantities performing line minimisation interpolating the total energy minimum taking into account their changes (iteration history). If the forces contain a significant component parallel to the previous search directions, the line minimisation is improved by further corrector steps using a variant of Brent's algorithm [153] until it is sufficiently accurate for the next trial step.

The parameter POTIM (default: 0.5) serves to scale the forces before the respective minimisation routine is called. The initial Hessian matrix of the accelerated Newton-Raphson algorithm is POTIM times the unit matrix. In the conjugate gradient algorithm POTIM controls the length of the trial steps. A lowered value (0.1 or 0.2) turned out to be more convenient.

The accuracy of the forces may be improved by reducing the noise in them with an additional grid (ADDGRID = .TRUE. instead of the default ADDGRID = .FALSE.) for more precise evaluation of the augmentation charges (see section 2.4). This was found to be helpful for the molecules in vacuum.

2.6.3. Cell shape and volume changes

Cell shape and volume changes might additionally be included in a single calculation, yet this requires caution. The Pulay stress (named for Peter Pulay (by analogy with the aforementioned Pulay force) by G. P. Francis and M. C. Payne in 1990 [154]), a new error in the stress tensor, arises due to the incompleteness of the basis set in conjunction with changes of the lattice vectors. The basis set initially consists of all available plane waves whose kinetic eigenenergies are not larger than E_{cut} (see sections 2.3, 2.4). These

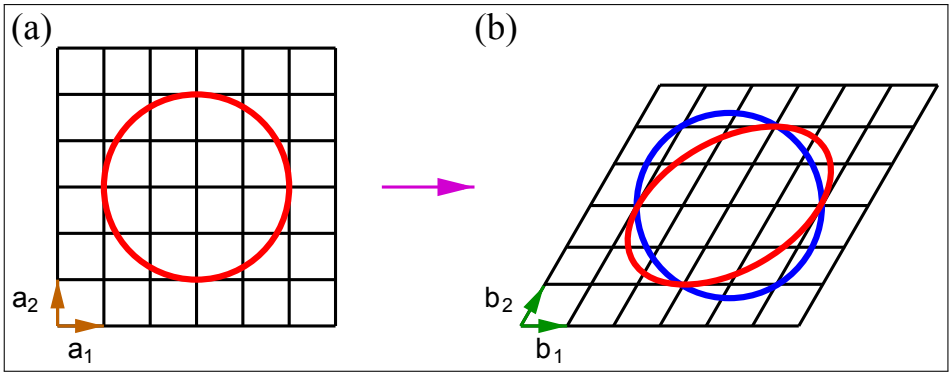

Figure 2.8.: Scheme of the origin of Pulay stress: Cell shape and volume changes transform the originally circular area of reciprocal lattice points used to construct the plane wave basis set into an ellipsis (borders marked in red). Pulay stress occurs since the sets of points contained in the blue circle and red ellipsis are not identical, although both correspond to the same energy cutoff E_{cut} (see also sections 2.3, 2.4). (a) original square reciprocal lattice, basis $\{\mathbf{a}_1, \mathbf{a}_2\}$ (b) new hexagonal reciprocal lattice, basis $\{\mathbf{b}_1, \mathbf{b}_2\}$

elements correspond to all points of the reciprocal lattice, which are contained in a sphere centered at the origin. The radius of this sphere is determined by E_{cut}.

As real and reciprocal lattice are equivalent to each other, this must also apply to any modification of them. Every point is described by a linear combination of the basis vectors with specific coefficients. The basis vectors are updated while the coefficients stay the same. Hence the aforementioned sphere is mapped onto an ellipsoid (cf. schematic Fig. 2.8). This unwanted effect on the basis set also leads to errors in ground state energy and equilibrium volume.

Pulay stress resp. its effects can be mitigated by a sufficient increase of E_{cut}, since it would not appear in case of basis set completeness. In practice this can be checked by performing a calculation with the new basis vectors kept fixed. If these and the ionic positions are successfully determined, E_{cut} might even be lowered again to proceed with a more sophisticated electronic structure treatment. This was also done for the ice bulk (see section A).

2.7. Many body perturbation theory

The fundamental strategy of many body perturbation theory (MBPT) consists in employing the formalism of quantum mechanical Green's functions to describe how the corresponding observables are affected by a perturbation.

It relies on knowledge of the non-interacting system and the perturbation operator including coupling strength. Here the perturbation is the Coulomb interaction between the electrons. The observable is the energy of either an additional electron resp. hole, which is treated within Hedin's GW approximation (GWA, see subsection 2.7.2), or an optical excitation, for which the Bethe-Salpeter equation (BSE, see subsection 2.7.4) is applied.

The quantum mechanical Green's functions are exceptionally powerful tools, since they determine the whole thermodynamics of the system [118]. For example the (differences between the positions of the) singularities of their energy-dependent representation correspond to the excitation energies. Unfortunately the equation of motion for a quantum mechanical Green's function involves another such function of a higher order. The self-energy concept (see subsection 2.7.1) is introduced to decouple these equations approximatively.

The shape of the spectral function in the energy space, more specifically its characteristic peaks centred at the single particle excitation energies, which are the positions of its maxima, illustrates how the quasiparticle (QP) concept works. It contains the same information as the corresponding Green's functions [118]. In the time space the spectral function of the interacting system with an additional electron or hole is under certain conditions formally analogous to a sum of non-interacting spectral functions for weighted perturbations of that kind with complex energies resp. specific lifetimes. Hence it can be interpreted as an ensemble of possibly decaying "quasiparticles" (QPs). These propagate freely, yet quantify the physical interaction by the values of their characteristic parameters (spectral weights, energies, lifetimes, etc.), which are determined by the self-energy (see subsection 2.7.1).

The self-energy is described by Hedin's equations and a Dyson equation. Using these equations selfconsistency for the self-energy and the appendant quantities is obtained via an iterative procedure starting from Green's function and screened Coulomb interaction of the non-interacting system (see subsection 2.7.2). This procedure employs Hedin's GW approximation (GWA) to scale down the computational effort to a feasible extent without severe loss of accuracy.

GW selfconsistency (see subsection 2.7.3) can only be obtained iteratively, because the self-energy is explicitly affected by the respective electronic energy level. Investigating its role serves not only to quantify the relevance of the underlying assumptions for the position of the ice band gap edges (with respect to vacuum). An estimate of the electronic structure error margin is necessary to justify subsequent G_0W_0 studies of larger (surface) systems. For these even partial GW selfconsistency would only come at prohibitive computational cost. The transition from Kohn-Sham scheme (see subsection

2.1.3) to quasiparticle concept leads to fully non-selfconsistent GW, which is termed "G_0W_0" [92]. Originally partial GW selfconsistency was enabled by iteratively updating the quasiparticle energies in the causal one-electron Green's function G (GW_0 [139]) and additionally for the screened Coulomb interaction W (GW [139]). Nevertheless choosing an appropriate starting point remains crucial [145]. These approaches were generalised by updating the orbital wave functions based on taking non-diagonal elements of the self-energy matrix Σ into account ($scGW_{(0)}$ [155]).

Optical excitations, i.e. hole-electron states, are described via the Bethe-Salpeter equation (BSE, see subsection 2.7.4). It is the equation of motion for an interacting two-particle Green's function. The electron-hole interaction kernel, as well as non-interacting and interacting electron-hole Green's function, is constructed exclusively from results of the respective underlying GW calculation.

2.7.1. Self-energy and quasiparticle concept

The basic features and the functionality of the quasiparticle (QP) concept are briefly explained. The present description follows the foundational work of Nolting [118]. Please consult this work for extensive derivations and detailed discussions.

The exact calculation of expectation values and correlation functions is only possible if the partition function of the system under consideration is known. Since this is generally not the case in many particle physics, perturbation theory is used to find approximations based on decomposing the full (perturbed) Hamiltonian into an original (unperturbed) part, for which the exact solutions are assumed to be available, and a perturbation. The formalism of quantum mechanical Green's functions is a fundamental tool and suitable approximations for them resp. to decouple their equations of motion are of paramount importance.

Hedin's GW approximation (GWA, see subsection 2.7.2) works with causal one-electron Green's functions. However the complete formalism of Green's functions knows three types of them: retarded (ret), advanced (av) and causal (c) (see equations (2.106), (2.107)). Green's functions for other operators, e.g. the electron-hole Green's functions used in the BSE (see subsection 2.7.4), can be defined analogously.

$$
\begin{aligned}
G^{\mathrm{ret}}_{a_{\mathbf{k}\sigma}a^{\dagger}_{\mathbf{k}\sigma}}(t,t') &:= \ll \hat{a}_{\mathbf{k}\sigma}(t);\hat{a}^{\dagger}_{\mathbf{k}\sigma}(t') \gg^{\mathrm{ret}} := -i\Theta(t-t')\langle[\hat{a}_{\mathbf{k}\sigma}(t),\hat{a}^{\dagger}_{\mathbf{k}\sigma}(t')]_{+}\rangle \\
G^{\mathrm{av}}_{a_{\mathbf{k}\sigma}a^{\dagger}_{\mathbf{k}\sigma}}(t,t') &:= \ll \hat{a}_{\mathbf{k}\sigma}(t);\hat{a}^{\dagger}_{\mathbf{k}\sigma}(t') \gg^{\mathrm{av}} := +i\Theta(t'-t)\langle[\hat{a}_{\mathbf{k}\sigma}(t),\hat{a}^{\dagger}_{\mathbf{k}\sigma}(t')]_{+}\rangle \\
G^{\mathrm{c}}_{a_{\mathbf{k}\sigma}a^{\dagger}_{\mathbf{k}\sigma}}(t,t') &:= \ll \hat{a}_{\mathbf{k}\sigma}(t);\hat{a}^{\dagger}_{\mathbf{k}\sigma}(t') \gg^{\mathrm{c}} := -i\langle T_{-}(\hat{a}_{\mathbf{k}\sigma}(t)\hat{a}^{\dagger}_{\mathbf{k}\sigma}(t'))\rangle \\
&= -i\Theta(t-t')\langle\hat{a}_{\mathbf{k}\sigma}(t)\hat{a}^{\dagger}_{\mathbf{k}\sigma}(t')\rangle + i\Theta(t'-t)\langle\hat{a}^{\dagger}_{\mathbf{k}\sigma}(t')\hat{a}_{\mathbf{k}\sigma}(t)\rangle
\end{aligned}
\tag{2.106}
$$

$$
G^{\alpha}_{\mathbf{k}\sigma}(t,t') := G^{\alpha}_{a_{\mathbf{k}\sigma}a^{\dagger}_{\mathbf{k}\sigma}}(t,t') \quad \forall \quad \alpha = \mathrm{ret,av,c} \tag{2.107}
$$

The "fermionic" time ordering operator of Wick T_{-} is defined for two operators according to equation (2.108).

$$
T_{-}(\hat{A}(t)\hat{B}(t')) := \Theta(t-t')\hat{A}(t)\hat{B}(t') - \Theta(t'-t)\hat{B}(t')\hat{A}(t) \tag{2.108}
$$

Note that the Heisenberg picture is conventionally used for the Green's functions. Moreover they are homogeneous in time, i.e. they depend merely on the difference between both time arguments ($G^{\alpha}_{\mathbf{k}\sigma}(t,t') = G^{\alpha}_{\mathbf{k}\sigma}(t-t')$), if the original Hamilton operator (Schrödinger picture) has no explicit time dependence[9] ($\frac{\partial}{\partial t}\hat{H}_{0,\mathrm{S}} = 0$).

$$
\begin{aligned}
i\hbar\frac{d}{dt}\hat{X}(t) &= [\hat{X}(t),\hat{\mathscr{H}}(t)]_{-} + i\hbar\frac{\partial}{\partial t}\hat{X}(t) \\
\text{with} \quad \frac{\partial\hat{X}_{\mathrm{H}}}{\partial t} &:= \hat{U}^{-1}(t,0)\frac{\partial\hat{X}_{\mathrm{S}}}{\partial t}\hat{U}(t,0)
\end{aligned}
\tag{2.109}
$$

Heisenberg's equation of motion (2.109) ($\hat{X}(t) \equiv$ arbitrary operator, $\hat{U}(t,0)$ $\equiv$ time evolution operator) leads to an equation of motion (2.110) that has the same shape for all types of Green's functions, but specific boundary conditions follow from the defining equations (2.106).

$$
\begin{gathered}
i\hbar\frac{\partial}{\partial t}G^{\alpha}_{a_{\mathbf{k}\sigma}a^{\dagger}_{\mathbf{k}\sigma}}(t,t') = \hbar\delta(t-t')\langle[\hat{a}_{\mathbf{k}\sigma},\hat{a}^{\dagger}_{\mathbf{k}\sigma}]_{+}(t)\rangle + G^{\alpha}_{[a_{\mathbf{k}\sigma},\hat{\mathscr{H}}]_{-}a^{\dagger}_{\mathbf{k}\sigma}}(t,t') \\
\forall \quad \alpha = \mathrm{ret,av,c}
\end{gathered}
\tag{2.110}
$$

(2.110) involves a Green's function of higher order and iteration produces an infinite chain of equations (2.111) that has no established general solution.

[9] Then it is also valid in the picture of Heisenberg or Dirac ($\frac{\partial}{\partial t}\hat{H}_{0,\mathrm{X}} = 0$ with X=H,D).

$$
\begin{aligned}
&i\hbar\frac{\partial}{\partial t}G^{\alpha}_{[a_{\mathbf{k}\sigma},\hat{\mathscr{H}}]_-^{(n)}a^{\dagger}_{\mathbf{k}\sigma}}(t,t') \\
&= \hbar\delta(t-t')\langle[[\hat{a}_{\mathbf{k}\sigma},\hat{\mathscr{H}}]_-^{(n)},\hat{a}^{\dagger}_{\mathbf{k}\sigma}]_+(t)\rangle + G^{\alpha}_{[a_{\mathbf{k}\sigma},\hat{\mathscr{H}}]_-^{(n+1)}a^{\dagger}_{\mathbf{k}\sigma}}(t,t') \\
&\forall \quad \alpha = \text{ret,av,c} \wedge n \in \mathbb{N} \\
\text{with} \quad &[\hat{a}_{\mathbf{k}\sigma},\hat{\mathscr{H}}]_-^{(1)} := [\hat{a}_{\mathbf{k}\sigma},\hat{\mathscr{H}}]_- \wedge [\hat{a}_{\mathbf{k}\sigma},\hat{\mathscr{H}}]_-^{(n+1)} := [[\hat{a}_{\mathbf{k}\sigma},\hat{\mathscr{H}}]_-^{(n)},\hat{\mathscr{H}}]_- \\
&\forall \quad n \in \mathbb{N}
\end{aligned}
\tag{2.111}
$$

It is convenient to convert (2.110) from a differential into an algebraic equation (2.112) via Fourier transformation. Of course it works analogously for the other parts of (2.111).

$$
EG^{\alpha}_{a_{\mathbf{k}\sigma}a^{\dagger}_{\mathbf{k}\sigma}}(E) = \hbar\langle[\hat{a}_{\mathbf{k}\sigma},\hat{a}^{\dagger}_{\mathbf{k}\sigma}]_+\rangle + G^{\alpha}_{[a_{\mathbf{k}\sigma},\hat{\mathscr{H}}]_-a^{\dagger}_{\mathbf{k}\sigma}}(E) \tag{2.112}
$$

$G^{\alpha}_{\mathbf{k}\sigma}$ (see equation (2.114)) for a – most generally macrocanonical – ensemble of non-interacting Bloch electrons (see equations (2.113)) are of fundamental importance for the treatment of more intricate problems. In the present case this refers to taking the Coulomb interaction between the electrons into account.

$$
\begin{aligned}
\hat{\mathscr{H}}_0 = \hat{H}_0 - \mu\hat{N} \wedge \hat{H}_0 = \sum_{\mathbf{k}\sigma}\varepsilon(\mathbf{k})\hat{n}_{\mathbf{k}\sigma} \wedge \hat{N} = \sum_{\mathbf{k}\sigma}\hat{n}_{\mathbf{k}\sigma} \wedge \hat{n}_{\mathbf{k}\sigma} = \hat{a}^{\dagger}_{\mathbf{k}\sigma}\hat{a}_{\mathbf{k}\sigma} \\
\Rightarrow \hat{\mathscr{H}}_0 = \sum_{\mathbf{k}\sigma}(\varepsilon(\mathbf{k})-\mu)\hat{a}^{\dagger}_{\mathbf{k}\sigma}\hat{a}_{\mathbf{k}\sigma}
\end{aligned}
\tag{2.113}
$$

$$
G^{\alpha}_{\mathbf{k}\sigma}(E) := \ll \hat{a}_{\mathbf{k}\sigma};\hat{a}^{\dagger}_{\mathbf{k}\sigma} \gg^{\alpha}_{E} = \int_{-\infty}^{+\infty} G^{\alpha}_{\mathbf{k}\sigma}(t-t')e^{+\frac{i}{\hbar}E(t-t')}d(t-t') \tag{2.114}
$$

The equation of motion (2.115) is solved analytically. It yields that the time-dependent one-electron Green's functions oscillate with a frequency corresponding to an excitation energy (see equations (2.116)). Note that $G^{\text{ret}}_{\mathbf{k}\sigma}$ and $G^{\text{av}}_{\mathbf{k}\sigma}$ could be unified by allowing complex values for the energy E. $G^{\text{c}}_{\mathbf{k}\sigma}$ is more complicated, since it involves the occupation number expectation value $\langle\hat{n}_{\mathbf{k}\sigma}\rangle$. $\langle\hat{n}_{\mathbf{k}\sigma}\rangle$ is calculated e.g. via the spectral theorem, which yields the familiar Fermi-Dirac distribution. Then $G^{\text{c}}_{\mathbf{k}\sigma}$ can be expressed via the two other Green's functions.

$$
EG^{\alpha}_{\mathbf{k}\sigma}(E) = \hbar\langle[\hat{a}_{\mathbf{k}\sigma},\hat{a}^{\dagger}_{\mathbf{k}\sigma}]_+\rangle + \ll [\hat{a}_{\mathbf{k}\sigma},\hat{\mathscr{H}}_0]_-;\hat{a}^{\dagger}_{\mathbf{k}\sigma} \gg^{\alpha}_{E} = \hbar + (\varepsilon(\mathbf{k})-\mu)G^{\alpha}_{\mathbf{k}\sigma}(E) \tag{2.115}
$$

$$
\begin{aligned}
G^{\text{ret}}_{\mathbf{k}\sigma}(E) &= \frac{\hbar}{E-(\varepsilon(\mathbf{k})-\mu)+i0^+} \;\Leftrightarrow\; G^{\text{ret}}_{\mathbf{k}\sigma}(t-t') = -i\Theta(t-t')e^{-\frac{i}{\hbar}(\varepsilon(\mathbf{k})-\mu)(t-t')} \\
G^{\text{av}}_{\mathbf{k}\sigma}(E) &= \frac{\hbar}{E-(\varepsilon(\mathbf{k})-\mu)-i0^+} \;\Leftrightarrow\; G^{\text{av}}_{\mathbf{k}\sigma}(t-t') = +i\Theta(t'-t)e^{-\frac{i}{\hbar}(\varepsilon(\mathbf{k})-\mu)(t-t')} \\
G^{\text{c}}_{\mathbf{k}\sigma}\underset{(t-t')}{(E)} &= (1-\langle\hat{n}_{\mathbf{k}\sigma}\rangle)G^{\text{ret}}_{\mathbf{k}\sigma}\underset{(t-t')}{(E)} + \langle\hat{n}_{\mathbf{k}\sigma}\rangle G^{\text{av}}_{\mathbf{k}\sigma}\underset{(t-t')}{(E)} \\
&\text{with} \quad \langle\hat{n}_{\mathbf{k}\sigma}\rangle = \frac{1}{1+e^{+\beta(\varepsilon(\mathbf{k})-\mu))}} \quad \wedge \quad \beta := \frac{1}{\mathrm{k_B}T}
\end{aligned}
\tag{2.116}
$$

Incorporating the Coulomb interaction between the electrons makes the equation of motion substantially more intricate (see equations (2.117) and (2.118), ${}^{\alpha}\Gamma^{\sigma\sigma'}_{\mathbf{pk};\mathbf{q}} \equiv$ higher Green's function).

$$
\hat{\mathscr{H}} = \hat{\mathscr{H}}_0 + \frac{1}{2}\sum_{\substack{\mathbf{kpq}\\ \sigma\sigma'}} v_{\mathbf{kp}}(\mathbf{q})\hat{a}^{\dagger}_{\mathbf{k}+\mathbf{q}\sigma}\hat{a}^{\dagger}_{\mathbf{p}-\mathbf{q}\sigma'}\hat{a}_{\mathbf{p}\sigma'}\hat{a}_{\mathbf{k}\sigma} \tag{2.117}
$$

$$
\begin{aligned}
(E-\varepsilon(\mathbf{k})+\mu)G^{\alpha}_{\mathbf{k}\sigma}(E) &= \hbar + \sum_{\substack{\mathbf{pq}\\ \sigma'}} v_{\mathbf{p},\mathbf{k}+\mathbf{q}}(\mathbf{q})\,{}^{\alpha}\Gamma^{\sigma\sigma'}_{\mathbf{pk};\mathbf{q}}(E) = \hbar + \Sigma^{\alpha}_{\sigma}(\mathbf{k},E)G^{\alpha}_{\mathbf{k}\sigma}(E) \\
&\text{with} \quad {}^{\alpha}\Gamma^{\sigma\sigma'}_{\mathbf{pk};\mathbf{q}}(E) := \ll \hat{a}^{\dagger}_{\mathbf{p}+\mathbf{q}\sigma'}\hat{a}_{\mathbf{p}\sigma'}\hat{a}_{\mathbf{k}+\mathbf{q}\sigma};\hat{a}^{\dagger}_{\mathbf{k}\sigma} \gg^{\alpha}_{E}
\end{aligned}
\tag{2.118}
$$

As it seems that no general solution exists, the self-energy $\Sigma^{\alpha}_{\sigma}(\mathbf{k},E)$ concept is introduced to search for suitable approximations. It postulates that the contribution of the higher Green's functions can be expressed as the product of self-energy and interacting basic Green's function (2.118). Under this assumption both basic Green's functions ($G^{(0)}_{\mathbf{k}\sigma}(E)$ and $G_{\mathbf{k}\sigma}(E)$) are of the same shape and hence linked by a Dyson equation, whose formal solution is also given (see equations (2.119) and (2.120)).

$$
G^{\alpha}_{\mathbf{k}\sigma}(E) = \frac{\hbar}{E-(\varepsilon(\mathbf{k})-\mu+\Sigma^{\alpha}_{\sigma}(\mathbf{k},E))} \tag{2.119}
$$

$$
G_{\mathbf{k}\sigma}(E) = \frac{\hbar G^{(0)}_{\mathbf{k}\sigma}(E)}{\hbar - G^{(0)}_{\mathbf{k}\sigma}(E)\Sigma_{\sigma}(\mathbf{k},E)} = G^{(0)}_{\mathbf{k}\sigma}(E) + \frac{1}{\hbar}G^{(0)}_{\mathbf{k}\sigma}(E)\Sigma_{\sigma}(\mathbf{k},E)G_{\mathbf{k}\sigma}(E) \tag{2.120}
$$

The spectral function $S_{\mathbf{k}\sigma}(t,t')$ (see equations (2.121)) contains the same information as the Green's functions. Note that the Heisenberg picture is not abandoned.

$$
\begin{aligned}
S_{\mathbf{k}\sigma}(t,t') &:= \frac{1}{2\pi}\langle[\hat{a}_{\mathbf{k}\sigma}(t),\hat{a}^{\dagger}_{\mathbf{k}\sigma}(t')]_{+}\rangle \\
\text{and if} \quad \frac{\partial}{\partial t}\hat{H} = 0 \quad &\Rightarrow \quad S_{\mathbf{k}\sigma}(t,t') = S_{\mathbf{k}\sigma}(t-t')
\end{aligned}
\tag{2.121}
$$

Analysing the dependence of the spectral function $S_{\mathbf{k}\sigma}$ on the self-energy $\Sigma^{\alpha}_{\sigma}(\mathbf{k},\ldots)$ gives insight into the functionality of the quasiparticle (QP) concept. Although $\alpha = \mathrm{c}$ is used in Hedin's GWA (see subsection 2.7.2), $\alpha = \mathrm{ret}$ is chosen here since this is much simpler and preferable for demonstration purposes (see equations (2.122)).

$$\begin{gathered}\Sigma^{\alpha}_{\sigma}(\mathbf{k},E) = R^{\alpha}_{\sigma}(\mathbf{k},E) + iI^{\alpha}_{\sigma}(\mathbf{k},E) \quad \forall \quad \alpha = \mathrm{ret,av,c} \\ \mathrm{Im}(G^{\mathrm{ret}}_{\mathbf{k}\sigma}(E)) = -\pi S_{\mathbf{k}\sigma}(E) = \frac{\hbar I_{\sigma}(\mathbf{k},E)}{\left[E - (\varepsilon(\mathbf{k}) - \mu + R_{\sigma}(\mathbf{k},E))\right]^2 + I^2_{\sigma}(\mathbf{k},E)} \leq 0\end{gathered} \tag{2.122}$$

$R^{\mathrm{ret}}_{\sigma}(\mathbf{k},\ldots)$ and $I^{\mathrm{ret}}_{\sigma}(\mathbf{k},\ldots)$ are the real and imaginary part of the retarded self-energy $\Sigma^{\mathrm{ret}}_{\sigma}(\mathbf{k},\ldots)$. The index "ret" is left out from now on. The maxima of $S_{\mathbf{k}\sigma}(E)$ lie at the resonance positions $E_{\mathrm{i}\sigma}(\mathbf{k})$ (excitation energies). While the non-interacting system exhibits delta distributions there, these are weighted (case A: $I_{\sigma}(\mathbf{k},E) = 0$ in an open interval containing $E_{\mathrm{i}\sigma}(\mathbf{k})$) or additionally broadened into Lorentzians (case B: $I_{\sigma}(\mathbf{k},E_{\mathrm{i}\sigma}(\mathbf{k})) \neq 0$, but $|I_{\sigma}(\mathbf{k},E)| \ll |\varepsilon(\mathbf{k}) - \mu + R_{\sigma}(\mathbf{k},E)|$ and $I_{\sigma}(\mathbf{k},E) \approx I_{\sigma}(\mathbf{k},E_{\mathrm{i}\sigma}(\mathbf{k})) = I_{\sigma}(\mathbf{k})$ for $E \approx E_{\mathrm{i}\sigma}(\mathbf{k})$) if a perturbation is introduced (see equations (2.123)). $S_{\mathbf{k}\sigma}(t-t')$ is essentially a sum over weighted harmonic oscillations with frequencies corresponding to the resonance positions and a linear damping in case B as following from the residual theorem.

$$\begin{gathered}E_{\mathrm{i}\sigma}(\mathbf{k}) \underset{\mathrm{i}=1,2,3,\ldots}{\overset{!}{=}} \varepsilon(\mathbf{k}) - \mu + R_{\sigma}(\mathbf{k},E_{\mathrm{i}\sigma}(\mathbf{k})) \wedge \alpha_{\mathrm{i}\sigma}(\mathbf{k}) := \left|1 - \frac{\partial}{\partial E}R_{\sigma}(\mathbf{k},E)\right|^{-1}_{E=E_{\mathrm{i}\sigma}(\mathbf{k})} \\ S^{(0)}_{\mathbf{k}\sigma}(E) = \hbar\delta(E - (\varepsilon(\mathbf{k}) - \mu)) \Leftrightarrow S^{(0)}_{\mathbf{k}\sigma}(t-t') = \frac{1}{2\pi}e^{-\frac{i}{\hbar}(\varepsilon(\mathbf{k})-\mu)(t-t')} \\ S^{\mathrm{A}}_{\mathbf{k}\sigma}(E) = \hbar\sum_{\mathrm{i}}\alpha_{\mathrm{i}\sigma}(\mathbf{k})\delta(E - E_{\mathrm{i}\sigma}(\mathbf{k})) \Leftrightarrow S^{\mathrm{A}}_{\mathbf{k}\sigma}(t-t') = \frac{1}{2\pi}\sum_{\mathrm{i}}\alpha_{\mathrm{i}\sigma}(\mathbf{k})e^{-\frac{i}{\hbar}E_{\mathrm{i}\sigma}(\mathbf{k})(t-t')} \\ S^{\mathrm{B}}_{\mathbf{k}\sigma}(E) = -\frac{\hbar}{\pi}\sum_{\mathrm{i}}\frac{\alpha^2_{\mathrm{i}\sigma}(\mathbf{k})I_{\mathrm{i}\sigma}(\mathbf{k})}{(E - E_{\mathrm{i}\sigma}(\mathbf{k}))^2 + (\alpha_{\mathrm{i}\sigma}I_{\mathrm{i}\sigma}(\mathbf{k}))^2} \\ \Leftrightarrow S^{\mathrm{B}}_{\mathbf{k}\sigma}(t-t') = \frac{1}{2\pi}\sum_{\mathrm{i}}\alpha_{\mathrm{i}\sigma}(\mathbf{k})e^{-\frac{1}{\hbar}|\alpha_{\mathrm{i}\sigma}(\mathbf{k})I_{\mathrm{i}\sigma}(\mathbf{k})||t-t'|}e^{-\frac{i}{\hbar}E_{\mathrm{i}\sigma}(\mathbf{k})(t-t')}\end{gathered} \tag{2.123}$$

$2\pi S_{\mathbf{k}\sigma}(t-t')$ is the probability amplitude for detecting an electron that was inserted into the system at t in the same state at t' (see equations (2.124) and (2.125), thermal effects neglected for reasons of clarity).

$$|\phi_0(t)\rangle := \hat{a}^{\dagger}_{\mathbf{k}\sigma}(t)\,|E_0\rangle \quad \text{with} \quad T = 0\mathrm{K} \wedge |\mathbf{k}| > k_{\mathrm{F}} \wedge t > t' \tag{2.124}$$

$$2\pi S_{\mathbf{k}\sigma}(t-t') = \left\langle \phi_0(t) | \phi_0(t') \right\rangle$$

$$\begin{cases} \overset{\text{non.}}{=} e^{-\frac{i}{\hbar}(\varepsilon(\mathbf{k})-\mu)(t-t')} & \forall\, |\text{stationary}\rangle \\ \overset{\text{int.}}{=} \sum\limits_{\text{n}} \left| \langle E_{\text{n}} | \hat{a}_{\mathbf{k}\sigma} | E_0 \rangle \right|^2 e^{-\frac{i}{\hbar}(E_{\text{n}}-E_0)(t-t')} = \begin{cases} \sum\limits_{\text{i}} \alpha_{\text{i}\sigma}(\mathbf{k}) e^{-\frac{i}{\hbar}E_{\text{i}\sigma}(\mathbf{k})(t-t')} & \forall\, |\text{interf.}\rangle \\ \sum\limits_{\text{i}} \alpha_{\text{i}\sigma}(\mathbf{k}) e^{-\frac{i}{\hbar}\eta^{\text{QP}}_{\text{i}\sigma}(\mathbf{k})(t-t')} & \forall\, |\text{decay.}\rangle \end{cases} \end{cases} \tag{2.125}$$

Starting directly in the time space furthermore demonstrates more clearly that the summands of the interacting $S_{\mathbf{k}\sigma}(t-t')$ might interfere destructively as the system propagates. This can lead to a decay of the excited state carrying the excess electron as the phase factors are distributed over the complex unit circle. The formally identical structure of non-interacting and interacting $S_{\mathbf{k}\sigma}(t-t')$ motivates the interpretation of the perturbation as an ensemble of quasiparticles (QPs) with complex energies $\eta^{\text{QP}}_{\text{i}\sigma}(\mathbf{k})$ and spectral weights $\alpha_{\text{i}\sigma}(\mathbf{k})$ (see equations (2.123) to (2.126)).

$$\begin{gathered} \eta^{\text{QP}}_{\text{i}\sigma}(\mathbf{k}) = \text{Re}(\eta^{\text{QP}}_{\text{i}\sigma}(\mathbf{k})) + i\text{Im}(\eta^{\text{QP}}_{\text{i}\sigma}(\mathbf{k})) \quad \text{with} \quad \text{Im}(\eta^{\text{QP}}_{\text{i}\sigma}(\mathbf{k})) < 0 \\ \text{Re}(\eta^{\text{QP}}_{\text{i}\sigma}(\mathbf{k})) = E_{\text{i}\sigma}(\mathbf{k}) \quad \wedge \quad \left| \text{Im}(\eta^{\text{QP}}_{\text{i}\sigma}(\mathbf{k})) \right| = |\alpha_{\text{i}\sigma} I_{\text{i}\sigma}(\mathbf{k})| = \frac{\hbar}{\tau_{\text{i}\sigma}(\mathbf{k})} \\ \frac{m^*_{\text{i}\sigma}}{m} = \frac{1 - (\frac{\partial R_\sigma}{\partial E_{\text{i}\sigma}(\mathbf{k})})_{\varepsilon(\mathbf{k})}}{1 + (\frac{\partial R_\sigma}{\partial \varepsilon(\mathbf{k})})_{E_{\text{i}\sigma}(\mathbf{k})}} \end{gathered} \tag{2.126}$$

While the real part of the complex energy coincides with the corresponding resonance position, spectral weight and imaginary part determine the inverse lifetime and it is possible to define an effective mass of the QP via the real part of the self-energy (see equations (2.126)). Holes can be treated analogously.

Note that expectancy values and correlation functions are accessible by time-dependent adiabatic perturbation theory. Feynman graphs enable a particularly vivid depiction of this method, e.g. they demonstrate that instead of treating an interacting Green's function directly, it is easier to approximate the self-energy first.

2.7.2. Hedin's GW approximation

Hedin's equations, with an iterative solution scheme, and his GW approximation (GWA), making the method feasible for practical calculations of a selfconsistent self-energy resp. interacting Green's function, are outlined following a survey article of Aulbur et al. (2000) [156]. Fig. 2.9 is a schematic summary. The discovery of Hedin's equations and the introduction of the GWA are described in his seminal paper (1965) [157]. Success, limitations

and technical aspects of the GWA have been discussed in a broad context by several survey articles, e.g. [156, 158, 159].

The aim is to calculate the interacting causal one-electron Green's function $G(\mathbf{r},\mathbf{r}';t-t')$ (see equations (2.127))[10].

$$\begin{aligned} G(\mathbf{r},t;\mathbf{r}',t') &:= -i\left\langle \mathrm{N},0\left|T_{-1}(\hat{a}(\mathbf{r},t)\hat{a}^{\dagger}(\mathbf{r}',t'))\right|\mathrm{N},0\right\rangle \\ \text{here:}\quad \frac{\partial\hat{\mathscr{H}}}{\partial t}=0 \quad &\Rightarrow \quad G(\mathbf{r},t;\mathbf{r}',t')=G(\mathbf{r},\mathbf{r}';t-t') \end{aligned} \tag{2.127}$$

Its spatial dependence stems from the usage of the field operators $\hat{a}^{(\dagger)}(\mathbf{r},t)=e^{+i\hat{\mathscr{H}}t}\hat{a}^{(\dagger)}(\mathbf{r})e^{-i\hat{\mathscr{H}}t}$. Expressing the Fourier transform $G(\mathbf{r},\mathbf{r}';E)$ via the quasi-particle (QP) energies E_{i} and amplitudes $\Psi_{\mathrm{i}}(\mathbf{r})$ identifies the former as its energy poles (see equations (2.128)).

$$\begin{aligned} G(\mathbf{r},\mathbf{r}';E) &= \sum_{\mathrm{i}}\frac{\Psi_{\mathrm{i}}(\mathbf{r})\Psi_{\mathrm{i}}^{*}(\mathbf{r}')}{E-E_{\mathrm{i}}} \\ \Psi_{\mathrm{i}}(\mathbf{r}) &:= \langle \mathrm{N},0\,|\hat{a}(\mathbf{r})|\,\mathrm{N{+}1},\mathrm{i}\rangle \quad \wedge \quad E_{\mathrm{i}} := E_{\mathrm{N+1,i}}-E_{\mathrm{N,0}} \quad \forall \quad E_{\mathrm{i}}\geq\mu \\ \Psi_{\mathrm{i}}(\mathbf{r}) &:= \langle \mathrm{N\text{-}1},\mathrm{i}\,|\hat{a}(\mathbf{r})|\,\mathrm{N},0\rangle \quad \wedge \quad E_{\mathrm{i}} := E_{\mathrm{N,0}}-E_{\mathrm{N\text{-}1,i}} \quad \forall \quad E_{\mathrm{i}}<\mu \end{aligned} \tag{2.128}$$

The non-interacting Green's function has an analogous spectral representation $G^{0}(\mathbf{r},\mathbf{r}';E)=\sum_{\mathrm{i}}\frac{\phi_{\mathrm{i}}(\mathbf{r})\phi_{\mathrm{i}}^{*}(\mathbf{r}')}{E-\varepsilon_{\mathrm{i}}}$. A Dyson equation (2.129) links both Green's function with the aid of the self-energy $\Sigma(\mathbf{r}_1,\mathbf{r}_2;E)$.

$$G(\mathbf{r},\mathbf{r}';E)=G^{0}(\mathbf{r},\mathbf{r}';E)+\int_{\mathbb{R}^3}\int_{\mathbb{R}^3}G^{0}(\mathbf{r},\mathbf{r}_1;E)\Sigma(\mathbf{r}_1,\mathbf{r}_2;E)G(\mathbf{r}_2,\mathbf{r}';E)dr_1dr_2 \tag{2.129}$$

Hedin's equations additionally involve the screened Coulomb interaction W, the irreducible polarisability P and the vertex function Γ. The notation $(\mathrm{n}\in\mathbb{N}):=(\mathbf{x}_{\mathrm{n}},t_{\mathrm{n}}):=(\mathbf{r}_{\mathrm{n}},\sigma_{\mathrm{n}},t_{\mathrm{n}})$ is an abbreviation for their variables. W results from the bare Coulomb interaction v and the inverse dielectric matrix ε^{-1} taking charge screening into account according to equations (2.130).

[10] From here on atomic units ($e=\frac{1}{4\pi\varepsilon_0}=m_{\mathrm{e}}=\hbar=1$) are used for the remainder of this section.

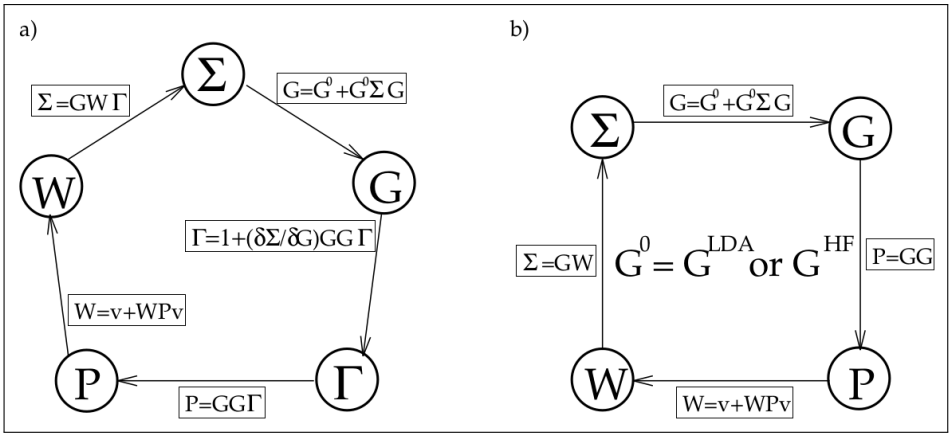

Figure 2.9.: Schematic circular flowchart for the calculation of selfconsistent quantities Σ, G, Γ, P, W by iterative solution of the Dyson equation $G = G^0 + G^0 \Sigma G$ and Hedin's equations (a) complete scheme (b) Hedin's GWA neglecting vertex corrections by setting Γ to 1; Aulbur et al. [156]

$$
\begin{aligned}
W(\mathbf{r},\mathbf{r}';\omega) &= \int_{\mathbb{R}^3} \varepsilon^{-1}(\mathbf{r},\mathbf{r}'';\omega) v(\mathbf{r}'',\mathbf{r}') dr'' \\
v(\mathbf{r},\mathbf{r}') = \frac{1}{|\mathbf{r}-\mathbf{r}'|} \quad \wedge \quad \varepsilon^{-1}(\mathbf{r},\mathbf{r}';\omega) &= \int_{-\infty}^{+\infty} \varepsilon^{-1}(\mathbf{r},\mathbf{r}';t) e^{i\omega t} dt \\
\varepsilon^{-1}(\mathbf{r},\mathbf{r}';t) & \\
= \delta(\mathbf{r}-\mathbf{r}')\delta(t) - i \int_{\mathbb{R}^3} v(\mathbf{r}-\mathbf{r}') &\left\langle \mathrm{N},0 \left| T_{-1}(\hat{n}'(\mathbf{r}'',t)\hat{n}'(\mathbf{r}',0)) \right| \mathrm{N},0 \right\rangle dr'' \\
\hat{n}'(\mathbf{r},t) := \hat{n}(\mathbf{r},t) - \langle \mathrm{N},0 |\hat{n}(\mathbf{r},t)| \mathrm{N},0\rangle \quad \wedge \quad \hat{n}(\mathbf{r},t) &:= \hat{a}^\dagger(\mathbf{r},t)\hat{a}(\mathbf{r},t)
\end{aligned}
\tag{2.130}
$$

$\hat{n}'(\mathbf{r},t)$ is the charge density fluctuation operator. P resp. Γ is defined as the functional derivative of the charge density n resp. the negative inverse interacting Green's function $-G^{-1}$ with respect to the total (Hartree plus external) potential V (see equations (2.131)).

$$
P(1,2) := \frac{\delta n(1)}{\delta V(2)} \quad \wedge \quad \Gamma(1,2;3) := -\frac{\delta G^{-1}(1,2)}{\delta V(3)} = \delta(1,2)\delta(1,3) + \frac{\delta \Sigma(1,2)}{\delta V(3)}
\tag{2.131}
$$

$$\begin{aligned}
\Sigma(1,2) &= i\int G(1,4)W(1^+,3)\Gamma(4,2;3)d(3,4) \overset{\text{GWA}}{\approx} iG(1,2)W(1^+,2)\\
W(1,2) &= v(1,2) + \int W(1,3)P(3,4)v(4,2)d(3,4)\\
P(1,2) &= -i\int G(2,3)G(4,2)\Gamma(3,4;1)d(3,4) \overset{\text{GWA}}{\approx} -iG(1,2)G(2,1)\\
\Gamma(1,2;3) &= \delta(1,2)\delta(1,3) + \int \frac{\delta\Sigma(1,2)}{\delta G(4,5)}G(4,6)G(7,5)\Gamma(6,7;3)d(4,5,6,7)
\end{aligned} \tag{2.132}$$

Hedin's equations (2.132) and the aforementioned Dyson equation ((2.120) resp. (2.129)) serve to calculate the quantities Σ, G, Γ, P, W. An iterative approach is chosen, because an analytic solution is generally not possible. Starting from the non-interacting Green's function and an approximation for the self-energy the process can be repeated in that order (cf. Fig. 2.9a). The solutions become selfconsistent (in the framework of the assumptions) when a fixed point is reached. Hedin's GWA neglects vertex corrections, i.e. Γ is set to 1 resp. a product of delta distributions so that only its last argument remains after the integration, and hence implies an enormous reduction of computational effort (cf. Fig. 2.9b). Subsection 2.7.3 discusses how the different versions of GW selfconsistency are obtained.

Hedin's equations (2.132) were originally deduced from the time-dependent Schrödinger equation of the electronic system with the Coulomb interaction between electrons and nuclei as perturbation [Hamilton operator according to equation (2.8) (summands defined by equations (2.2) to (2.4))] [157]. They follow after inserting the functional derivative of the interacting time evolution operator with respect to the nuclear Coulomb potential, incorporating Green's function theory and several algebraic conversions. Note that the newly introduced quantities Γ, P, W are also accessible by diagrammatic perturbation theory, more specifically the method of diagrammatic partial sums [118].

2.7.3. Quasiparticle energy levels and GW selfconsistency

The self-energy concept gives the electronic energy levels a direct physical interpretation, since they can be viewed as belonging to an excess electron (or hole) surrounded by its polarisation cloud (charge screening resp. solvation effects). In the underlying DFT calculations the determination of the electronic ground state density $n_0(\mathbf{r})$ is a problem of variational calculus according to the Hohenberg-Kohn theorem (see subsection 2.1.2). Furthermore, the Kohn-Sham (KS) orbitals and energies are described by the differential equation (2.133) (see also subsection 2.1.3).

$$\left(-\frac{1}{2}\nabla^2 + V_{\mathrm{eI}} + V_{\mathrm{H}}[n] + V_{\mathrm{XC}}[n]\right)\phi_{\mathrm{i}}(\mathbf{r}) = \varepsilon^{\mathrm{i}}_{\mathrm{KS}}\phi_{\mathrm{i}}(\mathbf{r}) \tag{2.133}$$

The results are the starting point for the iterative solution of its integro-differential counterpart (2.134) [92] in the subsequent quasiparticle (QP) calculations employing Hedin's GW approximation (GWA, see subsection 2.7.2). They are preferred over Hartree-Fock (HF) results, because they are generally closer to the ideal GW results. Hence the GW calculations are more likely to converge to the correct fixed point and also to be faster. This is due to the fact that DFT additionally incorporates correlation (C).

$$\left(-\frac{1}{2}\nabla^2 + V_{\mathrm{eI}} + V_{\mathrm{H}}[n]\right)\Psi_{\mathrm{i}}(\mathbf{r}) + \int_{\mathbb{R}^3}\Sigma(\mathbf{r},\mathbf{r}',\varepsilon^{\mathrm{i}}_{\mathrm{QP}})\Psi_{\mathrm{i}}(\mathbf{r}')d^3r' = \varepsilon^{\mathrm{i}}_{\mathrm{QP}}\Psi_{\mathrm{i}}(\mathbf{r}) \tag{2.134}$$

Here the focus lies on explaining how the QP energies and orbital wave functions are updated, because the different versions of GW selfconsistency have already been discussed at the beginning of this section.

(2.134) works with the self-energy $\Sigma(\mathbf{r},\mathbf{r}',\varepsilon^{\mathrm{i}}_{\mathrm{QP}})$, instead of the exchange-correlation potential $V_{\mathrm{XC}}[n]$, to quantify the quantum mechanical part of the electron-electron interaction. The self-energy concept takes the polarisation cloud of the excess electron into account instead of constructing a fictitious system of non-interacting electrons like in the KS formalism. Therefore $\Sigma(\mathbf{r},\mathbf{r}',\varepsilon^{\mathrm{i}}_{\mathrm{QP}})$ depends explicitly on the QP energy of this electron, whereas $V_{\mathrm{XC}}[n]$ exhibits no such dependence on its KS energy. The Newton-Raphson method for root finding is applied to solve for the QP energy[11]. This produces fully non-selfconsistent QP energies $E^1_{\mathbf{nk}}$ (G_0W_0 [92], see equation (2.135) with $E^0_{\mathbf{nk}} = E^{\mathrm{DFT}}_{\mathbf{nk}}$). Partial GW selfconsistency is obtained by successively repeating the process (see equation (2.135)) together with an update of the QP energies in G (GW_0 [139]) or additionally for W (GW [139]) until a fixed point is reached.

$$\begin{aligned} E^{\mathrm{N+1}}_{\mathbf{nk}} &= E^{\mathrm{N}}_{\mathbf{nk}} + Z^{\mathrm{N}}_{\mathbf{nk}}\,\mathrm{Re}\left(\left\langle\Psi_{\mathbf{nk}}\middle|\hat{T}+\hat{V}+\Sigma(E^{\mathrm{N}}_{\mathbf{nk}})\middle|\Psi_{\mathbf{nk}}\right\rangle - E^{\mathrm{N}}_{\mathbf{nk}}\right) \\ \text{with}\quad Z^{\mathrm{N}}_{\mathbf{nk}} &:= \left(1 - \mathrm{Re}\left(\left\langle\Psi_{\mathbf{nk}}\middle|\frac{\partial\Sigma(\omega)}{\partial\omega}|_{E^{\mathrm{N}}_{\mathbf{nk}}}\middle|\Psi_{\mathbf{nk}}\right\rangle\right)\right)^{-1} \end{aligned} \tag{2.135}$$

To make full GW selfconsistency attainable an update "sc" of the orbital wave functions, which come originally from the underlying DFT, is incorporated [155]. Applying the Newton-Raphson method leads to the non-Hermitian eigenvalue problem $\mathbf{H}(E^{\mathrm{N}}_{\mathrm{n}})\left|\Psi^{\mathrm{N+1}}_{\mathrm{n}}\right\rangle = E^{\mathrm{N+1}}_{\mathrm{n}}\mathbf{S}(E^{\mathrm{N}}_{\mathrm{n}})\left|\Psi^{\mathrm{N+1}}_{\mathrm{n}}\right\rangle$ (see equations (2.136)).

[11] This is a first-order Taylor expansion of $\Sigma(\mathbf{r},\mathbf{r}',\varepsilon)$ with respect to ε around the KS energy from DFT.

$$
\begin{aligned}
\Sigma(E_n^{N+1}) &\approx \Sigma(E_n^N) + \xi(E_n^N)(E_n^{N+1} - E_n^N) \quad \text{with} \quad \xi(E_n^N) := \frac{\partial \Sigma(\omega)}{\partial \omega}|_{E_n^N} \\
\mathbf{H}(E_n^N)\left|\Psi_n^{N+1}\right\rangle &= E_n^{N+1}\mathbf{S}(E_n^N)\left|\Psi_n^{N+1}\right\rangle \\
\text{with } \mathbf{H}(E_n^N) &:= \hat{T} + \hat{V} + \Sigma(E_n^N) - E_n^N\xi(E_n^N) \wedge \mathbf{S}(E_n^N) := 1 - \xi(E_n^N) \\
\left|\Psi_n^{N+1}\right\rangle &= \sum_m U_{N,mn}\left|\Psi_m^N\right\rangle \quad \text{with} \quad \left|\Psi_n^0\right\rangle = |\phi_n\rangle \\
\overline{X}_{N,mn} &= \text{Herm}(\left\langle\Psi_m^N\right|\mathbf{X}(E_n^N)\left|\Psi_n^N\right\rangle) \,\forall\, \mathbf{X} = \mathbf{H}, \mathbf{S} \\
(U_N)^\dagger(\overline{S}_N)^{-\frac{1}{2}}\overline{H}_N(\overline{S}_N)^{-\frac{1}{2}}U_N &= \Lambda_N \quad \text{with} \quad \Lambda_N = \text{diag}(E_1^{N+1}, E_2^{N+1}, ...)
\end{aligned}
\tag{2.136}
$$

Considering only the Hermitian part of Hamilton operator $\mathbf{H}$ and overlap operator $\mathbf{S}$ was found to be a suitable approximation. This Hermitian approximation of an operator $\mathbf{X}$ is defined as $\overline{\mathbf{X}} := \frac{1}{2}(\mathbf{X} + \mathbf{X}^\dagger)$. For the diagonal elements it is the same as neglecting their imaginary part. The old orbital wave functions Ψ_n^N are used as basis to calculate their matrix representation. The resulting Hermitian eigenvalue problem can always be solved since the existence of the unitary matrix U_N is guaranteed by the principal axis theorem. This matrix is also used to transform the old basis $\{\Psi_n^N\}$ into the new basis $\{\Psi_n^{N+1}\}$. scGW$_{(0)}$ is a generalisation of GW$_{(0)}$, since the former is reduced to the latter if the off-diagonal elements of H and S are neglected and the elements of the basis set thus stay identical to the DFT orbital wave functions ϕ_n.

2.7.4. Optical excitations and the Bethe-Salpeter equation

Optical absorption spectra are determined with the aid of the Bethe-Salpeter equation (BSE), which is needed to take electron-hole interaction into account. Energy, amplitude and character of optical excitations are obtained from a feasible implementation. This procedure and the suitable approximations enabling it are discussed. Strinati (1988) [160] describes the derivation of the BSE within a concise formalism and the practical realisation used here is treated by Rohlfing and Louie (2000) [161].

Optical excitations S of the ground state 0 that leave the electron number N invariant are considered, i.e. $|N,0\rangle \rightarrow |N,S\rangle$. According to Strinati (1988) [160] the BSE can be written as the Dyson equation (2.137) that provides a link between the electron-hole correlation functions $L_0(1,2;1',2') = G_1(1,2')G_1(2,1')$ (non-interacting) and $L(1,2;1',2')$ (interacting) via the electron-hole interaction kernel $K(3,5;4,6)$.

$$
\begin{aligned}
&L(1,2;1',2') \\
&= L_0(1,2;1',2') + \int L_0(1,4;1',3)K(3,5;4,6)L(6,2;5,2')d(3,4,5,6)
\end{aligned}
\tag{2.137}
$$

The four time arguments of the correlation functions are reduced to one, because in the context of optical excitations the creation of excess electron and hole can be considered simultaneous and time homogeneity is present (see subsection 2.7.1). Remember that the time dependences come solely from the construction operators in the Heisenberg picture. To solve the BSE it is convenient to perform a Fourier transform on it. Hence the quantities are denoted by $L_{(0)}(1,2;1',2';\omega)$ resp. $K(3,5;4,6;\omega)$.

L_0 can be expressed according to equation (2.138). Thereby v (valence) resp. c (conduction) stands for states that are occupied resp. empty in the ground state $|\mathrm{N},0\rangle$. Appropriate imaginary infinitesimals would have to be added in the denominators, but were left out for reasons of clarity.

$$\begin{aligned} &L_0(1,2;1',2';\omega) \\ &= i\sum_{\mathrm{vc}}\left[\frac{\Psi_\mathrm{c}(\mathbf{x}_1)\Psi_\mathrm{v}^*(\mathbf{x}_1')\Psi_\mathrm{v}(\mathbf{x}_2)\Psi_\mathrm{c}^*(\mathbf{x}_2')}{\omega-(E_\mathrm{c}-E_\mathrm{v})}-\frac{\Psi_\mathrm{v}(\mathbf{x}_1)\Psi_\mathrm{c}^*(\mathbf{x}_1')\Psi_\mathrm{c}(\mathbf{x}_2)\Psi_\mathrm{v}^*(\mathbf{x}_2')}{\omega+(E_\mathrm{c}-E_\mathrm{v})}\right] \end{aligned} \tag{2.138}$$

L (equation 2.139) has a shape resembling that of L_0 (equation 2.138). Ω_S is the energy required for the optical excitation S. $\chi_\mathrm{S}(\mathbf{x},\mathbf{x}')$ are the electron-hole amplitudes. Like these in equation (2.140) all quantities in the practical evaluation of the BSE are simply written in terms of the already available one-electron orbital wave functions from the underlying GW calculation (see subsection 2.7.3). This choice is also convenient, because the optical excitations are directly characterised.

$$L(1,2;1',2';\omega) = i\sum_{\mathrm{S}}\left[\frac{\chi_\mathrm{S}(\mathbf{x}_1,\mathbf{x}_1')\chi_\mathrm{S}^*(\mathbf{x}_2',\mathbf{x}_2)}{\omega-\Omega_\mathrm{S}}-\frac{\chi_\mathrm{S}(\mathbf{x}_2,\mathbf{x}_2')\chi_\mathrm{S}^*(\mathbf{x}_1',\mathbf{x}_1)}{\omega+\Omega_\mathrm{S}}\right] \tag{2.139}$$

$$\begin{aligned} \chi_\mathrm{S}(\mathbf{x},\mathbf{x}') &= -\left\langle \mathrm{N},0\left|\hat{a}^\dagger(\mathbf{x}')\hat{a}(\mathbf{x})\right|\mathrm{N},\mathrm{S}\right\rangle \\ &= \sum_\mathrm{v}\sum_\mathrm{c}(A_\mathrm{vc}^\mathrm{S}\Psi_\mathrm{c}(\mathbf{x})\Psi_\mathrm{v}^*(\mathbf{x}')+B_\mathrm{vc}^\mathrm{S}\Psi_\mathrm{v}(\mathbf{x})\Psi_\mathrm{c}^*(\mathbf{x}')) \end{aligned} \tag{2.140}$$

By putting everything together the BSE (2.137) is rearranged into a generalised eigenvalue problem (equations (2.141)) with a block matrix structure. The elements of the interaction matrices K^{AA} and K^{AB} depending on the excitation energies Ω_S are given by equation (2.144). K^{BA} and K^{BB} are defined analogously. Empirical testing revealed that the off-diagonal blocks K^{AB} and K^{BA} are usually negligible (see e.g. [161–163]). This is known as the "Tamm-Dancoff approximation" (TDA, [164, 165]). It yields one equation for the coefficients A_vc^S and B_vc^S each. Since these have the exact same solutions except for the sign of Ω_S, only one of them – here equation (2.142) – is to be considered.

$$\begin{aligned}
\Omega_S A^S_{vc} &= (E_c - E_v)A^S_{vc} + \sum_{v'c'} K^{AA}_{vc,v'c'}(\Omega_S)A^S_{v'c'} + \sum_{v'c'} K^{AB}_{vc,v'c'}(\Omega_S)B^S_{v'c'} \\
&\overset{\text{TDA}}{\approx} (E_c - E_v)A^S_{vc} + \sum_{v'c'} K^{AA}_{vc,v'c'}(\Omega_S)A^S_{v'c'} \\
-\Omega_S B^S_{vc} &= (E_c - E_v)B^S_{vc} + \sum_{v'c'} K^{BB}_{vc,v'c'}(\Omega_S)B^S_{v'c'} + \sum_{v'c'} K^{BA}_{vc,v'c'}(\Omega_S)A^S_{v'c'} \\
&\overset{\text{TDA}}{\approx} (E_c - E_v)B^S_{vc} + \sum_{v'c'} K^{BB}_{vc,v'c'}(\Omega_S)B^S_{v'c'}
\end{aligned} \tag{2.141}$$

$$\Omega_S A^S_{vc} \overset{\text{TDA}}{\approx} (E_c - E_v)A^S_{vc} + \sum_{v'c'} K^{AA}_{vc,v'c'}(\Omega_S)A^S_{v'c'} \tag{2.142}$$

Interestingly the TDA (equation (2.142)) is also obtained by expanding the optical excitations in non-interacting electron-hole pairs according to equation (2.143) [$\hat{e}^\dagger_c$ ($\hat{h}^\dagger_v$) creates the conduction electron (valence hole)].

$$\begin{aligned}
|vc\rangle &:= \hat{h}^\dagger_v \hat{e}^\dagger_c |N,0\rangle \\
|N,S\rangle &= \sum_v^{h^+}\sum_c^{e^-} A^S_{vc}\hat{h}^\dagger_v\hat{e}^\dagger_c |N,0\rangle = \sum_v^{h^+}\sum_c^{e^-} A^S_{vc}|vc\rangle
\end{aligned} \tag{2.143}$$

$$\begin{aligned}
K^{AA}_{vc,v'c'}(\Omega_S) &= i\int \Psi_v(\mathbf{x}_4)\Psi^*_c(\mathbf{x}_3)K(3,5;4,6;\Omega_S)\Psi^*_{v'}(\mathbf{x}_5)\Psi_{c'}(\mathbf{x}_6)d(3,4,5,6) \\
K^{AB}_{vc,v'c'}(\Omega_S) &= i\int \Psi_v(\mathbf{x}_4)\Psi^*_c(\mathbf{x}_3)K(3,5;4,6;\Omega_S)\Psi^*_{v'}(\mathbf{x}_6)\Psi_{c'}(\mathbf{x}_5)d(3,4,5,6)
\end{aligned} \tag{2.144}$$

Starting from its definition via functional derivative, the electron-hole interaction kernel K is approximated by applying the GWA like in the underlying quasiparticle calculation (see subsections 2.7.2, 2.7.3) and neglecting the remaining functional derivative (equations (2.145)), which implies a drastic reduction of complexity [160, 161].

$$\begin{aligned}
K(3,5;4,6) &:= \frac{\delta(V_{\text{Coul}}(3)\delta(3,4) + \Sigma(3,4))}{\delta G_1(6,5)} \\
&\overset{\text{GWA}}{\approx} -i\delta(3,4)\delta(5^-,6)v(3,6) + i\delta(3,6)\delta(4,5)W(3^+,4) \\
&\quad + iG_1(3,4)\frac{\delta W(3^+,4)}{\delta G_1(6,5)} \\
&\approx -i\delta(3,4)\delta(5^-,6)v(3,6) + i\delta(3,6)\delta(4,5)W(3^+,4) \\
K^x(3,5;4,6) &:= -i\delta(3,4)\delta(5^-,6)v(3,6) \\
K^d(3,5;4,6) &:= +i\delta(3,6)\delta(4,5)W(3^+,4)
\end{aligned} \tag{2.145}$$

Thereby K is simplified into a sum over two interaction terms called direct K^{d} and exchange K^{x} (equations (2.145)). In contrast to K^{x}, K^{d} involves the screened, instead of the bare, Coulomb potential. K^{d} is hence responsible for the attractivity of the interaction between electron and hole enabling the formation of bound states. The matrix elements of the interaction terms are given by equations (2.146).

$$\begin{aligned}
K^{AA,\mathrm{x}}_{\mathrm{vc},\mathrm{v'c'}} &= \left\langle \mathrm{vc} \left| K^{AA,\mathrm{x}} \right| \mathrm{v'c'} \right\rangle \\
&= \int \Psi^*_{\mathrm{c}}(\mathbf{x}) \Psi_{\mathrm{v}}(\mathbf{x}) v(\mathbf{r},\mathbf{r}') \Psi_{\mathrm{c'}}(\mathbf{x}') \Psi^*_{\mathrm{v'}}(\mathbf{x}') d\mathbf{x} d\mathbf{x}' \\
K^{AA,\mathrm{d}}_{\mathrm{vc},\mathrm{v'c'}}(\Omega_{\mathrm{S}}) &= \left\langle \mathrm{vc} \left| K^{AA,\mathrm{d}}(\Omega_{\mathrm{S}}) \right| \mathrm{v'c'} \right\rangle \\
&= \int \Psi^*_{\mathrm{c}}(\mathbf{x}) \Psi_{\mathrm{c'}}(\mathbf{x}) \Psi_{\mathrm{v}}(\mathbf{x}') \Psi^*_{\mathrm{v'}}(\mathbf{x}') \frac{i}{2\pi} \int e^{-i\omega 0^+} W(\mathbf{r},\mathbf{r}';\omega) \\
&\left[\frac{1}{\Omega_{\mathrm{S}} - \omega - (E_{\mathrm{c'}} - E_{\mathrm{v'}}) + i0^+} + \frac{1}{\Omega_{\mathrm{S}} + \omega - (E_{\mathrm{c}} - E_{\mathrm{v}}) + i0^+} \right] d\omega d\mathbf{x} d\mathbf{x}'
\end{aligned} \tag{2.146}$$

Due to the charge screening calculating those of K^{d} requires an additional frequency integration. It can be carried out analytically (and consistently) if a plasmon-pole model [166, 167] is used for the BSE (and the underlying GW) calculation (equations (2.147), (2.148)). To this end frequencies ω_{l} and spatial behaviour $W_{\mathrm{l}}(\mathbf{r},\mathbf{r}')$ of the plasmons have to be determined [166, 167].

$$W(\mathbf{r},\mathbf{r}';\omega) = \sum_{\mathrm{l}} W_{\mathrm{l}}(\mathbf{r},\mathbf{r}') \frac{\omega_{\mathrm{l}}}{2} \left(\frac{1}{\omega - \omega_{\mathrm{l}} + i0^+} - \frac{1}{\omega + \omega_{\mathrm{l}} - i0^+} \right) \tag{2.147}$$

$$\begin{aligned}
&\left\langle \mathrm{vc} \left| K^{AA,\mathrm{d}}(\Omega_{\mathrm{S}}) \right| \mathrm{v'c'} \right\rangle \\
&= -\sum_{\mathrm{l}} \int \Psi^*_{\mathrm{c}}(\mathbf{x}) \Psi_{\mathrm{c'}}(\mathbf{x}) \Psi_{\mathrm{v}}(\mathbf{x}') \Psi^*_{\mathrm{v'}}(\mathbf{x}') W_{\mathrm{l}}(\mathbf{r},\mathbf{r}') \frac{\omega_{\mathrm{l}}}{2} \\
&\left\{ \frac{1}{\omega_{\mathrm{l}} - [\Omega_{\mathrm{S}} - (E_{\mathrm{c'}} - E_{\mathrm{v'}})]} + \frac{1}{\omega_{\mathrm{l}} - [\Omega_{\mathrm{S}} - (E_{\mathrm{c}} - E_{\mathrm{v}})]} \right\} d\mathbf{x} d\mathbf{x}'
\end{aligned} \tag{2.148}$$

2.8. Fundamental properties of conical intersections

Radiationless decay of their initial transient state is obligatory for low-energy dissociation [DEA (see chapter 5) resp. neutral photodissociation (see chapter 6)] of halogenated aromatic hydrocarbons (see also chapter 1). Along the dissociation pathway another state of the excess electron (DEA) resp. electron-hole pair (neutral photodissociation) becomes energetically more favourable than the original. The obligatory nonadiabatic transition from one potential

energy surface to another can only happen at a conical intersection (also: molecular funnel, diabolic point) between them[12]. Hence the different types of energy level crossings and the conditions for their occurrence are discussed.

Von Neumann and Wigner (1929) [168] demonstrated that the adiabatic potential energy surfaces of two molecular electronic states can only cross if two constraints are imposed on the corresponding matrix elements of the Hamiltonian. This generally requires to fix two of the M independent internuclear coordinates[13]. This implies that the crossing points form an (M-2)-dimensional seam space. Its orthogonal complement, the two-dimensional branching space (also: branching plane), is defined for each specific crossing point, which is their sole common point. In its immediate vicinity the potential energy surfaces in the branching plane have the shape of an elliptical double cone (cf. Fig. 2.10a) [168,169]. This gave the conical intersections their name. The additional term "accidental" comes from the fact that the reasoning involves no symmetry assumptions up to this point.

According to the Jahn-Teller theorem (1937) [170] each nonlinear molecule eliminates degeneracies of its electronic system by reducing the nuclear symmetry. Hence Jahn-Teller molecules inevitably exhibit symmetry-induced [171] (also: symmetry-required) conical (cf. Fig. 2.10a) or glancing (cf. Fig. 2.11) intersections, however the crossing points exist only for highly symmetric nuclear configurations. These types of intersections differ as there is a true point of intersection between the energy levels for the former, while it is a mere point of contact for the latter. Glancing (also: Renner-Teller) intersections were first treated by Renner (1934) [172]. They can also occur in linear molecules that are at least triatomic.

Accidental conical intersections are far more abundant than those of the symmetry-induced type, because the latter are always tied to nuclear symmetries. However the accidental type is more difficult to locate by the same token, in particular for electronic states that exhibit the same symmetry representation. In addition to the usual dynamical phase factor an adiabatic electronic wave function also acquires a geometrical phase factor upon transport along a path in nuclear coordinate space. For a closed loop around a crossing point, e.g. in the appendant branching plane, it turns into a mere sign change. While Herzberg and Longuet-Higgins (1963) [174] gave the first theoretical example, Berry (1984) [175] developed a general description making the geometrical phase an important tool for the search after conical intersections. In diatomics

[12] In general nonadiabatic transitions are also possible at glancing (also: Renner-Teller) intersections. However this is of no relevance for the present study.

[13] Be $N = 2,3,4,...$ the number of atoms constituting the molecule. Then $M(2) = 1$ and $M(N \geq 3) = 3N - 6$.

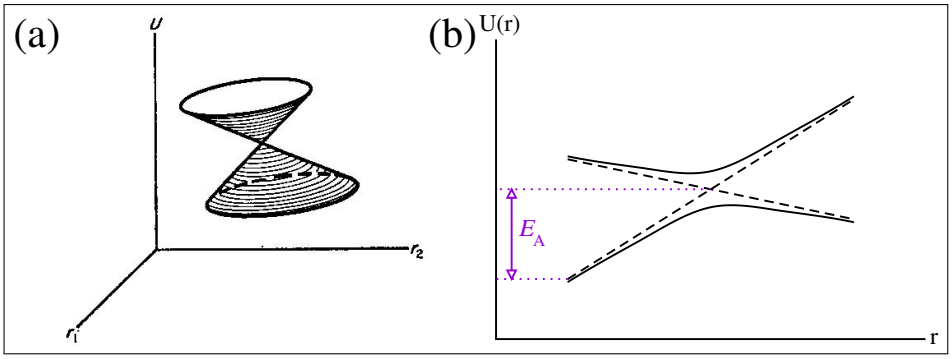

Figure 2.10.: (a) Conical intersection (taken from [169]) (b) Avoided crossing and activation energy E_A (violet)

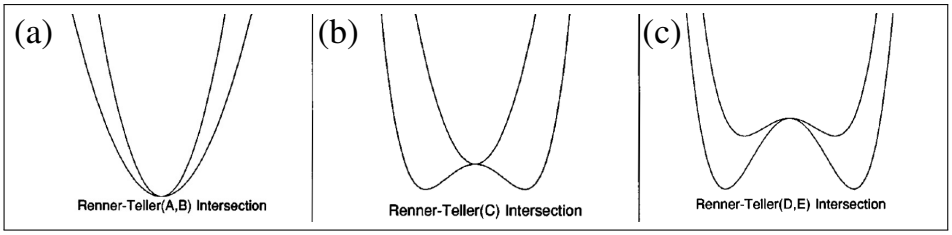

Figure 2.11.: Different kinds of glancing (also: Renner-Teller) intersections (taken from [173])

same-symmetry accidental conical intersections do not occur according to the non-crossing rule (also found by von Neumann and Wigner in the same year (1929) [176]), since only one independent nuclear coordinate, namely the internuclear distance, is available. Their existence was not unambiguously confirmed until ab-initio calculations for ozone (O_3) [177] and the quenching of molecular hydrogen (H_2) by atomic helium (He) invalidating the non-crossing rule [178] were performed in 1990. This study treats symmetry-allowed accidental conical intersections [171], which are an intermediate type. These occur between electronic states of different symmetry representations, which is favourable in search for them as one of the two aforementioned constraints is a priori fulfilled. Ab-initio calculations describing numerous specific examples have been performed in the 1990s, e.g. those for photoisomerisation of benzene (C_6H_6) and pyrazine ($C_4H_4N_2$) by Sobolewski et al. (1993) [179] or those for photodissociation of ozone (O_3) by Woywod et al. (1997) [180] or hydrogen sulphide (H_2S) by Simah et al. (1999) [181].

In general nonadiabatic transitions between different electronic states require the coupling of several vibrational modes [182]. This might not only concern the geometrical aspect, but also the activation energy E_A necessary for a predissociation mechanism (cf. Fig. 2.10b), which has to be provided by vibrational excitations. A higher E_A implies a less likely transition under otherwise identical conditions.

Locating a conical intersection can be seriously more complicated if diabatic effects are not negligible. High nuclear velocities along the dissociation pathways prevent the electronic system from coming sufficiently close to thermodynamic equilibrium. Hence the Born-Oppenheimer approximation (see subsection 2.1.1) is no longer feasible resp. accurate in the vicinity of a conical intersection. An avoided crossing (cf. Fig. 2.10b) might be found instead of a conical intersection (dashed lines) [173]. The problem can be approached via extending the Born-Oppenheimer approximation with a more general representation of the total wave function $\Psi(\mathbf{q}, \mathbf{Q})$ and the corresponding equations of motion. While an adiabatic representation might require a large basis set due to derivative couplings (coupling elements of the electronic wave functions involving their derivatives with respect to the nuclear coordinates), using a diabatic representation circumvents this issue [171, 173, 183, 184]. Fortunately only symmetry-allowed conical intersections are important in this work and varying a single nuclear coordinate is sufficient to locate them. Hence the adiabatic picture is employed and the more complicated diabatic picture is avoided.

3. Electronic structure of (antiferroelectric) hexagonal ice I_h

Despite numerous experimental and theoretical studies, the electronic structure of water resp. ice is not well understood until today [59, 62–65]. In natural science this fundamental problem is relevant to many diverse fields surrounding the interaction with surfaces. Some examples are fuel cells in electrochemistry [185] and protein folding and molecular recognition in biology [3] as well as the flow of confined water through membranes and pores which is topical in geology and waste water treatment [186]. New findings could also influence the research regarding heterogeneous nucleation on aerosol particles in the atmospheric sciences [186] and interstellar clouds in astrophysics [185]. The current knowledge is surprisingly limited, as e.g. the determination of the molecular arrangement for ice on metal surfaces is only possible in very few cases [186].

The (pristine) (antiferroelectric) bulk state of (hexagonal) ice I_h, which is the common form of ice (cf. Fig. 3.1), is studied within the GW+BSE framework. A systematic analysis of the (position of the) quasiparticle band gap edges with respect to vacuum is performed focussing on the selfconsistency of the GW calculations and their starting points. On top of that the complex dielectric function[1] is also treated with a BSE approach yielding the photoexcitation spectrum additionally to the photoemission spectrum.

Insight on excess electron solvation is yielded by a G_0W_0 investigation of the basal $I_h(0001)$ surface terminated by an (initially) intact bilayer. The enormously complicated physics of ice surfaces evokes the need for a prototypical system. Therefore this simplest hexagonal form was chosen. Defects on it are the main trapping sites. Proton disorder – orientational defects with reconstructions eliminating Bjerrum defects –, molecular vacancies and complexation of both kinds of deviations from the perfectly crystalline surface are considered. Their geometries and formation energies are calculated as well as the trap depths, i.e. (vertical) electron affinities, and the corresponding partial charge distributions. Trends connecting them are found and explained. Note

[1] The experimental electric field screening is much stronger, because defects enable molecular reorientations and proton hopping whose contributions are far larger than those of merely electronic effects. Hence ice is sometimes referred to as a "protonic semiconductor" [59].

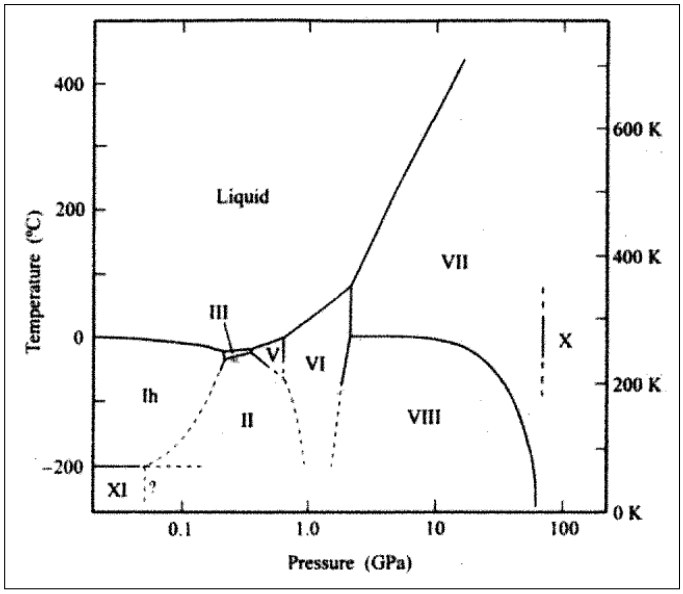

Figure 3.1.: Phase diagram of ice, roman numerals indicate crystalline phases [59]

that an estimate of the error margin justifies the neglect of GW selfconsistency in this context.

The equilibrium crystal structure (cf. Fig. 3.2) is assumed to be perfectly hexagonal. Strictly speaking this is not an exact result of the calculations, yet they demonstrate the validity of this simplified model. The geometry is especially advantageous due to the reduced number of parameters. Moreover the oxygen sublattice was found to be almost ideally tetrahedral.

An antiferroelectric proton order leading to Fletcher's striped phase [187] at the $I_h(000\bar{1})$ surface (cf. Fig. 3.2) is considered. The tremendous physical relevance of such structures is surprising if judging from the situation in the bulk alone. Bulk proton disorder can easily be induced by thermal effects (order-disorder transition at only 72K [188]) and high kinetic barriers might hinder the reverse process, explaining the archetypal geometrical frustration. According to a previous study [188] also applying the PBE XC-functional, the ferroelectric bulk state of ice I_h[2] is most stable, i.e. it possesses the highest sublimation energy E_{sub}. However the molecular termination of the corresponding $I_h(000\bar{1})$ is instable due to Coulomb repulsion between dangling hydrogens, which is a general problem for models of polar ice surfaces [105,188]. This does not pertain to the antiferroelectric system[2] and none of the proton-

[2] To be exact proton-ordered ice I_h is termed ice XI (experimentally found to be ferroelectric).

disordered structures turned out to be more stable. Lacking charge screening at the surface vastly raises the energy cost of molecular rotations and with it the order-disorder transition temperature. In Monte Carlo (MC) simulations with a rigid oxygen sublattice [189] even the transition to a partially disordered honeycomb phase did not occur below the bulk melting temperature (273K). Reaching the so-called "Tamman temperature" leads to the onset of oxygen sublattice disordering caused by thermal effects, which happens at the surface. It was measured by elastic helium (He) scattering ($\approx$ 180K) [190] and sum frequency generation (SFG) ($\approx$ 200K) [191]. This range was roughly confirmed by MC simulations with movable oxygens [189], but these were not carried out extensively such as to calculate a theoretical Tamman temperature. The Fletcher striped model is consistent with hitherto unexplained minor fractional peaks in the He diffraction pattern [192] as demonstrated by eikonal approximation calculations [189]. Moreover the agreement between computations [189] and SFG spectra [193] is improved compared to a disordered model. It was therefore proposed that $I_h(0001)$ favours Fletcher's striped phase in the entire range below the Tammann temperature [189].

This convenient basis enables a step by step analysis of increasingly complex systems.

3.1. Pristine (antiferroelectric) bulk state

The position of the valence band maximum (VBM) with respect to the vacuum potential Φ_{vac} (for its determination see section C) gives the vertical approximation for the negative ionisation potential (*IP*), while the conduction band minimum (CBM) is analogously related to the negative electron affinity (*EA*). Fig. 3.3 graphically sums up the most important findings, while the results of the systematic electronic structure investigation are displayed in Tab. 3.1 and 3.2. The DFT calculations were conducted with a Γ-centered 2-2-2 k-point sampling[3] and plane wave energy cutoff (see sections 2.2 and 2.3) E_{cut} = 400eV keeping the ionic geometry obtained from the initial PBE. As expected the well-known DFT (PBE) tendency to band gap underestimation is also present here, mainly since the VBM is placed too high, but the too low CBM position also makes a substantial contribution. Despite improving the electronic structure, hybrids (HSE06, PBE0) still exhibit the same deficiencies. Pure Hartree-Fock (HF), which entirely neglects correlation (C), produces a huge band gap overestimation with very strong opposite deficiencies. More

[3] A Γ-centered 3-3-3 k-point sampling was also tested. At Γ no major change in the electronic energy levels yielded by both DFT and the subsequent GW occurred.

generally, it was found that an increased proportion of Hartree-Fock exchange (HF-X) widens the band gap and lowers the dielectric constant accordingly.

Notably the subsequent GW calculations also preserved this tendency. They employed 1536 bands, response function energy cutoff $E_{\text{cut-GW}}$ = 200eV, 20 frequency points along the real axis and the spectral method. The transition from DFT to GW again widens the band gap in the same manner as the hybrids, bringing the CBM close to Φ_{vac}, implying that an excess electron in the pristine bulk would be neither stabilised nor rejected significantly unless the ionic geometry was drastically changed. GW selfconsistency barely affects unoccupied states, but substantially lowers valence states. Considering the positions of the respective energy levels and that a bulk structure is treated, the continuously more elaborate account of charge screening explains this behaviour.

Although converged the fully selfconsistent scGW results turned out to be inequivalent.

It is hence concluded that hybrids should be used for the electronic relaxation in DFT, yet transitioning to GW is and stays mandatory as expected. The *EA* depends only weakly on the degree of GW selfconsistency, so G_0W_0 suffices to calculate it. This is not the case for the *IP*, which should be treated with $\text{scGW}_{(0)}$.

Therefore G_0W_0(PBE0-electronic), which – beginning with section 3.2 – was chosen to investigate surface systems, is reliable in the context of excess electron solvation[4]. With the aforementioned settings it leads to $(\varepsilon_{\text{QP}}^{\text{MAX}} - \varepsilon_{\text{QP}}^{\text{VBM}})(\Gamma)$ = 125.640eV (see section C, esp. cf. Fig. 9.1). The highest converged values (4096 bands leading to $(\varepsilon_{\text{QP}}^{\text{MAX}} - \varepsilon_{\text{QP}}^{\text{VBM}})(\Gamma)$ = 242.372eV (see section C, esp. cf. Fig. 9.1)) for VBM resp. CBM are 193meV resp. 70meV lower, amounting to a band gap widening of 123meV.

As the *IP* has been calculated, the photoelectron emission spectrum of the system is characterised by its GW imaginary dielectric function (cf. Fig. 3.4). Shibaguchi et al. (1977) [63] aimed to reveal the energy level spectrum of ice by measuring VUV/UPS/XPS photoelectron emission spectra. UPS yielded 10.5eV for the *IP*. The calculated values (cf. Fig. 3.3, Tab. 3.1 and 3.2) are in very good agreement with this, but only at a sufficiently high level of theory. Hybrid electronic relaxation in the underlying DFT is required as well as GW selfconsistency, except maybe for the screened Coulomb interaction W. Starting from DFT(PBE0-electronic) it was found that distinct degrees of GW selfconsistency produce almost coinciding photoelectron emission spectra

[4] Using G_0W_0(HSE06-electronic) instead would have been the other possibility and even slightly less expensive. Yet from the point of view of a purist it might be unsatisfactory, since the HSE exchange (X) screening involves an additional empirical parameter (ω, see subsection 2.5.4).

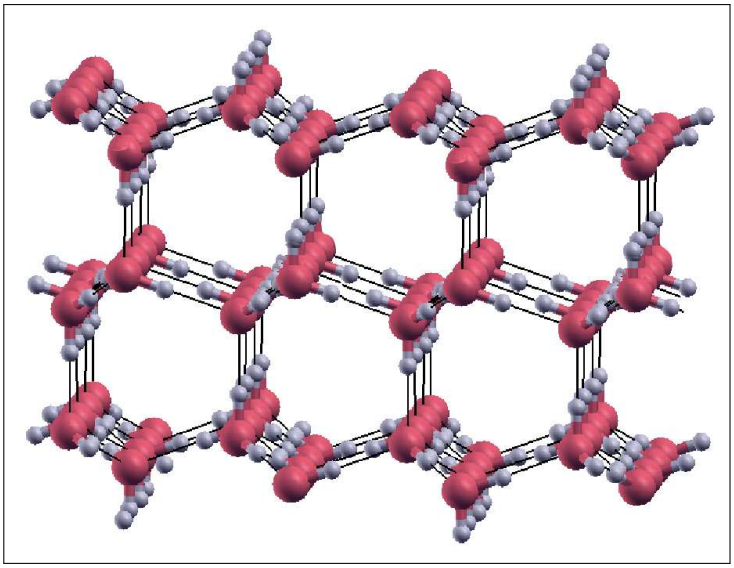

Figure 3.2.: Geometry of pristine antiferroelectric hexagonal ice I_h with a bilayer-terminated Fletcher-striped (0001) surface

apart from a constant energy shift, which mirrors their aforementioned effect on valence – more general: occupied – states. Only the orbital wave function update "sc" causes a shape change which might not be completely negligible.

From here on considerations beyond DFT are based on DFT(PBE0-electronic). Exceptions were made only for additional evidence to the meaningfulness of this choice.

To determine the (UV) photon absorption spectrum, the BSE complex dielectric function, which, contrary to GW, takes electron-hole interaction into account, was calculated based on the 50 highest valence resp. lowest conduction states from the previous GW (cf. Fig. 3.4, besides Tab. 3.3 and 3.4). Takahashi and Onaka (1968) [62] performed UV-transmission experiments to measure the first absorption maximum. Cubic ice exhibited a peak at 8.7eV. Seemingly due to sample preparation problems this could not be confirmed for other structures. VUV thin film absorption spectra of amorphous, cubic and hexagonal ice recorded by Shibaguchi et al. (1977) [63] were all dominated by a pronounced first absorption peak at ≈8.7eV, corroborating the widespread conception that ice is essentially a molecular crystal. The photon reflectivity spectrum of a hexagonal ice single crystal taken by Kobayashi (1983) [195] indicated the first absorption maximum at 8.6eV (cf. Fig. 3.4). The experimental spectra [62, 63, 195] and a comparison between GW and BSE imaginary dielectric function (cf. Fig. 3.4) demonstrate that the first absorp-

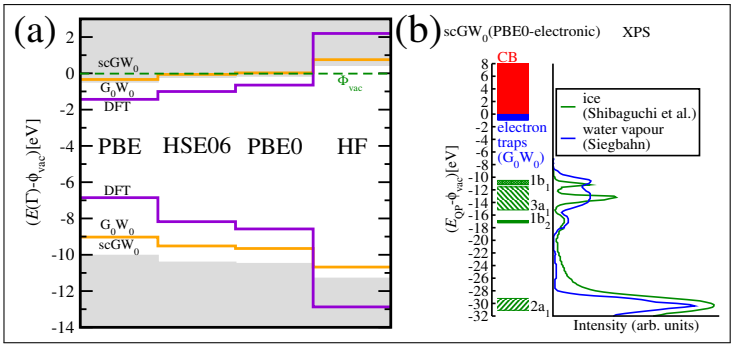

Figure 3.3.: Pristine bulk state of antiferroelectric ice I_h (DFT(PBE) geometry): (a) Position of the band gap edges at the gamma point for different theoretical approaches (b) Band energy ranges from $scGW_0$(PBE0-electronic) (k-point sampling 3-3-3) compared to the XPS signal intensity (density of states) measured for water vapour by Siegbahn (1974) [194] and for hexagonal ice by Shibaguchi et al. (1977) [63], G_0W_0(PBE0-electronic) electron trap energy range below the ice conduction band (CB) included (see section 3.2)

tion maximum is indeed of excitonic nature. The measured position is well reproduced by the BSE calculations (cf. Fig. 3.4, Tab. 3.4), but only if these are based on the previously discussed sufficiently high level of theory (besides cf. Tab. 3.3). The selfconsistency of the underlying GW affects the UV absorption spectrum from BSE in a very similar way as the UV photoelectron emission spectrum, which is directly characterised by it. Taking the BSE calculations beyond the Tamm-Dancoff approximation [TDA, see subsection 2.7.4 (equation (2.142), [164, 165]] turned out to be of only minor relevance. Compared to the results in Tab. 3.4 a mere TDA approach enlarged the first absorption energy by ≈2% with <10% smaller peak height, while the low-frequency limit of the relative permittivity (RPA) exhibited a marginal decrease of <1%.

Note that the suffix "LPEAD" stands for employing the finite difference method (FDM) to derive the cell-periodic part of the orbitals w.r.t. **k**. This was necessary for GW calculations with orbital wave function update ($scGW_{(0)}$), if beyond-TDA BSE calculations had to be performed based upon them. It may change the relative permittivity by some per cent, yet the electronic energy eigenvalues remain almost the same.

3.2. Electron traps at bilayer-terminated (antiferroelectric) $I_h(0001)$

As compared to water, the more rigid hydrogen bonded (H-bonded) molecular network of ice facilitates localisation, stabilisation and charge screening of

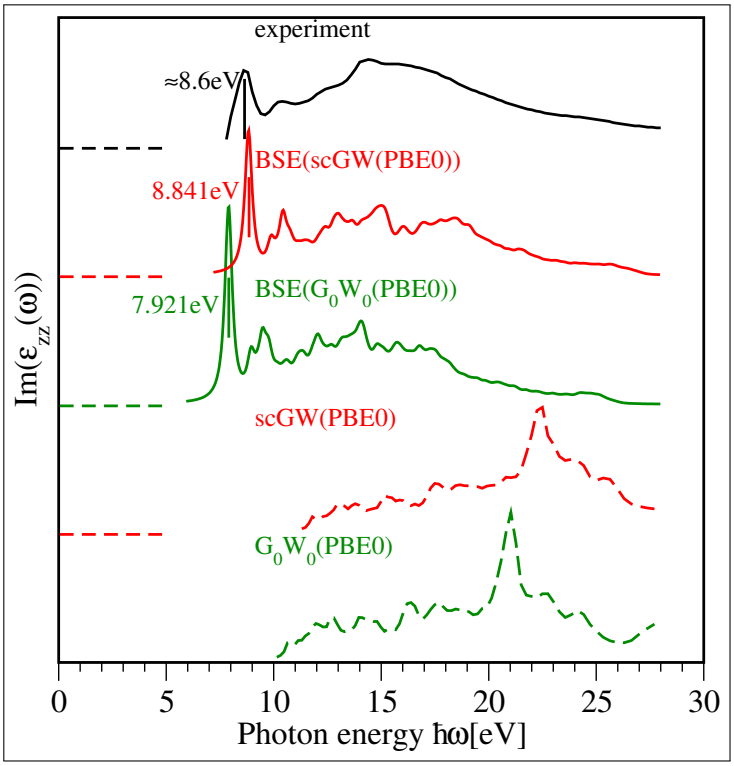

Figure 3.4.: Imaginary part of the dispersive complex relative permittivity in random phase approximation (RPA) for the pristine bulk state of antiferroelectric ice I_h. Curves were obtained from G_0W_0(PBE0-electronic) and scGW-LPEAD(PBE0-electronic) calculations - characterising photoelectron emission - and Bethe-Salpeter equation (BSE) calculations (beyond-TDA approach, coupling of positive and negative frequencies, artificial broadening 0.2eV) – characterising UV absorption – based on them. Experimental curve from photon reflectivity spectrum measurement by Kobayashi in 1983 [195]. First excitonic peak and its energy indicated.

Table 3.1.: Pristine bulk state of antiferroelectric ice I_h, DFT(PBE) geometry. KS and QP valence band maximum (VBM), conduction band minimum (CBM) and band gap (GAP) at the gamma point in eV for different XC-functionals $E_{XC}[n(\mathbf{r})]$ and degrees of GW selfconsistency, low-frequency limit of the relative permittivity in random phase approximation (RPA). Values were obtained within HF, DFT, G_0W_0 and partially selfconsistent GW with non-iterated screened Coulomb interaction W_0. The zero point of the energy scale is the vacuum potential Φ_{vac}.

$E_{XC}[n(\mathbf{r})]$		DFT	G_0W_0	GW_0	$scGW_0$	$\varepsilon_r^{RPA}(\omega \searrow 0)$
PBE-	VBM	-6.85	-9.03	-9.47	-10.05	1.91
ionic	CBM	-1.44	-0.34	-0.26	-0.46	
	GAP	5.42	8.69	9.21	9.59	
HSE06-	VBM	-8.18	-9.52	-9.74	-10.43	1.70
electronic	CBM	-1.00	-0.06	+0.02	-0.20	
	GAP	7.17	9.46	9.76	10.22	
PBE0-	VBM	-8.58	-9.66	-9.83	-10.50	1.63
electronic	CBM	-0.65	+0.03	+0.08	-0.14	
	GAP	7.93	9.68	9.91	10.36	
HF-	VBM	-12.88	-10.68	-10.50	-11.31	1.33
electronic	CBM	+2.20	+0.75	+0.70	+0.46	
	GAP	15.07	11.43	11.20	11.77	

excess electrons on top of the surface in vacuum. This is due to dipole reorientation, which essentially comes from molecular rotations, creating denser accumulations of dangling protons resp. positive partial charges attracting excess electrons by Coulomb force. It is aided by molecular vacancies, because the corresponding geometries are more favourable for charge screening. Furthermore they exhibit more low-coordinated sites, where under certain circumstances the dipole reorientation can proceed with diminished energy barriers. Note that similar effects might emerge from intrinsic adstructures of ice surfaces (e.g. from the hexagon adrows, admolecule reconstructions and combinations thereof analysed by Bockstedte et al. (2016) [61], see also section 7.1). These are not treated here, because the complexity of their potential energy landscapes currently prevents a systematic investigation of adsorption resp. DEA like that discussed in section 4.2 resp. chapter 5.

Corroborating previous results [105], GGA-DFT, namely PBE, yielded workable results for bulk geometry and sublimation energy per molecule $E_{sub}^{H_2O}$ (see section A), which can not be obtained from LDA or HF [105]. Hence it was assumed that DFT(PBE) is also suited to determine the formation energies E_f of defects, here at the $I_h(0001)$ surface. Besides the surface energy γ_{0001} =

Table 3.2.: Pristine bulk state of antiferroelectric ice I_h, DFT(PBE) geometry. QP valence band maximum (VBM), conduction band minimum (CBM) and band gap (GAP) at the gamma point in eV for different XC-functionals $E_{XC}[n(\mathbf{r})]$ and degrees of GW selfconsistency, low-frequency limit of the relative permittivity in random phase approximation (RPA). Values were obtained within GW and scGW with iterated screened Coulomb interaction W. The zero point of the energy scale is the vacuum potential Φ_{vac}.

$E_{XC}[n(\mathbf{r})]$		GW	$\varepsilon_r^{RPA}(\omega \searrow 0)$	scGW	$\varepsilon_r^{RPA}(\omega \searrow 0)$
PBE-	VBM	-10.03	1.65	-10.52	1.75
ionic	CBM	+0.07		-0.14	
	GAP	10.10		10.38	
HSE06-	VBM	-10.06	1.58	-10.65	1.67
electronic	CBM	+0.19		-0.08	
	GAP	10.25		10.58	
PBE0-	VBM	-10.10	1.54	-10.68	1.63
electronic	CBM	+0.22		-0.04	
	GAP	10.32		10.64	
HF-	VBM	-10.20	1.39	-10.93	1.46
electronic	CBM	+0.55		+0.13	
	GAP	10.75		11.07	

11.4meV Å^{-2} lies in the range produced by previous theoretical studies, but the experimental results are not conclusive (see section B). Nevertheless judging from the bulk situation it seems that regular DFT does not permit a very precise calculation of these material parameters. Thus at least hybrid XC-functionals (e.g. HSE06, PBE0) would be required yet correspondingly expensive. The justification of a simplified geometrical model with less parameters [105] is also confirmed (see section A).

The upper first bilayer consists of merely threefold coordinated molecules (cf. Fig. 3.2). Depending on whether such a molecule has a dangling proton or not, it can donate (index D) or accept (index A) an H-bond. Removing it creates a surface vacancy (V) (cf. Fig. 3.6), while rotating it in such a way that Fletcher's striped phase [196] is impaired leads to a specific kind of orientational defect (S) (cf. Fig. 3.5). These – and of course complexes thereof – are responsible for excess electron solvation by the surface. More specifically, the orientational defects enable this feature, while the vacancies enhance it upon complexating with them. Since the bulk configuration has to fulfil the

Table 3.3.: Pristine bulk state of antiferroelectric ice I_h, DFT(PBE) geometry. Energy E_1 and intensity $\mathrm{Im}(\varepsilon_r^{RPA}(\omega = \frac{E_1}{\hbar}))$ of the first absorption maximum (excitonic excitation) and low-frequency limit $\varepsilon_r^{RPA}(\omega \searrow 0)$ of the relative permittivity in random phase approximation (RPA). Values were obtained from Bethe-Salpeter equation (BSE) calculations (beyond-TDA approach, coupling of positive and negative frequencies) based on G_0W_0 calculations with different starting points.

BSE(G_0W_0(...))	E_1[eV]	$\mathrm{Im}(\varepsilon_r^{RPA}(\omega = \frac{E_1}{\hbar}))$	$\varepsilon_r^{RPA}(\omega \searrow 0)$
PBE-ionic	7.320	4.235	1.867
HSE06-electronic	7.773	3.321	1.692
PBE0-electronic	7.921	3.063	1.646
HF-electronic	9.010	1.473	1.346

Table 3.4.: Pristine bulk state of antiferroelectric ice I_h, DFT(PBE) geometry. Energy E_1 and intensity $\mathrm{Im}(\varepsilon_r^{RPA}(\omega = \frac{E_1}{\hbar}))$ of the first absorption maximum (excitonic excitation) and low-frequency limit $\varepsilon_r^{RPA}(\omega \searrow 0)$ of the relative permittivity in random phase approximation (RPA). Values were obtained from Bethe-Salpeter equation (BSE) calculations (beyond-TDA approach, coupling of positive and negative frequencies) based on GW calculations with the same starting point but different degrees of GW selfconsistency.

BSE(...(PBE0-electronic))	E_1[eV]	$\mathrm{Im}(\varepsilon_r^{RPA}(\omega = \frac{E_1}{\hbar}))$	$\varepsilon_r^{RPA}(\omega \searrow 0)$
G_0W_0	7.921	3.063	1.646
GW_0	8.131	3.044	1.630
GW	8.328	3.181	1.623
scGW_0-LPEAD	8.655	2.198	1.530
scGW-LPEAD	8.841	2.247	1.514

Bernal-Fowler rules[5] [197], any series of molecular rotations can only be valid if the number of dangling protons is left invariant. Therefore the present study considers S defects always in S_{AD} pairs. Moreover reconstruction at vacancies leads to complexation with these, possibly accompanied by the formation of pentagonal molecular structures. Note that other vacancies [198] and point defects [199] on crystalline ice surfaces were characterised by ab-initio methods before.

Due to reasons discussed in sections 2.7 and 3.1 G_0W_0(PBE0-electronic) was chosen to describe the electronic structures. Surface defects were modelled by 2x2-supercells (32 H_2O molecules per intact bilayer) with three resp. four (only

[5] also called "ice rules"

in case of the largest complex) bilayers. At these system sizes G_0W_0 was not taken beyond gamma point calculations, because at a meaningfully enlarged k-point sampling (e.g. 2-2-2) computational expense and virtual memory requirement were prohibitive. Nevertheless it can be expected that the quality of the resulting energy levels at the gamma point is not deteriorated as compared to the bulk case. This can be understood from the size of the structures inside the supercells and the fact that the respective k-point samplings concern reciprocal space. Judging from a comparison to the convergence properties of the pristine bulk system (see section C), the applied parameter values would correspond to $(\varepsilon_{\mathrm{QP}}^{\mathrm{MAX}} - \varepsilon_{\mathrm{QP}}^{\mathrm{VBM}})(\Gamma)$ = 88.7eV resp. 76.5eV (E_{cut} = 400eV, $E_{\text{cut-GW}}$ = 125eV, NBANDS = 10000)[6]. The highest converged band gap edges at the same $E_{\text{cut-GW}}$ deviate by -228meV resp. -294meV for the VBM and -98meV resp. -128meV for the CBM. Increasing $E_{\text{cut-GW}}$ to 200eV barely affects the CBM (+10meV), while the VBM drops significantly (-142meV). The position of the LUMO, i.e. the lowest orbital that is empty in the ground state and localised at the defect, relative to Φ_{vac} gives the negative trap depth. Hence it is crucial to surface excess electron capture, which is the key topic of this section. The LUMO of an effective trap has to lie inside the band gap, yet it is much closer to the CBM, which is also empty in the ground state, than to the VBM. Therefore it is assumed that the framework of the present investigation enables an appropriate description of the relevant physics considered.

Orientational defects were created by molecular rotations at the surface. Thereby produced Bjerrum defects were eradicated by further rotations of adjacent molecules, eventually yielding a bulk configuration that does not violate the Bernal-Fowler rules [197]. Proton disorder, particularly S_{AD} defects, remained as well as a net dipole moment. The geometries emerging from S_{AD} defect complexations were designed in such a way as to obtain the lowest possible formation energy E_{f}. Anyway these reactions are endothermic throughout due to Coulomb repulsion between accumulating surface dangling protons, whose positive partial charges increasingly stabilise the LUMO giving a clear trend (cf. Tab. 3.5 and Fig. 3.5). Since it is pulled from close to Φ_{vac} to significantly under it, excess electron solvation becomes possible at the surface. Remarkably E_{f} of S_{AD} and $3S_{\mathrm{AD}}$ not interacting with each other turned out to be smaller than for two such $2S_{\mathrm{AD}}$. This might be a small hint towards a sudden drop in $2S_{\mathrm{AD}}$ concentration at rising total concentration of (solely) orientational defects.

The mere single molecular vacancies V_{A} and V_{D} possess very similar E_{f} (cf. Tab. 3.5), indicating that their concentrations should be almost equal, at least

[6] 20 frequency points along the real axis, spectral method employed

Table 3.5.: Antiferroelectric ice I_h(0001) surface with various kinds of defects and complexes thereof (explanation see text). DFT(PBE) geometries and formation energies E_f. QP vertical electron affinity (EA) at the surface gamma point from G_0W_0(PBE0-electronic). For comparison: The EA of the analogously calculated QP CBM would be -0.03eV (cf. Tab. 3.1).

I_h(0001)	E_f[meV]	EA[eV]
ideal/pristine	0	≈0.00
S_{AD}	99	+0.05
$2S_{AD}$	356	+0.21
$3S_{AD}$	549	+0.29
$4S_{AD}$	898	+0.43
V_A	200	<0.00
V_D	210	<0.00
V_A-$2S_{AD}$	697	+0.33
V_D-S_{AD}	396	+0.18
$2V_DV_A$-$2S_{AD}$	1101	+0.98

for a sufficiently low number of them on the otherwise pristine surface. They are not suited for excess electron trapping, because the LUMO is a scattering state, i.e. above Φ_{vac}, in both cases (cf. Tab. 3.5). This could be expected since the Fletcher stripes are either not exploited (V_A) or impaired (V_D) (cf. Fig. 3.6).

Reconstruction, here in the shape of complexation with orientational defects, can change this, since additional dangling protons at the vacancies enhance their electrostatics (cf. Fig. 3.6). Indeed V_A-$2S_{AD}$ and V_D-S_{AD} turned out to be excess electron traps even deeper than their orientational components themselves, while any decomposition is exothermic (cf. Tab. 3.5). On the other hand at high defect concentrations the corresponding reactions might be hindered due to spatial limitations.

$2V_DV_A$-$2S_{AD}$, the largest defect complex investigated here, was found to be the deepest excess electron trap by far (cf. Tab. 3.5). It possesses several features not present for the other defects resp. complexes. Most importantly a subsurface dangling proton appears, because one of the lower first bilayer molecules is missing. Its positive partial charge aids excess electron localisation within the quadruple molecular vacancy. Hence the exceptional trap depth is conceivable. Except for producing its elementary components, i.e. non-complexated defects, all decompositions turned out to be endothermic (cf. Tab. 3.5). This is likely related to the formation of a new H-bond, from

which a pentagonal molecular structure in the first bilayer originates (cf. Fig. 3.6).

The calculated formation energies E_f for orientational defects, molecular vacancies and complexes thereof at the surface are of the same order of magnitude, more specifically some hundreds of meV (cf. Tab. 3.5). As endothermic decompositions were found for $2V_DV_A$-$2S_{AD}$, some (heterogeneous) complexations should become energetically favourable at increasing concentrations. Even so a more comprehensive analysis of defect complexation energetics – like [198] – would be required to enable fundamental statements regarding this aspect, especially if molecular vacancies are involved. According to [199] low-lying subsurface defects might also have to be taken into account, e.g. because the vast energy cost of surface molecular reorientations can confine the former to the bulk.

The electron trap formation energies E_f tend to correlate with the trap depth *EA* (cf. Tab. 3.5 and Fig. 3.5, 3.6). This trend is plausible considering that the positive partial charges of agglomerated dangling protons are the key factor in excess electron solvation. Additionally in conjunction with them molecular vacancies can support the excess electron charge screening based on their more favourable geometries. Combined with the present findings regarding the complexation energy balances, this speaks for the relevance of such heterogeneous defects, at least in case of sufficiently high concentrations.

3.3. Summary

The fundamental importance of several steps for theoretically describing the electronic structure of ice I_h within the GW+BSE approach has been demonstrated. Furthermore the formation of various $I_h(0001)$ surface defects and complexes thereof, as well as their ability to solvate excess electrons, were found to exhibit some general tendencies.

Ionic positions, material parameters and defect formation energies obtained with GGA-DFT (PBE) are considered reliable. Furthermore a previously discussed simplified geometrical model is found to be applicable.

However DFT(PBE) is not capable of an adequate electronic structure description, especially due to its vast band gap underestimation mainly caused by a too small *IP*. Electronically relaxing with hybrids (HSE06, PBE0) yields significant improvement, yet the same deficiencies are still exhibited (cf. Fig. 3.3 and Tab. 3.1). Transitioning to the GW approach is therefore necessary, while hybrids are applied to enhance the starting points.

As it could be expected due to ground state occupation numbers and energetic positions of the respective bands, $scGW_{(0)}$ is needed to bring the *IP*

values close to experiment (10.5eV according to [63]), while the *EA* is close to zero and depends only weakly on the degree of GW selfconsistency (cf. Fig. 3.3 and Tab. 3.1, 3.2). Hence G_0W_0(PBE0-electronic) is considered reliable for an investigation of excess electron solvation at defects. In the present case the dangling protons of these are at the surface, where the screening of their positive partial charges is even much weaker than in the bulk.

Like its energy minimum, the *IP*, the GW photoelectron emission spectrum (cf. Fig. 3.4) requires full GW selfconsistency by means of convergence except for the screened Coulomb interaction. Regarding the imaginary dielectric function, the various degrees of GW selfconsistency differ mainly by a constant frequency resp. energy shift. Apart from the orbital wave function update, for which it is also rather small, the curve shape change is negligible.

BSE calculations were carried out to determine the UV absorption spectrum (cf. Fig. 3.4). Only for an adequate starting point ($scGW_{(0)}$(PBE0-electronic)) the first exciton peak energy (cf. Tab. 3.4, besides Tab. 3.3) was found close to experiment (8.6-8.7eV according to [62, 63, 195]). GW selfconsistency turned out to have a very similar effect as previously mentioned for the (mere) photoelectron emission spectrum.

Based on estimates of the respective error margins, it is concluded that the achieved convergence is sufficiently high to appropriately serve the purposes of the present investigation, both for the bulk and the surface (see also section C).

According to the G_0W_0(PBE0-electronic) results pristine I_h(0001) neither rejects nor binds excess electrons substantially. As expected dangling protons turned out to be the key factor in surface trapping. Their agglomeration beyond the regular pattern of Fletcher stripes, or even subsurface appearance, allows to reach positive electron affinities. Higher formation energies tend to be correlated with stronger traps (cf. Tab. 3.5 and Fig. 3.5, 3.6). In particular for merely orientational defects (S_{AD}) both quantities follow a clear trend increasing with complex size. Single molecular vacancies (V_A, V_D) exhibit negative electron affinities, yet in the exemplary cases of heterogeneous complexation the LUMO was found to lie even deeper than for the orientational components alone. The exceptionally high calculated trap depth of $2V_DV_A$-$2S_{AD}$ is supposedly related to its subsurface dangling proton, which is unique in the present study. Several endothermic decompositions were found for this largest investigated complex. The formation energies obtained for orientational defects and molecular vacancies are typically some hundreds of meV. The exemplary complexation resp. decomposition energy balances evidence that the fraction of heterogeneous complexes is relevant at least for sufficiently high concentrations of the components. The depths of the traps are smaller

than their formation energies, yet usually they also amount to some hundreds of meV. Considering the differences between the values of these quantities for the various surface structures, it can be surmised that excess electron solvation aids the formation of surface defects and might possibly modify their types (see also section 7.1).

Apart from that lack of charge screening largely prevents stabilising reorientations of water molecules at the surface. Hence the abundance of defects sites on it should be substantial a priori, meaning that it is discovered remote from thermodynamic equilibrium in experiment.

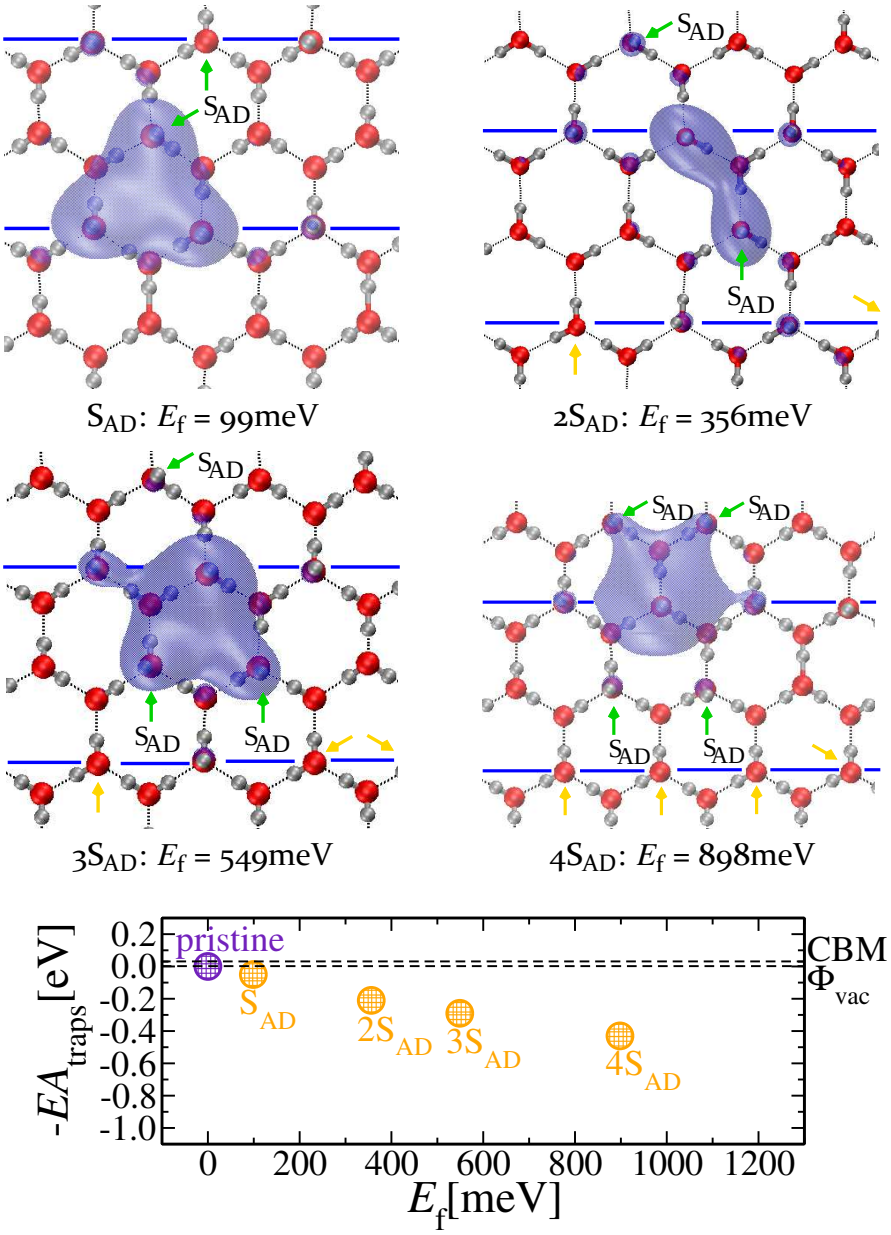

Figure 3.5.: Geometry, formation energy E_f, LUMO($\bar{\Gamma}$) partial charge density and negative vertical electron affinity (EA) of orientational S_{AD} defects

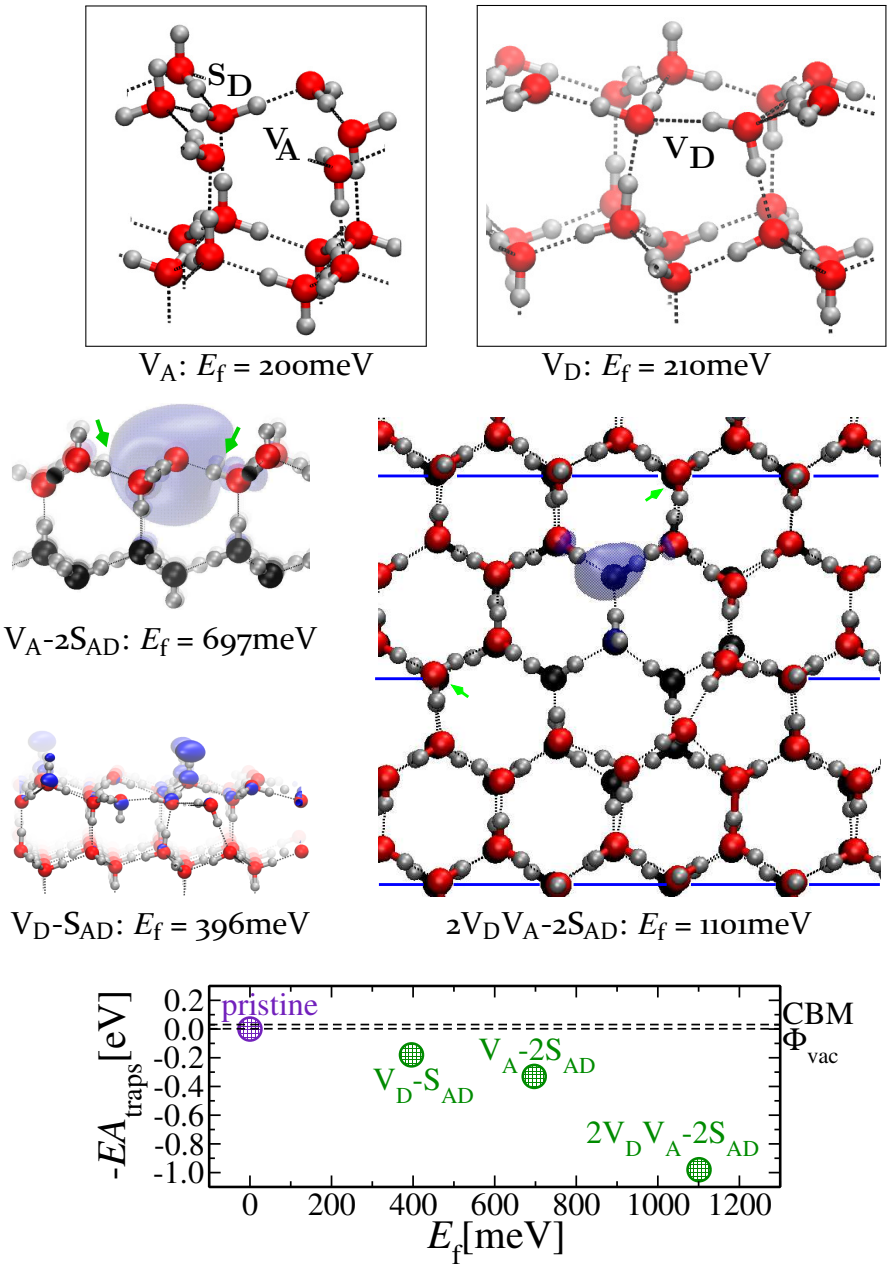

Figure 3.6.: Geometry, formation energy E_f, LUMO($\overline{\Gamma}$) partial charge density and negative vertical electron affinity (EA) of H_2O vacancies including reconstructions and complexes

4. Trends in the electronic structure of phenyl halogenides C_6H_5X

As a polar medium ice is not only suited to solvate excess electrons, but also molecules carrying an electric dipole moment. Phenyl halogenides (C_6H_5X with X=F,Cl,Br[1]), which are the simplest aromatic halocarbons, were considered as prototypical adsorbed molecules. From vacuum experiments it is known that their electron affinity diminishes if a heavier halogen is involved, yet stays negative (cf. Tab. 4.2). Hence the free molecules can capture excess electrons only temporarily by resonances, i.e. significantly localised discrete states above Φ_{vac}. The chief aim of chapters 4 and 5 is to evidence that dissociative electron attachment (DEA) to halocarbons is catalysed (lowered molecular resonances and reduced activation energy) and made more probable (enhanced dissociation probability) upon adsorption at the ice surface, particularly if it exhibits strong excess electron traps. Chapter 4 investigates adsorption and concomitant electronic structure modifications of the phenyl halogenides at a variety of previously discussed surface traps. Chapter 5 is concerned with modelling the electron-induced dissociation in the most exemplary cases. This also lays the foundations for an analysis of direct neutral photodissociation processes, which is discussed in chapter 6.

The resulting trends regarding the electronic structure of the free and adsorbed molecules are very clear and speak for the expected facilitation of DEA corroborated by the tendential correlation between trap depths and adsorption energies. Moreover it turns out that increasing the row of the halogen has similar influence supported by the smaller vacuum bond fission energy (cf. Tab. 5.2). Explanations for all these findings are given.

The positions of the respective energy levels relative to each other reveal that dissociation-inducing excess electrons can not be fully solvated, but must come from the ice conduction band or above.

4.1. Gas phase (ionisation and electron capture)

Fig. 4.1 displays the relevant molecular orbitals (MOs) of the phenyl halogenides, whose probability density distributions inherit the molecular symme-

[1] C_6H_5I is also investigated, but only in vacuum.

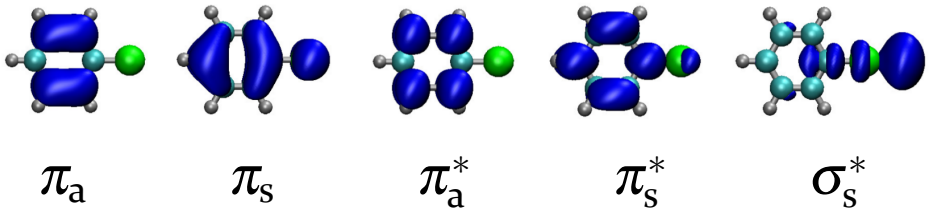

Figure 4.1.: Molecular and orbital geometry of phenyl halogenides C_6H_5X

tries (C_{2v} point group). The horizontal molecular symmetry plane is a nodal plane of all π orbitals, because these arise from the interaction of carbon and in some circumstances halogen $p_{(z)}$ orbitals orthogonal to it. Depending on the behaviour of the algebraic sign of the wave function upon reflection at the vertical molecular symmetry plane, the π orbitals are either symmetric (lower index "s") or antisymmetric (lower index "a"). A substantial consequence is that the latter have no contribution from the atoms lying in the vertical mirror plane of the molecule, particularly the halogen. It is distinguished between the occupied bonding π orbitals and their empty antibonding counterparts π^*, which exhibit the next higher number of algebraic sign changes between the contributing atomic orbitals of adjacent carbons compatible with the symmetry properties. This number is maximised by the π_0^* states, which are in a certain manner the "more antibonding version" of the π_s^* states. Thus they appear at much higher energies. The empty antibonding σ_s^* (also called $\sigma_{C\text{-}X}^*$) orbitals are essentially arising from, localised at and cylindrically symmetric to the C-X bond[2]. Their relative localisation at the halogen is clearly stronger than for any other type of electronic state that is empty and might hence capture an excess electron. Monohalosubstitution of benzene (C_6H_6) reduces the molecular symmetry from D_{6h} to C_{2v}. The emerging phenyl halogenides consist of conjugated radicals, namely the halogen and the phenyl group. The analogy between the molecular electronic structures (orbitals) is accounted for by the chemical similarity of the halogens, which comes from the fact that they all belong to the same group of the periodic table. Due to its higher electronegativity, the halogen has a negative inductive (-I) effect on the carbon to which it bonds resp. the phenyl group, evoking a molecular dipole. However regarding the molecular electronic structures it is important to understand that this effect also depends on the charge capacity of the halogen.

Before describing the electronic structure of phenyl halogenide molecules in the gas phase theoretically, experiments regarding it are considered. An adequate reproduction of their results must yield the positions of the electronic

[2] Except for C_6H_5F in vacuum, only very small deviations were found.

energy levels, especially HOMO and LUMO, relative to Φ_{vac} with sufficient accuracy and correct trends along the series of halogens. It will be seen that hybrid DFT or CDFT is not capable of this. However the former already provides the starting points for GW calculations solving the problem.

He(I) AR-UPS was performed by Kobayashi (1978) [200], to measure angular distributions of C_6H_5F photoelectrons. Two years later the other phenyl halogenides were investigated by Potts et al. (1980) [201] employing He(I/II) UPS. Combining their results reveals, that the ionisation potential (*IP*) decreases for higher row of the halogen (cf. Tab. 4.1). A more comprehensive study was conducted by Imura et al. (2001) [202]. He(I) UPS and $He^*(2^3S)$ PIES (Penning ionisation) were used for all molecules. They received coinciding *IP* values taking into account that the $He^*(2^3S)$ excitation (19.82eV resp. 62.6nm) requires 1.40eV energy less than the He(I) resonance photons (21.22eV resp. 58.4nm). Therefore the PIES spectra are shifted accordingly relative to the UPS spectra. The aforementioned trend was again observed with results very near those of the two previous studies (cf. Tab. 4.1). Photoelectron spectroscopy (PES) with higher resolution than previous experiments was performed by Palmer et al. (2015/16) [203–205] for C_6H_5X with X=F,Cl,Br. Their results are almost identical with those of the other studies, except for the slightly smaller *IP* of C_6H_5F.

Olthoff et al. (1985) [206] made ETS and TOFMS experiments to gain insight into (dissociative) electron attachment to benzene and its monohalogenated derivates, i.e. the phenyl halogenides, under single collision conditions. As ETS allows to determine changes in the total cross section for electron scattering, which depends on the kinetic energy of the incident electron, it yields the attachment energies, which can be identified as the negative vertical electron affinities. Mass and kinetic energy of charged fragments from DEA were measured by TOFMS. Anions of the investigated species were not detected, suggesting that no empty molecular orbitals below Φ_{vac} exist in the ground state. Therefore electron capture can only lead to TNIs. These must either reemit the excess electron by autodetachment (AD) or dissociate (DEA) with probabilities depending on the respective anion lifetime, electronic structure and dissociation potential landscape. Surprisingly the relative stability of the molecular resonances was found to increase with the row of the halogen (cf. Tab. 4.2). This effect presumably concerns σ^* resonances to a much larger extent than π^* resonances, yet a value for the position of the former was only given for C_6H_5Cl. Except for the unclear case of C_6H_5I, in which DEA originates from an unidentified resonance at smaller attachment energy, the lowest molecular resonances were found to be of π^* character. More precisely,

these are π_a^* and π_s^* states degenerate with each other apart from the C_6H_5F molecule, which exhibits the latter at 0.61eV higher energy (cf. Tab. 4.2).

Thus the HOMO-LUMO gap becomes smaller for higher row of the halogen.

Here the electronic structure of the phenyl halogenides in vacuum was initially addressed employing hybrid DFT(PBE0) (see subsection 2.5.3). The same plane wave energy cutoff as for the mere ice structures turned out to be ideal (E_{cut}=400eV, see chapter 3). Full relaxations demonstrated that cubic supercells with edge length $d = 15$Å are sufficiently large to converge ionic positions and Kohn-Sham energy eigenvalues demanding no more than Γ-point calculations. While the geometries are appropriately described (see section D), the electronic energy levels exhibit gross errors (cf. Tab. 4.1, 4.2).

$$IP(d) \overset{\text{vertical, CDFT}}{:=} (E_0^+(d) + \Phi_{vac}(d)) - E_0(d) \tag{4.1}$$

$$EA(d) \overset{\text{vertical, CDFT}}{:=} (E_0(d) + \Phi_{vac}(d)) - E_0^-(d) \tag{4.2}$$

To check if this issue can be remedied within the original framework, constrained density functional theory (CDFT(PBE0)) was applied to calculate the vertical values of ionisation potential (IP) and electron affinity (EA). Adopting the neutral geometries, the electron configurations of the singly charged molecular ions were fixed, so that these quantities could be evaluated based on the total energies $E_0^{(+/-)}(d)$ and the vacuum level $\Phi_{vac}(d)$, which is resp. converges to the potential energy of an electron in free space, according to equations (4.1) and (4.2). Charged periodic supercells, which were originally not considered, demand monopole (charge) corrections due to the divergence of their Coulomb potential. Hence these were "neutralised" by introducing an oppositely equal homogeneously distributed background charge (jellium)[3]. Moreover it was found that multipole corrections (dipole and quadrupole)[4] also make substantial, yet smaller, contributions to the total energies $E_0^{+/-}(d)$.

Limited computational resources prevented converging IP or EA with respect to d directly. Hence their values at $d = 15 - 30$Å in steps of 5Å were used to extrapolate them. All corrections vanish asymptotically, whereby the monopole part, which makes the largest contribution, exhibits the slowest convergence as it is proportional to d^{-1}. Assuming the same (asymptotic)

[3] The monopole corrections are proportional to the square of the supercell charge. In the present cases they amount to +20.428eVÅd^{-1}.

[4] Reliable multipole corrections could only be obtained, when a reference point ("charge center") was specified explicitly. To this end the center of the carbon ring was chosen. Taking the position of the halogen instead was also tested, but made merely irrelevant differences (<0.01eV). Contrary to monopole corrections, multipole corrections do not vanish identically for neutral systems, yet the respective contributions were found to be negligible (<1meV).

behaviour, the extrapolations were carried out by linear regressions (least square fits) to obtain the values at $d^{-1} \searrow 0$.

Despite the following large improvements for both quantities resp. each molecule, the overall result is still unsatisfactory. The experimental *IP* trend is confirmed, but the values are 0.12-0.38eV too small (cf. Tab. 4.1). While it could perhaps be argued if this is still acceptable, more serious discrepancies appear for the *EA*. CDFT(PBE0) produces rather the opposite than the measured trend (cf. Tab. 4.2). The relative stability of the corresponding singly occupied molecular orbital (SOMO) is 0.34-0.62eV too high for C_6H_5X with X=F,Cl,Br (cf. Tab. 4.2). Remember that C_6H_5I can not be discussed analogously due to lack of clarity from the experimental side.

Like in chapter 3, it was concluded that it is necessary to apply the GW method on the basis of the DFT results in order to reproduce the electronic structure adequately[5].

Judging from the calculated positions of HOMO and LUMO (relative to Φ_{vac}) states up to 145eV above the former (here: corresponding to a band number of NBANDS=12288) have to be taken into account for an adequate treatment of the electronic structures without superfluous computational cost. This energy interval width exceeds those of the regular mere ice calculations, yet to assess the quality of their results from the theoretical side even broader intervals were considered for the bulk (see chapter 3 and section C). Unlike the adsorbed molecules, the gas phase molecules were treated with a response function energy cutoff $E_{\text{cut-GW}}$ of only 100eV instead of 125eV. Randomly employing $E_{\text{cut-GW}}$=100eV for the adsorbed molecules led to a lowering of $\leq$0.09eV for the HOMO and $\leq$0.04eV for the LUMO. Therefore repeating the entire GW calculations for the free molecules with $E_{\text{cut-GW}}$=125eV was eschewed.

Theoretical and experimental results for the positions of the relevant molecular orbitals relative to Φ_{vac} are listed in Tab. 4.1 and 4.2. In most cases higher main resonances are also important due to their involvement in the DEA processes treated in chapter 5 and/or stronger localisation. Furthermore Fig. 4.2 shows the scGW$_0$(PBE0) MO diagram. In agreement with experiment, increasing the row of the halogen destabilises the occupied MOs and lowers the resonances, particularly those of σ_s^* character, while no empty states are found below Φ_{vac}. Hence the (vertical) *IP* decreases and the (vertical) *EA* becomes larger, yet stays negative. According to the calculations, the HOMO

[5] The GW approach works with one-electron Green's functions and the quasiparticle (QP) energies obtained from it possess a direct physical interpretation (see section 2.7). Hence treating neutral $(15\text{Å})^3$ supercells with DFT(PBE0) provides sufficient starting points and results of CDFT(PBE0) are not needed.

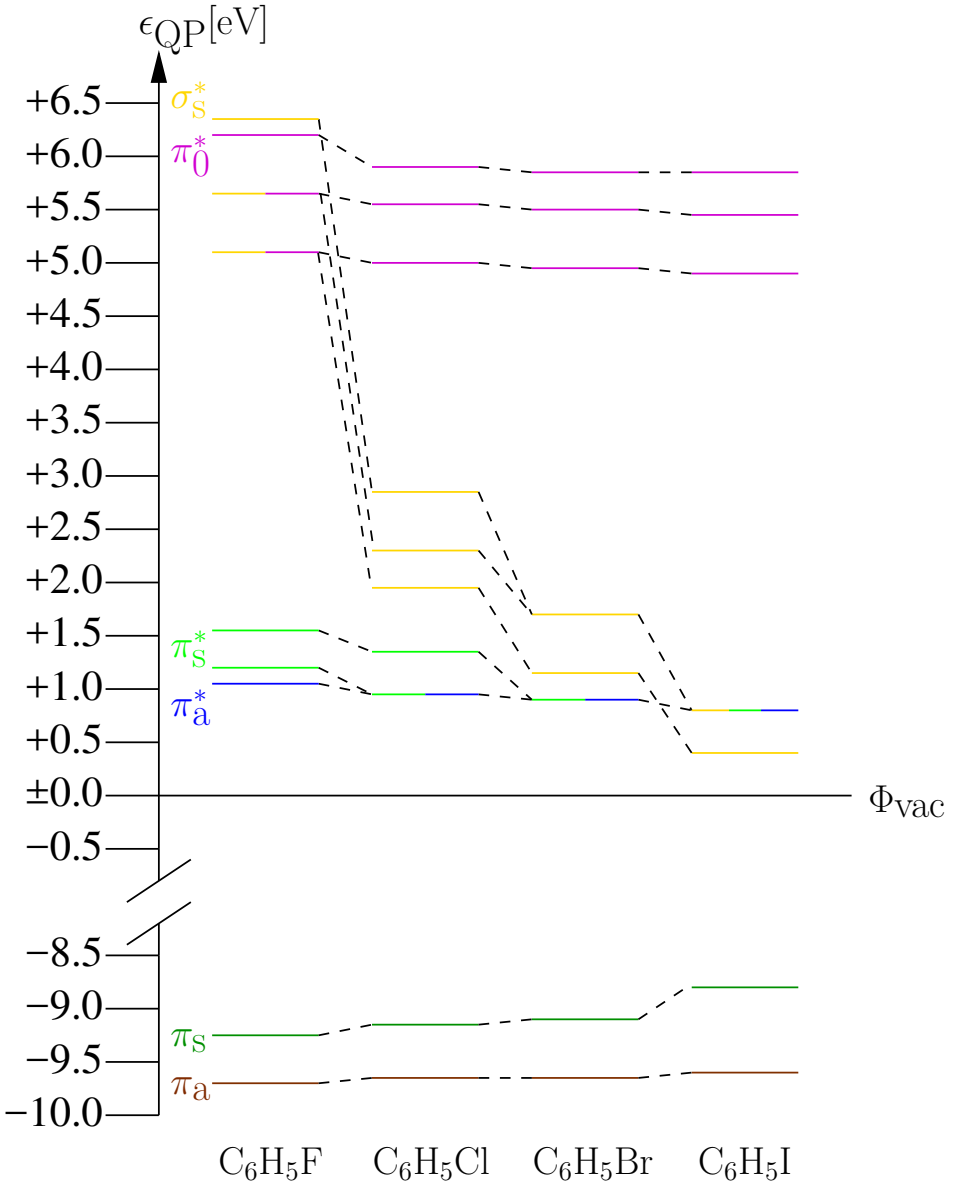

Figure 4.2.: Molecular orbital (MO) diagram of phenyl halogenides in vacuum from $scGW_0$(PBE0)

Table 4.1.: Vertical ionisation potential (*IP*) of phenyl halogenides in vacuum from $scGW_0$, underlying DFT(PBE0) and CDFT(PBE0) compared to experimental values, highest occupied π states

$IP(C_6H_5X)$[eV]				
X=	F	Cl	Br	I
exp. [200]	9.37	—	—	—
exp. [201]	—	9.07	8.99	8.77
exp. [202]	9.29	9.05	9.00	8.75
exp. [203–205]	9.21	9.07	9.03	—
DFT(PBE0)	7.30	7.17	7.11	6.88
CDFT(PBE0)	9.09	8.81	8.70	8.39
$scGW_0$(PBE0) π_s	9.25	9.15	9.08	8.81
$scGW_0$(PBE0) π_a	9.68	9.65	9.65	9.59

is a π_s state throughout. Its position is in very good agreement with the newest measurements, since the values yielded by them are only 0.04-0.08eV higher. Preceding experiments already produced basically the same results, except for C_6H_5F. The respective π_a MO is 0.43-0.78eV more stable. This energy difference grows with increasing row of the halogen. The *EA*s of C_6H_5X with X=F,Cl,Br are 0.19-0.22eV too small and the situation for C_6H_5I is not fully clear as aforementioned. For π_a^* and π_s^* states the calculations yielded results very similar to those of the measurements. It was confirmed that they constitute a degenerate LUMO in case of C_6H_5Cl or C_6H_5Br. A small splitting of 0.04eV favouring π_s^* was found for C_6H_5I, yet the LUMO, which could not be identified experimentally, turned out to be of σ_s^* character. A π_a^* LUMO and an almost equally localised π_s^* state 0.49eV (experimentally: 0.61eV) above it occurred for C_6H_5F (also cf. Fig. 4.4). Moreover the calculations produced a clearly weaker, yet still substantial, π_s^* resonance in between (also cf. Fig. 4.4). It seems that the σ_s^* resonance detected for C_6H_5Cl (2.5eV above Φ_{vac}) can be explained by the closer second (0.18eV lower) or stronger third (0.36eV higher) calculated MO of that type (also cf. Fig. 4.5). Three π_0^* resonances appeared for each molecule. Even the most stable of these still lies 0.30-0.61eV higher than the measured π_0^*. Nevertheless in chapter 5 it will be seen that C_6H_5F in vacuum is the sole system with relevance of π_0^* resonances for DEA in the low-energy range and the corresponding investigated process is very unlikely to happen. Therefore the error is considered tolerable. Overall the calculated resonances lie rather higher than their measured equivalents, while the opposite tendency with smaller energy differences is shown by the HOMO.

Table 4.2.: Vertical electron affinity (*EA*) of phenyl halogenides in vacuum from scGW$_0$, underlying DFT(PBE0) and CDFT(PBE0), lowest π^* and σ^* main resonances compared to experiment [higher main resonances with relevance for DEA (see chapter 5) and/or stronger localisation added in parentheses]

EA(C_6H_5X)[eV]				
X=	F	Cl	Br	I
exp. π_a^* [206]	-0.87	-0.73	-0.67	-0.59
exp. π_s^* [206]	-1.48	-0.73	-0.67	-0.59
exp. σ_s^* [206]	—	-2.5	—	—
exp. π_0^* [206]	-4.80	-4.50	-4.40	-4.3
DFT(PBE0)	+0.61	+0.65	+0.67	+0.87
CDFT(PBE0)	-0.25	-0.31	-0.33	-0.22
scGW$_0$(PBE0) π_a^*	-1.06	-0.94	-0.89	-0.82
scGW$_0$(PBE0) π_s^*	-1.19	-0.94	-0.89	-0.78
	(-1.55)	(-1.35)		
scGW$_0$(PBE0) σ_s^*	-5.08	-1.93	-1.14	-0.38
	(-5.63)	(-2.32)	(-1.71)	(-0.79)
	(-6.33)	(-2.86)		
scGW$_0$(PBE0) π_0^*	-5.10	-4.98	-4.96	-4.91
	(-5.64)	(-5.54)	(-5.51)	(-5.45)
	(-6.18)	(-5.88)	(-5.87)	(-5.86)

The bonding-antibonding state gaps, i.e. π_s-π_s^* and π_a-π_a^*, narrow if a heavier halogen is chosen (cf. Tab. 4.1, 4.2 and Fig. 4.2). This, in particular the surprising trend regarding the relative stability of each antibonding MO, is explained by the decreasing electronegativity difference between the atoms involved in the carbon-halogen bond. The halogen has a positive mesomeric (+M) effect on the delocalised π electrons from the carbon ring, because it adds another electron pair to the three of this mesomeric system. As previously discussed the π states arise from the interaction of $p_{(z)}$ orbitals (orthogonal to the horizontal molecular symmetry plane). For symmetric π MOs, the halogen contributes additionally to the carbon ring. The corresponding atomic orbital interaction becomes weaker for heavier halogens, because the carbon-halogen electronegativity difference decreases and the bond length increases. Hence the π_s-π_s^* gap width is reduced concomitantly. The π_a-π_a^* gap is only indirectly affected. Hence it exhibits the same trend yet to a much lesser extent. Moreover due to the larger analogous relevant main shells of the halogen, its charge capacity increases and the antibonding MOs are lowered. This kind of line of reasoning also pertains to the π_0^* and σ_s^* MOs, which are symmetric, but

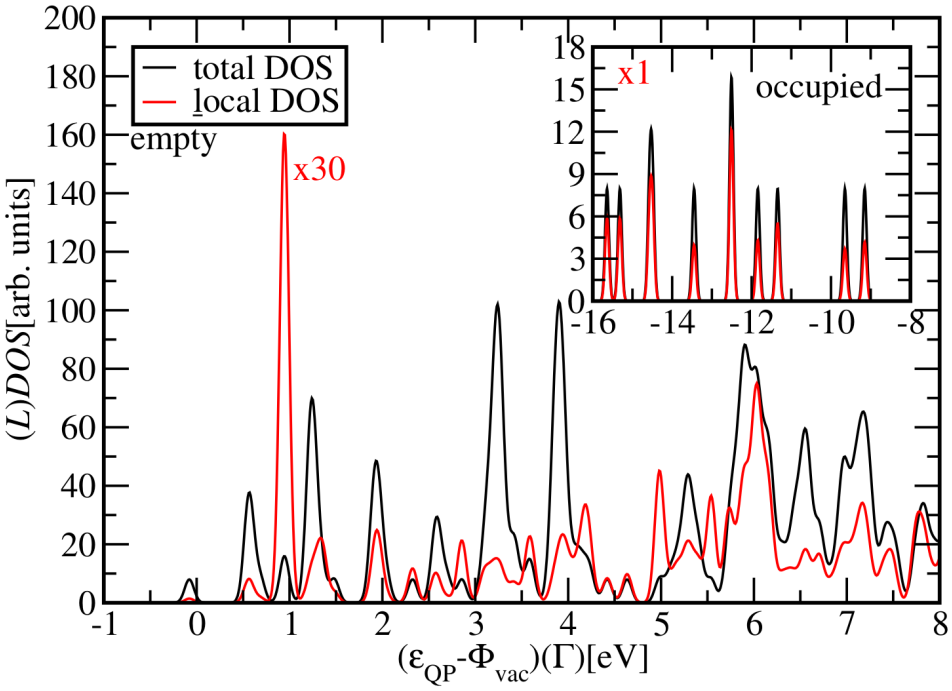

Figure 4.3.: Comparison of total and local density of states ((*L*)*DOS*) of phenyl chloride C_6H_5Cl from scGW$_0$(PBE0)

not to the bonding MOs, because they are occupied instead of empty. The particularly large extent of the stabilisation of the σ_s^* MOs originates from position and orientation of the major atomic orbitals from whose interaction they arise. These are initially centered at the atoms of the carbon-halogen bond resp. its axis, to which they are cylindrically symmetric. Hence their overlap for C_6H_5F resp. its decrease for higher row of the halogen is especially strong. According to Olthoff et al. (1985) [206] only C_6H_5F exhibits a main resonance splitting of π_s^* and π_a^*, because the coinciding rows of carbon and fluorine prevent the degeneracy.

Due to the negative electron affinity of the phenyl halogenides, only molecular resonances, i.e. significantly localised discrete states above Φ_{vac}, are relevant for excess electron capture. As Heisenberg's uncertainty relation (for energy and time) demonstrates, the (average) lifetimes of the arising transient negative ions (TNIs) tend to be longer for smaller energy uncertainty, which is evidenced by stronger localisation of the resonance to be occupied. Hence

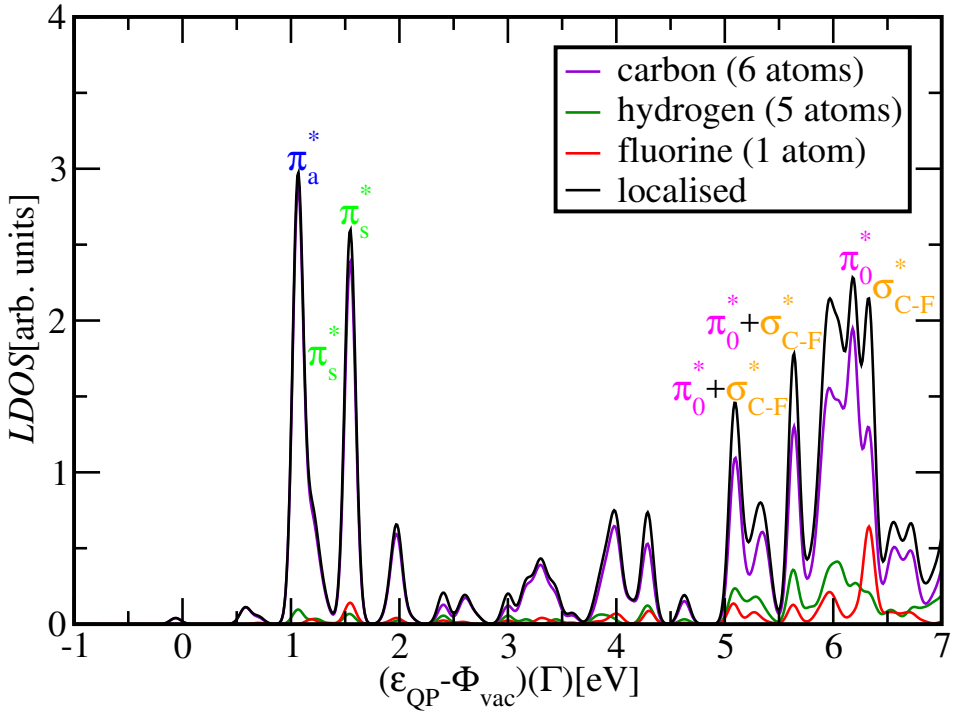

Figure 4.4.: Element-projected local density of states (*LDOS*) of phenyl fluoride C_6H_5F from scGW$_0$(PBE0)

the local (fraction[6] "p" of the) density of states (LDOS) is considered in more detail. Note additionally that TNI lifetime [38] and electron attachment cross section [43] among others exhibit an inverse dependence on the kinetic energy of the incident electron. Chapter 5 considers the energy resp. localisation of the excess electron state before it becomes stable in a similar way to discuss the appendant probability.
Fig. 4.3 gives a fundamental impression of the localisation of the molecular *DOS*. To this end it draws an exemplary comparison between *DOS* and *LDOS* of C_6H_5Cl. It is apparent that the overall localisation of the occupied states is very strong (see inset), while the opposite result is found for the empty states, whose local fraction was magnified by a factor of 30 for reasons of clarity. Hence strong resonances among the scattering states can be no more than scarce, but it will be seen that they appear in any case.

[6] The local fraction "p" of a state is defined as the sum of the integrals over the local parts of its probability density distribution. These are approximated from the projections of its wave function onto spherical harmonics (of s-, p- and d-character) centered at each atomic nucleus and restricted by a maximum ("Wigner-Seitz") radius RWIGS.

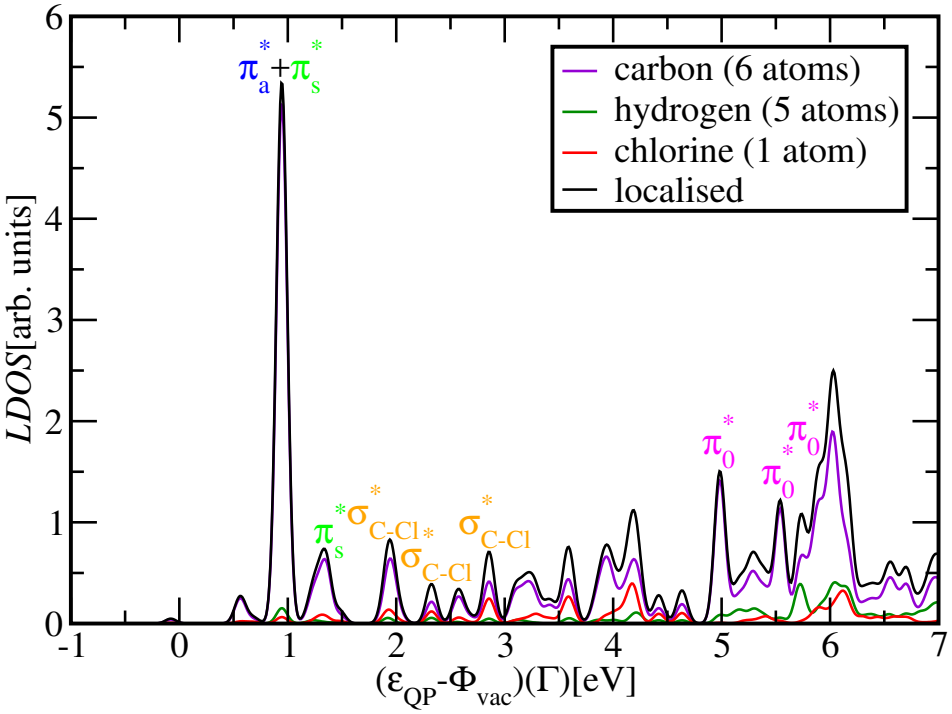

Figure 4.5.: Element-projected local density of states (*LDOS*) of phenyl chloride C_6H_5Cl from scGW$_0$(PBEo)

To corroborate and extend the insight regarding the interaction of the molecules with incident and captured electrons, the local density of their scattering states and its element-projected components are considered. These are displayed in Fig. 4.4 (C_6H_5F), 4.5 (C_6H_5Cl), 4.6 (C_6H_5Br) and 4.7 (C_6H_5I). The carbon component dominates throughout, while the hydrogen component is small and remains largely unaffected by changing the halogen. In the case of C_6H_5F the halogen component, which is of central importance for any DEA process investigated (see chapter 5), is roughly similar to the hydrogen component, however the former grows significantly for heavier halogens (also cf. Fig. 4.8) as it can be expected due to their larger analogous relevant main shells and the weaker carbon-halogen bond (cf. Tab. 5.2, 9.1, 9.2). The most intense peaks always come from a π_a^* and a π_s^* MO of similar local fraction, which are the strongest resonances. Apart from C_6H_5F the diagrams reveal no visible splitting of these. π_0^* MOs evoke peaks that are only slightly less intense but do not occur until 3.55-4.09eV above the former, whereby this energy difference increases with the row of the halogen (also cf. Tab. 4.2). The σ_s^* MOs are mostly more delocalised, yet still make some essential

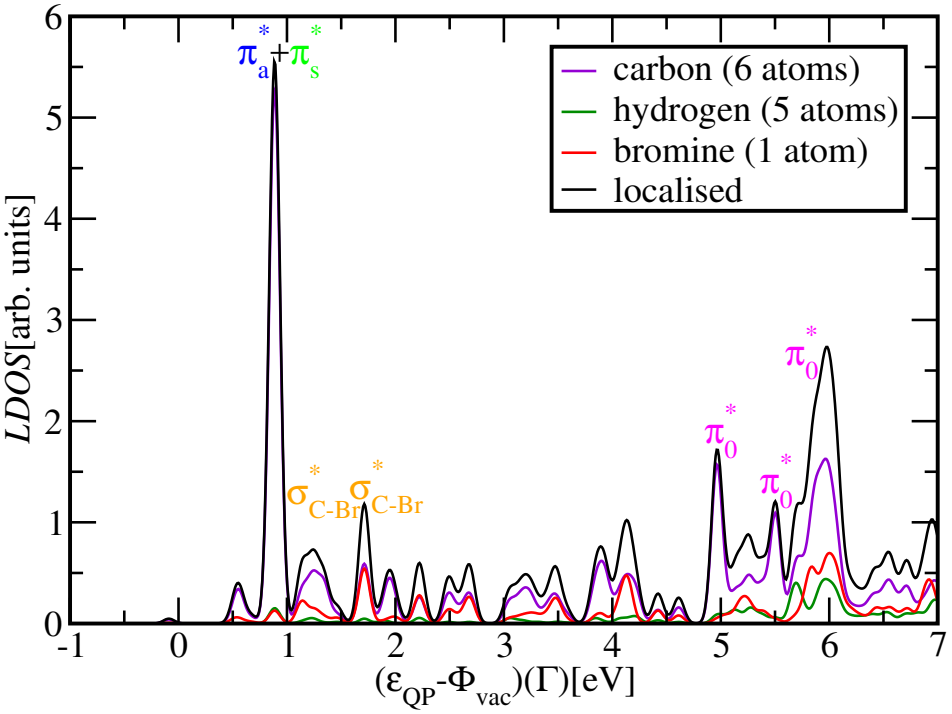

Figure 4.6.: Element-projected local density of states (*LDOS*) of phenyl bromide C_6H_5Br from scGW$_0$(PBE0)

contributions. As it can be expected in view of the previous discussion, these shift rapidly downward in energy for heavier halogens, while the positions of the π^* resonances are much less affected (also cf. Fig. 4.2). Located around the range of the π_0^* resonances for C_6H_5F, the σ_s^* resonances lie clearly lower for C_6H_5Cl and C_6H_5Br and finally arrive at and below the π_a^* and π_s^* peak(s) for C_6H_5I with one of them consequently even being the LUMO. Due to the MO symmetries explained earlier, any sufficiently large peak with vanishing halogen contribution has to be of π_a^* character. The most obvious example is the π_a^* resonance of C_6H_5F (cf. Fig. 4.4). The relative halogen contribution to π_s^* and π_0^* states is clearly smaller than for σ_s^* states. Hence, before considering the partial charge density distributions, the types of the peaks can to a certain extent already be conjectured on the basis of the element-projected components. Nevertheless it still has to be beared in mind that this alone is not fully sufficient, because some ambiguities remain primarily as peaks of different types might superimpose each other. Altogether σ_s^* peaks in the molecular ground states are widely overshadowed by π^* resonances. Those of π_a^* or π_s^* type are expected to possess the highest electron attachment cross

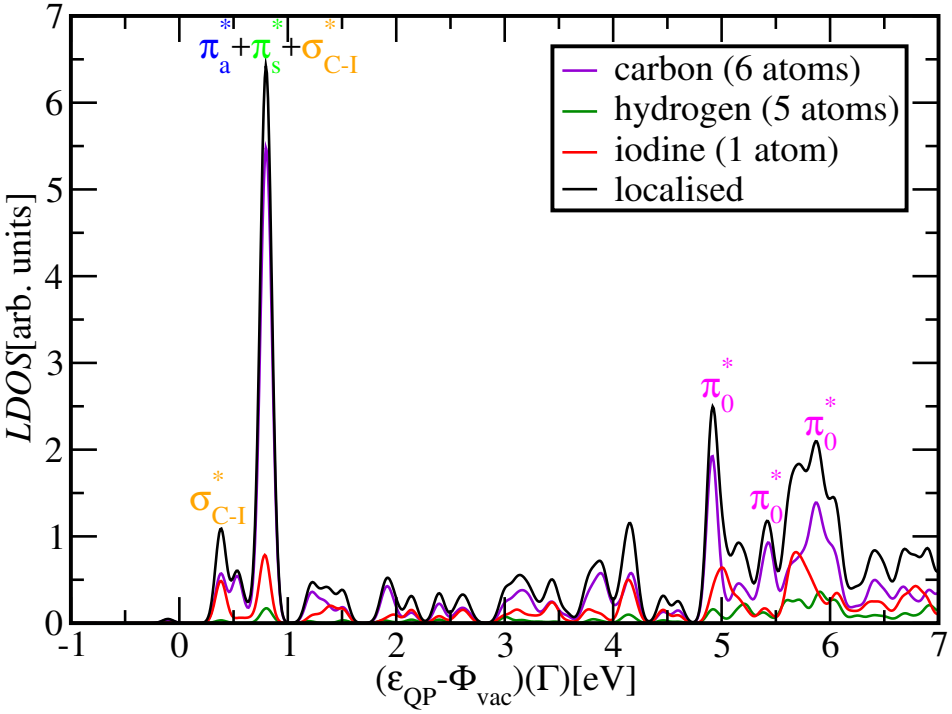

Figure 4.7.: Element-projected local density of states (*LDOS*) of phenyl iodide C_6H_5I from scGW$_0$(PBEo)

sections due to their superior relative stability, except for C_6H_5I. Judging from the peak heights π^* TNIs should exhibit the longest (average) lifetimes. Compared to the contribution made by the halogen, which clearly increases with its row, the *LDOS* is much less affected (also cf. Fig. 4.8). Hence the influence of σ_s^* MOs, which are of utmost relevance at the later stages of DEA (see chapter 5), grows accordingly. Consolidating these findings evidences that incident electrons are more likely to be captured by the molecular resonances at lower kinetic energies and to induce dissociation, if the row of the halogen is increased. In chapter 5 this will be considered in more detail by treating these DEA processes explicitly.

In the framework of this study a selfconsistent GW approach beyond G_0W_0 was not feasible for the molecules on the ice surface due to computational expense. To justify employing G_0W_0 for the treatment of DEA to the adsorbed molecules, the effect of the various degrees of GW selfconsistency on the electronic levels of the gas phase molecules is studied exemplarily for C_6H_5Br.

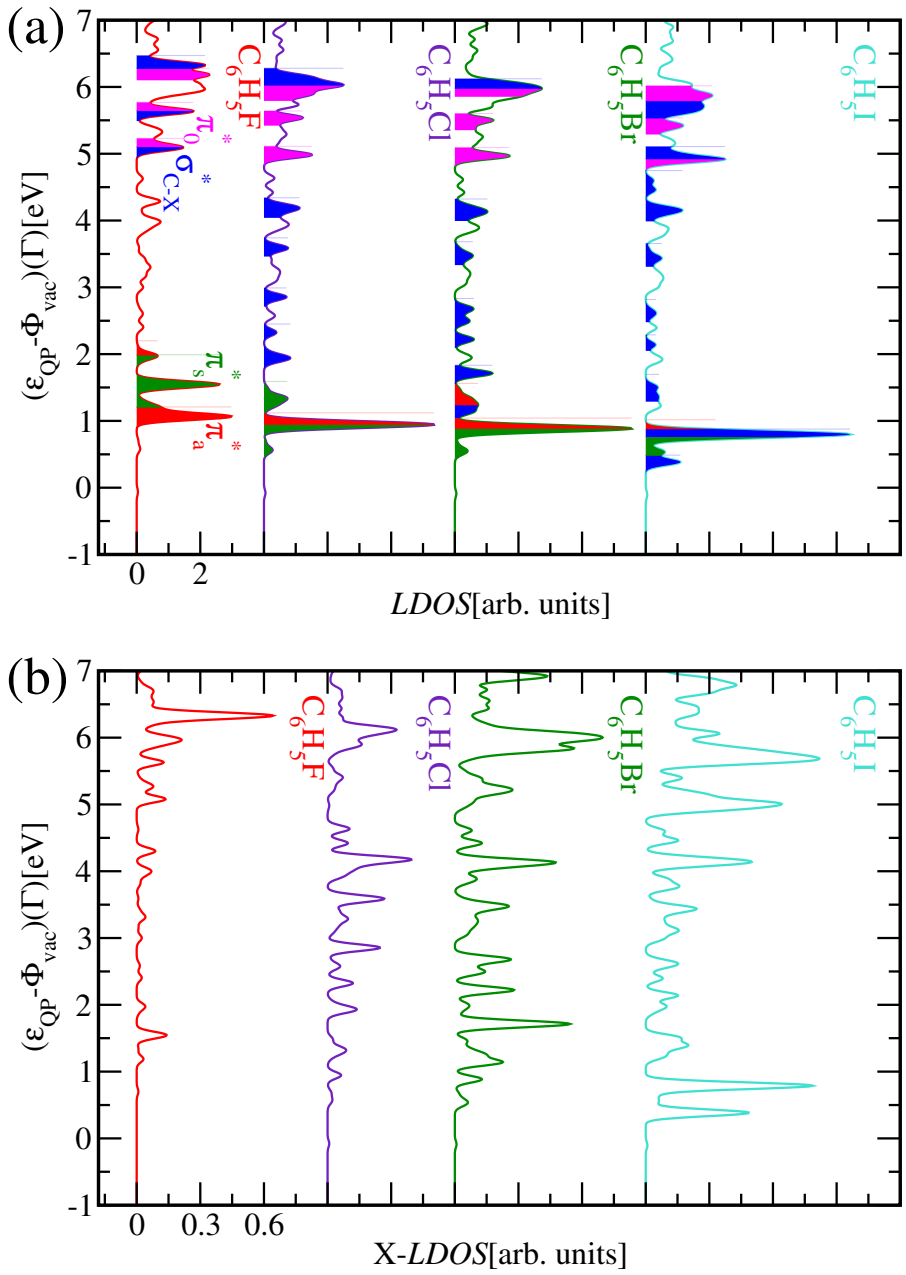

Figure 4.8.: Comparison of (a) local and (b) halogen-projected (X) local density of states (X-)*LDOS* for phenyl halogenides C_6H_5X with X=F,Cl,Br,I from scGW$_0$(PBE0)

Table 4.3.: Role of GW selfconsistency in the exemplary case of the phenyl bromide molecule C_6H_5Br in vacuum, character and position of HOMO and LUMO as well as significantly localised $\pi^{(*)}$ states close to them relative to Φ_{vac} and their local fraction "p"[4] ((15Å)^3 cubic supercell, plane wave energy cutoff E_{cut}=400eV, response function energy cutoff $E_{cut\text{-}GW}$=100eV, NBANDS=12288, Γ-point calculations (50 frequency points along the real axis, spectral method employed) based on DFT(PBE0))

C_6H_5Br	MO	ε_{QP}^{HOMO}[eV](p)	ε_{QP}^{LUMO}[eV] (p)	GAP[eV]
G_0W_0	π_s-π_s^*	-8.77 (0.541)	+1.07 (0.432)	9.84
	π_a-π_a^*	-9.28 (0.468)	+1.08 (0.415)	10.36
GW_0	π_s-π_s^*	-8.89 (0.541)	+1.10 (0.432)	9.99
	π_a-π_a^*	-9.40 (0.468)	+1.12 (0.415)	10.52
GW	π_s-π_s^*	-8.99 (0.541)	+1.19 (0.432)	10.18
	π_a-π_a^*	-9.51 (0.468)	+1.22 (0.415)	10.73
$scGW_0$	π_s-π_s^*	-9.08 (0.529)	+0.89 (0.322)	9.97
	π_a-π_a^*	-9.65 (0.466)	+0.89 (0.376)	10.54
scGW	π_s-π_s^*	-9.11 (0.529)	+0.91 (0.297)	10.02
	π_a-π_a^*	-9.68 (0.466)	+0.93 (0.366)	10.61

Table 4.4.: Role of GW selfconsistency in the exemplary case of the phenyl bromide molecule C_6H_5Br in vacuum, position of lowest significantly localised σ_s^* states relative to Φ_{vac} and their local fraction "p"[4] ((15Å)^3 cubic supercell, plane wave energy cutoff E_{cut}=400eV, response function energy cutoff $E_{cut\text{-}GW}$=100eV, NBANDS=12288, Γ-point calculations (50 frequency points along the real axis, spectral method employed) based on DFT(PBE0))

$C_6H_5Br(\sigma_s^*)$	ε_{QP}^{1}[eV] (p)	ε_{QP}^{2}[eV] (p)	ε_{QP}^{3}[eV] (p)	ε_{QP}^{4}[eV] (p)
G_0W_0	0.42 (0.110)	0.98 (0.258)	0.95 (0.078)	1.54 (0.036)
GW_0	0.43 (0.110)	1.00 (0.258)	0.95 (0.078)	1.54 (0.036)
GW	0.47 (0.110)	1.07 (0.258)	0.98 (0.078)	1.57 (0.036)
$scGW_0$	0.52 (0.014)	1.14 (0.066)	1.25 (0.031)	1.71 (0.148)
scGW	0.47 (0.012)	1.10 (0.045)	1.21 (0.037)	1.70 (0.139)

Position relative to Φ_{vac} and local fraction[7] "p" of the most relevant states are given in Tab. 4.3 (π character) and 4.4 (σ_s^* character).

Increasing the level of the GW selfconsistency scheme mainly stabilises the occupied π states (0.12-0.40eV compared to G_0W_0), while their empty counterparts experience a smaller shift (-0.19eV to +0.14eV). All π states are strongly localised throughout, while each position varies by 0.30-0.40eV (cf. Tab. 4.3). The π_a-π_a^* gap (10.36-10.73eV) is always wider (0.52-0.59eV) than the π_s-π_s^* gap (9.84-10.18eV), which is almost exclusively due to the energy difference between the occupied states (0.51-0.57eV). The positions of their empty counterparts, i.e. π_s^* and π_a^*, are mainly affected by stabilisation due to the orbital update sc ($GW_{(0)} \rightarrow scGW_{(0)}$). Updating Green's function G ($G_0W_0 \rightarrow GW_0$) or screened Coulomb interaction W ($GW_0 \rightarrow GW$ or $scGW_0 \rightarrow scGW$) has converse yet clearly smaller influence on them. Judging from their local fractions, these should be the most pronounced resonances. Transitioning from G_0W_0 to $scGW_0$ lowers them by 0.18-0.19eV. Additionally updating W causes only a marginal raise of 0.02-0.04eV.

For σ_s^* states the situation is more complicated (cf. Tab. 4.4). Overall their positions vary less, more specifically by merely 0.10-0.30eV. Contrary to π states, which behave rather conversely, they tend to be destabilised upon increasing the level of the GW selfconsistency scheme. While this lies in an acceptable range, the orbital update sc might at first sight seem indispensable due to its drastic effect on the localisation of the numerous σ_s^* resonances. However this is of lesser importance as π^* resonances, due to their much stronger localisation, are instead by far the most relevant candidates for the formation of the transient anion by excess electron capture. Judging from the calculated element-projected *LDOS* this pertains to C_6H_5X with X=F,Cl,Br (cf. Fig. 4.4 to 4.6). It has been confirmed by the aforementioned electron transmission spectroscopy (ETS) experiments of Olthoff et al. (1985) [206] and further studies of C_6H_5Cl [41, 45, 207, 208] and C_6H_5Br [209]. Moreover in chapter 5 it will be seen that upon C-X bond elongation (∼dissociation) the numerous σ_s^* resonances collapse into a strongly localised stable σ_s^* state, which harbours the excess electron at the later stages of DEA.

Judging from these considerations full GW selfconsistency, particularly due to the orbital update sc, can be expected to produce relatively more stable prevailing resonances capturing the excess electron and harbouring it in the early stages of DEA. This is a point for enhanced dissociation probabilities and the pertaining initial states stay strongly localised upon any change of GW selfconsistency. Insofar its neglect is indeed justified, because no essential

[7] Compared to G_0W_0, i.e. fully non-selfconsistent GW, p can only be modified if the orbitals are updated (sc), because the wave function is left invariant otherwise.

qualitative changes are found, the energy errors are tolerable and the DEA processes might occur even more frequently than evidenced in this study, esp. chapter 5. Based on a completing strategy also taking the later stages of DEA into account, it will be demonstrated that the correct dissociation mechanism is predicted at the applied level of theory (see section E).

4.2. Adsorption sites, modes and energies at $I_h(0001)$

Before investigating the influence of the ice substrate, especially its surface defects, on DEA to the molecules, their adsorption geometries and energies E_{ads} have to be determined. For this purpose different positions of the adsorbates (C_6H_5X with X=F,Cl,Br) at the idealised bilayer-terminated surface and each of the prototypical defect structures described in section 3.2 were examined (details to be elaborated later on).

Initially a full relaxation of the systems with gradient (GGA) DFT(PBE) (see subsubsection 2.5.2.2) was performed like in section 3.2 due to reasons of computational expense. Thereby only the oxygens at the slab surface opposite to the adsorbate were kept fixed. In a second step dispersion corrections were applied to the adsorbate geometries despite their highly probable reliability, because judging from the effect on the E_{ads} values it turned that the interaction between induced dipoles of adsorbate and substrate makes these indispensable. To this end the Grimme-D2 scheme for the PBE XC-functional (see subsubsection 2.5.2.3) was employed. In [101] it was suspected that this necessity of dispersion corrections is a common phenomenon (see also subsubsection 2.5.2.3). Despite the antiferroelectric structure of the substrate, whose bulk is essentially a molecular crystal, substantial dipoles, which can be aided by defects, exist at least locally at the surface, where charge screening is much weaker than in the bulk, as it exhibits dangling protons (see chapter 3). The adsorbates are already polar by themselves. It was found that London dispersion interaction contributes 100-500meV to the adsorption energies E_{ads} of the phenyl halogenide molecules. Its effect on the geometry of the ice substrate was neglected, because semiempirical dispersion corrections lead to considerable overbinding [61].

An adequate strategy is required to identify the most favoured adsorption geometry (highest E_{ads}) for each adsorbed molecule and surface structure, because relaxations on the complicated potential energy hypersurface often lead to one of its merely local minima. Several starting geometries and adsorption modes (flat-lying, vertical, inclined) have to be taken into account. Hence being aware of the underlying physics and recognising typical geometrical resp. bonding motifs, which can also be expected to have substantial influence

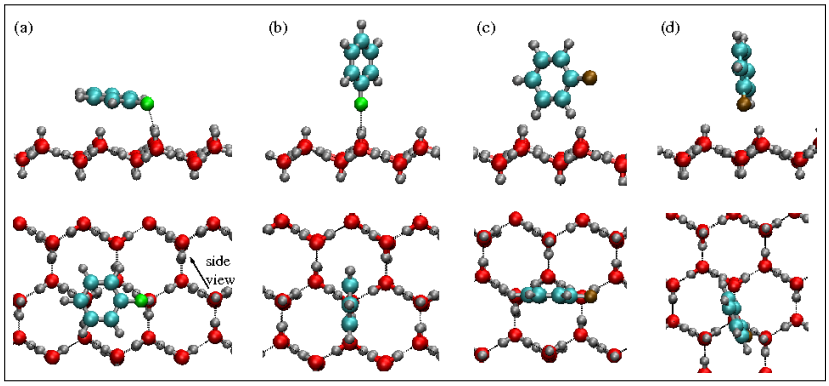

Figure 4.9.: Examined adsorption geometries of C_6H_5X with X=F,Cl,Br at ideal bilayer-terminated Fletcher-striped $I_h(0001)$: (a) flat-lying adsorption along the Fletcher stripe with the halogen X on top of a dangling proton, vertical adsorption (b) with X on top of a dangling proton (c) with the phenyl group H-bonded to two flat-lying surface water molecules (d) with X on top of a dangling proton and the phenyl group H-bonded to an adjacent flat-lying surface water molecule. The upper resp. lower panels display side resp. top views. The arrow in the lower panel of (a) indicates the direction of the side views.

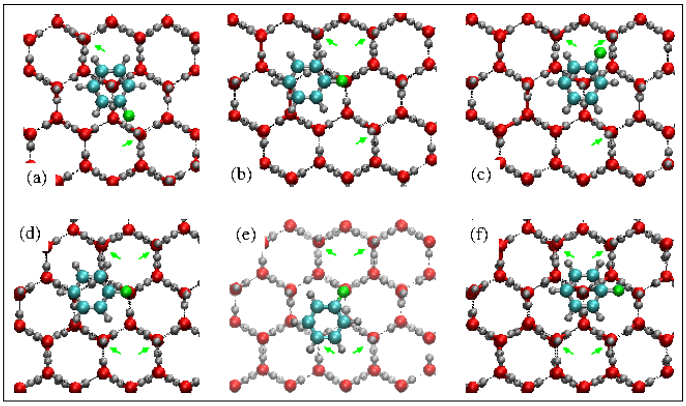

Figure 4.10.: Examined adsorption geometries of C_6H_5X with X=F,Cl,Br at orientational (S_{AD}) defects constituting different extents of surface proton disorder resp. accumulation of positive partial charges on $I_h(0001)$: (a) $2S_{AD}$, $3S_{AD}$ (b) halogen X on top of the central dangling proton (c) rotated phenyl group on top of the central dangling proton, $4S_{AD}$ (d) X on top of the central dangling proton (e) X on top of the central dangling proton and rotated phenyl group (f) phenyl group on top of the central dangling proton. The repositioned dangling protons are marked by green arrows.

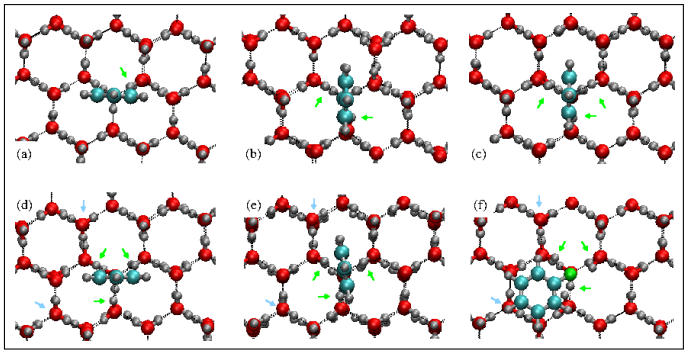

Figure 4.11.: Examined adsorption geometries of C_6H_5X with X=F,Cl,Br at molecular vacancies (V_A, V_D) and heterogeneous defect complexes on $I_h(0001)$: vertical adsorption with the halogen X inserted into the molecular vacancy (a) V_A with one dangling proton (b) V_D with two dangling protons (c) V_D-S_{AD} with three dangling protons (d) and (e) V_A-$2S_{AD}$ with three dangling protons, flat-lying adsorption (f) same defect as in the two previous cases with X situated above the molecular vacancy. The plane of the phenyl group is rotated against the direction of the Fletcher stripes in (b), (c) and (e). In (f) carbon-halogen bond and phenyl group are parallel, instead of orthogonal, to the surface, whereby the former is rotated against the aforementioned direction. Dangling protons pointing into the molecular vacancy resp. reoriented surface water molecules are indicated by green resp. blue arrows.

on the electronic structures of the adsorbed molecules, are of paramount importance. The knowledge gained by analysing systems of advancing complexity shall be incorporated successively. Thus the investigation progresses from pristine $I_h(0001)$ to orientational defects to molecular vacancies resp. heterogeneous complexes. A qualitative discussion of the relations between defect types, electron affinities – i.e. depths – of traps, adsorption geometries and adsorption energies taking into account the results for all considered systems is given. Fig. 4.9 to 4.11 display various adsorption geometries at the idealised bilayer-terminated ice surface and several defect structures. The dispersion-corrected E_{ads} values belonging to the most favoured geometries are listed in Tab. 4.5 and plotted against the electron trap depths in Fig. 4.12.

The upper first bilayer of ideal $I_h(0001)$ consists of alternating parallel rows of undercoordinated water molecules, which either exhibit a dangling proton or are flat-lying. Hence two main bonding motifs are possible. Due to Coulomb forces between the unlike partial charges, dangling protons attract the halogen, while hydrogen bonds might emerge between hydrogens of the phenyl group and oxygens of undercoordinated flat-lying water molecules. As previously discussed mere ab-initio DFT(PBE) calculations were performed to establish a basis before adding the semiempirical dispersion corrections.

Fig. 4.9 displays the geometries which were tested for all adsorbates. Flat-lying was favoured over vertical adsorption by about 100meV independently of the halogen. C_6H_5F was considered first. Rotations of the phenyl group affected flat-lying adsorption clearly less (E_{ads} varying by $<$25meV) than the vertical mode (60meV). This is not surprising, because after full relaxation the halogen was always found on top of a dangling proton in the former case, while different bonding motifs and sites had to be considered in the latter. Adsorption geometries (c) and (d), which exhibit approximately equal E_{ads}, are preferred over (b) (cf. Fig. 4.9). Hence it seems that the vertical mode is significantly enhanced if it involves at least one hydrogen bond. Qualitatively similar results were obtained using heavier halogens, except for the instability of (b). Adding dispersion corrections leads to stronger adsorption for all geometries, because London dispersion interaction is always attractive (see subsubsection 2.5.2.3). Roughly speaking flat-lying adsorption on the idealised bilayer-terminated surface is favoured by further 100meV (200meV in total), as E_{ads} is raised by 200meV, while exemplary calculations showed that it is only half for the vertical modes. This is found for all halogens in the series X=F,Cl,Br. Since the same adsorption mode with the halogen on top of a dangling proton as the central bonding motif is preferred for all adsorbates, it could be supposed that E_{ads} becomes smaller if a less electronegative halogen is used. This anticipation is partially confirmed and merely weakly violated, because the strongest adsorption occurs for C_6H_5F and E_{ads} is almost equal for the two remaining adsorbates (cf. Tab. 4.5 and Fig. 4.12). Applying dispersion corrections also to the substrate geometry was examined with C_6H_5Cl as adsorbed molecule, whereby no meaningful differences appeared.

To shed broader light on the role of dangling protons in the adsorption processes, orientational (S_{AD}) defects were introduced to create more pronounced agglomerations of them resp. their positive partial charges (cf. Fig. 4.10). For this purpose one of the two Fletcher stripes was incrementally disassembled, whereupon the dangling protons in question successively accumulate around a central dangling proton belonging to its intact analogue. Flat-lying adsorption was assumed to construct the initial guesses as motivated by the results for the ideal substrate and the fact that the oxygen sublattice stays regular at this point. Indeed the inclination of the carbon-halogen bond resp. the phenyl group towards the surface was never found to be more than a few degrees. Like for pristine $I_h(0001)$, the halogen prefers to be situated on top of the central dangling proton, while this position is clearly less favourable for the focus of the carbon ring. Even with the optimal position of the halogen and almost flat-lying adsorption rotating the phenyl group occasionally has substantial influence on the adsorption energy. Nevertheless it was found that under these

conditions positioning the phenyl group on top of the intact Fletcher stripe is always at least very close to the most favoured adsorption geometry. For reasons of convenience the subsequent investigations of adsorbate-substrate systems adopt this choice if no molecular vacancies are considered. As expected E_{ads} decreases upon using a less electronegative halogen (cf. Tab. 4.5 and Fig. 4.12). This trend is confirmed for all orientational defects, yet the influence of the cluster size or electron trap depth is more complicated. The anticipated rise of E_{ads} with them and compared to the ideal substrate is obviously distinct for $4S_{AD}$, but merely minor or even weakly reversed for the smaller clusters. The changes of E_{ads} for the different surface structures considered in this section until now are similar independently of the halogen. Hence it seems that the relevance of the phenyl group is not to be underestimated.

Introducing molecular vacancies (cf. Fig. 4.11) complicates the discussion. If the halogen enters one of them, the attraction of its negative partial charge may be enhanced at the cost of mitigating the adsorption of the phenyl group. Since both of these opposing effects compete, not only vertical, but also inclined, adsorption has to be considered. Moreover flat-lying adsorption with the halogen close to the molecular vacancy can not be excluded a priori. V_A resp. V_D exhibits one resp. two dangling protons pointing into the single molecular vacancy. V_A-$2S_{AD}$ and V_D-S_{AD} were constructed in an attempt to maximise the aforementioned attraction of the halogen by disordering the protonic subsystem such that each of the three water molecules neighbouring the vacancy possesses a dangling proton. Moreover adsorption at the largest defect complex $2V_DV_A$-$2S_{AD}$ is investigated. Flat-lying adsorption prevails for V_D and V_D-S_{AD}, while V_A and $2V_DV_A$-$2S_{AD}$ feature the inclined mode. The adsorbates tend to stand vertical at V_A-$2S_{AD}$, except for the flat-lying C_6H_5F. Overall the adsorption mode is still virtually independent of the halogen, but varies heavily if a molecular vacancy is involved. Furthermore the investigation demonstrates that it is not generally clear how the halogen electronegativity influences E_{ads} (cf. Tab. 4.5 and Fig. 4.12). As anticipated due to the more advantageous dangling proton order surrounding the vacancy E_{ads} rises for V_A-$2S_{AD}$ compared to V_A, but the opposite eventuates for V_D-S_{AD} compared to V_D. This is consistent with the appendant adsorption modes, which indicate that the former, but not the latter, vacancies harbour the halogen (sole exception flat-lying C_6H_5F at V_A-$2S_{AD}$). $2V_DV_A$-$2S_{AD}$ is by far the deepest electron trap. All previously treated bonding sites and motifs are available there (cf. Fig. 3.6). Additionally it exhibits a unique subsurface dangling proton, while four surface dangling protons point into the quadruple molecular vacancy. Especially due to the proton arrangement geared to it, this heterogeneous

defect complex is expected to enable the strongest adsorption, which turns out to be true except for the tiny preference of C_6H_5F at $4S_{AD}$.

This section has evidenced that the same stabilisation mechanism (Coulomb attraction) is active in excess electron solvation and molecular adsorption of phenyl halogenides. Fig. 4.12 resp. Tab. 4.5 suggests that both phenomena are spatially correlated if this mechanism is sufficiently pronounced, i.e. that deep electron traps are preferred for adsorption. However it is of crucial importance to keep in mind that this alone does not permit to assess the interplay of excess electron solvation and DEA, because the extent to which the substrate modifies the electronic structure of the adsorbate (and vice versa) has not yet been quantified. According to section 4.1 the relative localisation of σ_s^* MOs at the halogen is clearly stronger than for any other type of orbital that might capture an excess electron. Hence it can be expected that adsorption at deep electron traps stabilises these MOs most strongly, while the remaining empty states are affected to a lesser extent. Furthermore as adsorption at these sites is energetically favoured, it should occur even more frequently than indicated by their abundance.

Note that the discussion could be generalised by incorporating superstructures of the ice surface, e.g. based on the systematic investigation of Bockstedte et al. (2016) [61]. These are not treated here, because a reliable approach to adsorption (see section 4.2) resp. DEA (see chapter 5) at them is currently not available due to the complexity of the appendant potential energy landscapes.

Table 4.5.: G_0W_0(PBE0-electronic) ice surface trap depths (EA) compared to DFT(PBE) formation energies E_f and phenyl halogenide adsorption energies $E_{ads}(C_6H_5X)$ involving vdW corrections (explanation see text)

I_h(0001)	EA[eV]	E_f[meV]	$E_{ads}(C_6H_5X)$[meV]		
			X=F	X=Cl	X=Br
ideal/pristine	≈0.00	0	510	435	438
S_{AD}	+0.05	99	514	444	413
$2S_{AD}$	+0.21	356	470	410	350
$3S_{AD}$	+0.29	549	538	468	393
$4S_{AD}$	+0.43	898	773	729	670
V_A	<0.00	200	353	483	377
V_D	<0.00	210	400	359	387
V_A-$2S_{AD}$	+0.33	697	751 (523)[8]	668	631
V_D-S_{AD}	+0.18	396	300	225	294
$2V_DV_A$-$2S_{AD}$	+0.98	1101	772	808	847

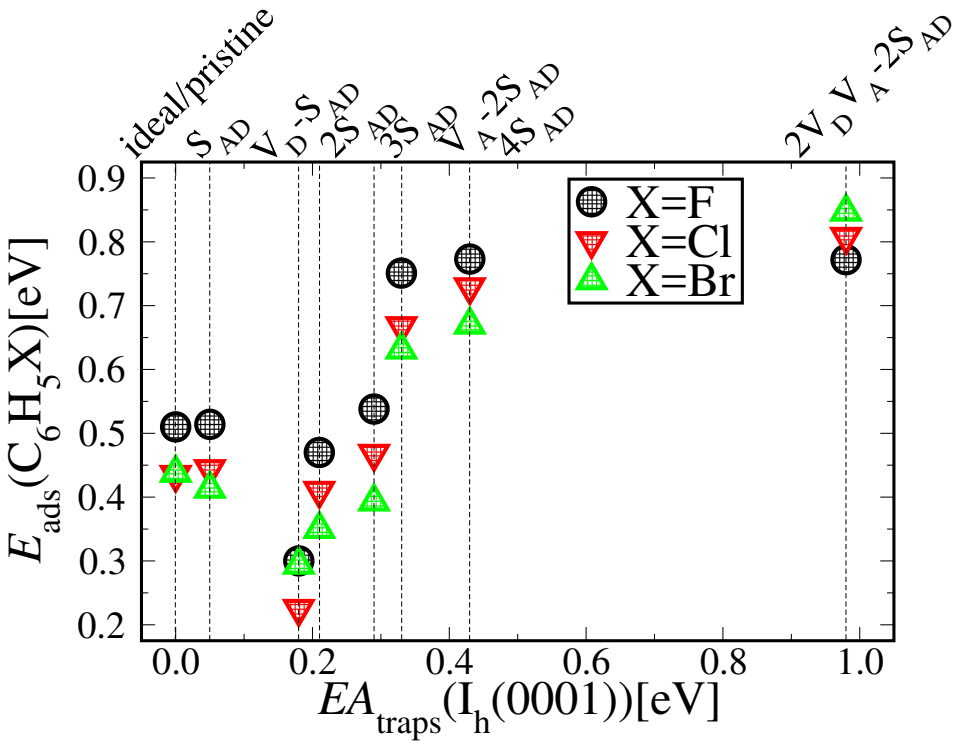

Figure 4.12.: Correlation of G_0W_0(PBEo-electronic) ice surface trap depths (*EA*) and DFT(PBE) phenyl halogenide adsorption energies $E_{ads}(C_6H_5X)$ involving vdW corrections (explanation see text)

4.3. Electronic structure modifications and new trends upon adsorption

The formation of the transient ions is governed by the molecular ground states, because excess electron attachment is rapid compared to nuclear motion. This section serves to demonstrate that adsorption at the ice surface evokes modifications of their electronic structures promoting DEA. For this purpose exemplary and most favourable adsorption sites, that also feature strong electron traps, were selected among those treated in section 4.2. G_0W_0 calculations were performed using improved starting points obtained by electronic relaxation with the PBEo XC-functional (see subsection 2.5.3). After a general discussion of positions and characters of the strongest antibonding resonances of the adsorbed molecules, their local density of states (*LDOS*)

[8] This value belongs to the vertical adsorption mode. This geometry is favoured by both other adsorbates and was used for the subsequent investigation of electronic structures.

and its element-projected components in prototypical cases are considered in detail to elucidate new trends appearing upon adsorption. This general discussion is visualised by Fig. 4.13, which incorporates the correlation with the ice surface electron trap depth (*EA*). Fig. 4.17 to 4.20 contain the quantitative results yielded by the advanced investigation of the *LDOS* at the adsorbate in the range relevant for low-energy excess electron capture. The corresponding system *LDOS* close to resp. below Φ_{vac} is also included, because adsorption at surface traps affects their electronic structure and hence their capability of excess electron solvation. It is not a priori known if a relation between the latter phenomenon and DEA exists. Remember that the ratio between the *LDOS* at the adsorbate and its halogen-projected component is indicative of strongly localised σ_s^* molecular orbitals (MOs)[9]. The mere surface electron trap depth allows no adequate description of the intricate effects of adsorption. Defect type and adsorption mode[10] also have to be taken into account. Fig. 4.14 to 4.16 serve to clarify this issue, particularly by demonstrating that the arising trends are largely independent of each other and the respective halogen. The vacuum results (scGW$_0$(PBE0), see section 4.1) are added for comparison. By analogy with Fig. 4.3, Fig. 4.22 is an example conveying a fundamental impression of the ratio of local to total density of occupied and empty states.

Adsorption lowers the strongest molecular resonances and this effect tends to increase with the trap depth, whereby σ_s^* MOs are by far most affected (cf. Fig. 4.2, 4.13, besides cf. Tab. 4.3, 4.4). These findings are explained by the bonding motifs discussed in the section 4.2: adsorption of the phenyl group at the surface due to hydrogen bonds and dispersion forces and attractive Coulomb interaction between the negative partial charge of the halogen and (surface) dangling protons. Judging from the orbital geometries, the *LDOS* and its element-projected components for the molecules in vacuum (see section 4.1), the former motif mainly concerns π^* states, while the latter prefers σ_s^* states. Hence the especially pronounced stabilisation of σ_s^* resonances is conceivable, because section 4.2 has evidenced that attraction of the negative

[9] In this energy range the *LDOS* at the adsorbate is dominated by strongly localised MOs of four different types, which occur with comparable frequencies as apparent from an inspection of the partial charge density distributions (like for the gas phase molecules, see section 4.1). The relative localisation of σ_s^* MOs at the halogen is clearly larger than for any other type of MO that might capture an excess electron (like for the gas phase molecules, see section 4.1).

[10] Strictly speaking the present study does not isolate these intertwined factors as far as possible from each other, since for each surface structure considered only the most favoured adsorption geometry (see section 4.2) was treated with G_0W_0. For a more precise investigation of this matter it would be very helpful to keep in mind that the qualitative trends given by the Kohn-Sham (KS) energies obtained with the aid of hybrid DFT(PBE0) are already correct (cf. e.g. Tab. 4.2). Therefore the computational expense can be reduced drastically.

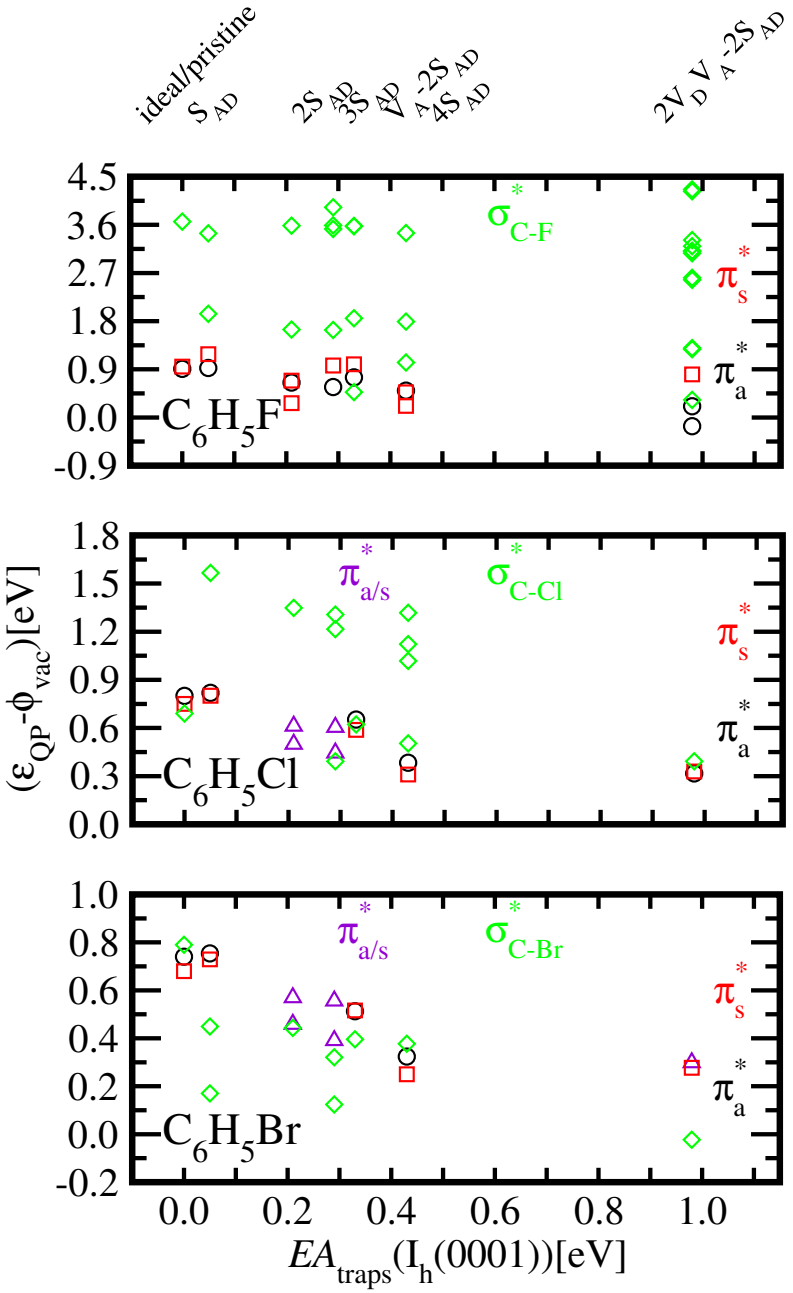

Figure 4.13.: Correlation of ice surface trap depths (*EA*) and position of the strongest resonances of the adsorbed molecules (both from G_0W_0(PBEo-electronic))

partial charge of the halogen is the key aspect of adsorption (at least regarding E_{ads} differences). For the same physical reasons as for the adsorption energy (see section 4.2), the lowering of molecular resonances does not rigorously correlate with the trap depths. Overall Fig. 4.13 demonstrates that considering deeper traps affects the electronic structure of the adsorbed molecules qualitatively similar to using a halogen of higher row, however the relation is not monotone this time (compare to Fig. 4.2 for the molecules in vacuum). Contrary to their vacuum analogues, the lowest resonances of the adsorbed molecules can be of σ_s^* character [e.g. for C_6H_5Br at the V_D-$2S_{AD}$ defect (cf. Fig. 4.13, 4.19c)]. Chapter 5 will evidence that this drastically reduces or eliminates the energy barriers for DEA in the low-energy range, because an orbital transition of the excess electron is not required anymore.

Fig. 4.14 to 4.16 display how the *LDOS* at the molecule and its halogen-projected component (X-*LDOS*) are modified upon adsorption at different surface structures of increasing trap depth. They evidence consistently that the lowering of σ_s^* states, esp. resonances, correlates with the trap depth as expected. The adsorption geometry has substantial additional influence on $\pi_{a,s}^*$ MOs, whereby the flat-lying mode is most preferred. Furthermore insights given by Fig. 4.13 regarding the (similarity of the) effects of different halogens and traps on the electronic structure of the adsorbed molecules, particularly the positions of the resonances (relative to each other), are corroborated.

Fig. 4.17 to 4.20 show that the qualitative trends regarding (the ratio between) the *LDOS* at the molecule and its element-projected components as well as their dependence on the halogen (see section 4.1) are preserved upon adsorption. In particular the halogen-projected component is indicative of σ_s^* states and a heavier halogen favours excess electron attachment. An essential difference is that the interaction with the ice substrate can pull empty MOs under the vacuum level Φ_{vac}, yet this requires very large defect complexes such as $2V_DV_A$-$2S_{AD}$ (cf. Fig. 4.20). Furthermore the calculations reveal that the electronic structure of the surface trap itself is also substantially affected. The trap states are raised by hybridisation with the MOs. This effect incapacitates originally shallow traps such as V_A-$2S_{AD}$ (cf. Fig. 4.19), i.e. they can not solvate (excess) electrons anymore.

Fig. 4.21 illustrates clearly that the *LDOS* at the molecule depends on the halogen to a much lesser extent than the component obtained from projection onto it. Like for the molecules in vacuum (cf. Fig. 4.8) this component grows rapidly with the row of the halogen, especially at low energies. Since the ratio between it and the *LDOS* is indicative of σ_s^* MOs, the growth signals their rising contribution.

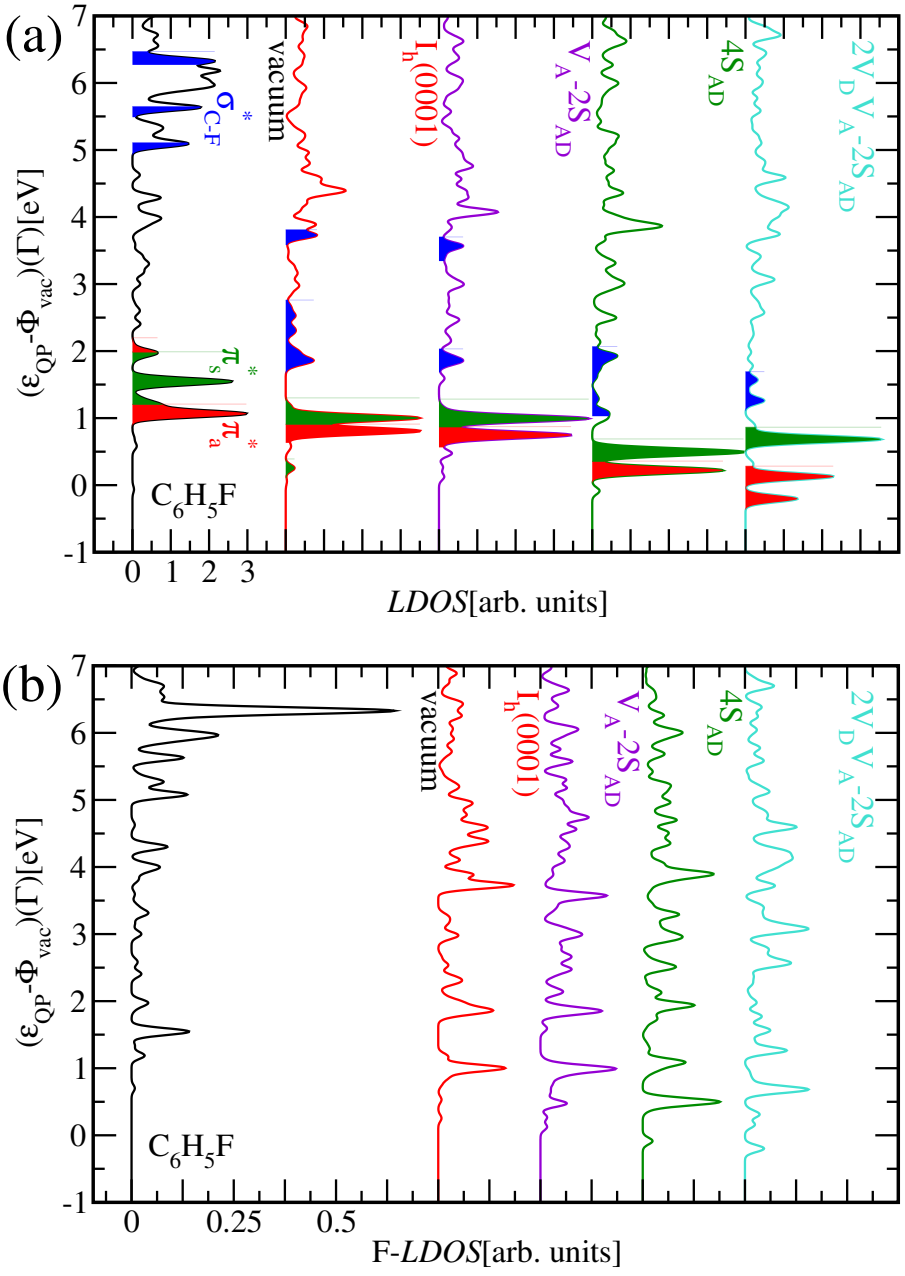

Figure 4.14.: *LDOS* (a) and fluorine-projected component (b) at a C_6H_5F molecule adsorbed at different surface structures on I_h(0001) from G_0W_0(PBE0-electronic), vacuum results from $scGW_0$(PBE0) added for comparison

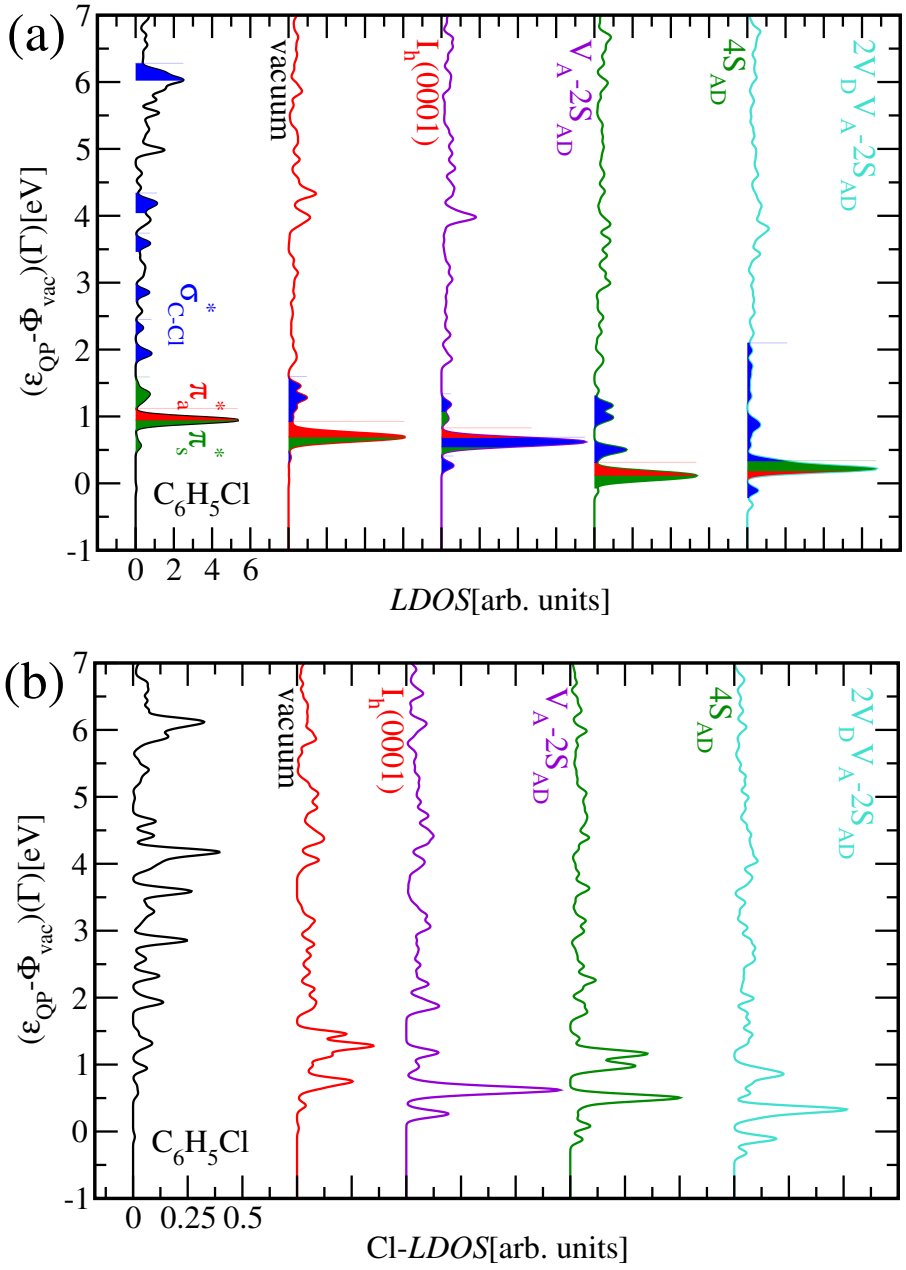

Figure 4.15.: *LDOS* (a) and chlorine-projected component (b) at a C_6H_5Cl molecule adsorbed at different surface structures on I_h(0001) from G_0W_0(PBE0-electronic), vacuum results from scGW_0(PBE0) added for comparison

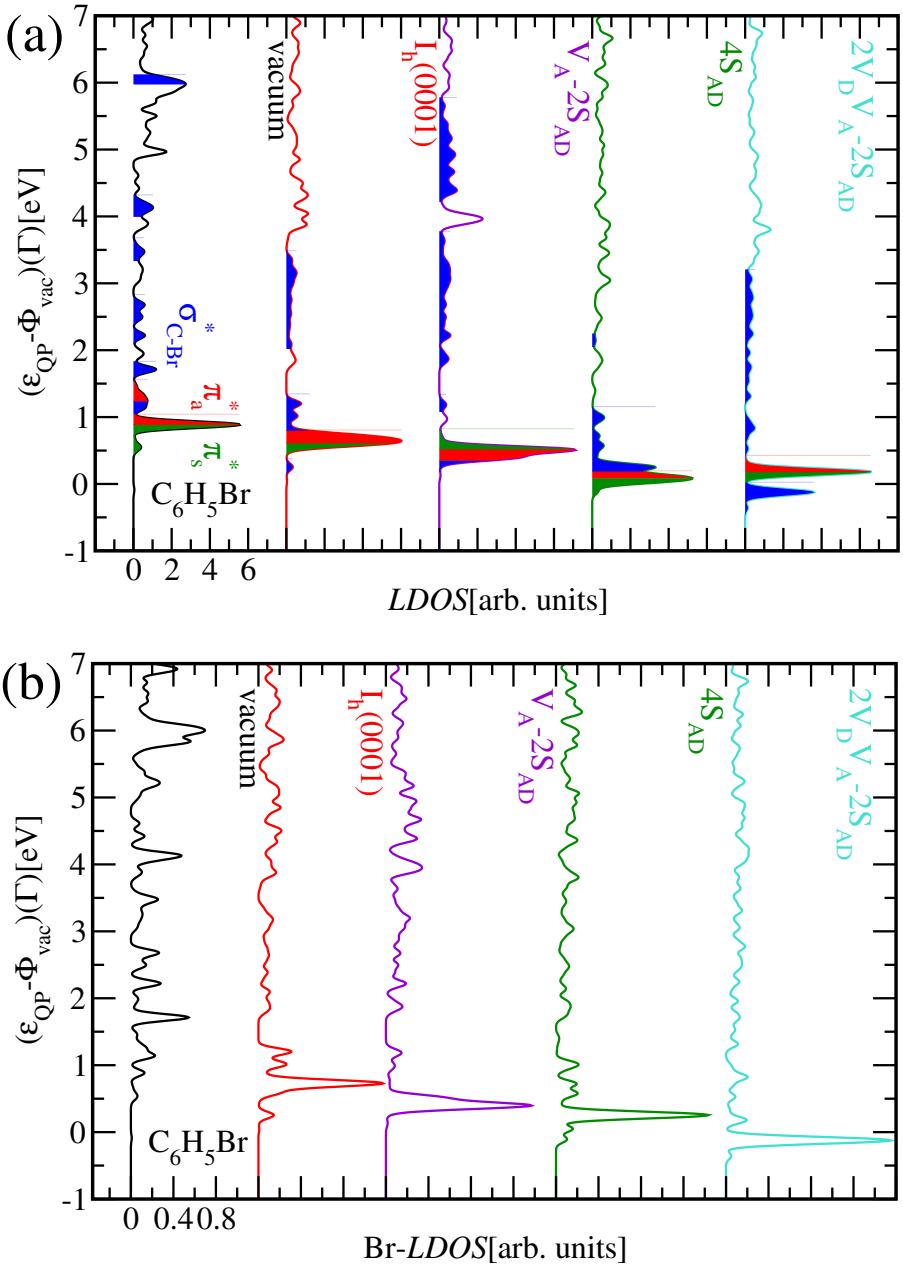

Figure 4.16.: *LDOS* (a) and bromine-projected component (b) at a C_6H_5Br molecule adsorbed at different surface structures on $I_h(0001)$ from G_0W_0(PBEo-electronic), vacuum results from $scGW_0$(PBEo) added for comparison

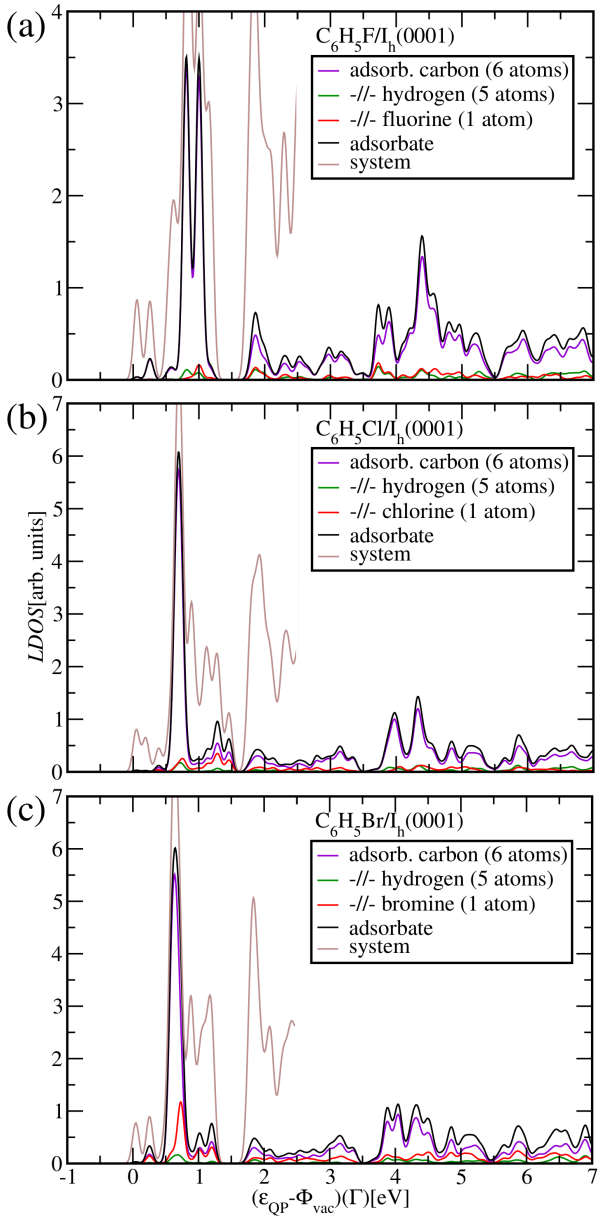

Figure 4.17.: *LDOS* and element-projected components at a (a) C_6H_5F or (b) C_6H_5Cl or (c) C_6H_5Br molecule adsorbed on pristine I_h(0001), system (three intact bilayers, 2x2-supercells) *LDOS* at low energies added to demonstrate the relation between excess electron solvation and DEA, from G_0W_0(PBE0-electronic)

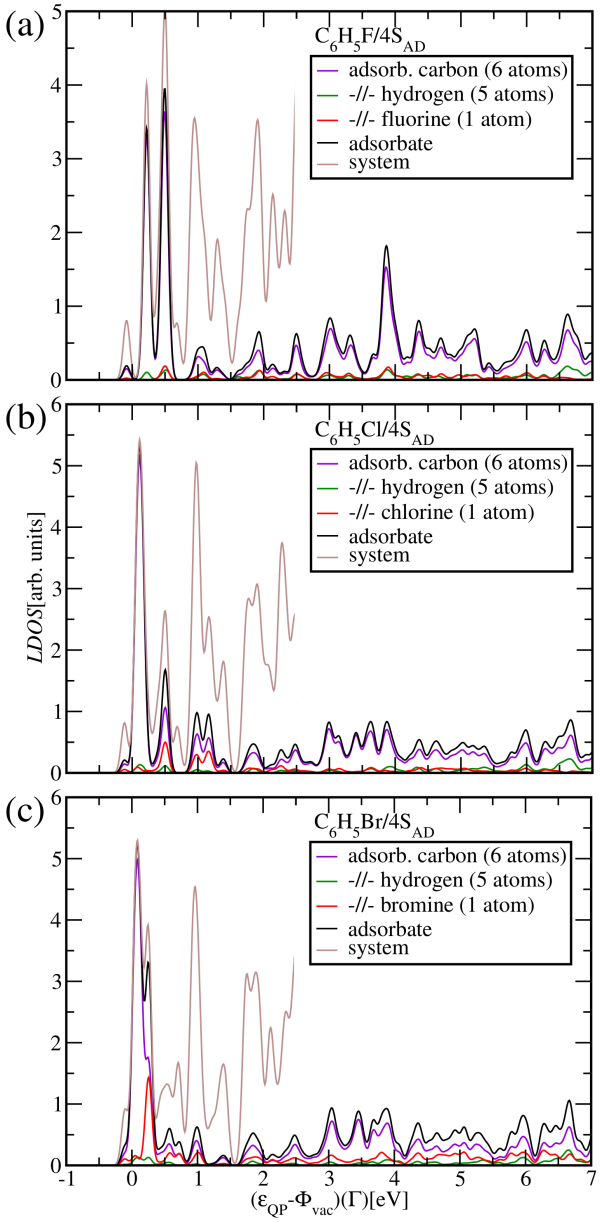

Figure 4.18.: *LDOS* and element-projected components at a (a) C_6H_5F or (b) C_6H_5Cl or (c) C_6H_5Br molecule adsorbed at a $4S_{AD}$ orientational defect complex on I_h(0001), system (three intact bilayers, 2x2-supercells) *LDOS* at low energies added to demonstrate the relation between excess electron solvation and DEA, from G_0W_0(PBE0-electronic)

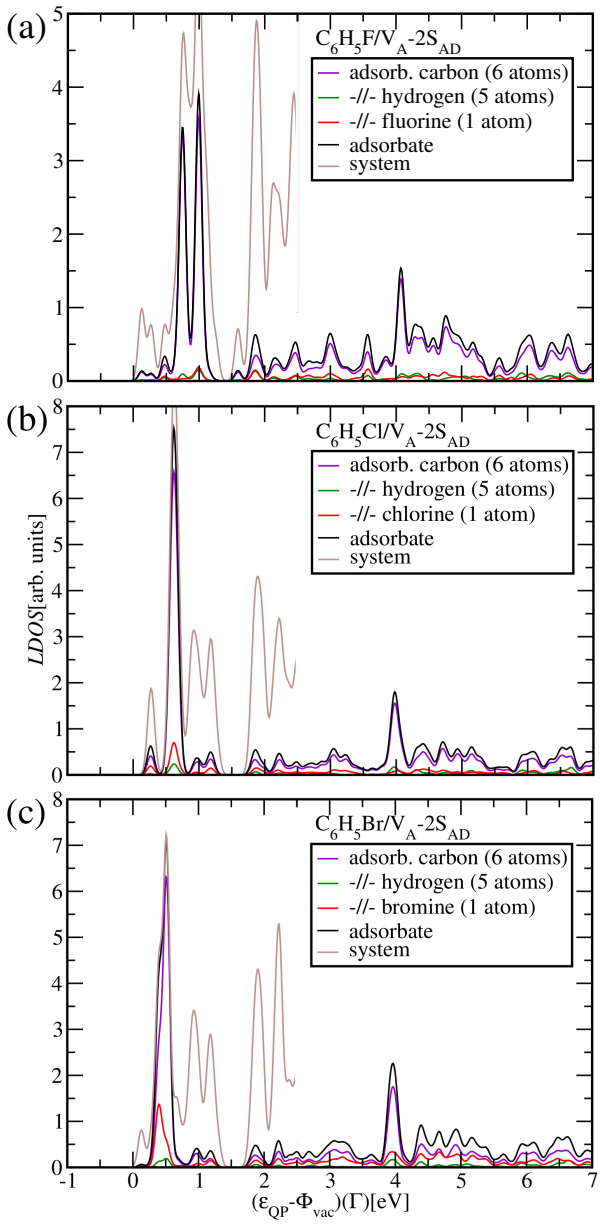

Figure 4.19.: *LDOS* and element-projected components at a (a) C_6H_5F or (b) C_6H_5Cl or (c) C_6H_5Br molecule adsorbed at a V_A-$2S_{AD}$ heterogeneous defect complex on I_h(0001), system (three intact bilayers, 2x2-supercells) *LDOS* at low energies added to demonstrate the relation between excess electron solvation and DEA, from G_0W_0(PBE0-electronic)

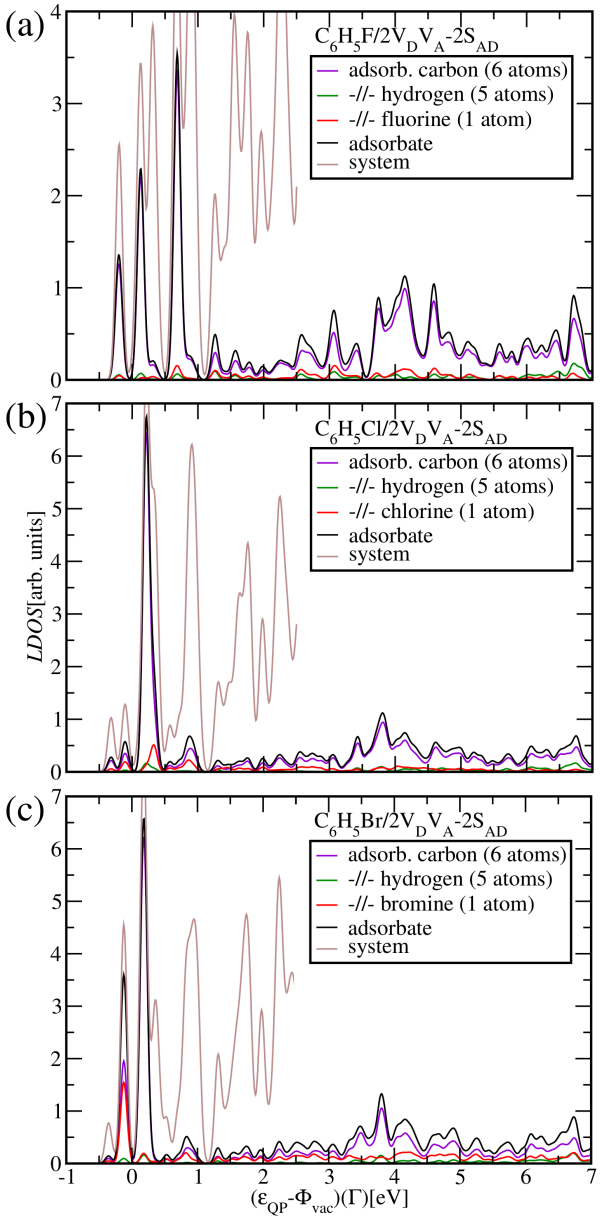

Figure 4.20.: *LDOS* and element-projected components at a (a) C_6H_5F or (b) C_6H_5Cl or (c) C_6H_5Br molecule adsorbed at a $2V_DV_A$-$2S_{AD}$ heterogeneous defect complex on $I_h(0001)$, system (three intact bilayers, 2x2-supercells) *LDOS* at low energies added to demonstrate the relation between excess electron solvation and DEA, from G_0W_0(PBE0-electronic)

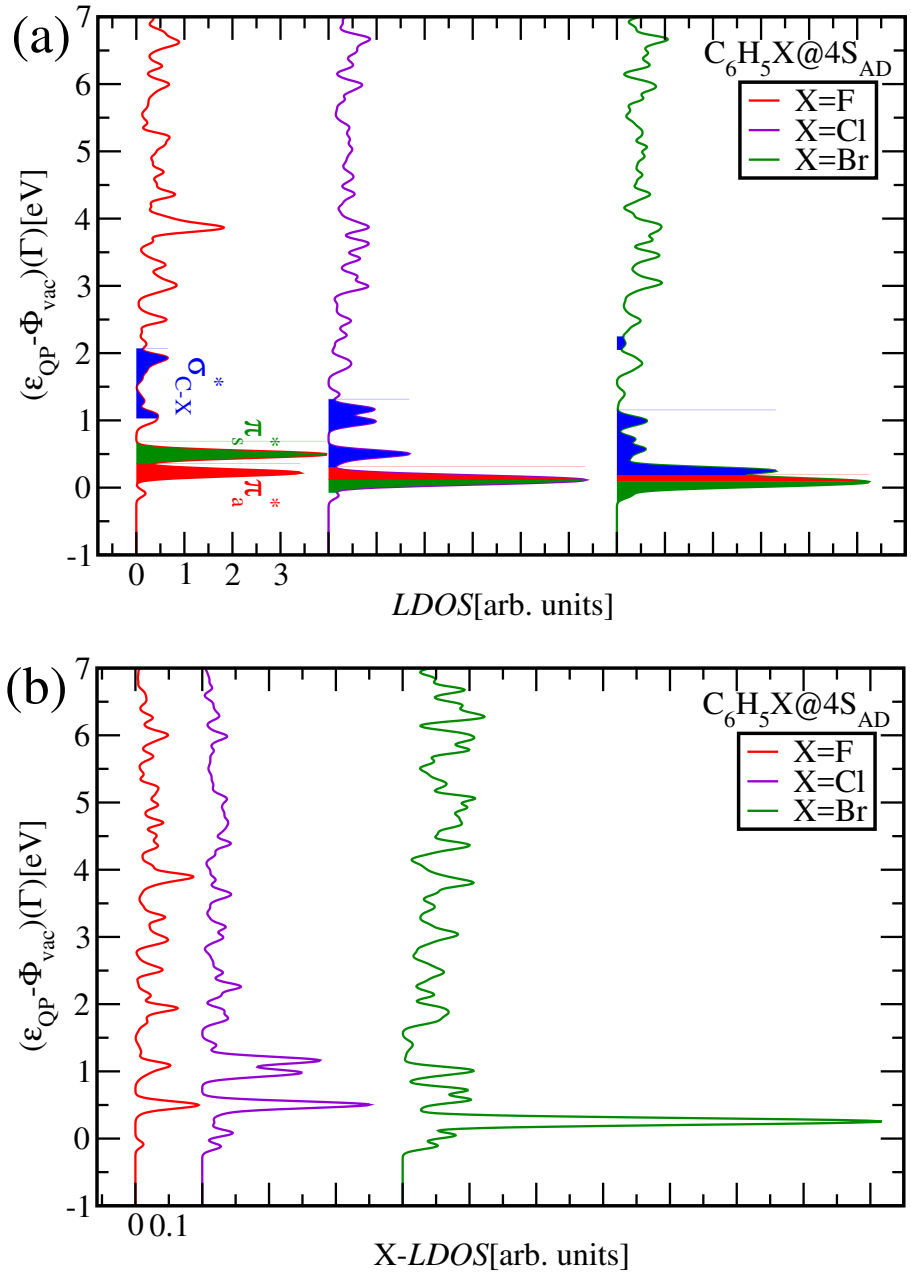

Figure 4.21.: *LDOS* (a) and halogen-projected component (b) at a C_6H_5X molecule with X=F,Cl,Br adsorbed at a $4S_{AD}$ orientational defect complex on I_h(0001) from G_0W_0(PBE0-electronic)

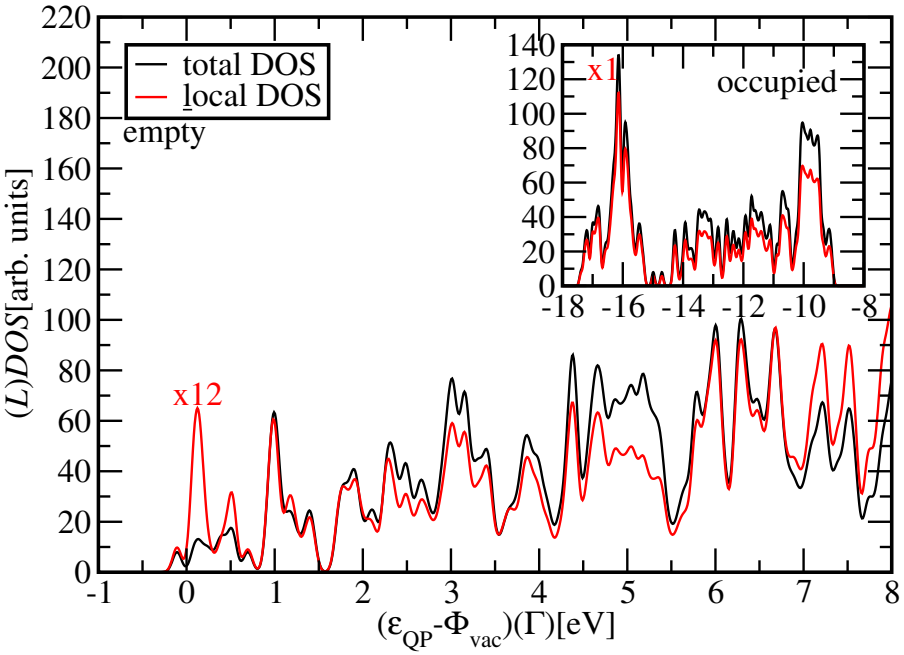

Figure 4.22.: Comparison of total and local density of states ((*L*)*DOS*) of the adsorbate-substrate system phenyl chloride C_6H_5Cl adsorbed at a $4S_{AD}$ orientational defect complex on $I_h(0001)$ (three intact bilayers, 2x2-supercell) from G_0W_0(PBE0-electronic)

Analogously to Fig. 4.3, which gives an example for the molecules in vacuum, Fig. 4.22 provides a fundamental impression of the relation between total and local *DOS* of the adsorbate-substrate systems treated in this study [three or four ice bilayers, 2x2-supercells (see section 4.2)]. The adsorbate-substrate system *DOS* is dominated by the substrate, which for the chosen structure consists of 96 H_2O molecules per supercell featuring 768 valence electrons, while the adsorbed molecule is always comprised of 12 atoms with 36 valence electrons in total. Like for the molecules in vacuum (cf. Fig. 4.3), the occupied states are strongly localised, whereas the localisation of the empty states is mainly weak. Hence strong resonances among the latter can be no more than scarce. Occupied and empty *DOS* are within the same order of magnitude.

The electronic structures obtained for the free and adsorbed molecules are directly comparable despite slightly different simulation parameter values. The adsorbate-substrate systems were originally treated with E_{cut} = 400eV and $E_{cut\text{-}GW}$ = 100eV just as the free molecules (see section 4.1) and 8000 bands[11]. Later increasing $E_{cut\text{-}GW}$ and NBANDS simultaneously to 125eV resp. 10000

[11] 20 frequency points along the real axis, spectral method employed

like for the pure ice surface systems, for which these parameter values have been justified (see section 3.2), was enabled. Due to coinciding supercell geometries, almost identical ice slabs and the very similar number of valence electrons (768 resp. 804 in case of three intact bilayers), it can be assumed that both types of systems are described with nearly equal adequacy. No substantial changes were discovered when using the improved parameter values (electronic energy level shifts $<$0.12eV, mostly much smaller). However to avoid unexpected errors, this was done for explicit modelling of surface dissociation processes [see sections 5.2 and 6.2 (based on the former)], i.e. on pristine $I_h(0001)$ and at the $4S_{AD}$ orientational defect complex. For DEA it will be seen that adsorption modifies the involved potential energy surfaces of the transient ions and their position relative to each other to an extent much larger than that arising from the different simulation parameter values.

4.4. Summary

Since according to GW calculations empty molecular orbitals, which are unbound[12], are redshifted by adsorption at the ice surface, it was found to create conditions favouring excess electron capture by phenyl halogenides as expected due to the polarity of both components. The electron attachment probabilities supposedly increase upon adsorption, because incident electrons, which might then be photoinjected thanks to the substrate, require less kinetic energy. This particularly concerns σ_s^* resonances and to a lesser extent $\pi_{a,s}^*$ resonances, which are generally stronger and lie lower[12]. These results were consistently explained based on the initial situation in the gas phase, bonding motifs, adsorption geometries and corresponding (dispersion-corrected) adsorption energies E_{ads}. Judging from the lowered molecular resonances and their undeteriorated localisation, it could be assumed that adsorption catalyses DEA. However this way of reasoning is incomplete as it does not include the influence of the substrate during the dissociation processes, which also affects their occurrence resp. probability. Hence chapter 5 treats these explicitly.

Investigating the molecules in the gas phase revealed that an adequate description of their geometries (see section D) or electronic structures (see section 4.1) requires a very similar level of theory as the ice systems (see chapter 3). It was ascertained that hybrid DFT(PBE0) produces reliable geometries (see section D), yet this does not pertain to the molecular Kohn-Sham energy levels as the resulting HOMO-LUMO gap is much too narrow throughout owing to both sides, i.e. *IP* and *EA*, which are vertical, despite correct trends

[12] except for adsorption at very large defect complexes

(cf. Tab. 4.1, 4.2). In an attempt to remedy this issue within the original framework constrained CDFT(PBE0) was applied. Both quantities, which had to be extrapolated due to the involvement of charged supercells and computational expense, exhibit very reduced total errors for all molecules and the previously wrong *EA* sign is corrected. While the HOMO position might be considered acceptable (cf. Tab. 4.1), the LUMO is still always too low, except possibly for the (less relevant) case of C_6H_5I, which is partially unclear as the experimental results lack some clarity, and its trend distorted (cf. Tab. 4.2). As this demonstrates the need for many body perturbation theory, $scGW_0$ calculations were performed on top of the original DFT(PBE0). The positions of resonances and highest occupied states are visualised in the $scGW_0$(PBE0) MO diagram (cf. Fig. 4.2) and follow entirely clear trends confirming the measurements with highly accurate quasiparticle energies (cf. Tab. 4.1, 4.2). The HOMO turned out to be of π_s character. With a positive deviation from experiment of merely 0.04-0.08eV for C_6H_5X with X=F,Cl,Br resp. 0.04-0.06eV for C_6H_5I its position is in excellent agreement with the latest PES studies conducted by Palmer et al. (2015/16) [203–205] resp. the older UPS and PIES by Imura et al. (2001) [202] or UPS by Potts et al. (1980) [201]. The position of the π_a MO is 0.43-0.78eV lower growing with the row of the halogen. According to $scGW_0$(PBE0) the character of the C_6H_5X LUMO depends on the halogen: π_a^* (X=F), degenerate π_a^* and π_s^* (X=Cl,Br), σ_s^* (X=I). The corresponding theoretical vertical *EA*s for X=F,Cl,Br are 0.19-0.22eV smaller than the ETS values obtained by Olthoff et al. (1985) [206] and the one of X=I is at least in line with the trends. Altogether the theoretical HOMO-LUMO gaps are only a bit too wide owing to both sides, mainly the *EA*. The positions of the resonances of each character (π_a^*, π_s^*, π_0^*, σ_s^*) confirm the trends found by the aforementioned experimental study, namely that using a heavier halogen surprisingly lowers the resonances, whereby those of σ_s^* type are by far most affected, and straitens the bonding-antibonding state gaps from both sides, and a more comprehensive picture corroborating them is drawn and consistenly explained based on the underlying physics. The total deviations are very small except for π_0^* resonances, which is tolerable since these are only of very minor relevance for the subsequent investigations.

The empty MOs are scattering states among which strong resonances occur for each phenyl halogenide. However these are scarce, because the overall localisation is very weak (cf. exemplary Fig. 4.3).

For the gas phase, the *LDOS* at the molecule, its element-projected components and the MO characters associated with its most distinct peaks (cf. Fig. 4.4 to 4.8) corroborate the electron transmission spectroscopy (ETS) experiments of Olthoff et al. (1985) [206] (cf. Tab. 4.2) and further studies of

C_6H_5Cl [41, 45, 207, 208] and C_6H_5Br [209] also applying ETS and stating that the highest electron attachment cross sections are exhibited by π_a^* and π_s^* resonances. The sole exception is made by C_6H_5I, which possesses a lower σ_s^* resonance. Based on the same data these can also be expected to have the longest TNI lifetimes. The similarity of the analogous results for the adsorbates (see section 4.3) evidences that this situation is also present on the ice surface. Choosing a heavier halogen shifts the relevant *LDOS* at the molecule slightly towards lower energies and causes only small curve shape changes, except for cancelling the obvious splitting of dominant π_a^* and π_s^* resonance distinguishing C_6H_5F. Consistently with the particularly strong lowering of σ_s^* resonances, the halogen-projected component experiences a much larger shift in this direction and grows rapidly, most of all at lower energies.

The neglect of GW selfconsistency for the adsorbate-substrate systems was forced due to limited computational resources, but could be justified based on estimates (cf. Tab. 4.3, 4.4, besides Fig. 3.3 and Tab. 3.1, 3.2) demonstrating that the errors are tolerable and the trends remain unchanged.

According to gradient DFT(PBE) with Grimme-D2 dispersion corrections adsorption of phenyl halogenide molecules on the ice surface is substantially influenced by several points and obeys some general tendencies. Their adsorption energies E_{ads} correlate with the electron trap depths *EA*, particularly for strong traps, which are most favoured (cf. Fig. 4.12 and Tab. 4.5). Like the *EA*s and trap formation energies E_f, E_{ads} is typically in the range of some hundreds of meV. Flat-lying adsorption with the halogen situated on top of a surface dangling proton is preferred unless molecular vacancies (V_A, V_D) are involved. Positioning the phenyl group such that the carbon-halogen (C-X) bond lies parallel to the respective intact Fletcher stripe was found to be an at least very close to ideal choice throughout, regardless of the number of orientational (S_{AD}) defects. Introducing a molecular vacancy tremendously complicates the situation. The vertical adsorption mode is favoured if the vacancy is sufficiently attractive for the halogen. This depends on its geometry as well as complexation with orientational defects. These findings are to a large extent explained by the similarity between excess electron solvation and attraction of the negative partial charge of the halogen, which are both contingent on (surface) dangling protons. It was demonstrated that this bonding motif is the key aspect of adsorption. The hence motivated supposition that E_{ads} grows if a more electronegative halogen is chosen holds true unless molecular vacancies are considered, except for a marginal violation in the case of the pristine surface. The other competing bonding motif is the adsorption of the phenyl group at the surface, which is enhanced if the adsorbed molecule lies more flat. For the largest defect complex the inclined mode presumably

eventuates due to this competition. Changing the halogen left the adsorption mode virtually unaffected. Grimme-D2 scheme dispersion corrections were applied to recalculate the adsorbate geometry and total energies in view of the adsorbate-substrate dispersion interaction. The already discovered tendencies are substantially reinforced by the consequently raised E_{ads} values, while no qualitative changes appear.

G_0W_0(PBE0-electronic) evidences that the modifications of the molecular electronic structures upon adsorption indeed promote excess electron attachment. The redshift of the strongest molecular resonances (compare Fig. 4.2 and 4.13) is consistent with the *LDOS* at the molecule, its element-projected components, the adsorption energies and their relation to the bonding motifs. It tends to increase with the trap depth *EA* (cf. Fig. 4.13), yet for the same physical reasons as for the adsorption energies there is no rigorous correlation. σ_s^* resonances are by far most affected. This is conceivable based on the insight that the attractive interaction between the negative partial charge of the halogen and surface dangling protons is the key bonding motif and the underlying knowledge obtained from the investigation of the gas phase molecules. The latter also helps to explain that the (less pronounced) redshift of $\pi_{a,s}^*$ resonances additionally correlates with the adsorption mode if it is taken into account that the adsorption of the phenyl group at the ice surface is fostered if the adsorbed molecule lies more flat. Contrary to the gas phase, σ_s^* resonances lower than the $\pi_{a,s}^*$ resonances, but still above Φ_{vac}, were found for C_6H_5Br and C_6H_5Cl in some cases [e.g. for C_6H_5Br at the V_D-$2S_{AD}$ defect (cf. Fig. 4.13, 4.19c) or for C_6H_5Cl at the $3S_{AD}$ defect (cf. Fig. 4.13)]. Chapter 5 will discuss that an excess electron captured by one of these can act dissociatively without undergoing internal conversion (at a conical intersection) and that this greatly reduces or eliminates the necessary activation energy. According to Fig. 4.17 to 4.20, which display results for the most basic and prototypical structures, the qualitative tendencies regarding the influence of the respective halogen and the ratio between the *LDOS* at the molecule and its element-projected components are preserved for the empty molecular states upon adsorption. Furthermore it is found that bound empty MOs occur at large defect complexes and that the hybridisation with the MOs blueshifts the trap states. Thus originally shallow traps are incapacitated. To illustrate the consistency of the crucial insights for each adsorbate more clearly, Fig. 4.14 to 4.16 display the *LDOS* at it, with the MO characters indicated where they are relevant for low-energy DEA, and its halogen-projected component, aiding to identify σ_s^* states, arranged according to the trap depth. The corresponding results for the gas phase molecules have been added for comparison. The exemplary Fig. 4.21 serves analogously to demonstrate that the choice

of a more electronegative halogen affects the electronic structures of the adsorbed molecules in the same way as for their gas phase counterparts, which is qualitatively similar to the tendency revealed by considering deeper traps.

5. Dissociative electron attachment to C_6H_5X

This chapter focuses on the modelling of prototypical reactions to evidence that dissociative electron attachment (DEA) to halocarbons is favoured upon their adsorption at the ice surface, particularly if preferably strong excess electron traps are present. Beginning with structures selected from those treated in chapter 4, the influence of the substrate during the dissociation is incorporated. Thereby the activation energy or bond elongation required to enable or complete the process is quantified and confirms the expectations. Together with the favourable electronic structure modifications discovered in chapter 4 this speaks for catalysis and enhanced probabilities of dissociation following electron capture. Furthermore it turns out that choosing a heavier halogen has similar effects.

As the empty molecular orbitals (MOs) of the (free or adsorbed) phenyl halogenide molecules are unbound[1] (see chapter 4), excess electron capture leads to transient negative ions (TNIs), because these can not be stabilised by photon emission (radiative stabilisation [38]). Hence the excess electron must either undergo autodetachment (AD), i.e. remission, or act dissociatively ($\rightarrow$ DEA) so that it finally occupies a newly created resp. stabilised state below the vacuum potential Φ_{vac}. Section 5.1 discusses the calculations for the free molecules and that their results are consistent with the literature on gas phase experiments. Section 5.2 is about the essentially analogous theoretical investigation of the adsorbates within the ab-initio DFT+GW framework.

Low-energy DEA is assumed to produce a singly negative halogen carrying the excess electron and the phenyl group. In appropriate gas phase experiments it has been observed that the charged ion current is constituted almost exclusively by the charged halogen (see section 5.1). The carbon-halogen (C-X) bond distance d is elongated and serves as the configuration coordinate for the dissociation pathway of free and adsorbed molecules. This enables a direct comparison allowing to judge the influence of the ice substrate during the dissociation.

[1] except for adsorption at very large defect complexes

$$\begin{array}{l} \qquad\qquad\qquad\qquad\qquad\qquad\qquad\qquad\qquad\qquad \xrightarrow{\text{DEA}} C_6H_5 + X^- \\ C_6H_5X + e^- \left(\xrightarrow{\text{TNI}} C_6H_5X^{-*} \right) \qquad\qquad\qquad\qquad\qquad\qquad\qquad\qquad \forall\ X{=}F, Cl, Br, I \\ \qquad\qquad\qquad\qquad\qquad\qquad\qquad\qquad\qquad\qquad \xrightarrow{AD} C_6H_5X + e^- \end{array} \tag{5.1}$$

The molecular orbital character of the excess electron generally has to change during low-energy DEA (except for C_6H_5I). This becomes obvious in view of reaction equation (5.1) and the electronic structure results from chapter 4. Intramolecular electron transfer from the phenyl group to the halogen has to take place [41]. After starting with phenyl chloride C_6H_5Cl based on experimental observations [210], the schematic anionic potential energy curves diagram Fig. 5.1 has been established for the gas phase by several experimental and theoretical studies (see section 5.1). The effect of the ice surface on its applicability is discussed in section 5.2. The excess electron is captured by a $\pi^*_{a,s}$ shape resonance. Activation energy E_A is required to elongate the carbon-halogen (C-X) bond until a conical intersection with a σ^*_s resonance is reached. Then the character of the singly occupied molecular orbital (SOMO) may be changed from $\pi^*_{a,s}$ to σ^*_s by internal conversion (IC). No mixing of these states occurs along the postulated dissociation pathway in vacuum, because it maintains the original C_{2v} symmetry of the molecules [41]. Note that the adsorbed molecules also stay at least close to C_{2v}-symmetric.

The simulation parameter values were already discussed in chapter 4. Remember that the vacuum scGW$_0$(PBE0) calculations were not repeated as examinations revealed no important changes, but the improved set was employed on the adsorbate-substrate G$_0$W$_0$(PBE0-electronic) to avoid unexpected errors.

The neglect of GW selfconsistency for the surface systems has been debated in chapters 3 and 4. Judging from the latter, the surface DEA processes might occur even more frequently than evidenced in this chapter. A completing strategy serves to demonstrate that the correct mechanism of DEA to the adsorbed molecules is predicted despite this neglect (see appendix section E).

5.1. Gas phase lowering of sigma resonances and activation energies

Irradiating gas phase phenyl halogenide molecules with electrons leads to collisions, i.e. TNIs can be created. These must decay by either AD or DEA. In the former case the reaction is a scattering process. It may be inelastic, because a change of the SOMO coupled to the vibrational (medium infrared range)

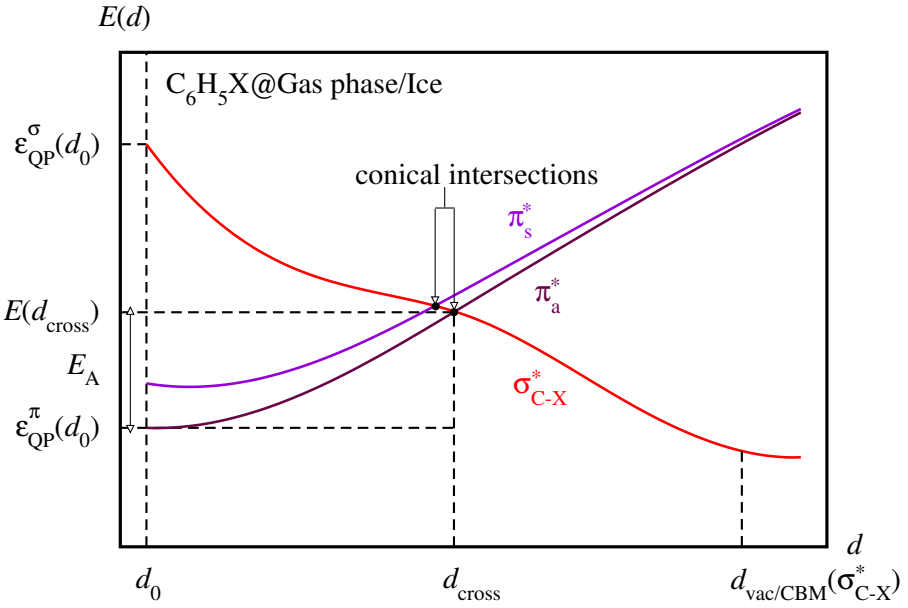

Figure 5.1.: Scheme of the anionic potential energy curves involved in low-energy DEA to phenyl halogenide molecules

and/or rotational (finer structure) molecular degrees of freedom can occur before remission of the excess electron. DEA is fully inelastic insofar as that the educt and product species differ from each other. In the low-energy range it can generally not proceed unless sufficient activation energy is provided, typically by vibrational excitations.

The attenuated transmitted electron current resp. its first derivative and the negative fragment ions formed can be detected as a function of the kinetic energy of the incident electrons. The former is measured with electron transmission spectroscopy (ETS), while abundance, velocity and charge-to-mass ratio of the latter are analysed mass spectrometrically employing time-of-flight mass spectrometry (TOFMS). Dissociative electron attachment spectroscopy (DEAS) determines the total anion current. These complementary spectroscopic methods yield spectra of the charged product species exhibiting consistent characteristics. The attenuation of the transmitted electron current is maximised (locally) at the positions of the molecular resonances with peak widths of some hundreds of meV. At only very slightly lower energies (shifts $\leq$0.1eV) this also pertains to the production of negative fragment ions [[45], [41] (shifts $\leq$0.03eV for C_6H_5Cl)], except if the activation energy is not available. Note that these peaks might exhibit significant asymmetry and their overlap can hamper the interpretation of results.

Spectra of the negative fragment ions have been measured for C_6H_5X with X=Cl,Br,I. Christophorou et al. (1966) [44] obtained these at room temperature by TOFMS and a combined swarm-beam method (including corrections resulting from the combination) to cause the collisions, except for C_6H_5I, for which only beam data was produced. The DEA cross sections peaked at E_{DEA}=0.86eV for C_6H_5Cl (cross section $1.4{\cdot}10^{-17}cm^2$), 0.84eV for C_6H_5Br ($9.6{\cdot}10^{-17}cm^2$)[2] and 0.00 resp. 0.38eV for C_6H_5I (absolute cross sections not given). These results were incorporated by Steelhammer and Wentworth (1969) [39] to demonstrate correlations between complementary data from electron (swarm-)beam and thermal electron attachment studies. With the aid of parameter values obtained by measurements of the latter type at θ=30-240°C, they used empirical potential energy curves to calculate the cross sections of DEA depending on the incident excess electron kinetic energy and reveal its mechanisms. Their model ascribes the captured excess electron either to the phenyl group or to the halogen, whereby the energetically favourable choice depends on the C-X bond elongation resp. the interaction between these moieties, implying that the dissociation processes involve intramolecular electron transfer (from the phenyl group to the halogen), except possibly for C_6H_5I. Good agreement between theoretical and experimental relative cross section distributions was found for C_6H_5Cl and C_6H_5Br. Only the analysis of C_6H_5I yielded a major mismatch regarding the kinetic energy the incident electron has to possess. This molecule seems to be fundamentally different from the others, since the aforementioned intramolecular electron transfer is not required according to their calculations. However no reason for the observation of two peaks was found. Overall increasing the row of the halogen lowered the potential energy curve(s) of the dissociating charged molecule relative to the neutral curve, explaining the lower resonances and enlarged cross sections. Despite this, it seems suspicious, that E_A (cf. equations (5.2)) for X=Cl,Br would be nonexistent resp. negative according to these curves. Shimamori et al. (1995) [40] applied the pulse-radiolysis microwave-cavity method combined with microwave heating to measure the DEA rate constants of the phenyl halogenide molecules with Xe as buffer gas at room temperature in the mean electron energy region between 0.04eV and ≈2eV. These were converted into the corresponding cross section distributions by an unfolding procedure. They obtained the peak positions E_{DEA}=0.7eV for C_6H_5Cl (cross section $5.5{\cdot}10^{-18}cm^2$), 0.30eV for C_6H_5Br ($1.2{\cdot}10^{-17}cm^2$) and ≤0.04eV for C_6H_5I ($\geq 6.4{\cdot}10^{-15}cm^2$). Dissociation of C_6H_5F was not observed in this energy region. In consequence of the similar differences between their values for DEA peak positions and exothermicities, it was surmised

[2] C_6D_5Br (fully deuterated phenyl bromide) yielded 0.80eV ($10.4{\cdot}10^{-17}cm^2$).

that the curvature of the potential energy $E(d)$ of the (dissociating) charged molecule is widely independent of the halogen (excluding fluorine). However as this would then also apply to the activation energies E_A, the present results demonstrate that it is an oversimplification.

All mass spectrometrical studies of DEA to gas phase phenyl halogenide molecules found that the charged ion current in the low-energy range is constituted essentially by the respective singly negative halogen [41,44,211–213]. The halogen is most favourable for the excess electron, because it exceeds any other chemical element contained in the molecule in electron affinity (and also electronegativity). Insofar it is also superior to the phenyl group [40]. In contrast to the carbons, who possess three conjugates, it can be separated from the molecule by breaking only one bond.

The dissociation dynamics of the benzyl chloride radical TNI ($C_6H_5CH_2Cl^{-*} \rightarrow C_6H_5CH_2 + Cl^-$) were modelled by Fontanesi et al. (2001) [55]. Their ab-initio DRC (dynamic reaction coordinate) analysis yielded a conical intersection between the lowest π and $\sigma^*_{C\text{-}Cl}$ anionic potential energy surface calculated as a function of the C-Cl bond elongation and the rotational angle between the chlorine and the $C(sp^2)$-$C(sp^3)$ bond. They were able to find that DEA starting from a conformer with the chlorine in the plane of the phenyl moiety proceeds through this conical intersection, because their method traces the reaction path. In contrast to this typically aromatic behaviour rotating the methyl chloride moiety by 90° around the $C(sp^2)$-$C(sp^3)$ bond led to dissociation without internal conversion as typical for aliphatic compounds. Assigning increasing amounts of energy to molecular vibrational or rotational modes barely influenced the aliphatic behaviour, but accelerated the aromatic dissociation significantly. While the model is quite comprehensive, a particular drawback consists in the level of theory [Hartree-Fock approximation (HFA, see subsection 2.5.1) for DRC calculations, single-point Møller-Plesset (MP) perturbation theory calculations]. E.g. greatly varying vertical *EA* values (-2.3eV to -0.8eV with -1.7eV from the HFA) were obtained for the lowest π^*_s MO of the conformer dissociating without internal conversion. Only a single-point open-shell MP calculation with an extended basis set controversially including diffuse orbitals brought the results close to the measured value (-0.65eV).

Feng and Tian (2016) [42] performed molecular dynamics simulations based on hybrid DFT(B3LYP) and the ADMP (atom-centered density matrix propagation) method to describe DEA to 1-chloroalkyl benzenes $C_6H_5(CH_2)_nCl$ with n=0,1,2,3,4. This includes C_6H_5Cl (n=0). Their ab-initio approach indeed yielded the aforementioned scenario. A vertical attachment energy (*VAE*) of 0.78eV resulted from the total energy difference between

TNI and neutral molecule. This value is comparable to the measured 0.73eV and the 0.94eV calculated here with scGW$_0$(PBE0) for the position of the $\pi^*_{a,s}$ main resonance (cf. Tab. 4.2). Furthermore a dissociation limit of 0.77eV was obtained. It equals the negative exothermicity -E^{DEA}_{EXO} (cf. Fig. 5.2) by definition. The experimental value is somewhat smaller (0.599(8)eV, cf. Tab. 5.2) and the present study found a similar total energy of the TNI at 50% C-X bond elongation ($E(\sigma^*_s)(d = 1.500d_0)$=0.6606eV from scGW$_0$(PBE0) and underlying DFT(PBE0), cf. Tab. 5.2). Both quantities will be discussed shortly afterwards. However the predictive capability of the model at this level of theory is seriously limited, because a very large empirical blueshift (1.00eV) of the SOMO had to be introduced in view of deviations from the experimental electron affinities, in particular to ensure that they are negative.

The need for an empirical energy shift of the SOMO resp. the empty states is a general problem of earlier studies conducted within the DFT framework [42,54,55]. The reliability of the positions of the conical intersections (relative to Φ_{vac}) is questionable, because it was not investigated if the shift is constant along the dissociation pathway or for different (types of) states of the excess electron.

This section validates the (projector-augmented) plane wave periodic supercell DFT+GW approach for DEA to the molecules in the gas phase. Employing a plane wave basis set (see section 2.2 and also 2.4 (PAW)) allows to treat states of greatly varying localisation, esp. delocalised states whose description with embedded clusters would necessitate a controversial extension of the basis set with diffuse orbitals. Hence only the presented approach comes in question for DEA to the molecules adsorbed on the ice surface (see section 5.2).
Fundamental insight on the energetic requirements of electron-induced dissociation of the free molecules according to reaction equation (5.1) is given by the exothermicity E_{EXO}, which is the potential energy difference between educts and products. Choosing the neutral molecule and the incident electron as educts leads to $E^{DEA}_{EXO} := EA - E_{BF} = -E(\sigma^*_s)(d \to \infty)$ (cf. Fig. 5.2). Should it be negative, its absolute value is a dissociation limit, i.e. a lower boundary for the energy needed to induce DEA[3]. Tab. 5.2 lists the values of the relevant observables. Theoretical C-X bond fission energies E_{BF} could be evaluated based on DFT(PBE0) potential energies, whereby spin-polarisation had to be taken into account for the neutral fragments. Like the experimental results, which are well reproduced (absolute deviations 0.04-0.18eV), they confirm the trend expected considering the electronegativity difference between C and X. The halogen electron affinities EA could not be calculated on the GW

[3] This energy essentially has to be provided by molecular vibrations and the motion of the incident electron in the barycentric system.

Table 5.1.: Experimental peak energies (E_{DEA}) and appendant cross sections ($\sigma(E_{\mathrm{DEA}})$) ascribed to DEA to gas phase phenyl halogenide molecules according to reaction equation (5.1) ([40, 41, 44, 45] discussed in the text)

C_6H_5X	E_{DEA}[eV]	$\sigma(E_{\mathrm{DEA}})$[cm^2]	$\sigma/\sigma_{\max}$
X=F			
Milhaud (1985) [211]	6.1	—	—
Fenzlaff and Illenberger (1984) [212]	6.3	—	—
X=Cl			
Modelli and Venuti (2001) [41]	0.75	—	—
Asfandiarov et al. (2000) [213]	0.74	—	—
Shimamori et al. (1995) [40]	0.7	$5.5{\cdot}10^{-18}$	—
Stricklett et al. (1986) [45]	0.72(54)	$2.7(5){\cdot}10^{-17}$	—
Milhaud (1985) [211]	0.32	$5.9{\cdot}10^{-19}$	3.0%
	0.77	$1.97(30){\cdot}10^{-17}$	100%
Dressler et al. (1985) [214]	0.75	—	—
Christophorou et al. (1966) [44]	0.86	$1.4{\cdot}10^{-17}$	—
X=Br			
Shimamori et al. (1995) [40]	0.30	$1.2{\cdot}10^{-17}$	—
Milhaud (1985) [211]	$\approx$0.3	—	—
	0.65	—	—
Christophorou et al. (1966) [44]	0.84	$9.6{\cdot}10^{-17}$	—
X=I			
Shimamori et al. (1995) [40]	$\leq$0.04	$\geq 6.4{\cdot}10^{-15}$	—
Christophorou et al. (1966) [44]	0.00	—	100%
	0.38	—	23%

level[4], however they were measured with extremely high precision. $E_{\mathrm{EXO}}^{\mathrm{DEA}}$ deduced from the experimental values increases with the row of the halogen and is negative, except for C_6H_5I. However if the interest is directed towards the chemical part of the reaction, the consideration has to start from the initial TNI. $E_{\mathrm{EXO}}^{\mathrm{TNID}} := \varepsilon^{\mathrm{SOMO}}(d_0) + E_{\mathrm{EXO}}^{\mathrm{DEA}}$ (cf. Fig. 5.2) is equal to the difference between the activation energies E_{A} for the backward and forward reaction[5]. Hence it is positive resp. negative if the forward resp. backward reaction is energetically favoured. Dissociation arising from electron capture by the $\pi^*_{\mathrm{a,s}}$

[4] Neither spin-polarised nor charged GW turned out to be reliable.

[5] In contrast to $E_{\mathrm{EXO}}^{\mathrm{DEA}}$, $E_{\mathrm{EXO}}^{\mathrm{TNID}}$ additionally depends on the energy of the molecular resonance capturing the incident electron.

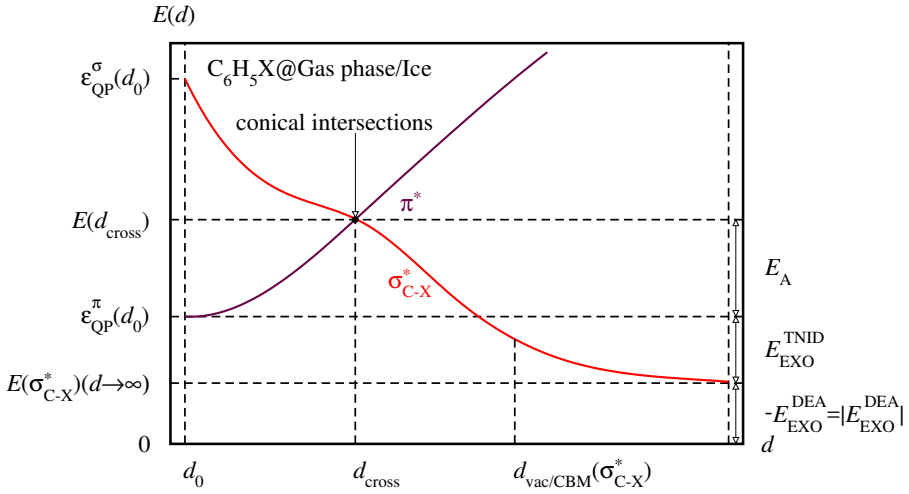

Figure 5.2.: Exothermicity scheme for low-energy electron-induced dissociation of phenyl halogenide molecules: Depending on the chosen starting point two different exothermicities E_{EXO}^{DEA} [$C_6H_5X+e^-$ (dissociative electron attachment)] and E_{EXO}^{TNID} [$C_6H_5X^{-*}$ (transient negative ion dissociation)] are defined.

main resonances is more favourable if a heavier halogen is involved (cf. Tab. 5.2). The appendant experimental E_{EXO}^{TNID} is positive, except for C_6H_5F. Generally the molecular electronic structure of course leads to further constraints that were and will be discussed.

To develop an adequate foundation for the subsequent scGW$_0$ calculations, different (relative) C-X bond elongations were examined employing the underlying DFT(PBE0). Full relaxations of the neutral molecules keeping these fixed yielded only very minor changes of the phenyl group geometry, indicating that mere electronic relaxations would have been sufficient already. Assuming that the fragments created are electrically neutral like the system itself would imply the emergence of local spin-polarisation due to their odd number of (valence) electrons. As expected in view of the Coulomb barrier this effect was found in spin-polarised calculations, yet relative C-X bond elongations >50% were necessary. It will be seen that the conical intersections and the stabilisation of the excess electron always occur before this range is reached. Hence DEA was modelled without spin-polarisation. The scGW$_0$(PBE0) calculations were performed for relative C-X bond elongations up to 50% in steps of 12.5%.

The conversion between relative and total C-X bond elongations is superficial, because the ground state bond lengths d_0(C-X) are to be found in Tab. 9.1.

Table 5.2.: Exothermicities and components from experiment: Carbon-halogen (C-X) bond fission energy (E_{BF}) of phenyl halogenides in the gas phase (also from spin-polarised DFT(PBE0)), see Tab. 4.2 and [206] for the main resonance energies ($\varepsilon^{SOMO}(d_0)$), halogen electron affinities (EA) and resulting exothermicities (E_{EXO}^{DEA}, E_{EXO}^{TNID}) for electron-induced dissociation according to reaction equation (5.1), TNI total energy ($-E(\sigma_s^*)(d = 1.500d_0)$) from scGW$_0$(PBE0) and underlying DFT(PBE0) added for comparison
E_{EXO}^{DEA}:=EA-$E_{BF} = -E(\sigma_s^*)(d \to \infty)$
E_{EXO}^{TNID}:=$\varepsilon^{SOMO}(d_0) + E_{EXO}^{DEA}$

X=	F	Cl	Br	I
$E_{BF}(C_6H_5X)$[eV]				
DFT(PBE0)	5.3764	4.1761	3.5270	2.9995
exp. [215]	5.514(12)	4.212(8)	3.567(13)	2.819(44)
EA(X)[eV]				
exp. [215]	3.4011897 (24)	3.612725 (27)	3.3635882 (19)	3.0590368 (10)
-$E(\sigma_s^*)(1.5d_0)$[eV]				
scGW$_0$(PBE0)	-2.1418	-0.6606	-0.1223	+0.2248
E_{EXO}^{DEA}[eV]				
exp. [215]	-2.113(12)	-0.599(8)	-0.203(13)	+0.240(44)
E_{EXO}^{TNID}[eV]				
exp. [206, 215] π_a^*	-1.24(1)	+0.13(1)	+0.47(1)	+0.83(4)
exp. [206, 215] π_s^*	-0.63(1)	+0.13(1)	+0.47(1)	+0.83(4)
exp. [206, 215] σ_s^*	—	+1.9	—	$\geq$+0.24(4)

To gain more detailed insight on probability and mechanism of DEA, Fig. 5.4 exemplifies the typical evolution of the molecular *LDOS* and its halogen-projected component along the postulated dissociation pathway. The $\pi_{a,s}^*$ main resonances, whose electron attachment cross sections should be the largest, experience marginal stabilisation, while their localisation stays almost the same. The σ_s^* MOs collapse into a state of the same character with rapidly increasing (relative) stability and localisation. It harbours the excess electron after internal conversion at the respective conical intersection and finally becomes stable. As explained for the neutral equilibrium geometries treated by chapter 4, the halogen-projected fraction of a sufficiently high peak is indicative of its σ_s^* (dissociative) character. The associated main resonance orbitals are displayed in Fig. 5.3.

Equations (5.2) are the core part of the method to gain insight into the DEA energy balance and its components from the acquired data.

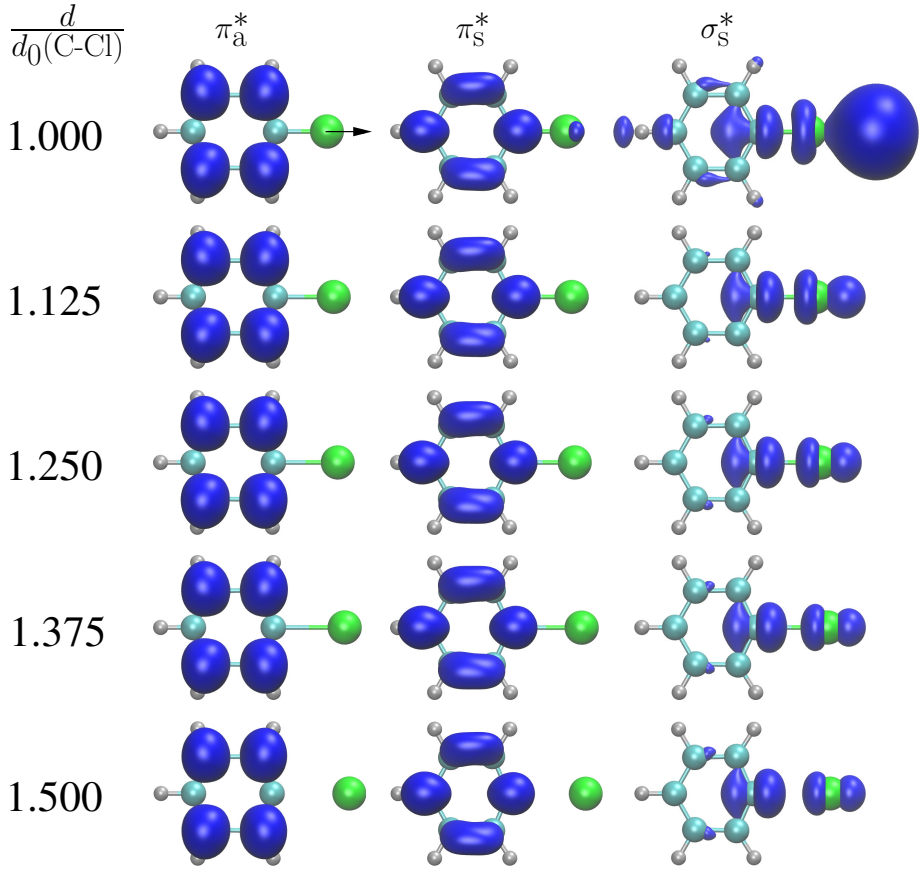

Figure 5.3.: Evolution of the most stable antibonding main resonance orbital of each type for C_6H_5Cl upon carbon-chlorine bond elongation along the path indicated in the upper left figure and assumed for DEA, from scGW$_0$(PBEo)

$$
\begin{aligned}
&E(d) = E^0(d) + \varepsilon_{\text{QP}}^{\text{SOMO}}(d) \\
&\varepsilon_{\text{QP}}^{\text{SOMO}}(d) = E_{\text{QP}}^{\text{SOMO}}(d) - \Phi_{\text{vac}}(d) \\
&E^0(d_0) = 0 \\
&E_{\text{A}} := E(d_{\text{cross}}) - E(d_0) \\
&E_{\text{A,add}} := \underset{d>d_0}{max}\{E(d) - E(d_{\text{cross}})\} \;\forall\; E_{\text{A,add}} > 0 \\
&E_{\text{A}}(\sigma_s^*) := \underset{d>d_0}{max}\{E(\sigma_s^*)(d) - E(\sigma_s^*)(d_0)\} \;\forall\; E_{\text{A}}(\sigma_s^*) > 0
\end{aligned}
\tag{5.2}
$$

The potential energy of the charged system $E(d)$ is approximated as the potential energy of the neutral system $E^0(d)$ plus $\varepsilon_{\text{QP}}^{\text{SOMO}}(d)$, which is the quasiparticle energy of the MO to be occupied by the excess electron relative

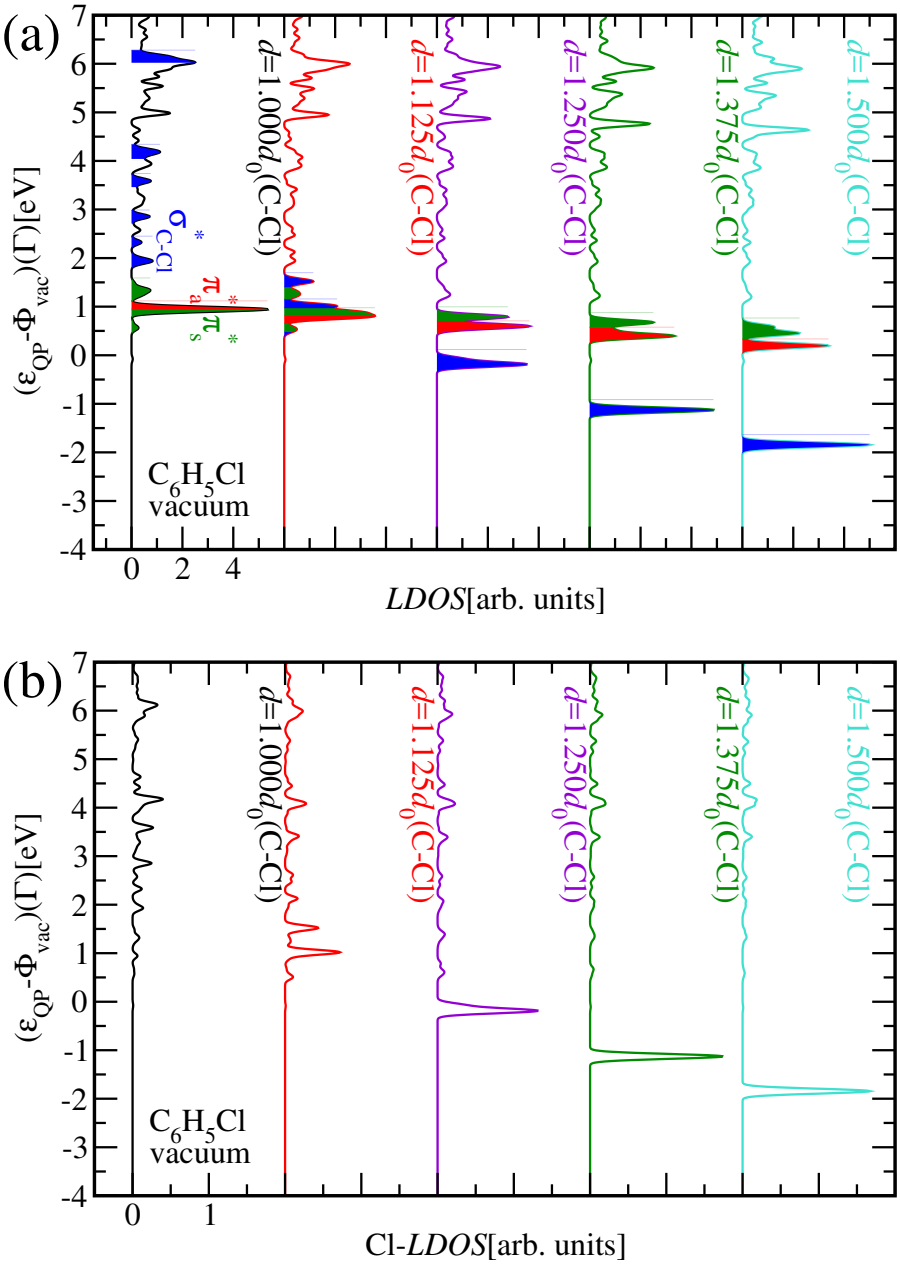

Figure 5.4.: Evolution of (a) *LDOS* and (b) chlorine-projected component upon DEA to C_6H_5Cl from scGW$_0$(PBE0)

to the vacuum potential[6] $\Phi_{\mathrm{vac}}(d)$. For the ground state geometry (d=d_0) this coincides with the vertical approximation. The ground state potential energy of the neutral system $E^0(d_0)$ is set to zero.

The dissociation of a TNI formed by excess electron attachment to a $\pi^*_{\mathrm{a,s}}$ shape resonance is an activated process. Apart from excess electron attachment, inelastic collisions with electrons or molecules can also transfer energy to the molecule by vibrational excitation. On the surface phonons may contribute additionally. Providing the activation energy allows the anion to reach the favourable σ^*_{s} potential energy surface by internal conversion so that the dissociation finally lowers the potential energy of the system, i.e. $E(d) < E(d_0)$ for sufficiently large d. $E(d_0)$ can also be interpreted as the total energy of the charged system[7].

Since the excess electrons are captured by molecular resonances, their state is initially instable. The competitive process AD may occur as long as $\varepsilon^{\mathrm{SOMO}}_{\mathrm{QP}}(d) > 0$. The antibonding states are continuously lowered upon carbon-halogen bond elongation [cf. Fig. 5.4 (gas phase), 5.10 (idealised $I_h(0001)$), 5.11 ($4S_{\mathrm{AD}}$ orientational defect complex) (C_6H_5Cl as example)]. Hence it has to reach a certain extent that can be construed as indicative of completion of DEA.

The activation energy E_{A} has to be transferred to the TNIs in order to reach the conical intersection at $d = d_{\mathrm{cross}}$, because the lowering of the initial $\pi^*_{\mathrm{a,s}}$ SOMO is not sufficient to compensate for the energy $E_0(d)$ needed to elongate the C-X bond (see $E_0(d)$ displayed in the potential energy curves diagrams of this chapter for DEA). The opposite pertains to the case of a σ^*_{s} SOMO, which eventuates after IC at the conical intersection. It can not a priori be excluded that DEA requires two further types of activation energies due to local violations of the aforementioned extents of the lowering of the SOMO. $E_{\mathrm{A,add}}$ takes into account that the global maximum of the anionic potential energy $E(d)$ may not always be at the conical intersection. $E_{\mathrm{A}}(\sigma^*_{\mathrm{s}})$ is the activation energy resulting if the excess electron occupies the σ^*_{s} state involved in the conical intersection at any C-X bond distance d. However both always turned out to be negligible if even existent.

[6] For the adsorbate-substrate supercells this means the vacuum potential at the side of the adsorbed molecule.

[7] $E(d)$ has no kinetic part, because the more sophisticated electronic structure treatments work with a stationary ionic geometry at a time. However without loss of generality it can be imagined that the reactions are described in the barycentric system. There the incident excess electron possesses the whole kinetic energy in very good approximation due to the vanishing total momentum and the mass ratio between it and the remaining bodies. Hence the above interpretation of $E(d_0)$.

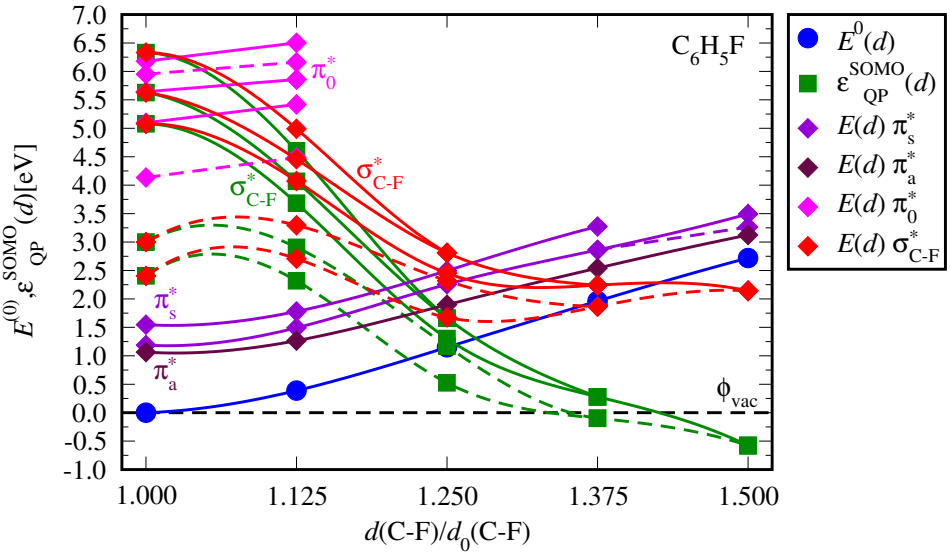

Figure 5.5.: Potential energy curves diagram for DEA to C_6H_5F from scGW$_0$ and underlying DFT(PBEo) ($E^0(d)$ (solid blue curve): ground state energy of the neutral molecule, $E(d)$ (σ^*_s (red), π^*_s (violet), π^*_a (maroon), π^*_0 (magenta (relevant only here))): potential energy of the anion, $\varepsilon^{SOMO}_{QP}(\sigma^*_s)(d)$ (green): quasiparticle energy of σ^*_s SOMO, subresonances displayed as dashed curves with the same colour code, splines serve as a guide to the eye between calculated points)

The potential energy curves relevant for DEA to each molecule in the gas phase are displayed in Fig. 5.5 to 5.8. The essential curves, representing the evolution of the respective component upon C-X bond elongation, were selected with the aid of a uniform purposeful scheme. If DEA shall occur, the lowering of the energy level of the excess electron and thermal fluctuations finally have to compensate for the energy $E^0(d)$ needed to elongate resp. break the C-X bond. The potential energy of the charged system $E(d)$ is given for the low-energy electron capture main resonances of each type and – as appropriate – subresonances, since these are lower in a few cases. Either permanently or at least after internal conversion at a conical intersection, which is still above Φ_{vac}, successful DEA requires the SOMO to be of σ^*_s character. The quasiparticle energy of this state is represented as the curve $\varepsilon^{SOMO}_{QP}(\sigma^*_s)(d)$. It becomes stable at $d = d_{vac}(\sigma^*_s)$, which is approximated by linear interpolation between the two adjacent points considered. The same was done to obtain the positions of the conical intersections.

It is apparent that $\pi^*_{a,s}$ of C_6H_5F play a special role among the main resonances of the molecules as they were detected below the dissociation limit. The amounts of energy lacking as the desired TNI dissociations are endother-

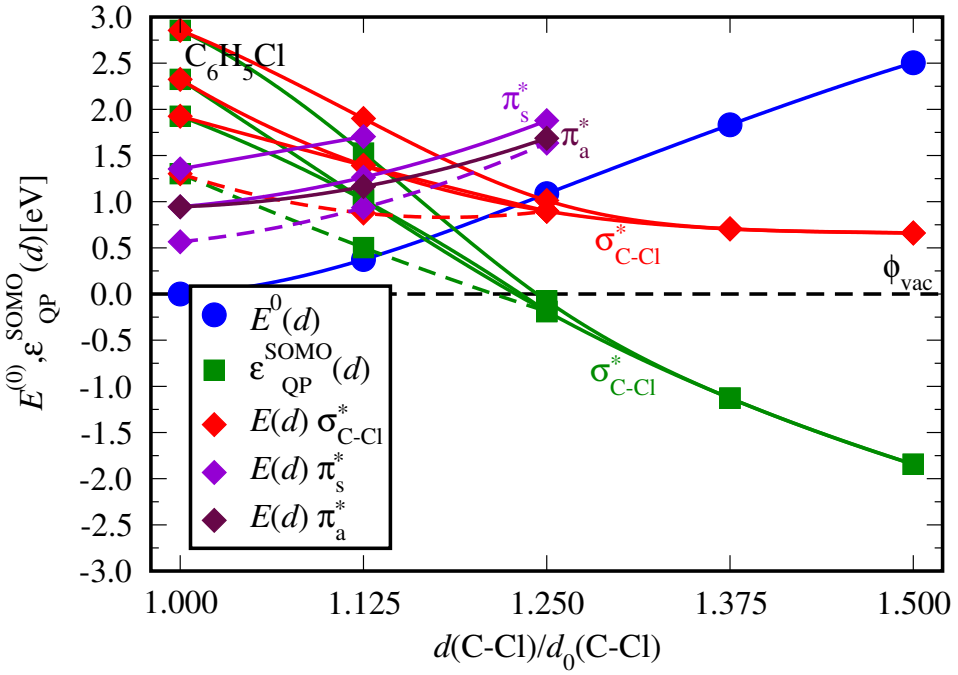

Figure 5.6.: Potential energy curves diagram for DEA to C_6H_5Cl from scGW$_0$ and underlying DFT(PBE0) (for explanation of colour code and design see Fig. 5.5)

mic were found to be very high and similar to the destabilisation of the anions yielded by the present theoretical study within the investigated range (0.63-1.24eV missing according to experiment [206, 215], (0.59-)0.95-1.08eV calculated, cf. Tab. 4.2 and 5.2). Hence both theory and experiment consistently yield that dissociation can not emerge from electron capture by these states unless it is aided by unusually strong vibrational excitations that are very unlikely to occur.

Tab. 5.3 summarises the observables characterising DEA and their values for the gas phase molecules, whereby the conical intersections between the main resonances are described. According to it the molecular scale model evidences the lowering of the main resonance of each type, the reduction of activation energies and the increase of DEA cross sections with the row of the halogen, i.e. the measured trends (cf. Tab. 5.1) are confirmed. This is due to several aspects. As already discussed in section 4.1, the electron capture cross sections should be enlarged because of the lower positions of the antibonding molecular main resonances. Their initial degree of localisation is similar if considering a specific type (σ^*_s, π^*_s, π^*_a, π^*_0 as displayed in Fig. 4.8). However, as exemplified by Fig. 5.4, C-X bond elongation affects σ^*_s states much more drastically than

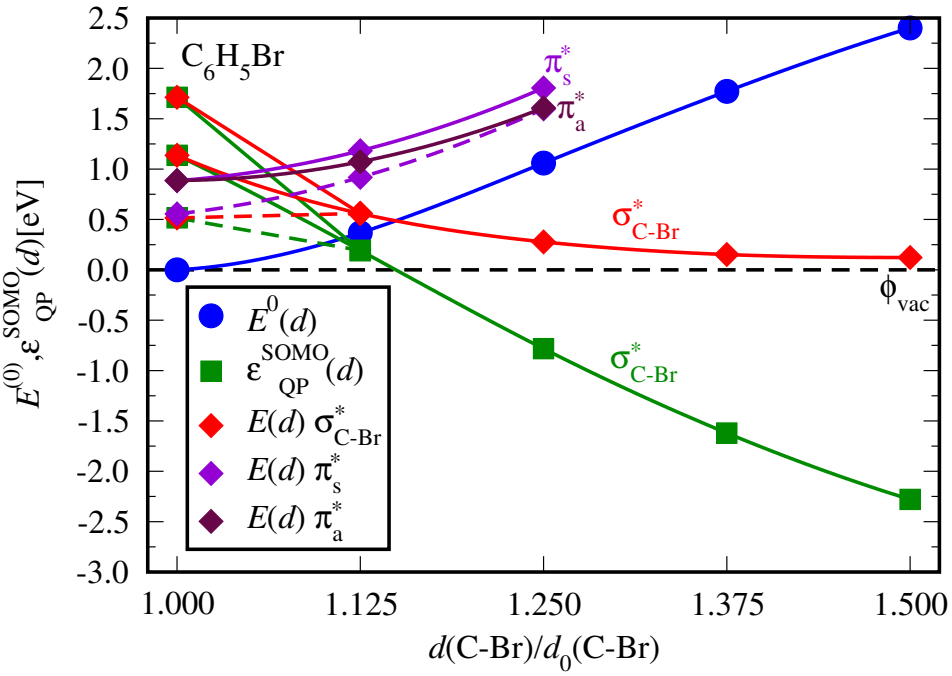

Figure 5.7.: Potential energy curves diagram for DEA to C_6H_5Br from scGW$_0$ and underlying DFT(PBE0) (for explanation of colour code and design see Fig. 5.5)

$\pi^*_{a,s}$ states. The former collapse into a molecular orbital of the same character that is rapidly lowered and localised, while the latter remain almost unchanged with only slightly diminished quasiparticle energies. Each conical intersection between them is still above Φ_{vac}. Hence if the excess electron is captured by a $\pi^*_{a,s}$ main resonance, it must undergo internal conversion there before the SOMO, which is of σ^*_s character afterwards, can become stable.

Upon increasing the row of the halogen, the conical intersections appear at significantly smaller C-X bond elongations (3.6-33.1% resp. 0.068-0.447Å) and with much reduced activation energies (0.061-1.251eV), while their position relative to Φ_{vac} varies clearly less (0.639-1.058eV), whereby C_6H_5I is initially excluded due to peculiarities that are discussed hereafter. Additionally the C-X bond elongations required to make the excess electron state stable also become smaller (15.0-41.6% resp. 0.283-0.561Å). Like the initial eigenenergy of the SOMO, the values of these quantities are similar or equal for $\pi^*_s \rightarrow \sigma^*_s$ and $\pi^*_a \rightarrow \sigma^*_s$ conical intersections. Hence its type (π^*_s or π^*_a) seems to possess only minor influence on the DEA cross section.

Low-energy DEA to C_6H_5Cl or C_6H_5Br originates from electron capture by the $\pi^*_{a,s}$ main resonance. This has been demonstrated by experimental (cf.

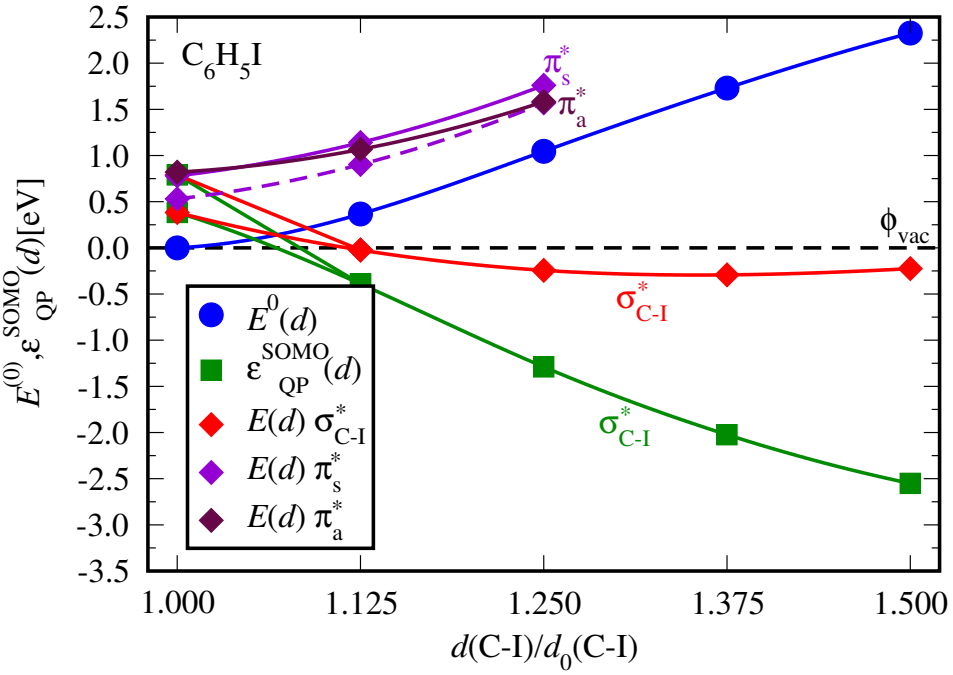

Figure 5.8.: Potential energy curves diagram for DEA to C_6H_5I from scGW$_0$ and underlying DFT(PBE0) (for explanation of colour code and design see Fig. 5.5)

Tab. 5.1), theoretical [42] and combined [39, 41, 210] studies in accordance with the results of the calculations performed here (cf. Tab. 5.3). However it does not pertain to C_6H_5F and no reliable interpretation was found for the case of C_6H_5I. Only C_6H_5F has the $\pi^*_{a,s}$ main resonances below the dissociation limit (cf. Tab. 5.2) and the activation energies E_A (1.214eV resp. 1.251eV) are too large to be provided by vibrational excitations. Hence the incident electron causing experimentally observable DEA has to possess much higher kinetic energy (6.1eV resp. 6.3eV) corresponding to the calculated positions of a higher σ^*_s and π^*_0 main resonance (compare Tab. 5.1 and Tab. 4.2), which lie close to each other. The contribution of the latter (type) is expected to be smaller, because of the necessity of internal conversion and the concomitant, albeit slight, activation energies in contrast to the former (type) (cf. Fig. 5.5). On the one hand it is uncertain why no peaks around the calculated range of lower suchlike main resonances (5.1-5.6eV) were measured, on the other hand it should be mentioned that the highest σ^*_s main resonance also exhibits substantially stronger localisation than the other two according to the calculations (cf. Fig. 4.4).

Table 5.3.: Low-energy DEA to C_6H_5X molecules with X=F,Cl,Br,I in vacuum: Characters and positions of main resonances and interpolated conical intersections between them and appendant activation energies E_A from scGW$_0$ and underlying DFT(PBE0)

X=	F	Cl	Br	I
ε_{QP}[eV]				
σ_s^*	+5.0778	+1.9254	+1.1368	+0.3831
				+0.7896
π_s^*	+1.1883	+0.9450	+0.8851	+0.7801
π_a^*	+1.0648	+0.9450	+0.8873	+0.8199
$E_A(\sigma_s^*)$[eV]	none	none	none	none
$\frac{d_{vac}(\sigma_s^*)-d_0}{d_0}$[%]	41.578	23.044	14.965	6.190
				8.364
$\pi_s^* \rightarrow \sigma_s^*$				
$\frac{d_{cross}-d_0}{d_0}$[%]	27.999	13.952	3.598	0.101
$\varepsilon_{QP}(d_{cross})$[eV]	+1.0576	+0.8788	+0.8649	+0.7800
$E(d_{cross})$[eV]	2.4019	1.3354	0.9707	0.7830
E_A[eV]	1.2136	0.3904	0.0856	0.0029
$E_{A,add}$[eV]	none	none	none	none
$\pi_a^* \rightarrow \sigma_s^*$				
$\frac{d_{cross}-d_0}{d_0}$[%]	33.117	15.316	4.089	—
$\varepsilon_{QP}(d_{cross})$[eV]	+0.6386	+0.7469	+0.8278	—
$E(d_{cross})$[eV]	2.3158	1.2813	0.9480	—
E_A[eV]	1.2510	0.3363	0.0607	—
$E_{A,add}$[eV]	none	none	none	—

Principally two peculiar facts may serve as explanations for the special role of C_6H_5I. Only for this molecule the calculations yielded a σ_s^* main resonance below those of the $\pi_{a,s}^*$ types. Hence the activation energy for low-energy DEA might vanish, additionally corroborating the expectation of its vastly enlarged cross section. It was indeed observed in the measurements, nevertheless the highest peak appeared for even lower energy, namely at or very close to 0.0eV (instead of 0.38eV), implying that the required amount of kinetic energy of the incident electron is extremely small. Furthermore it is the sole molecule whose C-X bond fission energy E_{BF} is exceeded by the halogen electron affinity EA (cf. Tab. 5.2), i.e. the DEA according to reaction equation (5.1) is exothermic. Hence electron attachment at any energy might be dissociative even if the molecule is not vibrationally excited. If the activation energy vanishes and the excess electron does not have to undergo internal conversion, dissociation would

essentially be triggered by electron attachment in itself, whose probability, among others, exhibits an inverse dependence on the kinetic energy of the incident electron [43]. Regardless of the molecular electronic structure, this is consistent with the experimental low-energy DEA cross section distributions.

5.2. Catalysis by the ice substrate

This section serves to evaluate how adsorption at the ice surface and its electron solvation sites influence DEA. Idealised $I_h(0001)$ and the $4S_{AD}$ orientational defect complex were chosen as prototypical systems for modelling the dissociation. The latter is the largest cluster of dangling OH groups treated here and exhibits the highest *EA* among the defects of this kind (cf. Tab. 4.5). The flat-lying adsorption geometry with the halogen situated on top of a surface dangling proton and the phenyl group positioned such that the carbon-halogen (C-X) bond lies almost parallel to the respective intact Fletcher stripe is at least very close to most favourable (see section 4.2). The halogen is kept fixed since the intramolecular excess electron transfer to it during the dissociation (change of the SOMO from $\pi^*_{a,s}$ to σ^*_s, see introduction to this chapter) reinforces its adsorption due to Coulomb interaction with the positive partial charges of surface dangling protons. The carbon-halogen (C-X) bond is elongated (cf. Fig. 5.9) like for the gas phase molecules (see section 5.1). As the inclination of the C-X bond towards the Fletcher stripe, and also the surface plane, is $\leq 5^\circ$ throughout, the phenyl group remains in a favourable position on top of the Fletcher stripe (see section 4.2) during its movement within the relevant range ($\leq$50% C-X bond elongation, mostly clearly less). No further ionic relaxation is performed. Incorporating molecular vacancies was eschewed since in view of the more complicated potential energy landscape a presently unavailable approach combining the G_0W_0 method with a force minimisation algorithm would be required to determine a meaningful dissociation pathway.

The differences found between the geometries of gas phase and adsorbed molecules are reasonably small. E.g. adsorption elongates d_0(C-X) by only 0.023-0.031Å resp. 1.34-2.30% (cf. Tab. 5.4 and 9.1). Furthermore the adsorbed molecules are still virtually C_{2v}-symmetric. The different levels of DFT employed to calculate vacuum and surface system geometries impose no essential restrictions on their comparability, because they reproduce the experimental results with high accuracy [gradient DFT(PBE) (see subsubsection 2.5.2.2) for the ice bulk (see section A), hybrid DFT(PBE0) (see subsection 2.5.3) for the gas phase molecules (see section D), Grimme-D2 vdW corrections (see

subsubsection 2.5.2.3) for the adsorbate geometry have no essential influence on it (see section 4.2)].

The relevant, i.e. i.a. significantly localised, molecular orbitals of the adsorbates are clearly identifiable. Their shapes are similar to those of their gas phase equivalents.

Table 5.4.: Equilibrium carbon-halogen bond lengths d_0(C-X) of phenyl halogenides (C_6H_5X with X=F,Cl,Br) adsorbed on pristine I_h(0001) and at a $4S_{AD}$ orientational defect complex, from DFT(PBE) with Grimme-D2 vdW corrections for the adsorbate geometry

d_0(C-X)[Å]	I_h(0001)	$4S_{AD}$
X=F	1.381	1.381
X=Cl	1.744	1.747
X=Br	1.915	1.919

The typical evolution of the *LDOS* at the adsorbed molecule and its halogen-projected component X-*LDOS* is exemplarily displayed for C_6H_5Cl in Fig. 5.10 and 5.11, which are counterparts of the vacuum Fig. 5.4. Comparing these figures to each other demonstrates that the trends regarding lowering and localisation of the main resonance peaks, as well as their halogen-projected fraction, are preserved upon adsorption. The lowering of the molecular main resonances by the ice substrate barely changes along the dissociation pathway. As discussed for the neutral equilibrium geometries in section 4.3 (cf. Fig. 4.13) this influence is stronger for adsorption at the electron trap and σ_s^* orbitals are by far most affected.

The surface DEA potential energy curves diagrams Fig. 5.12 to 5.14 were constructed according to the same scheme as their vacuum counterparts Fig. 5.5 to 5.7 discussed in section 5.1 to characterise the influence of the ice substrate more precisely. At the surface a reduction of the anionic potential energy, i.e. $E(d) < E(d_0)$, was always found within the investigated range. It is assumed that DEA is now energetically favourable independently of the molecule or the main resonance capturing the excess electron, because this finding strongly hints that the dissociation of each TNI on the ice surface reduces the total potential energy. Its curve $E(d)$ is modified upon adsorption resp. change of the adsorption site due to the energy shift of the electron capturing molecular resonances, the altered lowering of the SOMO (esp. σ_s^*) during C-X bond elongation resp. DEA and the different bond fission energy landscapes $E^0(d)$. It turns out that the first two are the major aspects. This is obvious, because gas phase and surface results are essentially comparable. Adsorption at pristine I_h(0001) lowers the $\pi_{a,s}^*$ main resonances by 0.186-0.290eV (cf. Tab. 5.3, 5.5).

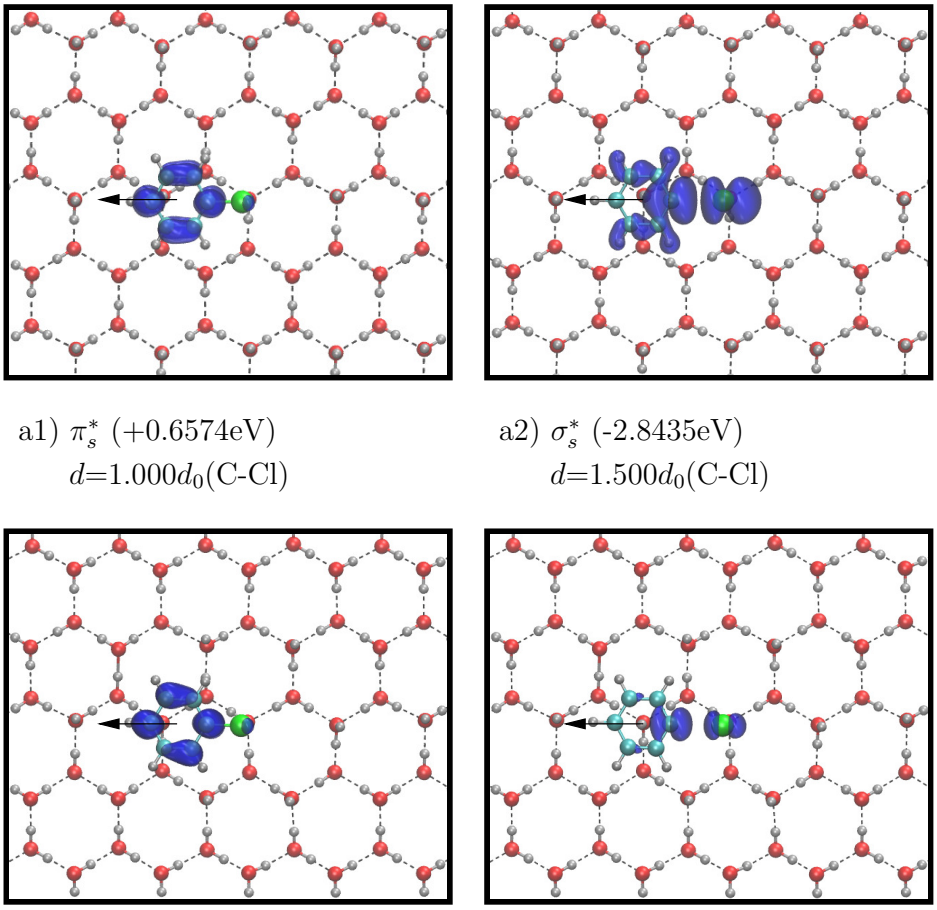

a1) π_s^* (+0.6574eV)
d=1.000d_0(C-Cl)

a2) σ_s^* (-2.8435eV)
d=1.500d_0(C-Cl)

b1) π_s^* (+0.0798eV)
d=1.000d_0(C-Cl)

b2) σ_s^* (-3.4217eV)
d=1.500d_0(C-Cl)

Figure 5.9.: Lowest significantly localised molecular orbitals above the HOMO for phenyl chloride C_6H_5Cl adsorbed on pristine I_h(0001) (a) and at a $4S_{AD}$ orientational defect complex (b) for the initial geometry (1) and 50% carbon-chlorine bond elongation (2) created by moving the phenyl group along the indicated direction (Fletcher stripe), position relative to Φ_{vac} given in parentheses, from G_0W_0(PBE0-electronic)

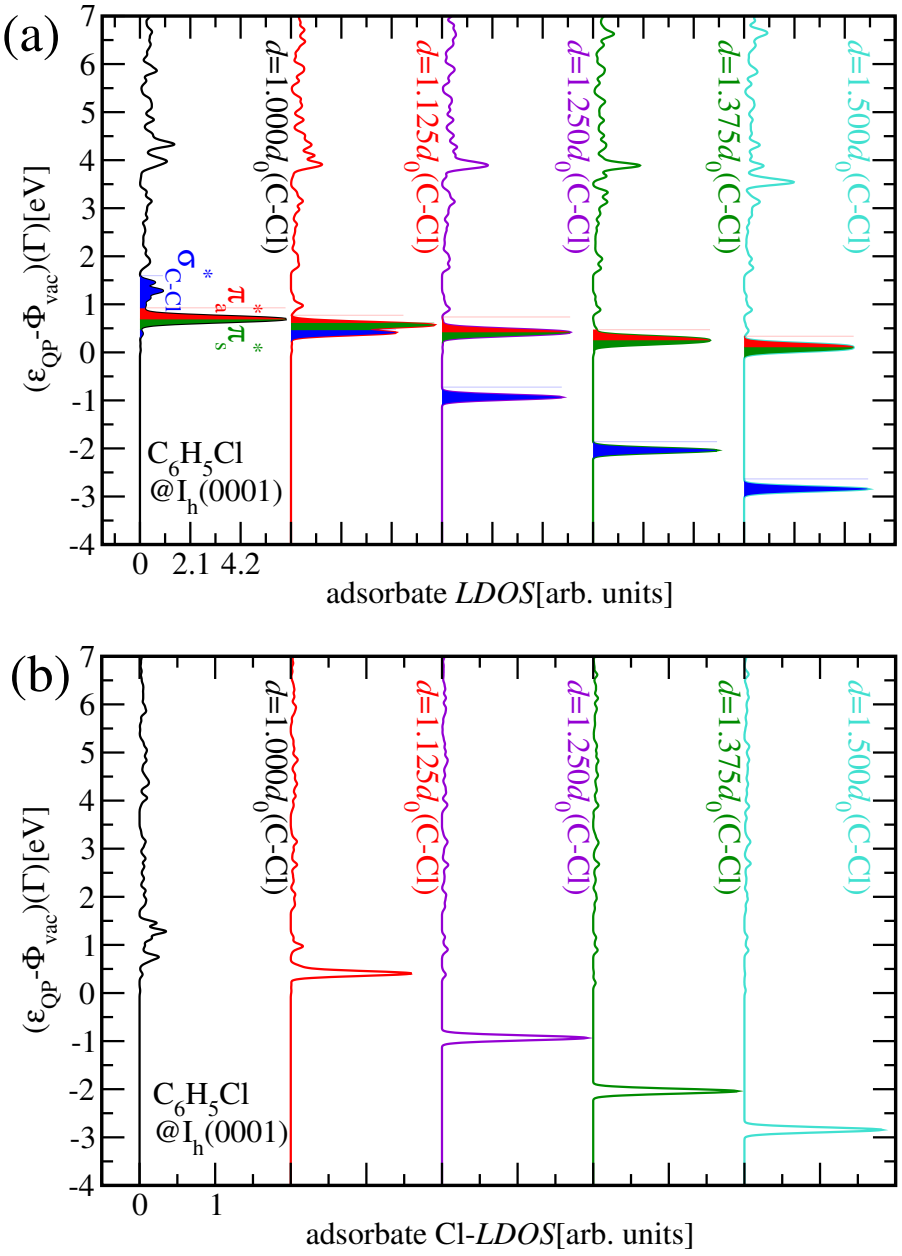

Figure 5.10.: Evolution of (a) *LDOS* at the adsorbed molecule and (b) chlorine-projected component upon DEA to C_6H_5Cl adsorbed on pristine I_h(0001) from G_0W_0(PBE0-electronic)

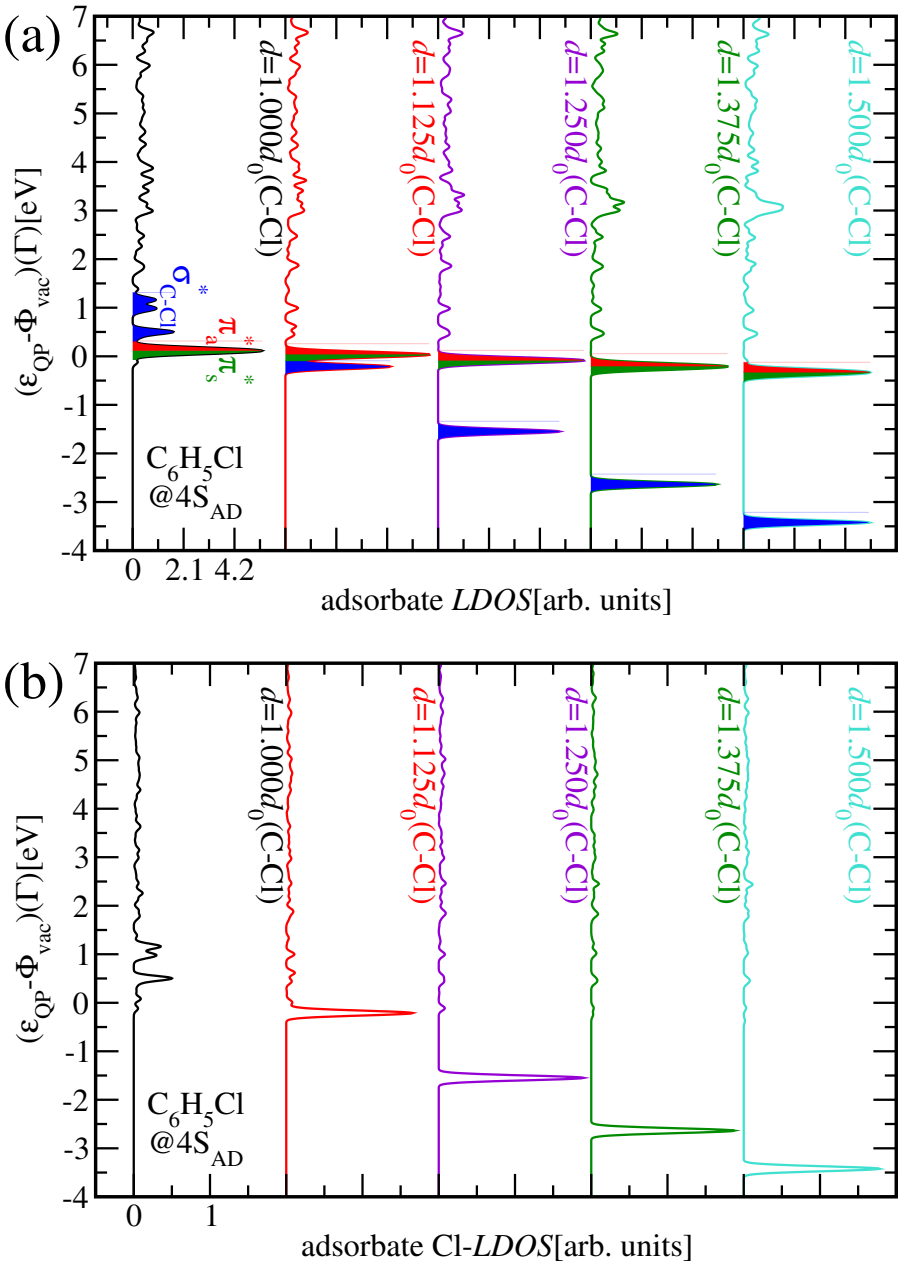

Figure 5.11.: Evolution of (a) *LDOS* at the adsorbed molecule and (b) chlorine-projected component upon DEA to C_6H_5Cl adsorbed at a $4S_{AD}$ orientational defect complex on $I_h(0001)$ from G_0W_0(PBEo-electronic)

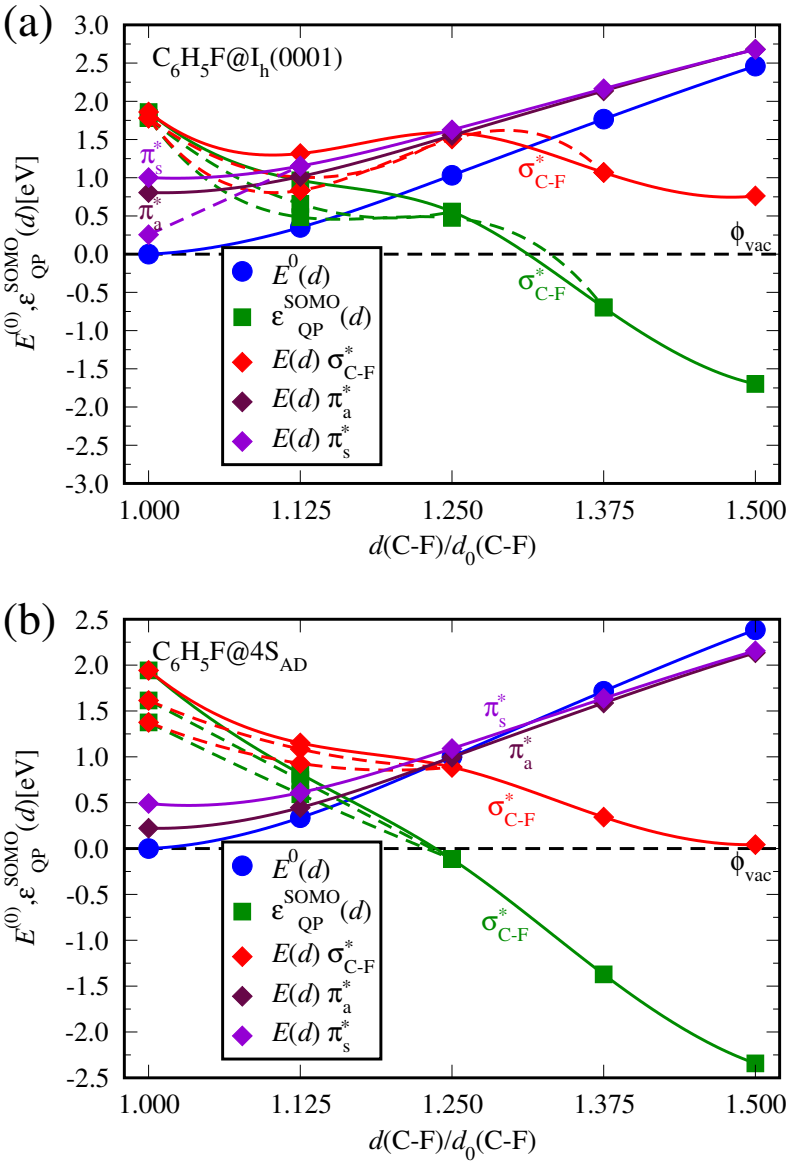

Figure 5.12.: Potential energy curves diagram for DEA to a C_6H_5F molecule adsorbed (a) on pristine I_h(0001) and (b) at a $4S_{AD}$ orientational defect complex from G_0W_0(PBE0-electronic) and underlying DFT(PBE) with Grimme-D2 vdW corrections for adsorbate geometry and electronic ground state energies (explanation see section 4.2 and introduction to this chapter) (for explanation of colour code and design see Fig. 5.5)

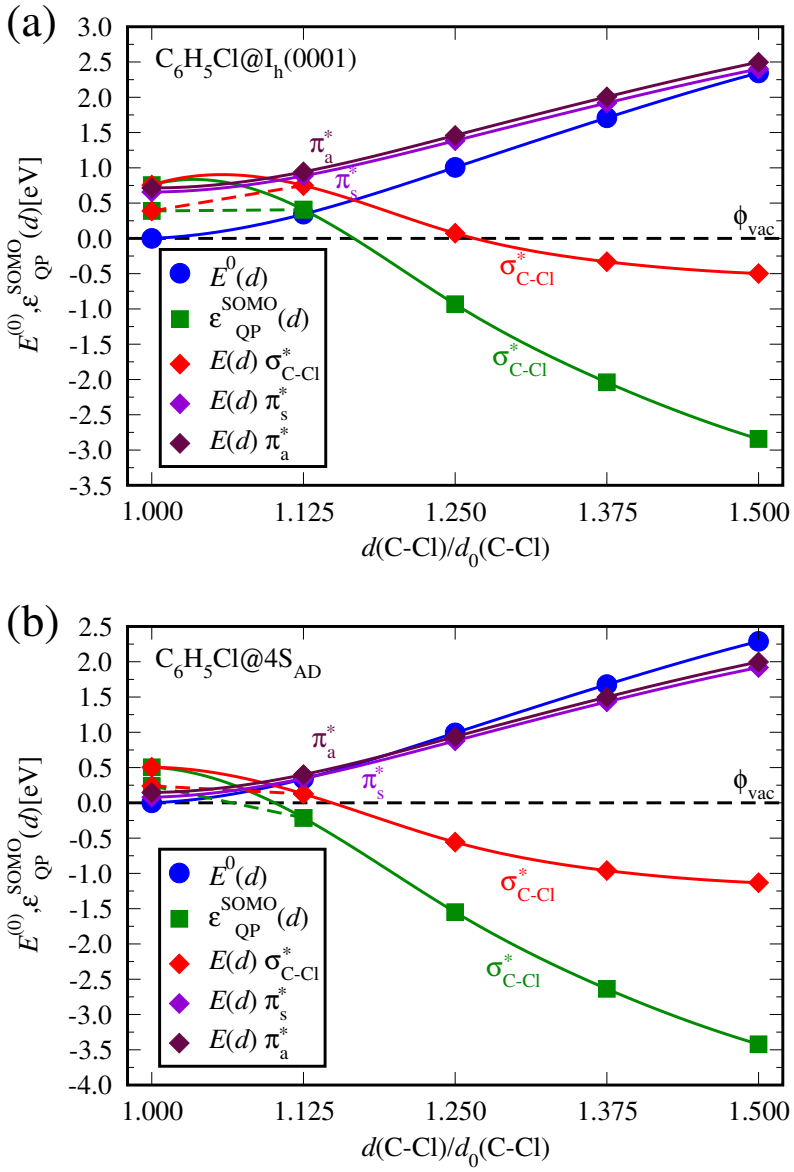

Figure 5.13.: Potential energy curves diagram for DEA to a C_6H_5Cl molecule adsorbed (a) on pristine I_h(0001) and (b) at a $4S_{AD}$ orientational defect complex from G_0W_0(PBE0-electronic) and underlying DFT(PBE) with Grimme-D2 vdW corrections for adsorbate geometry and electronic ground state energies (explanation see section 4.2 and introduction to this chapter) (for explanation of colour code and design see Fig. 5.5)

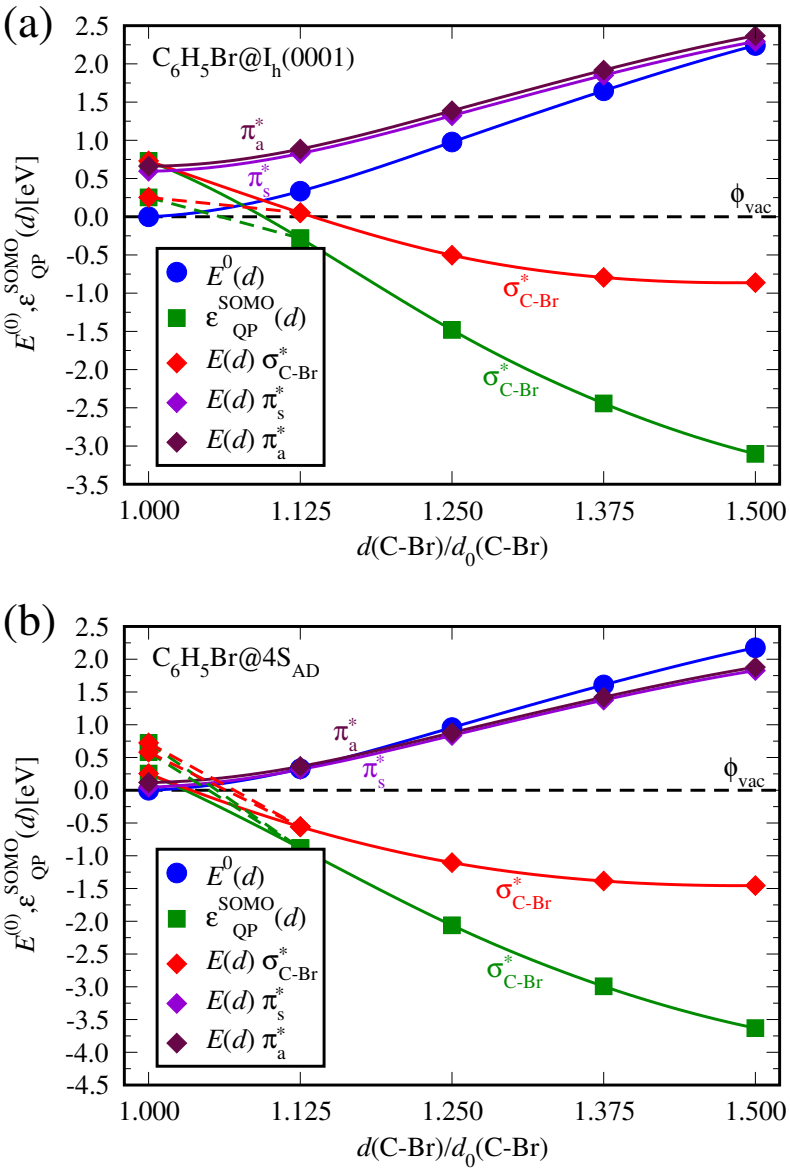

Figure 5.14.: Potential energy curves diagram for DEA to a C_6H_5Br molecule adsorbed (a) on pristine $I_h(0001)$ and (b) at a $4S_{AD}$ orientational defect complex from G_0W_0(PBEo-electronic) and underlying DFT(PBE) with Grimme-D2 vdW corrections for adsorbate geometry and electronic ground state energies (explanation see section 4.2 and introduction to this chapter) (for explanation of colour code and design see Fig. 5.5)

Judging from the discussion terminating section 4.1 these values should be higher if not for the different levels of theory, but no large change is to be expected. The $4S_{AD}$ orientational defect complex yields additional 0.511-0.585eV (cf. Tab. 5.5, 5.6). $\varepsilon_{QP}(\sigma_s^*)(d = 1.500d_0)$ is lowered by 0.824-1.121eV via the former and 0.528-0.644eV via the latter repositioning. This effect weakens together with the halogen electronegativity in both cases. Adjusting the degree of GW selfconsistency for surface to vacuum calculations can be expected to lower the respective σ_s^* MOs since they are strongly localised. However these shifts should be comparatively small as evidenced by the discussion terminating section 4.1. The energy required for the same relative – practically absolute (cf. Tab. 5.4 and 9.1) – C-X bond elongation is influenced by both adsorption sites in such a manner as the two other observables and the total change increases continuously as far as assessable. $E_0(d = 1.500d_0)$ is reduced by 0.159-0.259eV and further 0.056-0.076eV. These are the smallest deviations and both levels of theory are considered adequate for their respective application (see section 4.2, subsection 2.5.3, subsubsections 2.5.2.2, 2.5.2.3). The surface E_{BF} would have several values since it depends on the equivocal final position of the phenyl radical and hence this also pertains to the surface E_{EXO}^{DEA}. However it is remarkable that the contribution of the adsorbed phenyl group moving along the dissociation pathway (intact Fletcher stripe, cf. Fig. 5.9) should vary only slightly (see section 4.2), $E_{EXO}^{DEA} \approx$-$E(\sigma_s^*)(d = 1.500d_0)$ is well fulfilled for the free molecules (see section 5.1) and the surface $E(\sigma_s^*)(d)$ curves flatten nearly as rapidly as their vacuum equivalents. Therefore it could be that E_{EXO}^{DEA} of each adsorbate-substrate system extends merely over a narrow range and -$E(\sigma_s^*)(d = 1.500d_0)$ is within or close to it.

Electron capture by a main resonance is more likely to trigger dissociation if the molecule is adsorbed, preferably at a stronger electron trap. A condensed version of the central evidences for this statement is provided by comparing the vacuum Tab. 5.3 and the surface Tab. 5.5, 5.6. This order is expected, because the ice substrate is polar as well as the molecules and deeper electron traps are also more favourable for the adsorption of the halogen, in particular if it carries the excess electron. An unambiguous trend is found for the σ_s^* state as it becomes stable at markedly smaller C-X bond lengths $d_{vac}(\sigma_s^*)$ in the expected order independently of the molecule. The same applies to $\varepsilon_{QP}(d_{cross})$ for both main conical intersections, whereby going from the idealised to the defective surface makes an especially large difference. However choosing a heavier halogen does not modify its value in such a clearly favourable way as for the former quantity. Adsorption reduces the C-X bond elongation $d_{cross} - d_0$ needed to reach the conical intersection, whose trend regarding the halogen is preserved, yet this time going from the idealised to the defective surface has

Table 5.5.: Low-energy DEA to a C_6H_5X molecule with X=F,Cl,Br adsorbed on pristine $I_h(0001)$: Characters and positions of main resonances and interpolated conical intersections between them and appendant activation energies E_A from G_0W_0(PBE0-electronic) and underlying DFT(PBE) with Grimme-D2 vdW corrections for adsorbate geometry and electronic ground state energies (explanation see section 4.2 and introduction to this chapter)

X=	F	Cl	Br
ε_{QP}[eV]			
σ_s^*	+1.8597	+0.7565	+0.7300
π_s^*	+1.0024	+0.6574	+0.5956
π_a^*	+0.8061	+0.7154	+0.6621
$E_A(\sigma_s^*)$[eV]	none	none	none
$\frac{d_{vac}(\sigma_s^*)-d_0}{d_0}$[%]	30.545	16.295	9.019
$\pi_s^* \rightarrow \sigma_s^*$			
$\frac{d_{cross}-d_0}{d_0}$[%]	22.645	5.276	1.846
$\varepsilon_{QP}(d_{cross})$[eV]	+0.6334	+0.6089	+0.5658
$E(d_{cross})$[eV]	1.5373	0.7538	0.6299
E_A[eV]	0.5349	0.0964	0.0343
$E_{A,add}$[eV]	0.0512	none	none
$\pi_a^* \rightarrow \sigma_s^*$			
$\frac{d_{cross}-d_0}{d_0}$[%]	25.401	2.194	0.941
$\varepsilon_{QP}(d_{cross})$[eV]	+0.5159	+0.6951	+0.6463
$E(d_{cross})$[eV]	1.5718	0.7554	0.6790
E_A[eV]	0.7657	0.0400	0.0169
$E_{A,add}$[eV]	none	none	none

a converse effect for C_6H_5Cl and C_6H_5Br. The latter circumstance is of minor relevance due to the lower quasiparticle energy of the excess electron during dissociation, which indicates a reduced probability of autodetachment (AD). This is evidenced by the values of $\varepsilon_{QP}(\pi_{a,s}^*)(d_0)$, $\varepsilon_{QP}(d_{cross})$ and $d_{vac}(\sigma_s^*)$ (cf. Tab. 5.5 and 5.6) as well as contained in the DEA potential energy curves diagrams (cf. Fig. 5.12 to 5.14). The activation energy E_A may be provided by vibrational excitations of the adsorbate. It is assumed that energy can be efficiently transferred to the molecular vibrational degrees of freedom, because the halogen acts as an anchor binding the adsorbate to the substrate [the key bonding motif (see section 4.2)]. However diffusion resp. desorption generally is a competitive process if the vibrational energy exceeds the local binding energy E_B (here relative to the idealised surface: $E_B := E_{ads}(4S_{AD}) - E_{ads}(I_h(0001))$)

Table 5.6.: Low-energy DEA to a C_6H_5X molecule with X=F,Cl,Br adsorbed at a $4S_{AD}$ orientational defect complex on $I_h(0001)$: Characters and positions of main resonances and interpolated conical intersections between them and appendant activation energies E_A from G_0W_0(PBE0-electronic) and underlying DFT(PBE) with Grimme-D2 vdW corrections for adsorbate geometry and electronic ground state energies (explanation see section 4.2 and introduction to this chapter)

X=	F	Cl	Br
ε_{QP}[eV]			
σ_s^*	+1.9424	+0.5042	+0.2544
π_s^*	+0.4914	+0.0798	+0.0473
π_a^*	+0.2215	+0.1470	+0.1184
$E_A(\sigma_s^*)$[eV]	none	none	none
$\frac{d_{vac}(\sigma_s^*)-d_0}{d_0}$[%]	23.459	8.785	2.791
$\pi_s^* \rightarrow \sigma_s^*$			
$\frac{d_{cross}-d_0}{d_0}$[%]	21.599	8.238	2.394
$\varepsilon_{QP}(d_{cross})$[eV]	+0.1382	+0.0314	+0.0362
$E(d_{cross})$[eV]	0.9593	0.2556	0.0990
E_A[eV]	0.4679	0.1758	0.0517
$E_{A,add}$[eV]	none	none	none
$\pi_a^* \rightarrow \sigma_s^*$			
$\frac{d_{cross}-d_0}{d_0}$[%]	23.329	7.077	1.608
$\varepsilon_{QP}(d_{cross})$[eV]	+0.0096	+0.0980	+0.1079
$E(d_{cross})$[eV]	0.9228	0.2906	0.1500
E_A[eV]	0.7013	0.1436	0.0316
$E_{A,add}$[eV]	none	none	none

resp. the adsorption energy E_{ads}. Additional energy barriers are not expected to be more than small. The reason behind this is the weak adsorbate-substrate bonding of mixed dispersive and hydrogen bond character. The activation energies E_A behave analogously to d_{cross}. A significant reduction upon adsorption is observed throughout. The E_A values for C_6H_5Cl or C_6H_5Br on the ice surface lie in a range (0.017-0.176eV) below both E_B (0.232-0.294eV, cf. Tab. 4.5) and $E_{ads}(I_h(0001))$ (0.435-0.438eV, cf. Tab. 4.5). Hence the aforementioned converse effect is again of minor relevance. Furthermore the occurrence of electron-induced adsorbate dissociation at the $4S_{AD}$ orientational defect complex is favoured as the higher E_{ads} makes this adsorption site preferable as compared to idealised $I_h(0001)$ (cf. Fig. 4.12 and Tab. 4.5). This aspect is a key point as demonstrated by the experiments performed in

collaboration (see chapter 7). Only with an amorphous, i.e. defect-rich, ice surface rates of photoinduced DEA sufficiently high for the 2PPE experiments of Kemeny (2017) [50] were obtained (see section 7.2). Moreover the characteristic apparent height profiles on crystalline ice observed under the STM by Bertram (2017) [58] reveal that the adsorbates stay exclusively at defect sites and indicate that they dissociate upon illumination with photons able to inject electrons from the metal substrate into the ice conduction band[8] (see section 7.1). Judging from the theoretical results adsorption might catalyse DEA to C_6H_5F with outstanding magnitude in connection with a particular modification of the mechanism. $E(d) < E(d_0)$ can then also be reached if the electron capturing main resonance character is π^*_a or π^*_s instead of σ^*_s. However despite large reductions E_A (0.468-0.766eV) is comparable to E_{ads} (0.510eV resp. 0.773eV, cf. Tab. 4.5) and exceeds E_B (0.263eV). Diffusion should be preferred over DEA as there is no reason for significant additional energy barriers and even desorption has to be taken into account.

5.3. Summary

Modelling of DEA to the phenyl halogenide molecules in vacuum has yielded a comprehensive quantum mechanical explanation of the observations. In contrast to previous studies [39, 42], this work follows a systematic entirely ab-initio approach. It leads to qualitatively correct predictions throughout with rather small deviations from the experimental values as far as available. Subsequent essentially analogous investigations were also performed within the ab-initio DFT+GW framework and have further evidenced that adsorption of the molecules on the ice surface, particularly at strong electron traps, favours this dissociative process. This also pertains to choosing a heavier halogen. Additionally it turned out that the trends regarding lowering, localisation and evolution of the halogen-projected component of the main molecular resonances during DEA are preserved upon adsorption.

The carbon-halogen (C-X) bond fission energies E_{BF} are reproduced by hybrid DFT(PBE0) with minor total errors (-0.14 to +0.18eV) and coinciding trend (cf. Tab. 5.2).

Based on the results for the gas phase molecules it was concluded that it is sufficient to keep the phenyl group geometry fixed as the C-X bond is elongated.

The $\pi^*_{a,s}$ main resonances, for which the highest electron attachment cross sections of the gas phase molecules – except C_6H_5I – have been found (see (end of) section 4.1), experience marginal lowering and stay almost equally

[8] Consider additionally section 6.2 to understand why it is not about direct photodissociation.

localised along the dissociation pathway(s) (cf. Fig. 5.4, 5.10, 5.11 (C_6H_5Cl as example)). The σ_s^* molecular orbitals, whose quasiparticle energy is rapidly lowered while their localisation increases drastically, collapse into a state of the same character that harbours the excess electron after IC at the respective conical intersection and finally becomes stable. For an electronic state above the HOMO and with sufficiently strong localisation the contribution of the halogen remains indicative of its σ_s^* (dissociative) character.

$\pi_{a,s}^*$ of C_6H_5F play a special role among the main resonances of the gas phase molecules. Only these lie below the dissociation limit and the approximated amounts of energy lacking as the desired TNI dissociations are endothermic agree well with the experimental values and are unlikely to be provided by vibrational excitations (0.63-1.24eV missing according to experiment [206,215], (0.59-)0.95-1.08eV raising calculated, cf. Tab. 4.2 and 5.2). For all transient adsorbate anions the potential energy was found to be reduced within the investigated range.

The measured trends of DEA to the free molecules (cf. Tab. 5.1) are confirmed by the microscopic model as it evidences the lowering of the main molecular resonance of each type, the reduction of activation energies and the rise of the DEA cross section with increasing row of the halogen (cf. Tab. 5.3).

Gas phase phenyl halogenide molecules with a heavier halogen need drastically reduced activation energies E_A and C-X bond elongations to reach the main conical intersections and their SOMO can become stable at smaller C-X bond elongations (cf. Tab. 5.3). The position of the respective conical intersection relative to Φ_{vac} is much less affected (cf. Tab. 5.3). It seems to be of minor relevance for the DEA cross section if the incident electron is captured by the π_a^* or π_s^* main resonance, because their initial eigenenergies and the values of these quantities are similar or equal.

Experimental and theoretical data consistently indicate that low-energy DEA to C_6H_5Cl or C_6H_5Br originates from electron capture by the $\pi_{a,s}^*$ main resonance (cf. Tab. 5.1, 5.3). Due to prohibitively large activation energies E_A (1.214eV resp. 1.251eV, cf. Tab. 5.3), this is not the case for C_6H_5F, which is why the incident electron needs to possess much more kinetic energy (6.1eV resp. 6.3eV measured, cf. Tab. 5.1). This corresponds to the position of a higher σ_s^* or π_0^* molecular orbital (cf. Tab. 4.2). Based on the necessity of internal conversion and the concomitant, albeit slight, activation energies, the latter type is expected to contribute significantly less. Investigating C_6H_5I resulted in a unique low-energy DEA that is exothermic and does not require internal conversion or activation energy (cf. Tab. 5.2, 5.3). As expected the measurements yielded a vastly enlarged cross section, however the highest peak appeared at $\leq$0.04eV (cf. Tab. 5.1) instead of the calculated 0.38eV.

Idealised $I_h(0001)$ and the deepest excess electron trap constituted by an analysed orientational defect complex ($4S_{AD}$) were used to model DEA on the ice surface. The phenyl group is moved along the direction of the C-X bond (cf. Fig. 5.9), whose inclination towards the Fletcher stripe resp. the surface plane is $\leq 5^\circ$ throughout. Despite the adsorption-induced changes and the different levels of theory, the equilibrium length of this bond was only marginally modified (cf. Tab. 5.4, 9.1).

Adsorption leads to energy shifts of the main molecular resonances that are almost constant along the dissociation pathway (cf. Fig. 5.4, 5.10, 5.11 (C_6H_5Cl as example)).

Judging from the predicted reduction of the anionic potential energy, i.e. $E(d) < E(d_0)$, at sufficiently high C-X bond elongation all main resonances of the adsorbates lie above the dissociation limit (cf. Fig. 5.12 to 5.14). Going from vacuum to idealised $I_h(0001)$ to the $4S_{AD}$ orientational defect complex changes the potential energy curve $E(d)$ of a specific charged molecule resp. system due to the redshift of the electron capturing $\pi^*_{a,s}$ main resonances (0.186-0.290eV and further 0.511-0.585eV, cf. Tab. 5.3, 5.5, 5.6), the intensified lowering of the SOMO (esp. σ^*_s) during DEA ($\varepsilon_{QP}(\sigma^*_s)(d = 1.500d_0)$ lowered by 0.824-1.121eV via former and 0.528-0.644eV via latter repositioning) and the different bond fission energy landscapes ($E_0(d = 1.500d_0)$ by 0.159-0.259eV and further 0.056-0.076eV more favourable). The electronic structure modifications are the key point. This becomes obvious since the different levels of theory impose no essential limitations on the comparability of vacuum and surface results. In addition, since the excess electron is usually strongly localised, adjusting the degree of GW selfconsistency is expected to lower the surface SOMO even more. Hence the probability of dissociation following electron capture by a low main resonance should increase in the expected order independently of the molecule. This is further evidenced by the lower position of the SOMO during dissociation (compare vacuum Fig. 5.5 to 5.7 and surface Fig. 5.12 to 5.14) and the considerable reduction of activation energies E_A upon adsorption (cf. Tab. 5.3, 5.5, 5.6). E_A of C_6H_5Cl and C_6H_5Br at the surface deviates from the expected order (d_{cross} accordingly). However E_A lies in a range (0.017-0.176eV) below the adsorption energies E_{ads} at the idealised surface (0.435-0.438eV, cf. Tab. 4.5) and the binding energies E_B at the $4S_{AD}$ orientational defect complex with respect to them (0.232-0.294eV, cf. Tab. 4.5). Hence transferring the respective E_A to one of these adsorbate molecules is not considered to be sufficient to invoke its desorption or diffusion. The higher E_{ads} favours the occurrence of DEA at the orientational defect complex as compared to the reaction on the idealised ice surface (cf. Fig. 4.12 and Tab. 4.5). In particular the STM and 2PPE experiments performed in collaboration (see chapter 7)

demonstrate that the adsorbates stay (almost) exclusively at defects and that (photoinduced) DEA to C_6H_5Cl and C_6H_5Br indeed proceeds in the predicted energy range. Adsorption would catalyse DEA to C_6H_5F with outstanding magnitude if it was thereby enabled to originate from electron capture by the π_a^* or π_s^* main resonance. However the appendant E_A (0.468-0.766eV) is comparable to E_{ads} (0.510eV resp. 0.773eV, cf. Tab. 4.5) and exceeds E_B (0.263eV). Given the weak bonding to the ice surface of mixed dispersive and hydrogen bond character additional energy barriers are expected to be no more than small. Therefore diffusion is considered more likely than DEA and even desorption might occur.

If an analysis of the DEA rates on the ice surface is desired, it is important to understand that they are not determined by the activation energy E_A and heat supply (via phonons) alone. The initial energy of the excess electron and the presence of defects on the ice surface are also essential factors. The transfer of energy released upon the thermalisation of a photoexcited hot electron towards the lower conduction band edge is another way to excite the adsorbate vibrationally[9], in particular since the relevant temperature range is cryogenic.

For the gas phase molecules it should be possible to determine the energy-dependent probability of dissociation upon electron capture experimentally by combining DEAS – or better TOFMS – and ETS. However it seems that literature containing such values is not yet available.

[9] For the sake of completeness it should be mentioned that an incident electron can provide the necessary energy due to the inelasticity of the collision.

6. Photodissociation of C_6H_5X

In the atmosphere of the earth dissociative electron attachment (DEA) to halocarbons adsorbed on ice particles is mediated via photoexcitation of electrons into the conduction band at energies far below the width of the band gap (see section 3.1). These electrons come from states within the band gap arising due to the availability of dopants [51–53]. However an incident photon might also be absorbed by the adsorbate. The molecular optical excitation may lead to direct photodissociation (pho.). This additional dissociation channel may compete with DEA induced by the photoexcited electrons. The chief aim of this chapter is to investigate direct photodissociation on the ice surface. Since photodissociation of phenyl halogenides is well known for the gas phase (see section 6.1), the effect of adsorption on it is interesting per se. It is found that adsorption at the ice surface catalyses photodissociation to a much lesser extent than DEA. Furthermore no significant influence of defects on photodissociation was obtained, in contrast to DEA.

Low-energy molecular optical excitations occur at incident photon energies E_γ much smaller than the HOMO-LUMO gap or ionisation potential (IP) (cf. Fig. 4.2 and Tab. 4.1, 4.2), because the excited electron and the formally positive hole it leaves behind attract each other via Coulomb interaction.

$$\begin{array}{l} \xrightarrow{pho.}\ C_6H_5 + X \\ C_6H_5X + \gamma\,(\xrightarrow{exc.} C_6H_5X^*) \qquad\qquad \forall\ X{=}F, Cl, Br, I \\ \xrightarrow{REC}\ C_6H_5X + \gamma \end{array} \tag{6.1}$$

The energy E_{BF} (cf. Tab. 5.2) required to elongate resp. break the carbon-halogen (C-X) bond has to be provided by molecular vibrations (activation energy E_A) and the (subsequent) stabilisation of the hole-electron state. The typical scenario obtained from the calculations is illustrated as the schematic potential energy curves diagram Fig. 6.1. E_A is necessary to elongate the C-X bond such that the hole-electron state can undergo internal conversion (IC) from π_s-π_a^* to π_s-σ_s^* at the appropriate conical intersection. According to chapter 4 this means that an intramolecular transfer of the hole-electron state (esp. the excited electron) from the phenyl group to the halogen must occur.

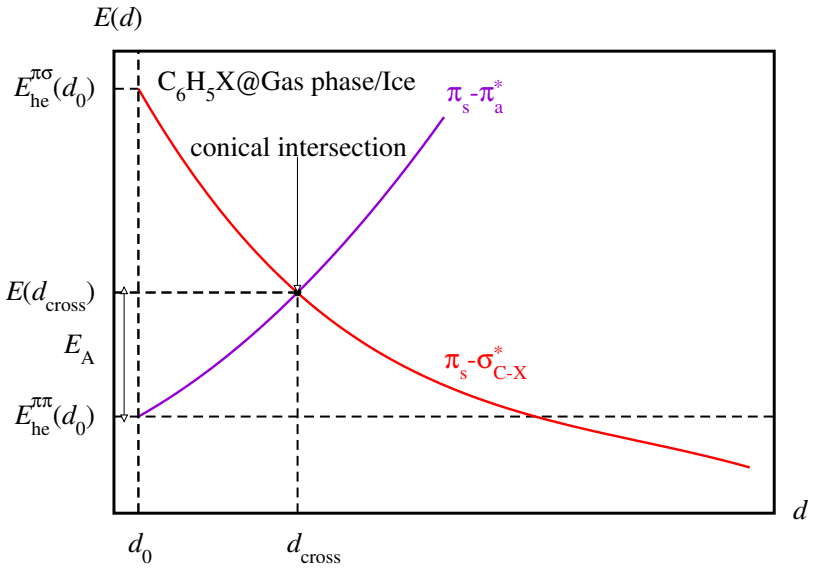

Figure 6.1.: Schematic molecular potential energy curves for the hole-electron states involved in low-energy photodissociation of phenyl halogenide molecules

Only afterwards the potential energy of the excited system is lowered by C-X bond elongation.

Since the hole-electron state has a finite lifetime, it can induce dissociation (pho., cf. reaction equation (6.1)) only within a certain timeframe. Otherwise it recombines (REC), whereby the electronic ground state of the molecule is restored and it emits a photon (cf. reaction equation (6.1)) or a molecular vibration (in the gas phase) resp. a phonon (on the ice surface) is excited. In general even a combination of both is possible.

Photodissociation is modelled by performing BSE (Bethe-Salpeter equation) calculations based on the GW(DFT) calculations discussed in chapter 5. This forces the assumption of geometrically identical dissociation pathways, whose justification is analysed in section 6.1. Before treating photodissociation on the ice surface in a largely analogous manner (see section 6.2), the approach is validated by reproducing the results of gas phase experiments (see section 6.1).

6.1. Microscopic mechanism in the gas phase

A hole-electron state in a gas phase phenyl halogenide molecule can be created by absorption of a photon with proper energy (optical excitation). It has a finite (average) lifetime, yet photodissociation (pho.) might occur be-

fore recombination (REC). Furthermore coupling of electronic and vibronic transitions also leads to remission of the photon at different energy, making the reaction inelastic. Like DEA (see chapter 5), photodissociation can be viewed as fully inelastic and does generally not proceed in the low-energy range unless sufficient activation energy is available due to heat supply.

Table 6.1.: Energies (E_γ) and corresponding wavelengths (λ) of photons upon whose absorption by gas phase phenyl halogenide molecules photodissociation (pho.) according to reaction equation (6.1), except for C_6H_5F, was observed experimentally are given including the method. Note that UV absorption spectra of C_6H_5X with X=F,Cl,Br exhibiting the onset at E_γ=4.6eV $\equiv$ λ=270nm for each molecule were recorded by Palmer et al. (2015/16) [203–205].

C_6H_5X	E_γ[eV]	λ[nm]	method
X=F			
Lee et al. (2006) [29]	6.42	193	TOFMS
	7.90	157	-//-
Wu et al. (2004) [28]	6.42	193	step-scan FTIR[1]
Huang et al. (2003) [22]	6.42	193	multimass ion imaging
X=Cl			
Wang et al. (1998) [23]	4.66	266	TOFMS
Ichimura et al. (1994) [33]	5.00	248	TOFMS
	6.42	193	-//-
X=Br			
Tang et al. (2003) [24]	4.64	267	(2+1) REMPI + TOFMS
	5.30	234	-//-
X=I			
Sage et al. (2011) [32]	3.76	330	VMI
	...	...	-//-
	6.02	206	-//-
Ashfold et al. (2010) [31]	4.66	266	VMI
	5.90	210	-//-
Hwang and El-Sayed (1996)	4.0695	304.67	(2+1) REMPI + TOFMS
[26]	4.0782	304.02	-//-
Cheng et al. (1995) [25]	4.46	278	(2+1) REMPI + TOFMS
Hwang and El-Sayed (1992) [27]	4.0695	304.67	(2+1) REMPI + TOFMS

[1] Fourier-transform infrared spectroscopy

To reveal the physics of photodissociation experimentally kinetic and internal (electronic and rovibronic) properties of the photofragments were investigated. To make spectroscopic techniques applicable they are photoionised with a laser, whereby their recoil velocity is barely affected. Furthermore if two photofragments are created as in each dissociative reaction considered in this section, the conservation of energy and momentum can be exploited to infer information about the state of one from the results of experiments on the other. Ion imaging techniques serve to determine the velocity distributions of state-selected photofragments. The original product imaging technique by Chandler and Houston (1987) [216] uses a molecular beam that is crossed first with a photolysis and then with short delay an ionisation laser beam, which are both pulsed. Acceleration by an electrostatic field allows to separate the singly positive ions of different masses, because they gain the same kinetic energy. This is also an important advantage in reducing noise. The three-dimensional velocity distribution of a specific photofragment in the barycentric system of the photolysis is computed based on its detected time-dependent two-dimensional spatial distribution with the aid of the inverse Abel transform [217]. The finite overlap of the molecular beam with the laser beams blurs the signal as it exceeds the channel width of the detector. Eppink and Parker (1997) [218] developed the velocity map(ped) (ion) imaging (VMI) technique to remedy this issue. It utilises an electrostatic lens such that ions of the same species and identical velocity are focussed on the same, ideally unique, spot at the detector if the voltages are properly adjusted. To a certain extent the recorded spectra already contain insight on the internal (electronic and rovibronic) state of the respective photofragment, because as both energy and momentum have to be conserved it determines the discrete possible angles between this velocity and the axis on which the educts move and finally collide in the barycentric system of the photolysis. Resonance-enhanced multiphoton ionisation (REMPI) photoexcites the reaction products (further) before photoionisation. Due to the quantum mechanical selection rules it depends not only on the initial internal (electronic and rovibronic) state of the reaction products but also the number of photons if they can be ionised resp. detected, i.e. the method is state-selective. REMPI can simultaneously be used to extract information on the photon absorption spectra of the molecules like in UV-vis spectroscopy. Combining REMPI with VMI or TOFMS furthers the insight gained by these spectroscopic methods, e.g. as it allows to determine branching ratios of photofragments with different internal states.

Low-energy photodissociation (pho.) of gas phase C_6H_5X with X=Cl,Br,I was experimentally (cf. Tab. 6.1) found to proceed according to reaction equation (6.1). Only for C_6H_5F measurements (cf. Tab. 6.1) revealed that other

photofragments (mainly HF, small amounts of H) are released in the low-energy range, whereas the halogen atom (F) does not appear.

The experimental trend (cf. Tab. 6.1) is that the photon energy needed to induce photodissociation of gas phase phenyl halogenide molecules is lower if a heavier halogen is considered. However it is almost equal for C_6H_5Cl and C_6H_5Br.

$$
\begin{aligned}
&E(d) \overset{\text{vertical}}{=} E^0(d) + E_{\text{he}}(d) \\
&E^0(d_0) = 0 \\
&E_{\text{A}} \coloneqq E(d_{\text{cross}}) - E(d_0) \\
&E_{\text{A,add}} \coloneqq \underset{d>d_0}{max}\{E(d) - E(d_{\text{cross}})\} \;\forall\; E_{\text{A,add}} > 0 \\
&E_{\text{A}}(\pi_{\text{s}} - \sigma_{\text{s}}^*) \coloneqq \underset{d>d_0}{max}\{E(\pi_{\text{s}} - \sigma_{\text{s}}^*)(d) - E(\pi_{\text{s}} - \sigma_{\text{s}}^*)(d_0)\} \;\forall\; E_{\text{A}}(\pi_{\text{s}} - \sigma_{\text{s}}^*) > 0
\end{aligned}
\tag{6.2}
$$

Equations (6.2) serve to extract the most important information about the ground and excited state potential energy surfaces and their components from the computational results. The potential energy $E(d)$ of the excited system is vertically approximated, i.e. it is the sum of the electronic ground state potential energy $E^0(d)$ already known from chapter 5 and the energy $E_{\text{he}}(d)$ required for the optical excitation under the assumption that the ionic geometry is left invariant. $E^0(d_0)$ is set to zero.

Endothermic reactions, i.e. here those with $E(d) > E(d_0)$ also at large d, can not proceed without being driven by molecular vibrations. Otherwise the law of energy conservation would be violated. By analogy with the chapter 5, the vertical excitation energy $E(d_0)$ can additionally be interpreted as the total energy of the excited system.

The crucial point of photodissociation in the low-energy range is usually internal conversion (IC) of the initial π_{s}-π_{a}^* hole-electron state into a dissociative π_{s}-σ_{s}^* hole-electron state. It is only possible by reaching the associated conical intersection at $d = d_{\text{cross}} > d_0$. Quantum mechanical requirements need to be fulfilled and the respective activation energy E_{A} has to be provided. It consists primarily of the attendant fraction of the C-X bond fission energy E_{BF}, but the continuous destabilisation of the initial π_{s}-π_{a}^* state contributes too. Albeit in principle local deviations from the typical evolution of the hole-electron state energy $E_{\text{he}}(d)$ can necessitate providing the activation energy $E_{\text{A,add}}$ or $E_{\text{A}}(\pi_{\text{s}} - \sigma_{\text{s}}^*)$, it turned out to be negligible if not even vanishing. $E_{\text{A,add}}$ occurs exactly if the highest potential energy of the excited system is not reached at the conical intersection. $E_{\text{A}}(\pi_{\text{s}} - \sigma_{\text{s}}^*)$ is the activation energy required for photodissociation starting directly from the $\pi_{\text{s}} - \sigma_{\text{s}}^*$ state.

The BSE calculations were beyond the Tamm-Dancoff approximation (TDA, see subsection 2.7.4) and employed a complex shift (CSHIFT = 0.2) twice as large as the default value. For the free molecules all 18 occupied bands and the 1000 most stable empty bands were used to model the wave function of each hole-electron state constructible on this basis. Each hole-electron state is labelled by the character of the band predominantly contributing to the hole resp. excited electron (e.g. π_s-π_a^* or $\pi_s - \sigma_s^*$).

Due to the electron-hole interaction optical excitations are possible at energies far below the *IP* of the respective molecule (cf. Fig. 4.2 and Tab. 4.1). The reaction products of photodissociation possibly induced by one of them also have to be neutral in view of their *IPs* [215, 219] and the bond fission energies E_{BF} (cf. Tab. 5.2). For low-energy photodissociation the missing energy (few eV) is too large to be provided by molecular vibrations.

Unless additional energy is provided, absorption of a photon whose energy E_γ is below the carbon-halogen bond fission energy E_{BF} (cf. Tab. 5.2) of the respective molecule can not lead to dissociation as postulated. According to the comparison with Tab. 6.2 such an optically excited state does not exist except for C_6H_5F, which is the only molecule preferring another dissociation pathway. Indeed photodissociation has exclusively been observed for E_γ about 1eV or more above the measured E_{BF} (compare Tab. 6.1 with 5.2). The remaining requirements are investigated hereafter.

Fig. 6.2 to 6.5 are the photodissociation potential energy curves diagrams. The evolution of the essential components during the reaction is presented. $E^0(d)$ has to be gained from molecular vibrations and stabilising the optical excitation so that the system can evolve on the dissociation pathway with the carbon-halogen bond length d as the generalised reaction coordinate. Judging from the results obtained under these assumptions, photodissociation may be induced by exciting the dissociative $\pi_s - \sigma_s^*$ state directly, except for C_6H_5F. However it takes less energy if the $\pi_s - \pi_a^*$ state is excited first and the activation energy E_A for its internal conversion to the $\pi_s - \sigma_s^*$ state at the conical intersection is provided afterwards, except for C_6H_5I. The positions of the conical intersections were obtained like in chapter 5.

The optical excitation can only lead to a singlet state as selection rules apply, but at a conical intersection with a triplet the excited singlet may undergo intersystem crossing in consequence of spin-orbit coupling, which is stronger if a heavier halogen is chosen. Triplets also exist at lower excitation energies than singlets and their inclusion often allows to find photodissociation channels with lower activation energy than those following from the singlets alone [220]. Spin-polarised BSE calculations were not possible in the framework of the present study, i.e. only singlets could be described. However the primary

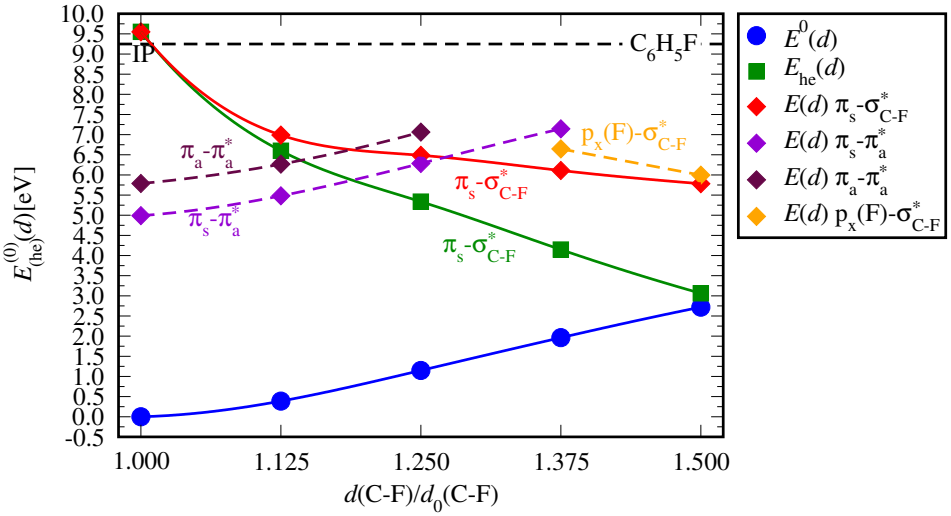

Figure 6.2.: Potential energy curves diagram for photodissociation of C_6H_5F from BSE(scGW$_0$) and underlying DFT(PBEo) ($E^0(d)$ (solid blue curve): ground state energy of the neutral molecule, $E(d)$ ($\pi_s - \sigma_s^*$ (solid red), $\pi_s - \pi_a^*$ (dashed violet), $\pi_a - \pi_a^*$ (dashed maroon, added only if relevant), $p_x(X) - \sigma_s^*$ (dashed orange, added only if relevant)): potential energy of the optically excited molecule, $E_{he}(\pi_s - \sigma_s^*)(d)$ (solid green): energy of the dissociative $\pi_s - \sigma_s^*$ optical excitation, splines serve as a guide to the eye between calculated points)

objective is to analyse the influence of adsorption on the ice surface on optical excitations and photodissociation of the molecules. Hence investigating singlet states is considered sufficient.
According to the calculated UV absorption spectrum of C_6H_5Br shown in Fig. 6.6 absorption within the molecular plane is preferred and the lowest optical excitations are optically dark. Orthogonal absorption is clearly weaker and occurs only at much higher photon energies. Furthermore the imaginary part of the off-diagonal terms of the symmetric complex dielectric tensor is very small throughout. The same characteristics were also found for the other phenyl halogenide molecules.

Low-energy photodissociation of the gas phase molecules is characterised by Tab. 6.2. Starting from the initially most stable $\pi_s - \pi_a^*$ state the components of the activation energy E_A and the bond elongation needed to reach the conical intersection occurring between it and the dissociative $\pi_s - \sigma_s^*$ state during the reaction are given. The vertical excitation energy $E_{he}(d_0)$ resp. E_γ (excitation by

[2] This value is above the vertical ionisation potential (IP) of the molecule (9.2490eV, cf. Tab. 4.1).
[3] This value is below the bond fission energy E_{BF} of the molecule (5.3764eV, cf. Tab. 5.2).

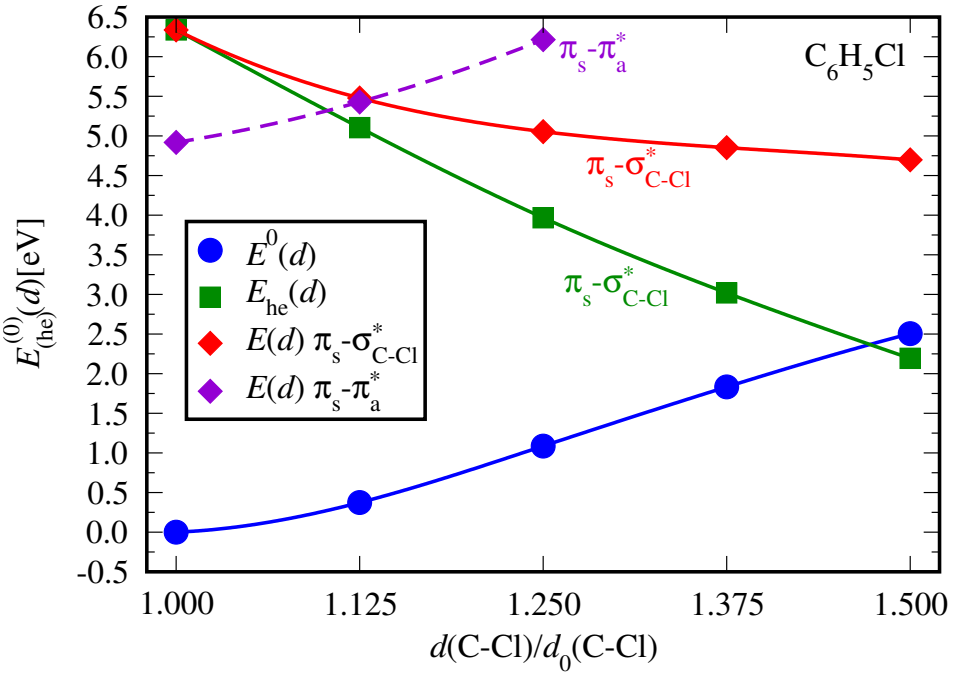

Figure 6.3.: Potential energy curves diagram for photodissociation of C_6H_5Cl from BSE(scGW$_0$) and underlying DFT(PBE0) (for explanation of colour code and design see Fig. 6.2)

photon absorption) for $\pi_s - \pi_a^*$ is barely affected by choosing a heavier halogen (4.852-4.989eV), whereas it diminishes drastically for $\pi_s - \sigma_s^*$ (4.427-6.337eV resp. 9.550eV[2]). Since C_6H_5F is the sole molecule that can absorb at $E_\gamma < E_{BF}$, $\pi_a - \pi_a^*$, which has the smallest $E_\gamma > E_{BF}$, was additionally considered in this case. Moreover, in contrast to the other molecules, the optical excitation $\pi_s - \sigma_s^*$ of C_6H_5F can not be made directly, because E_γ is larger than the *IP* and this π_s is the HOMO (cf. Fig. 4.2 and Tab. 4.1). Hence ionisation would occur. Only for C_6H_5I $\pi_s - \sigma_s^*$ requires smaller E_γ than $\pi_s - \pi_a^*$. This peculiar feature enables photodissociation without internal conversion. Therefore no conical intersection belonging to C_6H_5I was described.
The experimental observations (cf. Tab. 6.1) are most widely explained by the compendious theoretical results (cf. Tab. 6.2). The energy trend is correctly reproduced and except for C_6H_5F the comparison evidences that photodissociation following the lowest optical excitation has indeed occurred. Judging from the necessity of internal conversion and the position of the appendant conical intersections, i.e. the reduction of activation energies E_A and C-X bond elongations, photodissociation could be expected to be favoured if a heavier

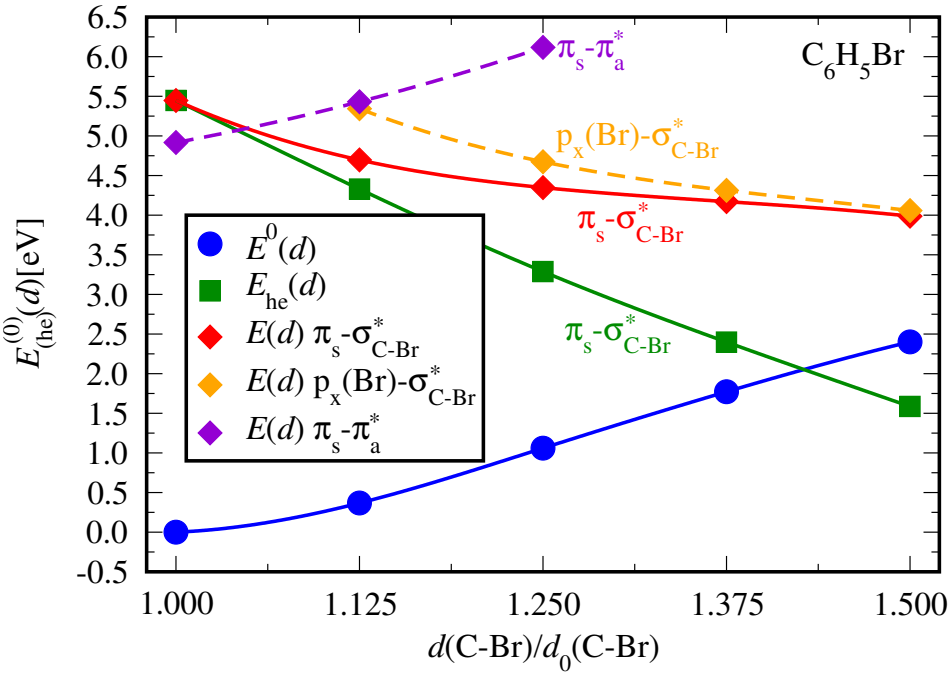

Figure 6.4.: Potential energy curves diagram for photodissociation of C_6H_5Br from BSE(scGW$_0$) and underlying DFT(PBE0) (for explanation of colour code and design see Fig. 6.2)

halogen is chosen. However as no statements regarding the probability distributions of absorption and recombination are made, the photodissociation cross sections are considered inaccessible at this point.

The calculated onset of optical absorption agrees well with those from the TDDFT studies of Palmer et al. (2015/16) and the CASPT2 study of Liu et al. (2004) (cf. Tab. 6.3). In particular the former yields a coinciding trend, i.e. a monotonous decrease with higher row of the halogen. Mixed results were obtained in other studies that treated only one of the molecules from the homologous series.

Along the homologous series of C_6H_5X with X=F,Cl,Br the conical intersection is reached at significantly smaller activation energy E_A (0.216-1.436eV, cf. Tab. 6.2) and C-X bond elongation (5.2-27.0% resp. 0.098-0.365Å, cf. Tab. 6.2) if a heavier halogen is considered. Molecular vibrations should easily provide E_A for photodissociation of C_6H_5Br, while from the present results it is less obvious for C_6H_5Cl. However the larger E_A is also available, since the experiments confirm that the E_γ threshold for these molecules is nearly identical (cf. Tab. 6.1, 6.2). For C_6H_5F the predicted E_A is prohibitive and

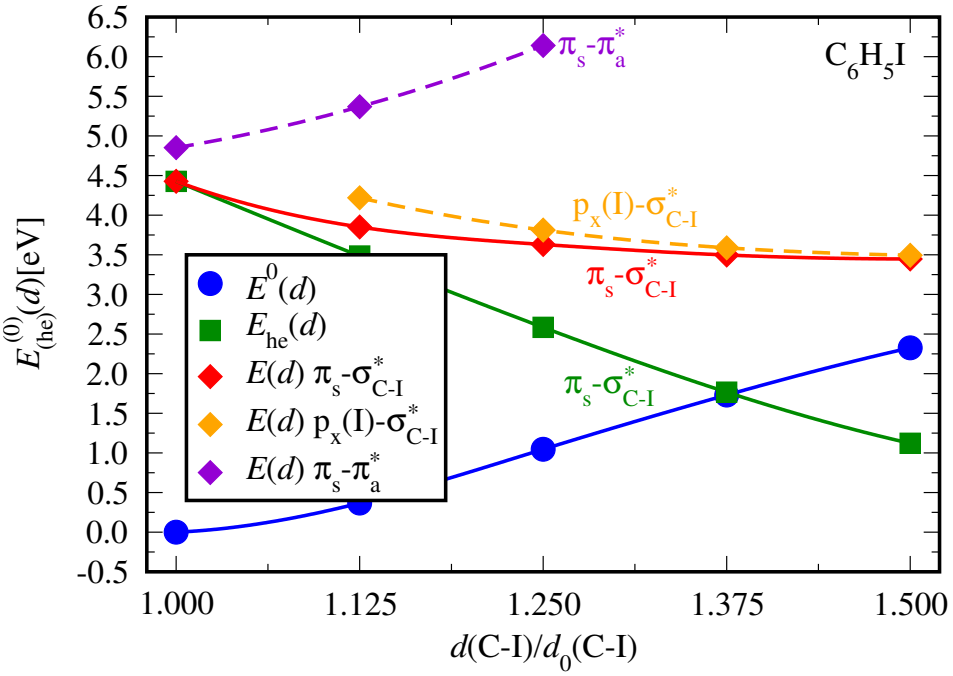

Figure 6.5.: Potential energy curves diagram for photodissociation of C_6H_5I from BSE(scGW$_0$) and underlying DFT(PBE0) (for explanation of colour code and design see Fig. 6.2)

hence explains that the reaction product F is not observed at incident photon energies E_γ comparable to the threshold for Cl or Br. Photodissociation of C_6H_5Cl (E_γ=4.66eV [23]) resp. C_6H_5Br (E_γ=4.64eV [24]) was investigated in a chamber with $8.0{\cdot}10^{-4}$Pa resp. $4.0{\cdot}10^{-4}$Pa pressure. C_6H_5F was irradiated with E_γ=6.42eV photons at T=298K and a total pressure of 4.7Pa [28] or T=283K and $4.8{\cdot}10^{3}$Pa [29] but the products were HF (C_6H_4) or more rarely H (C_6H_4F) instead of F (C_6H_5) (also [22]).

6.2. Role of the ice substrate

To reveal how the photodissociation of the molecules is modified upon their adsorption at the ice surface, the surface potential energy curves diagrams Fig. 6.7 to 6.9 have been elaborated by analogy with their vacuum equivalents Fig. 6.2 to 6.4 discussed in the section 6.1. The 64 nearest bands below resp. above the Fermi edge were taken into account for modelling of surface photodissociation. Reduced potential energy of the excited molecules, i.e. $E(d) < E(\pi_s - \pi_a^*)(d_0)$, within the investigated range was found just like in

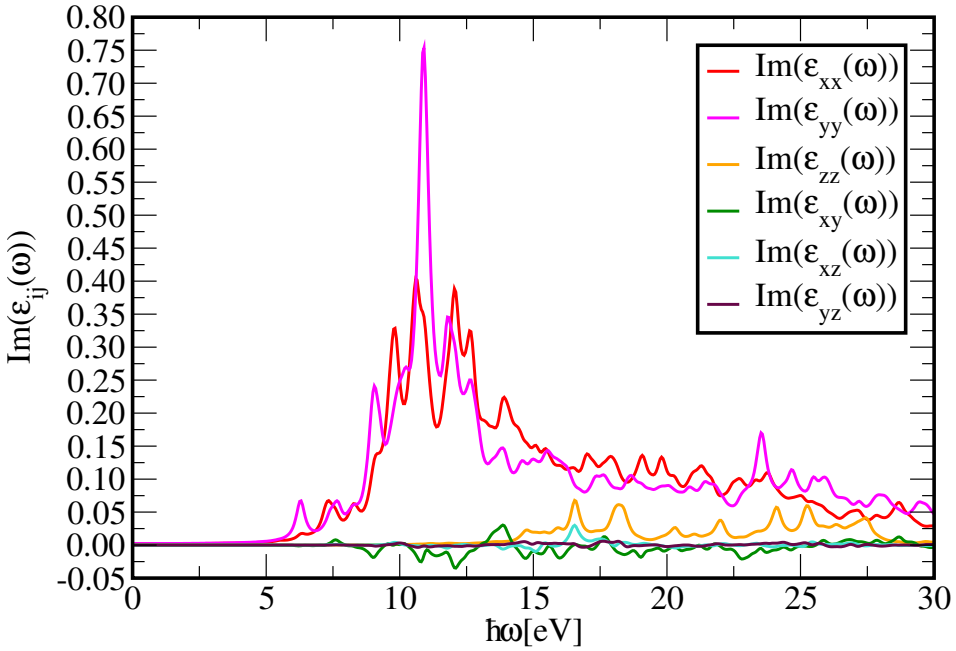

Figure 6.6.: UV absorption spectrum of C_6H_5Br from BSE(scGW$_0$(PBE0))

vacuum, i.e. for C_6H_5Cl and C_6H_5Br, but not C_6H_5F, whose dissociation should preferably yield HF and smaller amounts of H (judging primarily from [22] and an estimate of the effects of adsorption, further [28–30]). Adsorption affects the vertical excitation energies, their evolution along the dissociation pathway and the bond fission energy landscape $E^0(d)$. The reduced energy of the lowest $\pi_s - \sigma_s^*$ optical excitation is the main reason for the lesser activation energy E_A and hence the small catalytic effect of adsorption yielded by the present analysis. However it might include a significant contribution arising from the neglect of selfconsistency for the underlying surface GW calculations (see section E).

Adsorption at the pristine ice surface shifts the relevant $\pi_s - \pi_a^*$ optical excitation[4] of the molecules by -74 to +5meV and $\pi_s - \sigma_s^*$ is lowered by 450 to 935meV (cf. Tab. 6.2, 6.4). Proceeding from there to the orientational defect complex modifies the former by -21 to +112meV and the latter by -104 to +233meV (cf. Tab. 6.4, 6.5). Hence the initial hole-electron states are rather destabilised upon this transition to an electron trap. Considering $E_{he}(\pi_s - \sigma_s^*)(d = 1.500d_0)$ in the same order of substrate types leads to changes of -312

[4] On pristine I_h(0001) it is $\pi_{(a/)s}$ instead of π_s for the adsorbed C_6H_5F molecule (cf. Tab. 6.4).

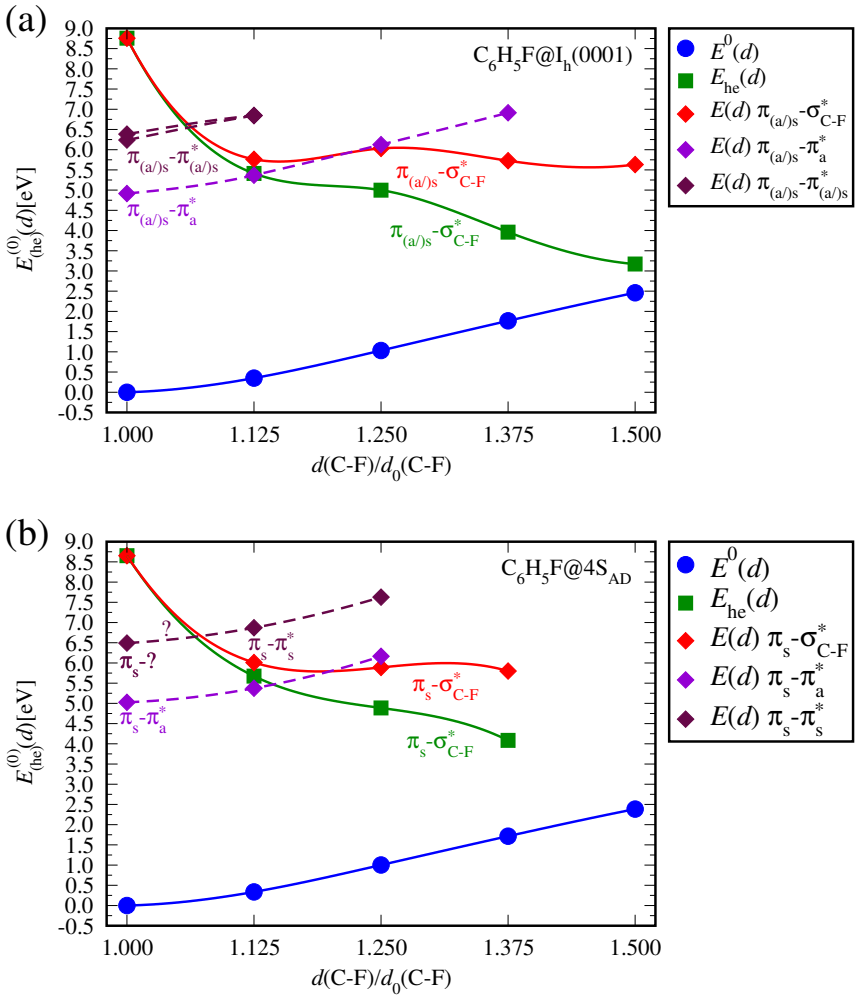

Figure 6.7.: Potential energy curves diagram for photodissociation of a C_6H_5F molecule adsorbed (a) on pristine I_h(0001) and (b) at a $4S_{AD}$ orientational defect complex from BSE(G_0W_0(PBEo-electronic)) and underlying DFT(PBE) with Grimme-D2 vdW corrections for adsorbate geometry and electronic ground state energies (explanation see section 4.2 and introduction to chapter 5) (for explanation of colour code and design see Fig. 6.2)

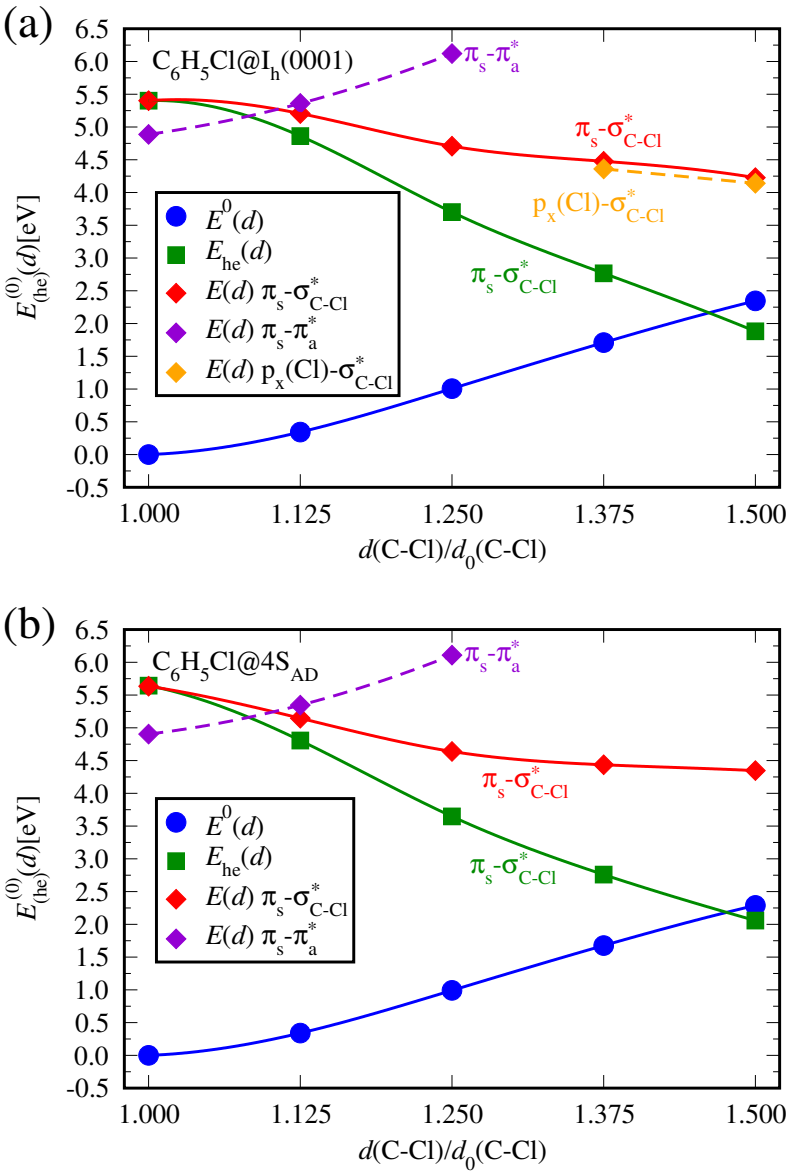

Figure 6.8.: Potential energy curves diagram for photodissociation of a C_6H_5Cl molecule adsorbed (a) on pristine $I_h(0001)$ and (b) at a $4S_{AD}$ orientational defect complex from BSE(G_0W_0(PBEo-electronic)) and underlying DFT(PBE) with Grimme-D2 vdW corrections for adsorbate geometry and electronic ground state energies (explanation see section 4.2 and introduction to chapter 5) (for explanation of colour code and design see Fig. 6.2)

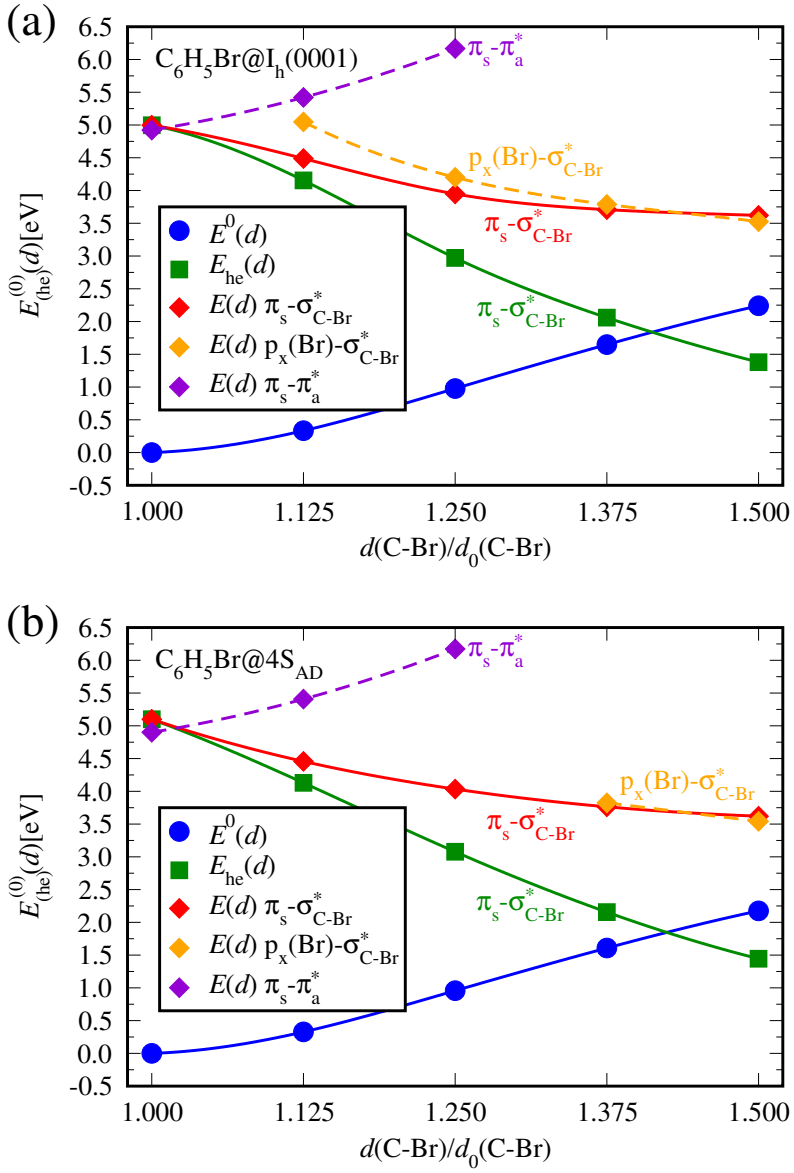

Figure 6.9.: Potential energy curves diagram for photodissociation of a C_6H_5Br molecule adsorbed (a) on pristine $I_h(0001)$ and (b) at a $4S_{AD}$ orientational defect complex from BSE(G_0W_0(PBEo-electronic)) and underlying DFT(PBE) with Grimme-D2 vdW corrections for adsorbate geometry and electronic ground state energies (explanation see section 4.2 and introduction to chapter 5) (for explanation of colour code and design see Fig. 6.2)

Table 6.2.: Low-energy photodissociation of C_6H_5X molecules with X=F,Cl,Br,I in vacuum: Dominant characters and eigenenergies of hole-electron states and interpolated conical intersections between them and appendant activation energies E_A from BSE(scGW$_0$) and underlying DFT(PBE0)

X=	F	Cl	Br	I
$E_{he}(d_0)$[eV]				
$\pi_s - \sigma_s^*$	9.5501[2]	6.3372	5.4474	4.4269
$\pi_{s(a)} - \pi_a^*$	4.9893[3] (5.7873)	4.9182	4.9170	4.8518
$E_A(\pi_s - \sigma_s^*)$[eV]	none	none	none	none
$\pi_{s(a)} - \pi_a^* \to \pi_s - \sigma_s^*$				
$\frac{d_{cross}-d_0}{d_0}$[%]	27.043 (19.448)	13.016	5.241	—
$E_{he}(d_{cross})$[eV]	5.1431 (5.8984)	5.0576	4.9786	—
$E^0(d_{cross})$[eV]	1.2821 (0.8114)	0.4032	0.1540	—
$E(d_{cross})$[eV]	6.4252 (6.7098)	5.4608	5.1326	—
E_A[eV]	1.4359 (0.9225)	0.5736	0.2156	—
$E_{A,add}$[eV]	none (none)	none	none	—

to +109meV and +66 to +176meV[5]. This means that the lowering of this hole-electron state by absorption is much weakened or even reversed over the course of photodissociation as expected due to its rapid stabilisation. Adsorption at the orientational defect complex again turned out to be unfavourable as compared to the idealised ice surface. The influence of adsorption on the bond fission energy landscape $E^0(d)$ of the molecules was already discussed in section 5.2. It favours photodissociation, in particular at the defective ice surface, but plays only a minor role.

For the position of the conical intersection relative to the initial optical excitation both the halogen and adsorption on the ice surface play an essential role. Like in the gas phase (cf. Tab. 6.2) it is reached with smaller (relative) carbon-halogen bond elongation $d_{cross} - d_0$ ($d_{cross}/d_0 - 1$) and activation energy E_A if a heavier halogen is chosen (cf. Tab. 6.4, 6.5). This trend is always very strong and unambiguous. Upon adsorption on the ice surface the values of these quantities are significantly reduced for each phenyl halogenide molecule. This is mainly due to the initially much superior stability of the

[5] It is unclear if the corresponding value for C_6H_5F lies within the latter range, however $E_{he}(\pi_s - \sigma_s^*)(d = 1.375d_0)$ does (+124meV).

[6] It is unclear if this amount of energy is sufficient for photodissociation.

[7] $\pi_{(a/)s}$ instead of π_s for X=F.

[8] Presumably π_s^*.

Table 6.3.: Theoretical onset of optical absorption at the minimum photon energy $E_{he}^{min}(d_0)$ for C_6H_5X molecules with X=F,Cl,Br,I in vacuum: The BSE(scGW$_0$(PBE0)) results of the present study (cf. Tab. 6.2) are compared to those of previous investigations [32, 34, 203–205, 220–223] applying other methods.

C_6H_5X	$E_{he}^{min}(d_0)$[eV]	method
X=F		
present study (cf. Tab. 6.2)	4.9182	BSE
Palmer et al. (2016) [205]	5.0918	TDDFT
Mondal and Mahapatra (2010) [221, 222]	5.055	coupled-cluster
Liu et al. (2004) [220]	4.74	CASPT2
X=Cl		
present study (cf. Tab. 6.2)	4.9170	BSE
Palmer et al. (2016) [204]	4.8916	TDDFT
Liu et al. (2004) [220]	4.64	CASPT2
Sobolewski and Domcke (2000) [34]	4.16	CASPT2
X=Br		
present study (cf. Tab. 6.2)	4.8518	BSE
Palmer et al. (2015) [203]	4.876	TDDFT
Liu et al. (2004) [220]	4.74	CASPT2
X=I		
present study (cf. Tab. 6.2)	4.4269	BSE
Palmer et al. (2015) [223]	4.272	TDDFT
	4.770	MRDCI
Sage et al. (2011) [32]	3.90	SOC-CASPT2
Liu et al. (2004) [220]	4.50	CASPT2

$\pi_s - \sigma_s^*$ state and it makes barely any difference if the idealised or the defective surface is considered. Starting from $\pi_s - \pi_a^*$ and independently of the substrate E_A is uncritical for C_6H_5Br, disputable for C_6H_5Cl and prohibitive for C_6H_5F. Adsorption possibly enables photodissociation arising from the next lower optical excitation of C_6H_5F due to the concomitant reduction of E_A. Note that, in contrast to the $\pi_s - \pi_a^*$, its vertical excitation energy is strongly raised upon adsorption and its character is modified.

Table 6.4.: Low-energy photodissociation of a C_6H_5X molecule with X=F,Cl,Br adsorbed on pristine $I_h(0001)$: Dominant characters and eigenenergies of hole-electron states and interpolated conical intersections between them and appendant activation energies E_A from G_0W_0(PBE0-electronic) and underlying DFT(PBE) with Grimme-D2 vdW corrections for adsorbate geometry and electronic ground state energies (explanation see section 4.2 and introduction to chapter 5)

X=	F	Cl	Br
$E_{he}(d_0)$[eV]			
$\pi_s - \sigma_s^*$	8.7573	5.4019	4.9969
$\pi_s - \pi_a^*$	4.9154[6] (6.2378)	4.8872	4.9221
$E_A(\pi_s - \sigma_s^*)$[eV][7]	none	none	none
$\pi_s - \pi_a^* \rightarrow \pi_s - \sigma_s^*$[7]			
$\frac{d_{cross}-d_0}{d_0}$[%]	22.602 (8.744)	9.614	0.928
$E_{he}(d_{cross})$[eV]	5.0778 (6.4175)	4.9866	4.9343
$E^0(d_{cross})$[eV]	0.9025 (0.2448)	0.2640	0.0248
$E(d_{cross})$[eV]	5.9803 (6.6623)	5.2506	4.9591
E_A[eV]	1.0649 (0.4245)	0.3634	0.0370
$E_{A,add}$[eV]	0.0512 (none)	none	none

6.3. Summary

It was found that the catalytic effect of adsorption at the ice surface on low-energy photodissociation of phenyl halogenide molecules (C_6H_5X with X=F,Cl,Br) is very small at best (compare Tab. 6.2 with 6.4, 6.5 and Fig. 6.2 to 6.4 with 6.7 to 6.9). This BSE study is based on the preceding GW(DFT) calculations performed to analyse DEA (see chapter 5). Hence the dissociation pathway(s) had to be adopted (pho., reaction equation (6.1)).

The assumption coincides with the experimental observations of photodissociation in the gas phase, except for C_6H_5F (references given in Tab. 6.1). These are most widely explained by the computational results (consolidated in Tab. 6.2 (X=F,Cl,Br,I)), which among others reproduce the experimental energy threshold trend correctly with reasonable comprehensible deviations from the measured values (cf. Tab. 6.1). The onset of optical absorption was found to lie lower if a heavier halogen is involved and it is in good agreement with other theoretical studies also considering the homologous series (cf. Tab. 6.3). Optical excitation of the $\pi_s - \pi_a^*$ hole-electron state happens at very similar photon energy E_γ for all free molecules. While $\pi_s - \pi_a^*$ is slightly destabilised along the postulated dissociation pathway, $\pi_s - \sigma_s^*$ is lowered drastically. Choosing a heavier halogen also causes the latter and hence favours

Table 6.5.: Low-energy photodissociation of a C_6H_5X molecule with X=F,Cl,Br adsorbed at a $4S_{AD}$ orientational defect complex on $I_h(0001)$: Dominant characters and eigenenergies of hole-electron states and interpolated conical intersections between them and appendant activation energies E_A from G_0W_0(PBE0-electronic) and underlying DFT(PBE) with Grimme-D2 vdW corrections for adsorbate geometry and electronic ground state energies (explanation see section 4.2 and introduction to chapter 5)

X=	F	Cl	Br
$E_{he}(d_0)$[eV]			
$\pi_s - \sigma_s^*$	8.6530	5.6347	5.1000
$\pi_s - \pi_a^*(?^8)$	5.0265^6 (6.4916)	4.9039	4.9009
$E_A(\pi_s - \sigma_s^*)$[eV]	none	none	none
$\pi_s - \pi_a^*(?^8) \rightarrow \pi_s - \sigma_s^*$			
$\frac{d_{cross}-d_0}{d_0}$[%]	21.219 (8.965)	9.815	2.164
$E_{he}(d_{cross})$[eV]	5.1248 (6.5221)	4.9859	4.9319
$E^0(d_{cross})$[eV]	0.8009 (0.2414)	0.2652	0.0567
$E(d_{cross})$[eV]	5.9257 (6.7635)	5.2511	4.9886
E_A[eV]	0.8992 (0.2719)	0.3472	0.0877
$E_{A,add}$[eV]	none (none)	none	none

photodissociation energetically. More specifically for X=F,Cl,Br the conical intersection at which internal conversion from the initial $\pi_s - \pi_a^*$ to the dissociative $\pi_s - \sigma_s^*$ is enabled can be reached with essentially smaller activation energy E_A, whose values also explain why the reaction product F is not observed in contrast to the other halogen atoms. Moreover it occurs at much reduced C-X bond elongation. Photodissociation of C_6H_5I is possible without internal conversion, because optically exciting $\pi_s - \sigma_s^*$ requires less E_γ than $\pi_s - \pi_a^*$.

Primarily due to the initial stabilisation of the $\pi_s - \sigma_s^*$ hole-electron state, the conical intersections of the adsorbed molecules occur at smaller C-X bond elongation and can be reached with less activation energy E_A than their vacuum equivalents, although $\pi_s - \pi_a^*$ is optically excited at almost identical E_γ. The resulting catalytic effect of adsorption is very small and seems to exhibit no preference for electron traps. Furthermore it might to some extent be influenced by the practically forced neglect of GW selfconsistency for the underlying surface calculations. Increasing the row of the halogen has essentially the same repercussions as in vacuum. Reduced potential energy of the excited system was always found within the investigated range except for C_6H_5F (cf. Fig. 6.2 to 6.9), which should be the sole (adsorbed) molecule

dissociating along another pathway. Independently of the substrate E_A is uncritical for C_6H_5Br, disputable for C_6H_5Cl and prohibitive for C_6H_5F.

7. Comparison of theoretical predictions to results of experiments performed in collaboration

The theoretical model developed in this thesis has been verified by experiments performed in collaboration. This means primarily that the trends found for ice surface DEA to adsorbed phenyl halogenide molecules (C_6H_5X with X=F,Cl,Br) coincide resp. have a consistent interpretation so that more light is shed on the underlying microscopic mechanisms. Theory and experiment evidence that hot, instead of solvated, excess electrons from the ice conduction band induce this type of reaction, which occurs preferably at defects and is favoured if a heavier halogen is involved. This chapter aims for a discussion of the experiments and the meaning of their results. The collaborators employed low-temperature (7.5-11K) scanning tunnelling microscopy (STM, Cord Bertram[1] [58]) as well as time- and angle-resolved two-photon photoelectron spectroscopy (2PPE, Ishita Kemeny[2] [50]). They systematically investigated modifications evoked by illumination for the adsorbed phenyl halogenide molecules on a Cu(111) transition metal substrate also with amorphous ultrathin films or crystalline nanoislands of D_2O ice. Setup, execution and evaluation of the experiments are detailed in their PhD theses (2017) [50, 58].

Molecular reorientations upon illumination of mere ice structures were assessed with the aid of characteristic apparent height profiles obtained from STM imaging. New or modified electron traps might emerge thereby (see section 3.2), in particular this affects the local electron affinities and possibly also those at longer range. It was revealed that they occur preferably in the vicinity of defects and are directly linked with excess electron solvation at them. DEA to C_6H_5Cl and C_6H_5Br was investigated on the same basis. At 3.8eV incident photon energy E_γ this process is enabled by deposing a BL (bilayer, see chapter 3) amount of amorphous porous or crystalline D_2O ice on the Cu(111) substrate.

Illumination leads to several processes affecting the work function, i.e. the minimum energy required to release an electron from the metal substrate, primarily due to surface charging. Their extent, time-dependence and nature were analysed with 2PPE. For all molecules (C_6H_5X with X=F,Cl,Br) adsorbed

[1] Ruhr-University Bochum, supervisor Prof. K. Morgenstern

[2] University Duisburg-Essen, supervisors Prof. U. Bovensiepen and Dr. M. Ligges

on ultrathin ice films two processes increasing the work function are observed: a fast uniform one interpreted as excess electron attachment to or photoannealing of shallow electron traps with an adsorbed molecule and a slow one more intense for heavier halogens that is assigned to photoinduced ionisation or dissociation (DEA) of the adsorbates. Before the systems reached a photostationary state a converse third process was found for C_6H_5Cl or C_6H_5Br adsorbates at E_γ=3.8eV and sufficiently high photon flux. The work function change can only be induced by photons able to create excess electrons in the ice conduction band. Despite exhibiting the same trends the corresponding reaction rates diminish drastically for crystalline as compared to amorphous ice. In a broader sense the experiments, involving comparative analysis, serve to demonstrate that the DEA cross section enhancement of halogenated organic molecules upon their adsorption on polar surfaces is caused by delocalised excess electrons and preexisting electron traps. Furthermore the results imply that the observed work function change is a spectroscopic signature from the transient anionic state of the adsorbates, especially because it is not found for the mere D_2O/Cu(111) structures.

The theoretical results (see chapters 5 and 6) indicate that the observed dissociative processes have to be DEA, because the incident photon energies are insufficient for direct neutral photodissociation whereas excitation of electrons from the metal substrate into the ice conduction band occurs as demonstrated by 2PPE experiments.

7.1. Low-temperature scanning tunnelling microscopy

Crystalline (cf. Fig. 7.1) and amorphous porous (cf. Fig. 7.2) ice structures on Cu(111), including their shape and characteristic apparent height profiles, were successfully reproduced by resorting to previously described approaches [61, 185, 224–226], whereby incorporating already available knowledge was enabled. Among these are nanoislands terminated by incomplete bilayers. For crystalline ice their height and diameter are greater and the terminating incomplete bilayers form superstructures such as (2x1) or (2x2). Earlier studies [3, 227, 228] reported 2PPE spectra showing that bilayer amounts of D_2O on metal substrates indeed solvate excess electrons. Those of Stähler et al. (2007 and later private communication) [227, 229] are directly related to the systems under consideration (see also [58]). In both cases signatures of the solvated electrons were detected at 2.6-3.2eV above the Fermi edge of the metal substrate, whereas its surface states and image potential states lie higher (time delay Δt=0-200fs). Upon crystallisation the solvated electron feature diminishes by two orders of magnitude since the ice surface defect density

is extremely reduced. Electron trap depths of up to 0.98eV relative to the ice conduction band resulted from the G_0W_0(PBE0-electronic) calculations discussed in section 3.2 and the same approach yielded 0.57eV [230] gained by reorientation of dangling OH groups at the (2x1)-superstructure[3] displayed in Fig. 7.1. This energy range agrees well with the lowering of the energy of (photoexcited) excess electrons measured for D_2O/Ru(001) (0.6eV reached by continuous increase in binding energy, 2BL crystalline ice, Bovensiepen et al. (2009) [3], also cf. Fig. 1.2) and D_2O/Cu(111) (0.6eV larger vertical binding energy, 2.5(5)BL amorphous solid water, Stähler et al. (2015) [228]). A total amount of 0.9BL of D_2O was deposed on Cu(111). After obtaining the desired structures, the system was cooled down to 7.5K. Laser illumination caused heating, yet the temperature stayed below 11K. Hence mere thermal effects are not sufficient to induce molecular reorientations [231, 232].

Fig. 7.1 displays the modification of a crystalline ice structure observed with STM and a structural model for clarification. As demonstrated by Bockstedte et al. (2016) [61], each protrusion corresponds to a single water molecule. Hence it is about a laser-induced (λ=400nm $\equiv$ E_γ=3.10eV) collective repositioning within the top (bright protrusions) and bottom (weaker protrusions) incomplete bilayer, whereby the defects in these (2x1)-adrows are eradicated so that its long-range order is not interrupted anymore. It concerns not only the D_2O molecules directly at the originally existing defects. The direction of the four adjacent dimolecular chains between those in the bottom incomplete bilayer changes by $\approx$30° anticlockwise. This collective motion exemplifies the existence of long-range interactions within the molecular network. The structural model illustrates the necessity of breaking hydrogen bonds between adjacent oxygen atoms as some molecules move to neighbouring adsorption sites.

How should it be possible that excess electron solvation triggers molecular reorientations? The large band gap of ice I_h (see section 3.1) does not permit the released energy to dissipate other than by vibronic excitations of the molecules surrounding the defect. However when the energy is momentarily accumulated as heat by a few molecules adjacent to the defect, higher vibronic excitations are possible. Instead of or additionally to being subject to further dissipation, these can also couple anharmonically to translational (or rotational) modes considering the required amount of energy (DFT(BLYP) (GGA) calculated hydrogen bond breaking energy (cf. Fig. 7.1) 140meV in the (2x1)-superstructure and 163meV in the bottom dimolecular chains [61]).

[3] Note that Bockstedte et al. (2016) [61] calculated the geometries and formation energies of such terminations. Thereby they provided a theoretical basis for the investigation of electron solvation at them.

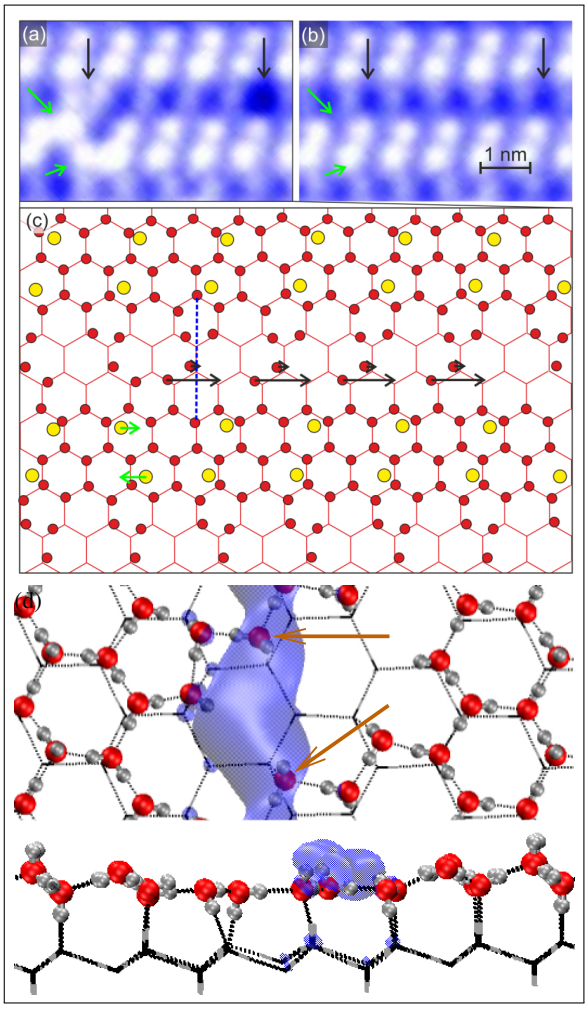

Figure 7.1.: Laser-induced molecular reorientations at the surface of 0.9BL crystalline D_2O on Cu(111) (a,b) STM images (-0.1V, 2pA) (a) before (b) after illumination (t=15.2h, λ=400nm $\equiv$ E_γ=3.10eV, $2.6{\cdot}10^5$ photons per molecule), modifications of both incomplete bilayers indicated by green (top) and black arrows (bottom) (c) structural model with arrows adopting this colour code to indicate directions and length of the molecular translations (yellow dots: top molecules, red dots: bottom molecules, red hexagonal lattice: highest complete bilayer) (d) top (above, arrows point to two reoriented molecules) and side view (below) of the calculated charge density (blue) of an electron solvated between the interconnecting chains (0.57eV trap depth according to G_0W_0(PBE0-electronic) [230]); (a-c) from Bertram (2017) [58]

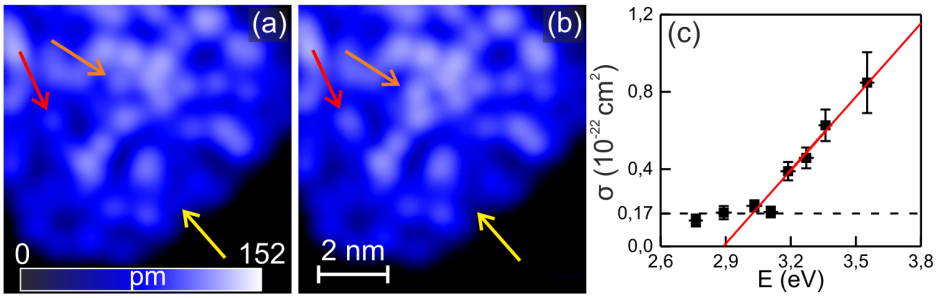

Figure 7.2.: Laser-induced molecular reorientations at the surface of 0.9BL amorphous porous D_2O on Cu(111) (a,b) STM images (0.1V, 8pA) (altitude scale in (a), latitude scale in (b)) (a) before (b) after illumination (t=7h, λ=390nm $\equiv E_\gamma$=3.18eV, $2.5{\cdot}10^5$ photons per molecule), modifications indicated by arrows (c) cross section of modifications compared to the energy of incident photons (lines serve to guide the eye); Bertram (2017) [58]

This phenomenon was discussed with a specific example and counterexample by Komeda et al. (2002) [233]. It explains the occurrence of hydrogen bond breaking and the thereby enabled collective molecular motions affecting the STM images.

How can it be verified that the laser-induced collective molecular repositionings are mediated by excess electron solvation? To that end amorphous porous D_2O on Cu(111) (cf. Fig. 7.2a,b) was illuminated with photons in the energy range from 2.75eV (451nm) to 3.65eV (340nm). This ice structure exhibits the highest surface defect density. Hence it is most suited to solvate excess electrons and the cross section of photoinduced modifications should be maximised. The lower ice conduction band edge lies at ≈3.0eV above the substrate Fermi level (measured 2.9eV with STS [227] and 3.25eV with 2PPE [234]) and the defects broaden it by at least 0.2eV [226, 228]. Fig. 7.2a,b display modifications evoked by illumination with 3.18eV (390nm) photons. The water molecules can move parallel (orange arrow), towards (yellow arrow) or away (red arrow) from the substrate. Like on crystalline ice (cf. Fig. 7.1a,b) it seems that they stay intact, because there is no fundamental change in the appearance of the protrusions. The cross section of laser-induced collective molecular repositionings was found to be almost constant at $0.17(5){\cdot}10^{-22}\mathrm{cm}^2$ up to a threshold of 3.0(1)eV (≡ 400-428nm) incident photon energy (cf. Fig. 7.2c). Above it grows linearly at a rate of $1.3(2){\cdot}10^{-22}\mathrm{cm}^2\mathrm{eV}^{-1}$ (cf. Fig. 7.2c). Because the threshold energy coincides with the aforementioned position of the lower ice conduction band edge relative to the substrate Fermi level, it is concluded that the cross section increase is due to the solvation of excess electrons from the ice conduction band. Furthermore it is consistent with the

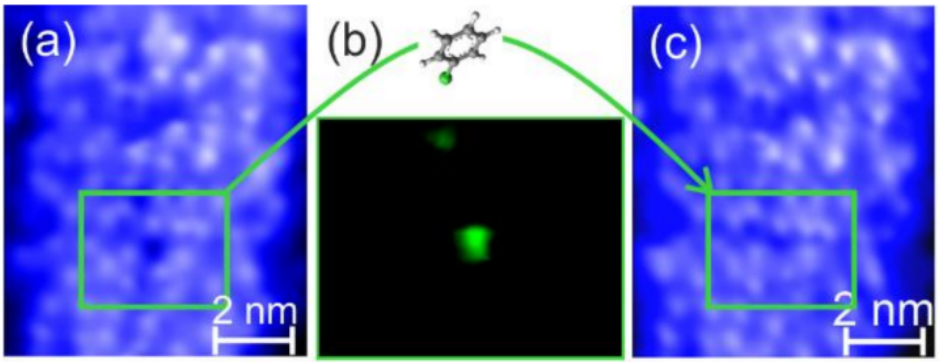

Figure 7.3.: Identification of a molecular adsorption site on 0.9BL crystalline D_2O on Cu(111) (a,c) STM images recorded at 7.5K (-0.1V, 1pA) (a) before (c) after deposition of C_6H_5Cl (0.05 $\frac{\text{molecules}}{\text{nm}^2}$ at 11K) (b) difference between the tagged rectangular areas in green enlarged by a factor of 4; Bertram (2017) [58]

also monotonic rise of solvated electron density in a very similar energy range indicated by 2PPE spectra recorded for crystalline D_2O on Ru(001) [3].

The observed correlation between molecular reorientations and the solvation of excess electrons substantiates the aforementioned 2PPE study of Bovensiepen et al. (2009) [3], who surmised that it proceeds continuously through several conformational substates, i.e. molecular configurations. Regarding the concomitant energy transfer it should be noted that the formation energies and depths obtained for the electron traps discussed in section 3.2 are similar.

The STM images provide insight into adsorption behaviour and photoinduced reactions of the adsorbates (C_6H_5Cl and C_6H_5Br). This is clarified by successively considering the various elements of their morphology. After deposing the molecules a typical scenario is discovered. New protrusions (cf. Fig. 7.3) higher and more elliptical than the previously identified water molecules appear at or close to ice surface defects, frequently at the edges of ice nanoislands and in clusters on the metal substrate. Their unique characteristic apparent height profile suggests that the adsorbed molecules are represented one-to-one. Since they avoid defect-free sites at the ice surface and form clusters on the metal substrate, the adsorbed molecules must already be mobile in this low-temperature range. Furthermore their distribution is consistent with the calculated adsorption energies (cf. Tab. 4.5), especially because ice nanoisland edges should exhibit the highest density of suited defects. These are sufficiently strong adsorption sites and tendentially deep electron traps. DEA is favoured by this spatial correlation, however it is induced by ice conduction band, instead of fully solvated, excess electrons (see chapter 5). With

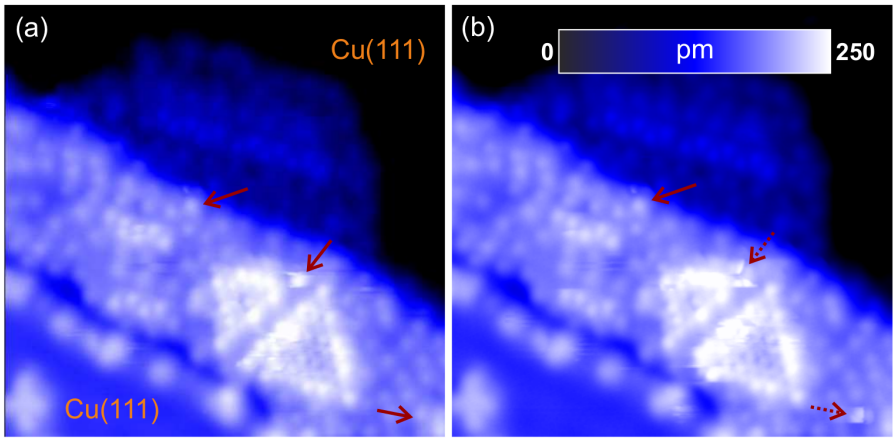

Figure 7.4.: Photoinduced reaction (dissociation) of C_6H_5Br molecules adsorbed on 0.9BL crystalline D_2O on Cu(111) (a,b) STM images (0.1V, 2pA) (altitude scale in (b)) (a) before (b) after illumination (λ=330nm $\equiv E_\gamma$=3.76eV, $2.0{\cdot}10^5$ photons per water molecule), C_6H_5Br molecules (solid arrows) and new characteristic apparent height profiles appearing upon illumination (dashed arrows) indicated; Bertram (2017) [58]

the regular metallic STM tip it is difficult to distinguish between amorphous ice and adsorbed phenyl halogenide molecules. Functionalising the STM tip by attaching one of these molecules to its apex substantially improves the STM image resolution so that this issue is remedied. It works because they interact with their own as well as the other species via hydrogen bonds. These are responsible for the formation of mere ice structures and adsorbate molecule clusters on the metal substrate. Furthermore they also play an important role in the positioning of the adsorbates on the ice surface (see also section 4.2).

C_6H_5Br on crystalline D_2O was investigated first to demonstrate lucidly that photoinduced reactions of the adsorbed molecules indeed occur (see Fig. 7.4). New characteristic apparent height profiles are indicative of reaction products, because those of the aforementioned species are invariant under molecular reorientations[4]. After illumination with λ=330nm ($\equiv E_\gamma$=3.76eV) photons two areas of different apparent heights were observed instead of some adsorbed C_6H_5Br molecules previously detected at the same ice surface sites. Their global maximum is much higher than that of intact C_6H_5Br. The distance between them and their orientation relative to each other were found to exhibit essentially no variation. Hence it is concluded that photoinduced reactions involving C_6H_5Br proceed, but only an unidentified product can be

[4] Surface water molecules can be reoriented during, or as a consequence of, excess electron solvation. Adsorbed molecules diffuse under certain conditions.

detected. The characteristic apparent height profile, in particular its width, depends very strongly on the tunnelling parameters. A systematic variation of these left the alleged reaction product stable. Thereby it turned out to be anchored at the surface while trying to follow the STM tip with a springing movement. The experimental results are most easily explained by photoinduced dissociation of the C_6H_5Br molecules. This interpretation is assumed since there seems to be no reason to consider more complicated processes. Experiments with C_6H_5Cl on amorphous porous ice were performed to enable detailed statements about the photoinduced reactions. These ice surfaces should be ideal due to their superior density and variety of defects. A catalytic effect is revealed by irradiating the sample with λ=326nm ($\equiv E_\gamma$=3.80eV) photons, because it leads to dissociation of C_6H_5Cl molecules on them but neither at the edges of the nanoislands nor on the metal substrate as discovered employing the functionalised STM tip. On the amorphous porous ice surface the density of reaction products is very similar to the density of C_6H_5Cl molecules before illumination, implying that (almost) all adsorbed molecules must have reacted and that it exhibits (almost) no adsorption sites preventing the reaction.

Photons of 3.8eV energy should allow excess electrons to reach positions up to 0.8(1)eV above the lower ice conduction band edge if judging from the measurements. According to the calculations these excess electrons are able to induce DEA (see chapter 5), but the photon energy is not sufficient for direct neutral photodissociation (see chapter 6). This suggests that the observed reactions of C_6H_5Cl and C_6H_5Br molecules are solely DEA processes. The 2PPE experiments of Kemeny (2017) [50] yield further insight into this topic (see section 7.2).

Assuming DEA the aforementioned catalytic effect of the amorphous porous ice surface is attributed to its polarity in combination with the presence of defects. The C_6H_5Cl molecules at its nanoisland edges stayed intact presumably because their interaction with the metal substrate is still too strong. Interestingly a similar result was obtained from a 2PPE study of $CFCl_3/H_2O$/Ag(111) performed by Ryu et al. (2006) [235]. For 1ML $CFCl_3$ molecules deposing an ultrathin ice film (8ML) on the metal substrate enhanced the cross section of DEA – supposedly producing $CFCl_2$ molecules and Cl^- anions – at 3.5eV incident photon energy by an order of magnitude.

7.2. Two-photon photoelectron spectroscopy

Monochromatic 2PPE with $\leq$3.79eV photon energy E_γ was employed to measure the evolution of the work function $\Phi(t)$ of 1.0(3)ML C_6H_5X molecules

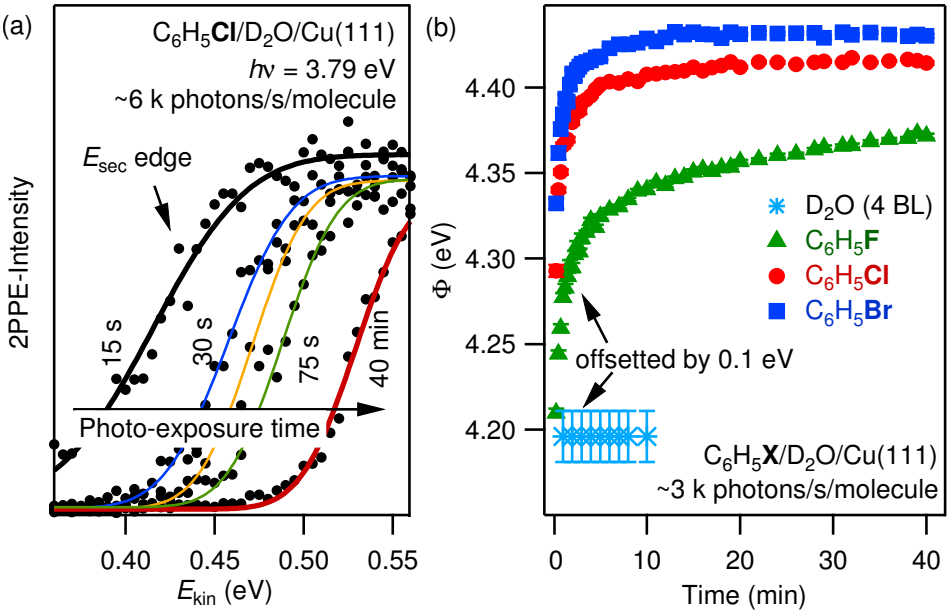

Figure 7.5.: Work function $\Phi(t)$ evolution of 1.0(3)ML C_6H_5X molecules (X=F,Cl,Br) on 4.0(5)BL amorphous porous D_2O on Cu(111) under illumination with 3.79eV photons for up to 40min at T=95(5)K measured with monochromatic 2PPE (a) evolution of the secondary edge for X=Cl and $6{\cdot}10^3$ $\frac{\text{photons}}{\text{s}\cdot\text{molecule}}$ (b) $\Phi(t)$ for all systems and $3{\cdot}10^3$ $\frac{\text{photons}}{\text{s}\cdot\text{molecule}}$, D_2O/Cu(111) added for comparison; Kemeny (2017) [50]

(X=F,Cl,Br) on 4.0(5)BL amorphous porous D_2O ice on a Cu(111) metal substrate at fluxes ranging from $4{\cdot}10^2$ to $1.75{\cdot}10^4$ $\frac{\text{photons}}{\text{s}\cdot\text{molecule}}$ and T=95(5)K with photoexposure time (up to 40min). As it will be seen the efficiency of the photoinduced electron transfer process is reflected by the rate of work function change.

Fig. 7.5a exemplifies the upward shift of the secondary edge during photoexposure (at E_γ=3.79eV). This evolution of the lowest kinetic energy photoelectron distribution indicates a continuous work function increase. The same qualitative result is found for all systems as shown in Fig. 7.5b. Φ(t) finally saturates implying that a photostationary state is reached. Asymptotic work function and speed of convergence are larger for heavier halogens. While they are similar for C_6H_5Cl and C_6H_5Br molecules, C_6H_5F molecules lead to large deviations. These observations suggest DEA to the former, but mere photoionisation of the latter. This interpretation is consistent with the calculations discussed in chapter 5 as the lower ice conduction band edge lies at ≈3.0eV above the metal substrate Fermi level (see section 7.1).

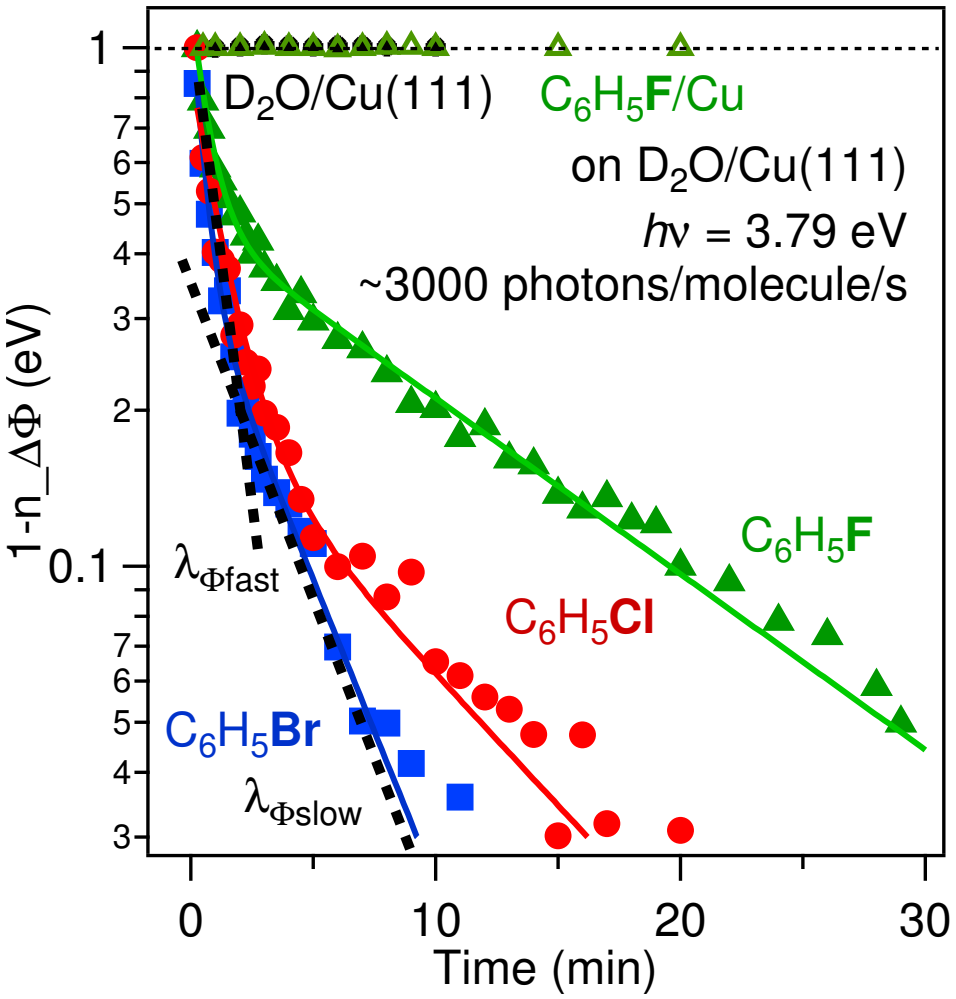

Figure 7.6.: Normalised work function change 1-$\frac{\Delta\Phi(t)}{\Delta\Phi_{max}}$ for 1.0(3)ML C_6H_5X molecules (X=F,Cl,Br) on 4.0(5)BL amorphous porous D_2O on Cu(111) under illumination with 3.79eV photons at a flux of $3{\cdot}10^3$ $\frac{\text{photons}}{\text{s}{\cdot}\text{molecule}}$ for up to 40min at T=95(5)K measured with monochromatic 2PPE, D_2O/Cu(111) and C_6H_5F/Cu(111) added for comparison; Kemeny (2017) [50]

The work function increase is caused by two reciprocally exponential processes as illustrated in Fig. 7.6 displaying the time-dependent normalised work function change 1-$\frac{\Delta\Phi(t)}{\Delta\Phi_{max}}$ for the same photon energy and flux as in Fig. 7.5b. The faster uniform one (macroscopic rate constant $\lambda_{\Phi fast}$) is interpreted as excess electron attachment to or photoannealing of shallow electron traps with an adsorbed molecule and the slower one (macroscopic rate constant $\lambda_{\Phi slow}$) more intense for heavier halogens is assigned to the aforementioned photoionisation resp. DEA.

Could there be other reasons for the observed work function change? A previous 2PPE study of D_2O/Cu(111) by Gahl et al. (2002) [236] demonstrated that metallic electrons are indeed excited into the ice conduction band and that these originally delocalised excess electrons localise at attractive trapping sites. However since this alone does not modify the work function (cf. Fig. 7.5b and 7.6), photoinduced dissociation of the amorphous porous ice is excluded. Furthermore, the photoelectron count is too low for significant space-charge effects. Sample ageing is also excluded, since the same constant work function is observed on different parts of the sample as long as it is not illuminated. With 2PPE it is difficult to disentangle effects of surface diffusion or reorientation of the intact molecules or reaction products and excess electron attachment to them. However, surface diffusion should play a minor role at best, because the halogen masses would speak for the opposite trend in work function change resp. convergence and the STM experiments of Bertram (see section 7.1) indicate no mobility of the reaction products.

Since photon flux and energy E_γ affect the excess electron density, this also pertains to the concentrations of neutral and ionised species. Hence different macroscopic rate constants and photostationary states resp. asymptotic work functions are observed if these parameters are varied. An improved knowledge of the underlying processes can be obtained by analysing their influence on the evolution of the normalised work function change 1-$\frac{\Delta\Phi(t)}{\Delta\Phi_{max}}$ displayed in Fig. 7.7. At E_γ=3.78eV it is flux independent in case of adsorbed C_6H_5F molecules. However for adsorbed C_6H_5Cl or C_6H_5Br molecules both macroscopic rate constants grow substantially with photon flux as indicated by the steeper slopes. This is reconcilable with the previous suggestions if excess electron attachment and the subsequent dissociation proceed on similar time scales, while excess electron detachment resp. recombination takes much longer so that it has only minor influence on the evolution of the work function. Moreover the work function of these systems starts to decrease after a critical photoexposure time t_c if the flux is sufficient, because a third exponentially decaying component dominating the change can be measured. Smaller t_c are reached by increasing the flux further or considering C_6H_5Br instead of

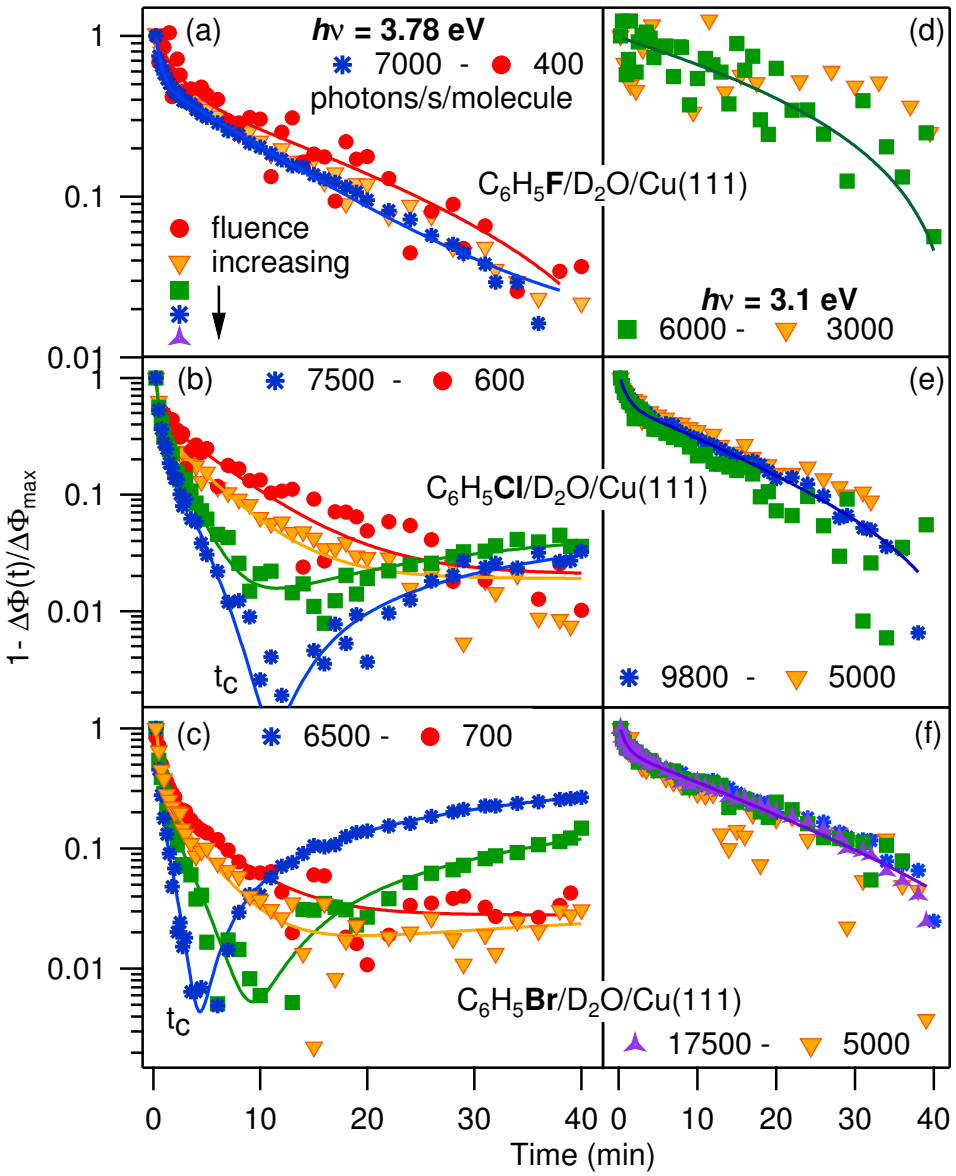

Figure 7.7.: Normalised work function change $1\text{-}\frac{\Delta\Phi(t)}{\Delta\Phi_{max}}$ for 1.0(3)ML C_6H_5X molecules (X=F,Cl,Br) on 4.0(5)BL amorphous porous D_2O on Cu(111) under illumination with photons of energy E_γ at fluxes ranging from $4{\cdot}10^2$ to $1.75{\cdot}10^4$ $\frac{\text{photons}}{\text{s}\cdot\text{molecule}}$ for up to 40min at T=95(5)K measured with monochromatic 2PPE left panel: E_γ=3.78eV right panel: E_γ=3.10eV (a,d) X=F (b,e) X=Cl (c,f) X=Br; Kemeny (2017) [50]

C_6H_5Cl molecules. At the reduced E_γ=3.10eV, which does not permit excess electrons higher than very close to the lower ice conduction band edge, all systems behave essentially like the C_6H_5F/D_2O/Cu(111) analysed with the original E_γ=3.78eV, but the macroscopic rate constants are much inferior. This can be explained if the reduced E_γ allows excess electron attachment but not DEA to the adsorbates and the former is the vital reason for the occurrence of work function change. These assumptions are also supported by the measurements at the original photon energy in combination with the calculations discussed in chapter 5 and the comparative analysis.

The change in work function trend is associated with a decline of the surface dipole enabled by the interplay of dissociation channels and charge screening effects. Several scenarios consistent with the observations can be imagined and deciding between them seems to be subject of future research. Screening the halogen ion released upon dissociation of the ionised adsorbate should be easier due to its smaller size. Dissociation products might form new species, e.g. biphenyl (Ullmann-type reaction), in secondary reactions. For the dissociable C_6H_5Cl and C_6H_5Br adsorbates a large density of further negative (ionised, dissociated and perhaps charged secondary) species might accumulate at the surface so that additional screening effects play a role. All possibilities support the theoretical interpretation of the measurements as they imply that a change in work function trend occurs only if the adsorbed molecules dissociate. These systems reach the photostationary state (saturated work function) faster, because they do not have to rely on the slow excess electron detachment resp. recombination. The various interpretations hint that t_c is reached when a certain fraction of the neutral adsorbed molecules is consumed and within the error limits the critical photon dose is indeed the same for different fluxes (C_6H_5Cl: 5.1(1.2)·10^6 $\frac{\text{photons}}{\text{molecule}}$, C_6H_5Br: 2.1(7)·10^6 $\frac{\text{photons}}{\text{molecule}}$). Hence t_c is smaller for increased flux and also for the heavier halogen (enhanced reaction rates). The ab-initio calculations can explain the latter finding since resonance positions, activation energies and C-X bond elongations required to reach the conical intersection are higher when considering the C_6H_5Cl instead of the C_6H_5Br adsorbate (see chapter 5). The present discussion provides reason to expect that the critical concentration of consumed adsorbed molecules decreases with their original coverage. Hence t_c should diminish concomitantly if the surface power density of incident photons is kept constant. Kemeny (2017) [50] also performed further experiments confirming this successfully.

$$E_{\text{im}} = -\frac{3.6\text{eV}}{\varepsilon z[\text{Å}]} \tag{7.1}$$

In the STM (see section 7.1) and 2PPE (this section) experiments image potential effects occurring due to the metal substrate play no substantial role for the redshift of the molecular antibonding states or the catalysis of DEA upon adsorption. The exemplary GW(DFT) modelling of DEA (see chapter 5) yielded a redshift of 186-865meV resp. 407-3218meV for the $\pi^*_{a,s}$ resp. σ^*_s main resonance and 29-746meV reduction of the activation energy (cf. Tab. 5.3, 5.5, 5.6). Although it was found that image potential effects might contribute substantially to the enhancement of halomethane reaction rates on ice structures supported by a metal substrate [36], the corresponding redshift in the experiments reported here is expected to be 125meV at most and, as there is no preference for a specific type of resonance, it leaves the activation energies essentially unchanged. This estimate comes from formula (7.1) [67], which gives the energy level shift in the absence of strong covalent interaction. Thereby $\varepsilon \approx 3.2$ is the high-frequency limit of the relative permittivity of the ice [59, 237] and $z[\text{Å}]$ is the distance between molecule and metal substrate. The ice film thickness at an adsorption site is at least 2BL [226], i.e. $z = 9\text{Å}$.

7.3. Summary

The accordance resp. consistency of theoretical predictions and experimental observations [low-temperature STM (7.5-11K) by Bertram (2017) [58] and 2PPE (95(5)K) by Kemeny (2017) [50]] yields strong evidences for the proposed reaction mechanism of DEA (cf. Fig. 5.1) to adsorbed phenyl halogenide molecules (C_6H_5X with X=Cl,Br but only ionisation for X=F) on the ice surface ($I_h(0001)$) as found by modelling with its idealised and a defective structure. More generally this demonstrates that the fundamental motifs are correctly described. Hence the *ab-initio* approach employed here should be adequate for DEA to halogenated hydrocarbons on polar solid surfaces and the scenario displayed in Fig. 7.8 is suggested. DEA is induced by hot, instead of solvated, electrons from the ice conduction band as confirmed by 2PPE experiments analysing the time evolution of the work function change during photoexposure. Under the STM it can be seen that the adsorbates prefer to stay at ice surface defects. There DEA is catalysed or the reaction probabilities are enhanced as predicted, because 2PPE measurements show that the reaction rates on amorphous porous ice are much higher than on crystalline ice while exhibiting the same trends. In particular DEA is favoured if a heavier halogen is involved. Apart from that the STM study revealed that excess electron solvation at defects can affect their suitability as electron traps, e.g. by annealing them, because it can induce reorientations of the ice film molecules, even at long range.

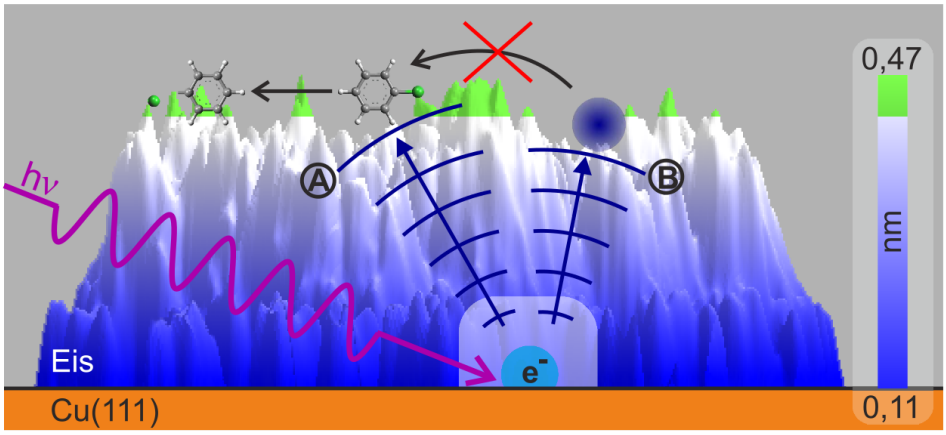

Figure 7.8.: Proposed scenario: Excess electrons at the ice (polar solid) surface (A) attach to halogenated hydrocarbon adsorbates and possibly induce their dissociation (B) undergo solvation at defects thereby excluding (A); Bertram (2017) [58]

Modifications upon laser illumination were investigated with STM for both crystalline (cf. Fig. 7.1) and amorphous porous (cf. Fig. 7.2) ice structures produced from 0.9BL of D_2O on Cu(111). A collective molecular repositioning (photoannealing) was observed on crystalline D_2O at E_γ=3.10eV (cf. Fig. 7.1). It is an example of long-range interactions within the molecular network and involves hydrogen bond breaking as illustrated by a structural model. To verify that these laser-induced molecular repositionings are mediated by excess electron solvation the amorphous porous ice, which should then maximise their cross section due to its maximised surface defect density, was illuminated with 2.75eV $\leq E_\gamma \leq$ 3.65eV (cf. Fig. 7.2). The cross section of photoinduced modifications is approximately constant at $0.17(5)\cdot10^{-22}$cm^2 up to a threshold of 3.0(1)eV and then rises linearly with a slope of $1.3(2)\cdot10^{-22}$cm^{2}eV^{-1} (cf. Fig. 7.2c). At the threshold energy electrons begin to reach the ice conduction band. Hence it is concluded that their solvation indeed mediates the molecular repositionings. This corroborates an earlier 2PPE study of crystalline D_2O on Ru(001) by Bovensiepen et al. (2009) [3], who measured a monotonic rise of the density of excess electrons in a very similar energy range and proposed that their solvation proceeds continuously through several conformational substates. Interestingly the calculated electron trap formation energies and depths are only slightly different from each other (cf. Tab. 3.5). Since the STM images exhibit no fundamental change in the appearance of the protrusions, the molecules seem to stay intact for both kinds of ice structures (cf. Fig. 7.1a,b and 7.2a,b).

STM imaging identified C_6H_5Cl and C_6H_5Br molecules adsorbed on crystalline ice as protrusions with a characteristic apparent height profile higher and more elliptical than that of the previously identified D_2O molecules. These appear at or close to ice surface defects, frequently at the edges of ice nanoislands and in clusters on the metal substrate. This typical distribution is consistent with the calculated adsorption energies (cf. Tab. 4.5) and implies that the adsorbed molecules are mobile despite the extremely cryogenic temperature. DEA to the molecules adsorbed on the ice surface is favoured by the spatial correlation of strong adsorption sites and deep electron traps (see chapter 5). Note that problems in distinguishing between amorphous porous ice structures and adsorbed phenyl halogenide molecules were solved with functionalising the originally metallic STM tip by attaching one of these molecules to its apex.

After illuminating C_6H_5Br on crystalline D_2O with E_γ=3.76eV a new characteristic apparent height profile was found instead of some adsorbates previously detected at the same surface sites (cf. Fig. 7.4). This illustrates the occurrence of photoinduced reactions involving the adsorbates. The new characteristic apparent height profile exhibits a global maximum much higher than that of intact C_6H_5Br and belongs ostensibly to an unidentified reaction product. A systematic variation of the tunnelling parameters, during which it stayed stable and tried to follow the STM tip with a springing movement, revealed its anchoring at the ice surface. Photoinduced dissociation of adsorbed C_6H_5Br molecules is assumed in view of these experimental results.

A catalytic effect of amorphous porous ice on the photoinduced dissociation of adsorbed C_6H_5Cl molecules is discovered with the aid of exploiting its superior density and variety of surface defects. Illumination at E_γ=3.80eV causes dissociation of C_6H_5Cl on top of the D_2O nanoislands but neither at their edges nor on the metal substrate. Barely any of the adsorption sites exhibited by this ice surface prevents the reaction, because a density of the unidentified product very similar to the original adsorbate density was measured there.

All observed reactions of adsorbed C_6H_5Cl and C_6H_5Br molecules are assumed to be caused by DEA to them since the calculations indicate that excess electrons from the ice conduction band, whose energy here reaches up to 0.8(1)eV above its bottom, can act dissociatively (see chapter 5) while the energy E_γ=3.8eV of the incident photons used for their creation is not sufficient for direct neutral photodissociation (see chapter 6).

The catalytic effect of amorphous porous ice is hence attributed to its polarity and surface defects. This interpretation is corroborated by a similar result of Ryu et al. (2006) [235], who investigated $CFCl_3/H_2O$/Ag(111) with 2PPE.

Monochromatic 2PPE served to determine the work function $\Phi(t)$ of 1.0(3)ML C_6H_5X molecules (X=F,Cl,Br) on 4.0(5)BL amorphous porous D_2O ice with a Cu(111) metal substrate for up to 40min photoexposure time.

All adsorbate species are photoionised, but, in contrast to C_6H_5Cl and C_6H_5Br, C_6H_5F does not undergo DEA at E_γ=3.79eV. This interpretation is proposed to explain the continuous increase of the work function originally observed at a flux of $3{\cdot}10^3$ $\frac{\text{photons}}{\text{s}\cdot\text{molecule}}$ (cf. Fig. 7.5b). As the evolution of the normalised work function change $1\text{-}\frac{\Delta\Phi(t)}{\Delta\Phi_{max}}$ illustrates, it is caused by two reciprocally exponential processes (cf. Fig. 7.6). The faster uniform one seems to be excess electron attachment to or photoannealing of shallow electron traps with an adsorbed molecule. The attribution of the slower process to the aforementioned photoionisation resp. DEA is based on several aspects. For heavier halogens it is more intense just like the asymptotic work function belonging to the final photostationary state and the associated speed of convergence are higher. Furthermore the proposed interpretation is consistent with the calculations discussed in chapter 5, since the incident photons can generate excess electrons up to 0.8(1)eV above the ice conduction band bottom (see section 7.1).

Surface diffusion or reorientation of the adsorbates or reaction products are considered the only alternative reasons for the work function change. Nevertheless their total contribution can not be more than small as the halogen masses should then lead to the opposite of the observed trends and no mobile reaction products were found according to the STM study of Bertram (2017) [58]. Photoinduced dissociation of the amorphous porous ice and sample ageing are excluded on the basis of comparative analysis. Space-charge effects can not be relevant here since the photoelectron count is too low.

Excess electrons attaching to the adsorbates can only induce their dissociation if they are not from below the ice conduction band. Both effects happen on the same time scale for sufficient incident photon energy, whereas excess electron detachment resp. recombination takes clearly longer. These conclusions are drawn judging from the influence of different incident photon energies and fluxes on the normalised work function change $1\text{-}\frac{\Delta\Phi(t)}{\Delta\Phi_{max}}$ (cf. Fig. 7.7). Increasing the photon flux barely affects $1\text{-}\frac{\Delta\Phi(t)}{\Delta\Phi_{max}}$ for the original E_γ=3.78eV and adsorbed C_6H_5F molecules but leads to higher rates of slow and fast process if C_6H_5Cl or C_6H_5Br are chosen instead. In the latter cases enough flux allows to measure that the work function begins to diminish after a critical photoexposure time t_c. No sign of DEA is found at the reduced E_γ=3.10eV corresponding to the ice conduction band bottom as all systems behave qualitatively like the originally investigated C_6H_5F/D_2O/Cu(111) de-

spite much inferior macroscopic rate constants. This picture is corroborated by the theoretical results from chapter 5.

Several explanations involving charge screening or back resp. secondary reactions come in question for the third process diminishing the work function. All these require DEA and indeed it could only be measured when this condition was fulfilled according to theory (see chapter 5). The critical photon dose for the different fluxes does not vary beyond the experimental error limits (C_6H_5Cl: $5.1(1.2)\cdot10^6$ $\frac{\text{photons}}{\text{molecule}}$, C_6H_5Br: $2.1(7)\cdot10^6$ $\frac{\text{photons}}{\text{molecule}}$). This implies that the same fraction of the adsorbates is consumed at each t_c. Moreover the lower critical photon dose for C_6H_5Br instead of C_6H_5Cl molecules is comprehensible in view of the theoretical treatment of DEA (see chapter 5). Kemeny generalised her experimental results by demonstrating that the critical concentration of consumed adsorbate decreases with the primordially intact coverage as indicated by the concomitantly lowered t_c.

Although a selfconsistent picture emerges, some key observations still have no definite explanation. Deeper insights are necessary to identify the reaction products experimentally and to decide between several options for the underlying mechanisms of the first and third process affecting the work function.

8. Conclusions and outlook

Atmospheric chemistry is crucial to the understanding of anthropogenic modifications of the global climate, which is indispensable in modern times (see chapter 1). The emission of chlorofluorocarbons (CFCs) by industrial facilities contributes to global warming, because their dissociation on icy grains in the atmosphere of the earth yields halogens responsible for ozone depletion. The onset of these reactions is caused by (photoinduced) dissociative electron attachment (DEA). Hence the description of low-energy DEA to halogenated hydrocarbons on the ice surface is a major topic. Although processes of this type have been understood to a decent level for the gas phase, reproducing the relevant electronic structures still requires empirical parameters to avoid qualitatively wrong results, such as obtaining bound empty states instead of resonances, and has not taken the role of the ice substrate into account until now. Furthermore treating the electronic structure of ice also provides insight into electron solvation on its surface. The nascent species is of general interest since it can induce reactions of adsorbates spanning a wide range of transferred energy and time scales, while the ice might act as a catalyst. This study has developed a systematic ab-initio model of (low-energy) DEA to halogenated hydrocarbons both in the gas phase and on the ice surface. Previous theoretical works [39, 42, 54, 55] are exceeded in accuracy, scope and predictive capability, since the aforementioned issues are remedied. The model is supported by an analysis of the surface processes with cryogenic STM and 2PPE experiments performed by Cord Bertram[1] (2017) [58] and Ishita Kemeny[2] (2017) [50] as part of a joint project (see chapter 7). Employing a GW approach based on plane wave periodic supercell DFT yielded that low-energy DEA to the prototypical phenyl halogenide molecules (C_6H_5X with X=F,Cl,Br[3]) is an activated process favoured by a heavier halogen in both environments (see chapters 4 and 5). More specifically, it releases the excess electron initially captured by a $\pi^*_{a,s}$ shape resonance into a dissociative σ^*_s state via internal conversion at a symmetry-allowed accidental conical intersection between them (cf. Fig. 5.1). It turned out that the ice substrate influences the electronic structure of the adsorbates essentially by redshifting the molecular resonances

[1] STM, Ruhr-University Bochum, supervisor Prof. K. Morgenstern
[2] 2PPE, University Duisburg-Essen, supervisors Prof. U. Bovensiepen and Dr. M. Ligges
[3] The exception C_6H_5I is only considered for the gas phase.

and catalysing DEA. Surface defects exhibit localised bound states within the ice band gap suited for electron solvation, while the ice conduction band is delocalised and unbound (see chapter 3). The depth of strong electron traps tends to correlate not only with favourable modifications of the electronic structure of the adsorbates adsorbed at such traps, but also with the adsorption energy. They act as anchor sites ensuring that desorption or diffusion does not compete with low-energy DEA. However this type of chemical reaction can only be induced by the "hot" excess electrons from the conduction band, because the (fully) solvated states lie too deep to permit attachment to the adsorbate resonances. Including the experimental results of the joint project strongly evidences that the molecules adsorb and dissociate (almost) exclusively at large defect complexes. The subsequent BSE investigation of direct photodissociation (see chapter 6) successfully reproduced previous experimental results for the gas phase and confirmed that it can not be induced by the UV photons (up to 3.8eV) the collaborators used to excite the excess electrons from a Cu(111) metal substrate into the ice, since their energy is insufficient. In the low-energy range photodissociation, just like DEA, is an activated process ($\pi_s - \pi_a^* \rightarrow \pi_s - \sigma_s^*$, cf. Fig. 6.1) favoured by a heavier halogen in both environments. However adsorption leaves the onset of optical excitation ($\pi_s - \pi_a^*$), which is similar for all molecules, almost unchanged and has a very small catalytic effect at best. In conclusion a microscopic ab-initio model of (low-energy) DEA to halogenated hydrocarbons in the gas phase and on the ice surface is provided. The potential landscape of the prototypical phenyl halogenide molecules is characteristic for halogenated aryls. The problem is known to be similar but simpler for halogenated alkyls, since low-energy DEA to them usually starts directly with electron capture by a dissociative σ_s^* state (see chapter 1). Considering the success of the model, in particular in describing the relevant electronic structures, it is hence assumed that it is suited for both kinds of halogenated hydrocarbons. The former need of empirical assumptions to avoid qualitatively wrong predictions is removed.

GW+BSE accurately reproduces the electronic structure of ice I_h, while the underlying DFT is merely suited for ionic geometries and material parameters (see chapter 3). The results of the GW are significantly improved by performing hybrid electronic relaxation (PBE0) on top of the underlying gradient DFT(PBE) before applying it. Photoelectron emission (GW) and UV absorption (BSE) spectrum (cf. Fig. 3.4) require full GW selfconsistency, except for W. Only then ionisation potential (*IP*) (cf. Fig. 3.3 and Tab. 3.1, 3.2, 10.5eV [63]) and first absorption peak (cf. Tab. 3.4, 8.6-8.7eV [62, 63, 195]) are close to experiment. However excess electron solvation at $I_h(0001)$ surface defects was investigated with G_0W_0(PBE0-electronic), since GW selfconsis-

tency for the surface systems is computationally too expensive but has only weak influence on the electron affinity (*EA*), which is representative of empty states (*EA* always close to zero, cf. Fig. 3.3 and Tab. 3.1, 3.2). Agglomeration of surface dangling protons beyond the regular Fletcher stripe pattern turned out to be the key aspect. A corresponding clear trend exists for the trap depth of increasingly large orientational defect clusters and their exemplary complexations with molecular vacancies were also found to be favourable (cf. Tab. 3.5 and Fig. 3.5, 3.6). Excess electron solvation is expected to affect the defect types, because the depths of the traps (G_0W_0), while being smaller, typically also amount to some hundreds of meV like their formation energies (PBE) and they tend to correlate with each other (cf. Tab. 3.5 and Fig. 3.5, 3.6).

The molecular $\pi^*_{a,s}$ main resonances are most suited for electron capture, whereas the σ^*_s resonances, which are characterised by their high halogen-projected fraction, are weaker and lie generally higher[3] (see chapter 4). Gas phase ETS measurements confirmed that the $\pi^*_{a,s}$ main resonances possess the highest electron attachment cross sections[3] [[206] (all molecules), [41, 45, 207, 208] (C_6H_5Cl), [209] (C_6H_5Br)] and the same reasoning speaks for high TNI lifetimes (see section 4.1). Using a heavier halogen lowers the empty molecular orbitals, whereby the σ^*_s states are much more drastically affected than those of the $\pi^*_{a,s}$ type[4] as explained based on the underlying physics. The bonding-antibonding state gaps of the gas phase molecules are straitened from both sides (cf. Fig. 4.2). Adsorption favours electron capture, because it redshifts the antibonding states, especially the σ^*_s orbitals, without diminishing their localisation as expected due to the polarity of both components (cf. Fig. 4.14 to 4.16). Like for the ice, DFT provides reliable geometries (cf. Tab. 9.1, besides 5.4) and total energies (cf. e.g. Tab. 5.2), but subsequent GW calculations must be performed to describe the molecular electronic structures adequately (cf. e.g. Tab. 4.1, 4.2). The $scGW_0$(PBE0) quasiparticle energy levels of the gas phase molecules are highly accurate and follow entirely clear trends that are confirmed by the measurements and were explained within a comprehensive picture (cf. Fig. 4.2 and Tab. 4.1, 4.2). While the HOMO of C_6H_5X is always a π_s state, the LUMO character depends on the halogen: π^*_a for X=F, degenerate π^*_a and π^*_s for X=Cl or Br, σ^*_s for X=I. The forced neglect of GW selfconsistency for the adsorbate-substrate systems was justified based on estimates (cf. Tab. 4.3, 4.4, besides Fig. 3.3 and Tab. 3.1, 3.2). Adsorption tends to be stronger at deep electron traps, where it correlates with their electron affinity, and if a lighter, i.e. more electronegative, halogen is involved (cf. Fig. 4.12 and Tab. 4.5). The most stable adsorption mode was found to be determined essentially via the

[4] Except that the splitting of the dominant π^*_a and π^*_s resonance distinguishing C_6H_5F is cancelled.

defect, whereby the Coulomb attraction between the negative partial charge at the halogen and the positive partial charges of surface dangling protons is the key bonding motif (see section 4.2). For merely orientational defect complexes flat-lying adsorption with the halogen on top of the central dangling proton is preferred and placing the carbon-halogen bond parallel to the intact Fletcher stripe always turned out to be at least very close to ideal (cf. Fig. 4.9, 4.10). Since molecular vacancies (complexated with the former defects) are occasionally more attractive for the halogen, they can favour vertical or, as the bonding of the phenyl group to the ice surface becomes a competing motif, inclined adsorption (cf. Fig. 4.11). Like the typical PBE formation energies and G_0W_0(PBE0-electronic) depths of the traps, the PBE adsorption energies amount to some hundreds of meV and furthermore Grimme-D2 corrections necessitated by the London dispersion interaction between adsorbate and substrate substantially reinforce the already discovered trends (cf. Tab. 4.5). The adsorption-induced redshifts are consistent with the molecular orbital geometries displayed in Fig. 4.1. While the G_0W_0(PBE0-electronic) positions of the σ_s^* states correlate with the trap depth, those of the $\pi_{a,s}^*$ states tend to be lower if the molecule lies more flat (cf. Fig. 4.13 to 4.16). Should the type of the lowest resonance be σ_s^* instead of $\pi_{a,s}^*$, the activation energy might be greatly reduced or eliminated as this permits DEA without internal conversion (see chapter 5). Furthermore it is not clear if weakly bound molecular states are relevant for DEA. However these cases are rare exceptions and/or require very large defect complexes (cf. Fig. 4.19c, 4.20). Apart from that it turned out that adsorption blueshifts the electron trapping states and hence incapacitates shallow traps (compare Tab. 4.5 with Fig. 4.17 to 4.20).

A monotonous lowering of the antibonding states was found along the dissociation pathway [cf. Fig. 5.4, 5.10, 5.11 (C_6H_5Cl as example)]. While the (electron capturing) $\pi_{a,s}^*$ main resonances are only marginally affected, it is rapid for the (dissociative) σ_s^* molecular orbitals. The localisation of the former remains nearly equal, but it grows drastically for the latter, which collapse into each other and become stable. Like electron capture, low-energy DEA is favoured if a heavier halogen is involved, because internal conversion requires less activation energy and, as well as the stabilisation of the SOMO, it happens earlier on the dissociation pathway (cf. Tab. 5.3, 5.5, 5.6 and Fig. 5.5 to 5.8 and 5.12 to 5.14). The gas phase measurements are confirmed by an accurate reproduction of carbon-halogen bond fission energies (PBE0, cf. Tab. 5.2) and resonance positions ($scGW_0$, cf. Tab. 4.2) including their trends. The calculated evolution of position and localisation of the antibonding states corroborates the observation of a higher DEA cross section peak (cf. Tab. 5.1) when a heavier halogen is involved. Considering the appendant activation

energies (cf. Tab. 5.3) explains why low-energy DEA to C_6H_5Cl or C_6H_5Br originates from electron capture by the $\pi^*_{a,s}$ main resonances, while it is the much higher σ^*_s or π^*_0 for C_6H_5F and the lower σ^*_s in the unique exothermic case of C_6H_5I. The ice surface favours DEA mainly due to the adsorption-induced redshifts of the main molecular resonances, which stay nearly constant during it, while the energy required to elongate the carbon-halogen bond becomes only very slightly smaller. Concomitantly, the activation energies diminish to a large extent. Idealised $I_h(0001)$ and the $4S_{AD}$ orientational defect complex, which lowers the SOMO even more, served as model systems, whereby the carbon-halogen bond was elongated via moving the phenyl group starting from the ideal adsorption geometry (cf. Fig. 5.9). Transferring the activation energy to C_6H_5Cl or C_6H_5Br is not considered sufficient to invoke their desorption, because it is clearly less than the adsorption energies (cf. Tab. 4.5). Furthermore diffusion away from the defect complex is unlikely to occur only due to this, since the binding energy relative to the idealised ice surface also exceeds it. However no such results are obtained for C_6H_5F, indicating that its $\pi^*_{a,s}$ main resonances are still not suited for DEA.

Low-energy photodissociation is an activated chemical reaction enabled via internal conversion[5] between the initially optically excited $\pi_s - \pi^*_a$ hole-electron state and the dissociative $\pi_s - \sigma^*_s$[3] (cf. Fig. 6.1). While $\pi_s - \pi^*_a$ is slowly raised, $\pi_s - \sigma^*_s$ experiences extremely fast stabilisation (cf. Fig. 6.2 to 6.5 and 6.7 to 6.9). The energy of $\pi_s - \pi^*_a$ is similar for all molecules, but that of $\pi_s - \sigma^*_s$ is much smaller when a heavier halogen is involved (cf. Tab. 6.2, 6.4, 6.5). Hence this favours photodissociation by placing the conical intersection at substantially reduced activation energy and carbon-halogen bond elongation. The BSE study forced the adoption of the dissociation pathway from the underlying GW(DFT) calculations, which coincides with the results of the gas phase experiments, except for C_6H_5F (see references in Tab. 6.1). The energy threshold trend observed for the gas phase is correctly reproduced without major deviations from the measured values (compare Tab. 6.1 and 6.2). The prohibitive activation energy explains why the reaction product F has not been detected in contrast to the other halogens. Apart from that the lowest optical excitations were always found to be optically dark [cf. Fig. 6.6 (C_6H_5Br as example)]. Although the ice surface barely modifies the energy of $\pi_s - \pi^*_a$, a very small catalytic effect of adsorption, mainly due to the initial stabilisation of $\pi_s - \sigma^*_s$, was obtained. However it could to some extent be related to the neglect of GW selfconsistency for the underlying surface calculations. The activation energy for C_6H_5F is still prohibitive.

[5] In principle the nonadiabatic transition can also be intersystem crossing (see section 6.1). However as selection rules apply the optical excitation can only lead to a singlet state.

The model yields that DEA to phenyl halogenides on the ice surface is catalysed by it, induced by hot, instead of solvated, electrons and favoured by the presence of defects as well as the choice of a heavier halogen (see chapters 4 and 5). The experiments performed in collaboration corroborate the proposed scenario (see chapter 7). The successful description of the fundamental motifs and their explanation based on the underlying physics indicate that DEA to halogenated hydrocarbons on polar solid surfaces generally follows a qualitatively identical or very similar scenario (cf. Fig. 7.8). STM images of C_6H_5Cl or C_6H_5Br (cf. Fig. 7.3, 7.4a) reveal that it adsorbs (almost) exclusively at defects as expected in view of the calculated adsorption energies (cf. Fig. 4.12 and Tab. 4.5). The spatial correlation of adsorption sites and strong electron traps implies that these molecules are mobile even at the cryogenic temperature and favours electron attachment as well as dissociation induced thereby. 2PPE measurements of the work function evolution during photoexposure confirmed that DEA is induced by hot, instead of solvated, electrons and that the activation energy for C_6H_5F is prohibitive (cf. Fig. 7.7). While solvated electrons (electron excitation with 3.1eV photons corresponds to the ice conduction band bottom) lead to a fast uniform process, hot electrons (here: E_γ=3.8eV) invoke a slow second process[6] also increasing the work function for C_6H_5Br (more intense) and C_6H_5Cl (less intense), but not C_6H_5F. Varying the photon flux and performing comparative analysis allowed to demonstrate that the second process is DEA. The paramount importance of surface defects for DEA is substantiated by the fact that only the reaction rates on amorphous porous, but not crystalline, ice were sufficiently high for the 2PPE experiments. A catalytic effect of amorphous porous ice on DEA to C_6H_5Cl was observed under the STM. Illumination of $C_6H_5Cl/D_2O/Cu(111)$ with 3.8eV photons led to dissociation of C_6H_5Cl on top of the D_2O nanoislands, but neither on their edges, nor on the metal substrate, which is not polar. In particular barely any of the adsorption sites of the first type prevent the reaction, because there the product density was found to be nearly identical with the original adsorbate density. In conclusion the catalytic effect of amorphous porous ice is attributed to its polarity and surface defects. This corroborates similar results of Ryu et al. (2006) [235]. Apart from the fact that the D_2O molecules stay intact, an STM analysis of $D_2O/Cu(111)$ illuminated with 2.75-3.65eV laser photons also revealed the occurrence of collective hydrogen bond breaking repositionings within their network, even at long range (cf. Fig. 7.1). These are induced by excess electron solvation, since their cross section is constant up to a threshold of E_γ=3.0(1)eV, which corresponds to the ice conduction band bottom, and then rises linearly (cf. Fig. 7.2). Such a result was expected

[6] Sufficiently high photon flux also eventuates in a converse third process.

as the calculated depths of the traps are comparable to their formation energies (cf. Tab. 3.5 and Fig. 3.5, 3.6) and corroborates an earlier 2PPE study of Bovensiepen et al. (2009) [3].

What could be done to get deeper insight into DEA to halogenated hydrocarbons and the influence of polar solid substrates? It is proposed to measure the gas phase reaction rates resp. DEA cross sections by combining DEAS – or better TOFMS – and ETS (see section 5.1). Important steps towards a theoretical assessment of these quantities, and possibly also their surface counterparts, could be taken by calculating the molecular vibrational energy levels (and frequencies) and the transition matrix elements relevant for the probability of internal conversion. A general dissociation pathway finding algorithm is desirable, e.g. since the involvement of molecular vacancies currently makes the potential energy landscapes too complicated. Unfortunately it seems that performing a real-time molecular dynamics simulation by alternating iteratively between an adapted DFT force minimisation (ionic relaxation) and GW electronic structure treatment is either impossible or far too expensive. However if a relation between (extrapolated) CDFT and GW(DFT) results, such as approximately constant energy shifts, was established, determining the dissociation pathway via the former method might be valid. More general statements about the role of different chemical bonding types, molecular geometries and surface defects could be enabled by considering a larger variety of systems. Furthermore trends along series of isomers or homologous molecules might be confirmed or revealed. GW selfconsistency could be added to improve the results for DEA, and subsequently direct neutral photodissociation, on the ice surface, if sufficient computational power and memory were available. It would also be helpful if a stable algorithm for spin-polarised and/or charged calculations beyond DFT was known, e.g. to calculate the halogen electron affinities or to incorporate hole-electron triplet states. The experimental identification of the reaction products observed under the STM (cf. e.g. Fig. 7.4b) and the decision between several options for explaining the first resp. third process affecting the evolution of the work function during the 2PPE experiments (cf. Fig. 7.7) are open questions.

9. Acknowledgements

This work is the realisation of a lifetime dream to enrich the history of physics and benefit mankind. I would like to express my gratitude towards the many people who made it possible and motivated me as I met them on my way.

At the Friedrich-Alexander-University (FAU) Erlangen-Nuremberg I studied physics in a competent social environment, which gradually modified my ways of thinking, and decided to do my doctorate on it there. The Chair of Theoretical Solid State Physics (formerly: Prof. Oleg Pankratov, now: Prof. Martin Eckstein) offers a pleasant atmosphere for conducting research. I cordially thank Prof. Michel Bockstedte, who supervised my diploma thesis and my PhD thesis. He was always very patient and available to answer my questions, in particular those regarding scientific methods and organisational matters. I am especially impressed by the huge effort he made to improve the quality of our joint work. Together with experimental groups from the Ruhr-University Bochum (STM by Prof. Karina Morgenstern and Dr. Cord Bertram) and the University Duisburg-Essen (2PPE by Prof. Uwe Bovensiepen, Dr. Manuel Ligges and Dr. Ishita Kemeny (formerly Agarwal)) we carried out a joint project funded by the Deutsche Forschungsgemeinschaft (DFG research grants BO 1841/3-1, BO 1823/5-1, MO960/18-1) and the Cluster of Excellence (RESOLV research grant EXC 1069). I thank them for their very friendly attitude, a lot of fruitful discussions and countless important contributions. Together we discovered that their experimental observations and our theoretical modelling support each other. In particular I am happy that these fascinating coherences are an essential part of the theses of my former fellow PhD students Dr. Cord Bertram (2017) [58] and Dr. Ishita Kemeny (2017) [50] as well as of my own. Computation time at the HPC cluster of the RRZE of the FAU Erlangen-Nuremberg and at the research centre Jülich is appreciated. My hope is that joint publications making this research accessible to the scientific community will prove its worth for the benefit of mankind, e.g. via a role in environmental protection.

My parents Johann and Beate Auburger deserve huge respect for supporting me morally and financially during many hard times. Additionally everybody who helped me to grow as a person and as a physicist has earned my proper respect for that (Ferdinand Ptak, Julia Weiland, Meyana Avenna, Gerold von

Lachemair, Stefan Lücken, Dr. Lutz Hammer, Tanja Fischer, Dr. Manuel Kolb, Amanda Uppendahl and many others).

Appendix: Treatment of systems and convergence of fundamental parameters

A. Ice I_h bulk geometry and sublimation energy

The pristine bulk geometry was initially determined by simultaneously relaxing basis vectors and ions. These calculations began at a perfectly hexagonal crystal structure with the experimental lattice constants $a_{exp} = 8.9938(4)\text{Å} \wedge c_{exp} = 7.3211(6)\text{Å}$ [59] for H_2O ice I_h measured by Röttger et al. (1994, addendum 2012) [238,239] with synchrotron X-ray powder diffraction at 10K, yielding a ratio of $\left(\frac{c}{a}\right)_{exp} = 0.81402(8)\text{Å}$, which deviates by only -0.3% from the value $\left(\frac{c}{a}\right)_{ideal} = \frac{\sqrt{6}}{3} \approx 0.81650$ of an idealised regularly tetrahedral oxygen sublattice. Very similar values were received by them for D_2O instead of H_2O and by Line and Whitworth (1996) [240], who used neutron powder diffraction to investigate KOD-doped D_2O ice XI[1] at temperatures down to 5K. Exactly one proton (hydrogen) was placed on each connecting line between two adjacent oxygens, in such a way that the Bernal-Fowler rules [197] were fulfilled and an antiferroelectric structure, whose supercell contains 16 H_2O molecules, was obtained (cf. Fig. 3.2). The DFT(PBE) trials comprised Γ-centered k-point samplings as large as 5-5-5 and plane wave energy cutoffs (see sections 2.2 and 2.3) up to E_{cut} = 1000eV. 2-2-2 and 800eV were found to be sufficient for converging supercell shape, volume and total energy in common with practically eliminating any errors due to Pulay stress (see subsection 2.6.3). The relaxed basis vectors deviated by only $<0.2^\circ$ from their original directions. Both of them parallel to the (0001) plane differed marginally by $<0.3\%$ in length. A simplified model was employed to recalculate ionic positions and total energy, because the introduced errors are correspondingly small and it works with a reduced number of parameters. Moreover it makes Pulay stress vanish a priori. Therefore only E_{cut} = 400eV is required. The crystal structure was kept perfectly hexagonal with lattice constants $a = 8.8110\text{Å} \wedge c = 7.1952\text{Å}$ obtained from the previous considerations. As expected this constitutes a slight overbinding ($\frac{a-a_{exp}}{a_{exp}}$ = -2.0% $\wedge$ $\frac{c-c_{exp}}{c_{exp}}$ = -1.7%), but $\frac{c}{a}$ = 0.81662 is almost

[1] Ice XI is the proton-ordered phase of ice I_h. It was experimentally found to be ferroelectric. KOH- resp. KOD-doping serves to enable the phase transition (at 72K/76K for H_2O/D_2O ice I_h), which would normally be prevented due to insufficient hydrogen mobility.

identical (+0.015%) to the aforementioned idealised ratio. The volume per supercell ($V = \frac{\sqrt{3}}{2}a^2c = 483.75\text{Å}^3$) resp. molecule ($V_{H_2O} = \frac{V}{16} = 30.234\text{Å}^3$) is 5.7% smaller than the experimental value ($V_{exp} = 512.85(6)\text{Å}^3$ resp. $V_{H_2O,exp} = 32.053(4)\text{Å}^3$). Note that a study by Casassa et al. (2005) [105], which also employed GGA-DFT but a different XC-functional (PW91) and fixed directions of the basis vectors, also yielded only very small deviations from the length ratios in the idealised structure (<0.3%) stating that it could be about a general tendency of hexagonal ice structures as it was also confirmed for the ferroelectric case. This corroborates the assumption that using simplified geometries resp. reduced numbers of parameters to describe these structures is justified.

Whalley (1957, 1976) [241, 242] extrapolated calorimetric measurements gaining 611meV = $14.09\frac{\text{kcal}}{\text{mol}}$ for the sublimation energy, i.e. the sublimation enthalpy at the zero point of the Kelvin scale, per molecule $E_{sub}^{H_2O}$. Insofar with $E_{sub}^{H_2O} = \frac{16F_{vac}-F_{bulk}}{16} = 664\text{meV} = 15.31\frac{\text{kcal}}{\text{mol}}$ the present investigation found diminished overbinding as compared to 698meV = $16.10\frac{\text{kcal}}{\text{mol}}$ obtained by Watkins et al. (2011) [198]. The latter study also employed the PBE XC-functional and treated an antiferroelectric system, yet maximised the proton disorder.

B. $I_h(0001)$ surface energy

DFT(PBE) was employed to calculate the surface energy γ_{0001} based on the simplified model described in section A and settings as in section 3.1. From simulating two to nine bilayer slabs $\gamma_{0001} = 11.4\text{meVÅ}^{-2}$ is assumed converged to <2%. Keeping the oxygens at one of the two slab surfaces fixed to their bulk positions led to the reduced value 10.4meVÅ^{-2}, demonstrating that the relaxation processes induced by creation of the surface significantly stabilise it resp. the slab. Pan et al. (2008) [188] found 12.2meVÅ^{-2} applying the same XC-functional. Moreover they drew the conclusion that introducing proton disorder substantially influences the surface energy, while the bulk cohesive energy is largely independent of it, which is comprehensible due to charge screening effects (see introduction to chapter 3). According to two other studies DFT(BLYP) produces somewhat smaller values (9.7meVÅ^{-2} by Pan et al. (2010) [60], 8.97meVÅ^{-2} by Michl (2011) [76]).

Several attempts have been made to determine the surface energy of ice experimentally, with contact angle measurements being the most popular method (1967-1993) [243–248]. The results are not conclusive due to unacceptably large variance and it is also not clear if they are specific to $I_h(0001)$.

C. G_0W_0 convergence properties for bulk ice I_h

Bulk system and $I_h(0001)$ surface were compared regarding the local potential averaged orthogonal to the bilayers, because the former in itself does not allow to evaluate the vacuum potential Φ_{vac}. If the number of bilayers and the vacuum region within the surface supercell are large enough, it can be assumed that the energy difference between an appropriate point on the potential curve and Φ_{vac} is the same as it would be for bulk I_h. This point has to be sufficiently geometrically deep inside the bulk region resp. energetically as close as possible to Φ_{vac}. In this way the difference between the potential curves at it resp. the absolute error of its position relative to Φ_{vac} is minimised.

Due to reasons outlined in sections 2.7 and 3.1 the position of bulk valence band maximum (VBM) and conduction band minimum (CBM) in dependence of $(\varepsilon_{QP}^{MAX} - \varepsilon_{QP}^{VBM})(\Gamma)^{2,3}$ and response function energy cutoff $E_{cut\text{-}GW}$ has to be investigated for the G_0W_0(PBE0-electronic) approach (cf. Fig. 9.1). VBM and CBM fall relative to Φ_{vac} as a reliable energy interval of empty bands is taken into account. Remarkably the CBM converges much faster than the VBM and its dependence on $E_{cut\text{-}GW}$ is much weaker. Because of their energetic positions and the bulk structure, both is presumably due to the increasingly more precise description of charge screening. An analogous reasoning leads to the insight the VBM resp. CBM can be viewed as representative for valence resp. conduction states in terms of convergence. This analysis is of additional importance since the surface systems are treated with the same approach, yet for them proceeding analogously is prohibited by computational expense. Hence it not only serves to optimise simulation parameters, but also enables an estimate of the precision attainable within the available computational power. Furthermore it might be helpful if an extrapolation of the ε_{QP}^{i} values for the surface systems is desired.

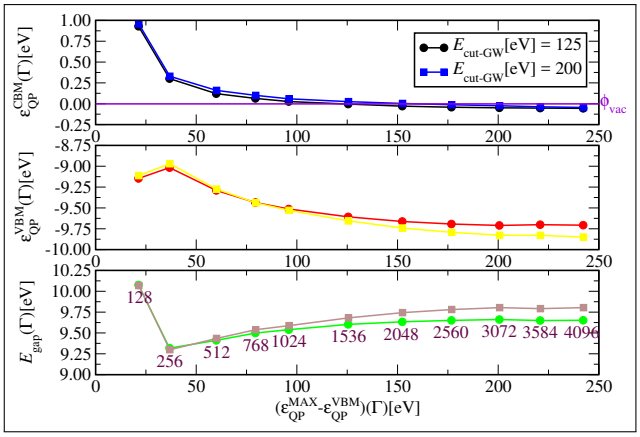

Figure 9.1.: Convergence properties of G_0W_0(PBEo-electronic) calculations (Γ-centered 2-2-2 k-point sampling, E_{cut} = 400eV) with DFT(PBE) geometry for the pristine antiferroelectric bulk state of ice I_h (16 H_2O molecules supercell). QP energies at the gamma point Γ relative to the vacuum potential Φ_{vac}. $(\varepsilon_{QP}^{MAX} - \varepsilon_{QP}^{VBM})(\Gamma)$ is determined by the number of bands chosen for the respective calculation (indicated in the $E_{gap}(\Gamma)$ diagram) and deduced from the highest converged values. $E_{gap}(\Gamma) = (\varepsilon_{QP}^{CBM} - \varepsilon_{QP}^{VBM})(\Gamma)$

Table 9.1.: DFT(PBEo) bond length table for benzene (C_6H_6) and phenyl halogenides (C_6H_5X) in vacuum ($(15Å)^3$ cubic supercell, plane wave energy cutoff E_{cut}=400eV, Γ-point calculations)

C_6H_6		d_0(C-H)[Å]	d_0(C-C)[Å]
		1.084	1.389
C_6H_5X	d_0(C-X)[Å]	$\overline{d_0}$(C-H)[Å]	$\overline{d_0}$(C-C)[Å]
X=F	1.350	1.084(0)	1.386(3)
X=Cl	1.721	1.084(0)	1.388(0)
X=Br	1.889	1.084(1)	1.388(1)
X=I	2.089	1.084(1)	1.388(0)

D. Geometry of C_6H_5X in vacuum

Hybrid DFT(PBEo) (see subsection 2.5.3) was employed to determine the molecular geometries. Benzene (C_6H_6) served as a basis to construct the initial

[2] $(\varepsilon_{QP}^{MAX} - \varepsilon_{QP}^{VBM})(\Gamma)$ was deduced from the values for the respective states yielded by the calculation with the highest number of bands, because these should exhibit the best convergence. Yet deducing it directly was found to make only a minor difference (<1.2eV) tendencially

guesses. This mesomeric molecule is planar and perfectly hexagonal. Hence the ionic positions are already specified by the C-C and C-H bond lengths. The former coincides with the radius of the aromatic (carbon) ring, while the latter is equivalent to the radii difference between the hydrogen ring and it. Obviously the angles formed by neighbouring chemical bonds are exactly 120°. After calculating the geometry of benzene, one of the hydrogens was allowed to move maintaining the direction of its C-H bond. The initial geometry for each phenyl halogenide (C_6H_5X with X=F,Cl,Br,I) was created by elongating this bond to twice the covalent radius of the respective halogen substituting its hydrogen. Thereby the molecular symmetry is reduced from the D_{6h} to the C_{2v} point group. Nevertheless the lengths of the remaining original bonds are only marginally affected (cf. Tab. 9.1). Moreover d_0(C-X) increases with the row of the halogen (cf. Tab. 9.1) because of its larger atomic/ionic radius resp. the smaller (Pauling-scale) electronegativity difference between these atoms. The aforementioned angles change only slightly as they deviate by $<2°$ from their original value.

Table 9.2.: Experimental bond lengths for benzene (C_6H_6) and phenyl halogenides (C_6H_5X) in vacuum

C_6H_6		d_0(C-H)[Å]	d_0(C-C)[Å]
[215]		1.101	1.399
C_6H_5X	d_0(C-X)[Å]	$\overline{d_0}$(C-H)[Å]	$\overline{d_0}$(C-C)[Å]
X=F [249]	1.356	1.100(3)	1.396(4)
X=Cl [215]	1.737	1.083	1.400
[250]	1.737	1.083(8)	1.400(1)
X=Br [215]	1.85	1.072	1.399(18)
[251]	1.898	1.089(5)	1.395(1)
X=I [252]	2.098	1.107(5)	1.396(1)

The calculated geometries (cf. Tab. 9.1) are in reasonable agreement with the measurements (cf. Tab. 9.2). While the (average) experimental bond lengths are mostly a bit larger, no deviations beyond 2% were found.

---

decreasing as more unoccupied states are treated and negligible for any reasonable number of bands.

[3] The average number of unoccupied states per H_2O molecule would also be a convergence parameter independent of system size (except for influences due to the size of a vacuum region if existent, but these should be negligible in cases of reasonable convergence). Yet it alone would not contain information regarding energy or density of these states. Furthermore a comparison to systems of other species might be (more) difficult.

E. Predicted dissociation mechanisms and level of theory

It is evidenced that the model developed in this study predicts the same reaction mechanism of DEA resp. photodissociation for phenyl halogenides (C_6H_5X with X=F,Cl,Br) adsorbed on the ice surface despite the neglect of GW selfconsistency. C_6H_5Br was chosen to discuss the adequacy of the different levels of theory, because it exhibits the typical aromatic dissociation channels and it is the most reactive molecule investigated here both in the gas phase and on the ice surface. The initial energetic order of the most relevant and exemplary excess electron resp. hole-electron states is the key point of this consideration as their characteristic evolution along the dissociation pathway is known from chapter 5 ($\rightarrow$ DEA) resp. 6 ($\rightarrow$ photodissociation). For DEA it will be seen that the correct energetic order is already contained in the underlying hybrid DFT(PBE0(-electronic)). While the neglect of GW selfconsistency leads to deviating results in the gas phase, the correlation between energy shifts and localisation (local fraction "p"[4]) of the states clearly indicates that this problem does not arise on the ice surface. An analogous result concerning the degree of selfconsistency in the GW calculations underlying the BSE calculations for photodissociation is found.

Fig. 9.2 is the potential energy curves diagram for DEA to C_6H_5Br in the gas phase according to hybrid DFT(PBE0). Like in the subsequent $scGW_0$ (cf. Fig. 5.7) the initial main $\pi^*_{a,s}$ states lie below the significantly localised σ^*_s states and DEA to the former is an activated process possible due to conical intersections between them and the latter. Despite this remarkable success and in contrast to the subsequent $scGW_0$, hybrid DFT(PBE0) is not able to reproduce the experimental observations (see section 4.1), because it predicts that these excess electron capturing states are bound instead of resonant.

The energy shift of the initial main $\pi^*_{a,s}$ states consists primarily in the raising due to the transition from Kohn-Sham (KS) formalism to quasiparticle (QP) concept (DFT(PBE0) $\rightarrow$ G_0W_0: +1.7555eV for π^*_a, +1.7178eV for π^*_s), whereas adding GW selfconsistency yields a much smaller lowering contribution ($G_0W_0 \rightarrow scGW_0$: -0.1936eV for π^*_a, -0.1809eV for π^*_s) while they stay strongly localised (cf. Tab. 9.3, 9.4). On the ice surface the former transition leads to similar energy shifts of these states (+1.5824eV resp. +1.5837eV for π^*_a,

[4] The local fraction p of a state is defined as the sum of the integrals over the local parts of its probability density distribution. These are approximated from the projections of its wave function onto spherical harmonics (of s-, p- and d-character) centered at each atomic nucleus and restricted by a maximum ("Wigner-Seitz") radius RWIGS. Compared to G_0W_0, i.e. fully non-selfconsistent GW, p can only be modified if the orbitals are updated (sc), because the wave function is left invariant otherwise.

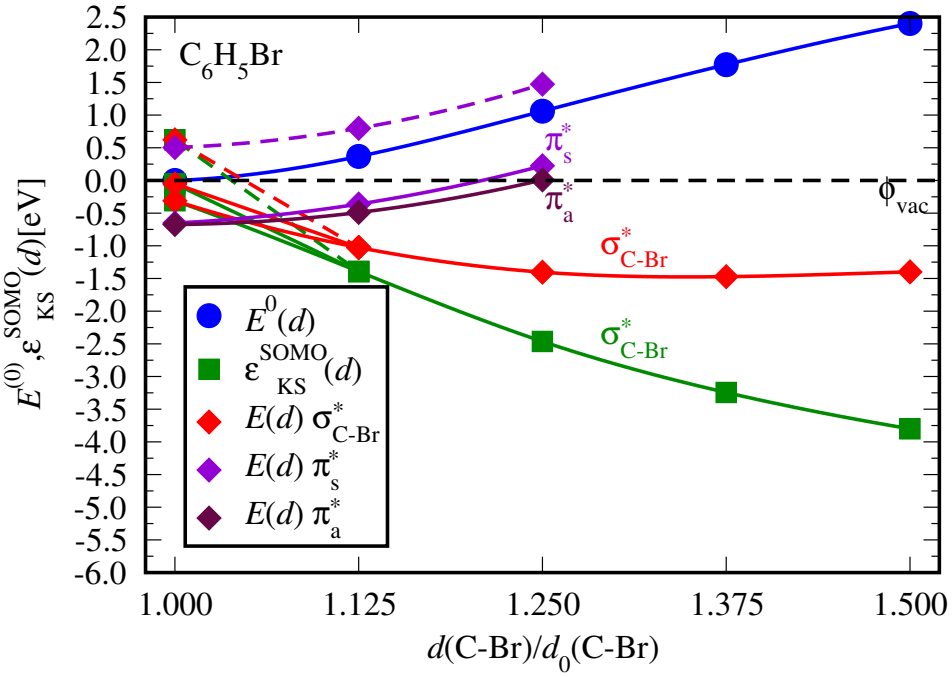

Figure 9.2.: Potential energy curves diagram for DEA to C_6H_5Br from hybrid DFT(PBE0) (for explanation of colour code and design see Fig. 5.5)

+1.5720eV resp. +1.5608eV for π_s^*) and their localisation is almost unchanged by the adsorption.

To see how the predicted DEA mechanism depends on the level of theory, Tab. 9.5 gives the energetic order of the most localised low antibonding states for all exemplary systems. Hybrid DFT(PBE0(-electronic)) always yields $\pi_{a,s}^* < \sigma_s^*$ and the subsequent G_0W_0 reverses this order only in the gas phase where the addition of selfconsistency ($G_0W_0 \rightarrow scGW_0$) reverses it again and leads to good agreement with the measurements (see section 4.1). Hence selfconsistent GW calculations for the adsorbate-substrate systems, which could not be conducted due to prohibitive computational cost, are expected to produce the same energetic order as the underlying calculations.

The same mechanism of DEA to the adsorbate is expected to be obtained at all three levels of theory unless strongly localised $\pi_{a,s}^*$ and σ_s^* states occur very close to each other. This is evidenced by the suitable correlation of the energy shifts with the localisation of the states found upon the transition from hybrid DFT(PBE0(-electronic)) to the subsequent G_0W_0 and because they turned out to be much smaller with a difference of similar absolute value but opposite sign between them when GW selfconsistency was added for the gas phase (cf.

Table 9.3.: Energy and local fraction "p"[4] of the main π_a^* state of C_6H_5Br for the different levels of theory: DFT(PBE0(-electronic)) and subsequent G_0W_0 for gas phase and adsorption on the idealised $I_h(0001)$ ice surface or its $4S_{AD}$ orientational defect complex, $scGW_0$ for the gas phase used to extrapolate the ice surface results from G_0W_0 to $scGW_0$ (blue), for geometries and simulation parameters see chapter 4 and sections A, D

$C_6H_5Br(\pi_a^*)$	DFT(PBE0(-el.))	G_0W_0	$scGW_0$
gas phase[eV] (p[%])	-0.6746 (41.5)	1.0809 (41.5)	0.8873 (37.6)
$I_h(0001)$[eV] (p[%])	-0.9203 (42.2)	0.6621 (42.2)	0.4685
$4S_{AD}$[eV] (p[%])	-1.4653 (42.0)	0.1184 (42.0)	-0.0752

Table 9.4.: Energy and local fraction "p"[4] of the main π_s^* state of C_6H_5Br for the different levels of theory: DFT(PBE0(-electronic)) and subsequent G_0W_0 for gas phase and adsorption on the idealised $I_h(0001)$ ice surface or its $4S_{AD}$ orientational defect complex, $scGW_0$ for the gas phase used to extrapolate the ice surface results from G_0W_0 to $scGW_0$ (blue), for geometries and simulation parameters see chapter 4 and sections A, D

$C_6H_5Br(\pi_s^*)$	DFT(PBE0(-el.))	G_0W_0	$scGW_0$
gas phase[eV] (p[%])	-0.6518 (43.2)	1.0660 (43.2)	0.8851 (32.2)
$I_h(0001)$[eV] (p[%])	-0.9764 (43.8)	0.5956 (43.8)	0.4147
$4S_{AD}$[eV] (p[%])	-1.5135 (42.5)	0.0473 (42.5)	-0.1336

Tab. 9.6 to 9.8). Upward shifts of the antibonding electronic energy levels, that are essentially a monotonically increasing function of their localisation, result from performing G_0W_0 based on hybrid DFT(PBE0(-electronic)). On the ice surface the shift of the main σ_s^* state is significantly stronger and much closer to the shift of the main $\pi_{a,s}^*$ states than in the gas phase and the localisations change correspondingly. Due to the concomitant reduction of the difference between them the energetic order $\pi_{a,s}^* < \sigma_s^*$ remains unchanged for the adsorbate even though these states lie only 0.2944-0.4117eV apart from each other in hybrid DFT(PBE0-electronic). In the gas phase it is reversed despite the larger original separation of 0.6008-0.6236eV.

The theoretical UV absorption spectrum of C_6H_5Br in the gas phase (BSE(...(PBE0)) calculations) is substantially blueshifted and also reshaped by the update "sc" of the orbital wave functions, whereas modifying the degree of GW selfconsistency in another way influences it only marginally (cf. Fig. 9.3). The two lowest optical excitations are always optically dark with dominant molecular orbital characters $\pi_s - \sigma_s^*$ and $\pi_s - \pi_a^*$. Their energetic

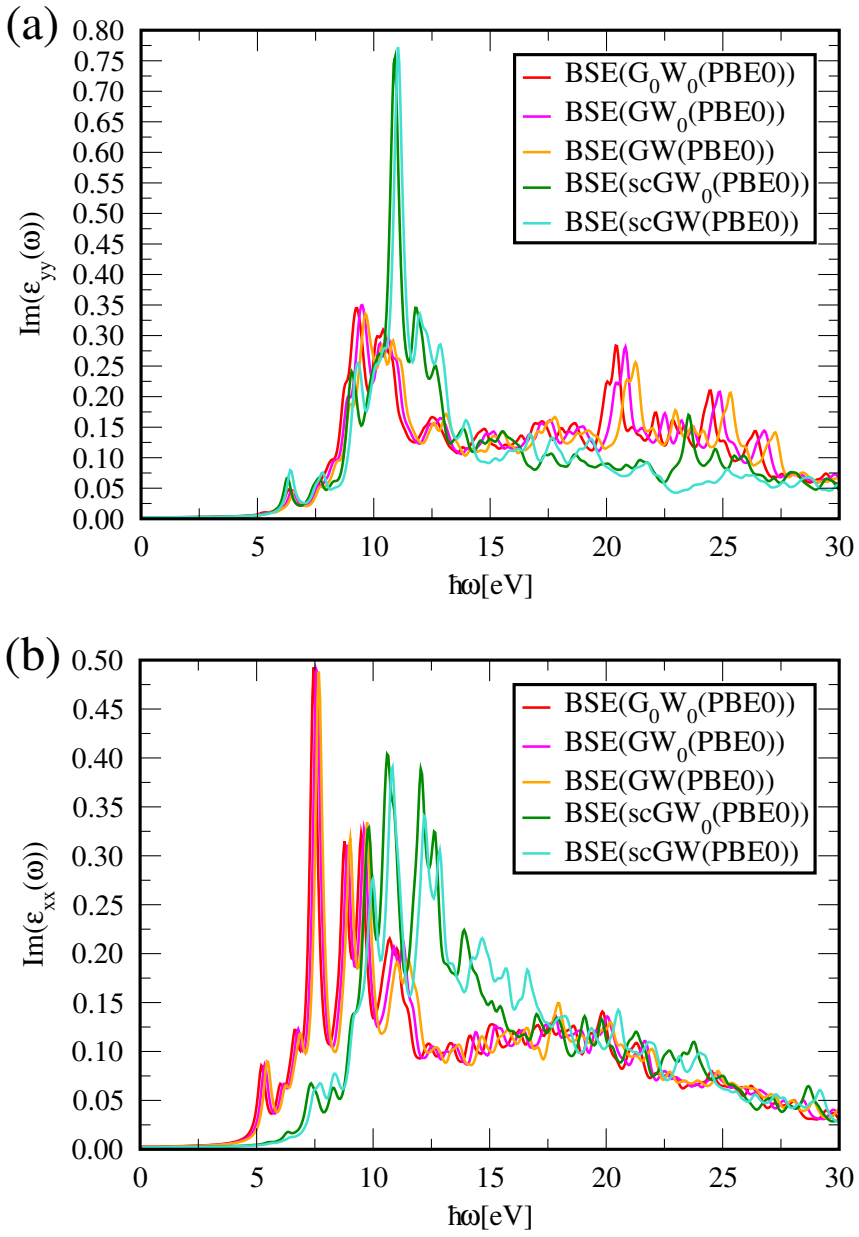

Figure 9.3.: UV absorption spectrum of C_6H_5Br for photon incidence within the molecular plane (a) parallel and (b) orthogonal to the C-Br bond from BSE(...(PBE0)) with simulation parameters like in section 6.1 and depending on the degree of self-consistency in the underlying GW calculations

Table 9.5.: Energetic order of the most localised low antibonding states of C_6H_5Br and levels of theory: DFT(PBE0(-electronic)) and subsequent G_0W_0 for gas phase and adsorption on the idealised $I_h(0001)$ ice surface or its $4S_{AD}$ orientational defect complex, $scGW_0$ for the gas phase used to extrapolate the ice surface results from G_0W_0 to $scGW_0$ (blue), incorrect order marked in red, for geometries and simulation parameters see chapter 4 and sections A, D

C_6H_5Br	DFT(PBE0(-el.))	G_0W_0	$scGW_0$
gas phase	$\pi^*_{a,s} < \sigma^*_s$	$\sigma^*_s < \pi^*_{a,s}$	$\pi^*_{a,s} < \sigma^*_s$
$I_h(0001)$	$\pi^*_{a,s} < \sigma^*_s$	$\pi^*_{a,s} < \sigma^*_s$	$\pi^*_{a,s} < \sigma^*_s$
$4S_{AD}$	$\pi^*_{a,s} < \sigma^*_s$	$\pi^*_{a,s} < \sigma^*_s$	$\pi^*_{a,s} < \sigma^*_s$

Table 9.6.: Correlation between local fraction "p"[4] and energy shift upon increasing the level of theory for the main $\pi^*_{a,s}$ and lowest σ^*_s states of C_6H_5Br in the gas phase: energy levels from DFT(PBE0) and subsequent G_0W_0 or $scGW_0$, energy shift Δ upon transition from DFT(PBE0) to G_0W_0 marked in orange, for geometries and simulation parameters see sections 4.1, D

C_6H_5Br gas phase	DFT(PBE0)	G_0W_0	Δ	$scGW_0$
π^*_a [eV] (p[%])	-0.6746 (41.5)	1.0809 (41.5)	1.7555	0.8873 (37.6)
π^*_s [eV] (p[%])	-0.6518 (43.2)	1.0660 (43.2)	1.7178	0.8851 (32.2)
σ^*_s [eV] (p[%])	-0.3109 (11.0)	0.4209 (11.0)	0.7318	0.5156 (1.4)
σ^*_s [eV] (p[%])	0.6212 (7.8)	0.9461 (7.8)	0.3249	1.1368 (6.6)
σ^*_s [eV] (p[%])	-0.0510 (25.8)	0.9835 (25.8)	1.0345	1.2495 (3.1)
σ^*_s [eV] (p[%])	1.3165 (3.6)	1.5396 (3.6)	0.2231	1.7128 (14.8)

order $\pi_s - \sigma^*_s < \pi_s - \pi^*_a$ is reversed by "sc", because the blueshift of the former hole-electron state is much stronger than that of the latter (cf. Tab. 9.9). Like for DEA, this indicates that a different dissociation mechanism would have been found if GW selfconsistency had not been included.

However this does not raise the photodissociation mechanism obtained for the adsorbed molecule to question, because the ice surface blueshifts both states such that the $\pi_s - \pi^*_a$ is the lowest optical excitation anyway (cf. Tab. 9.10). Furthermore the same energetic order ($\pi_s - \pi^*_a < \pi_s - \sigma^*_s$) with an even larger separation between the optical excitations was found for the adsorbates C_6H_5Cl and C_6H_5F (see section 6.2).

Table 9.7.: Correlation between local fraction "p"[4] and energy shift upon increasing the level of theory for the main $\pi^*_{a,s}$ and lowest σ^*_s states of C_6H_5Br adsorbed on the idealised $I_h(0001)$ ice surface: energy levels from DFT(PBE0) and subsequent G_0W_0, energy shift Δ upon this transition marked in orange, for geometries and simulation parameters see sections 4.2, 4.3, A, D

C_6H_5Br $I_h(0001)$	DFT(PBE0-el.)	G_0W_0	Δ
π^*_a[eV] (p[%])	-0.9203 (42.2)	+0.6621 (42.2)	+1.5824
π^*_s[eV] (p[%])	-0.9764 (43.8)	+0.5956 (43.8)	+1.5720
σ^*_s[eV] (p[%])	-0.6091 (4.2)	+0.2532 (4.2)	+0.8623
σ^*_s[eV] (p[%])	-0.5647 (32.5)	+0.7300 (32.5)	+1.2947

Table 9.8.: Correlation between local fraction "p"[4] and energy shift upon increasing the level of theory for the main $\pi^*_{a,s}$ and lowest σ^*_s states of C_6H_5Br adsorbed at a $4S_{AD}$ orientational defect complex on the ice surface: energy levels from DFT(PBE0) and subsequent G_0W_0, energy shift Δ upon this transition marked in orange, for geometries and simulation parameters see sections 4.2, 4.3, A, D

C_6H_5Br $4S_{AD}$	DFT(PBE0-el.)	G_0W_0	Δ
π^*_a[eV] (p[%])	-1.4653 (42.0)	+0.1184 (42.0)	+1.5837
π^*_s[eV] (p[%])	-1.5153 (42.5)	+0.0473 (42.5)	+1.5608
σ^*_s[eV] (p[%])	-1.1709 (40.2)	+0.2544 (40.2)	+1.4253
σ^*_s[eV] (p[%])	-0.1343 (6.7)	+0.5811 (6.7)	+0.7154
σ^*_s[eV] (p[%])	-0.0682 (4.7)	+0.7234 (4.7)	+0.7916

Table 9.9.: Photon energy required for the two lowest optical excitations of C_6H_5Br in the gas phase from BSE(...(PBE0)) with simulation parameters like in section 6.1 and depending on the degree of selfconsistency in the underlying GW calculations, oscillator strengths (OS[arbitrary units]) given in parentheses

BSE(...(PBE0))	$\pi_s - \pi^*_a$[eV] (OS[arb.])	$\pi_s - \sigma^*_s$[eV] (OS[arb.])
G_0W_0	4.7197 (0.4545)	4.1984 (0.6126)
GW_0	4.8841 (0.4535)	4.3340 (0.5692)
GW	4.9932 (0.4951)	4.3321 (0.7259)
$scGW_0$	4.9170 (0.1536)	5.4474 (0.7105)
scGW	5.0457 (0.1190)	5.5553 (0.4564)

Table 9.10.: Photon energy required for the two lowest optical excitations of C_6H_5Br from BSE(G_0W_0(...)) with simulation parameters like in section 6.1 for the gas phase and like in section 6.2 for the molecule adsorbed on the idealised I_h(0001) ice surface or at the $4S_{AD}$ orientational defect complex, oscillator strengths (OS[arbitrary units]) given in parentheses

BSE(G_0W_0(...))	$\pi_s - \pi_a^*$[eV] (OS[arb.])	$\pi_s - \sigma_s^*$[eV] (OS[arb.])
gas phase PBE0	4.7197 (0.4545)	4.1984 (0.6126)
I_h(0001) PBE0-electronic	4.9221 (1.0584)	4.9969 (2.9573)
$4S_{AD}$ PBE0-electronic	4.9009 (0.5412)	5.1000 (2.7720)

Bibliography

[1] E. J. Hart and J. W. Boag. Absorption spectrum of the hydrated electron in water and in aqueous solutions. *J. Am. Chem. Soc.*, 84(21):4090–4095, 1962.

[2] K. R. Siefermann, Y. Liu, E. Lugovoy, O. Link, M. Faubel, U. Buck, B. Winter, and B. Abel. Binding energies, lifetimes and implications of bulk and interface solvated electrons in water. *Nat. Chem.*, 2(4):274–279, 2010.

[3] U. Bovensiepen, C. Gahl, J. Stähler, M. Bockstedte, M. Meyer, F. Baletto, S. Scandolo, X.-Y. Zhu, A. Rubio, and M. Wolf. A dynamic landscape from femtoseconds to minutes for excess electrons at ice-metal interfaces. *J. Phys. Chem. C*, 113(3):979–988, 2009.

[4] B. Abel, U. Buck, A. L. Sobolewski, and W. Domcke. On the nature and signatures of the solvated electron in water. *Phys. Chem. Chem. Phys.*, 14(1):22–34, 2012.

[5] J. R. R. Verlet, A. E. Bragg, A. Kammrath, O. Cheshnovsky, and D. M. Neumark. Observation of large water-cluster anions with surface-bound excess electrons. *Science*, 307(5706):93–96, 2005.

[6] K. Onda, B. Li, J. Zhao, K. D. Jordan, J. Yang, and H. Petek. Wet electrons at the $H_2O/TiO_2(110)$ surface. *Science*, 308(5725):1154–1158, 2005.

[7] K. R. Siefermann and B. Abel. The hydrated electron: A seemingly familiar chemical and biological transient. *Angew. Chem. Int. Ed.*, 50(23):5264–5272, 2011.

[8] J. Stähler, C. Gahl, and M. Wolf. Dynamics and reactivity of trapped electrons on supported ice crystallites. *Acc. Chem. Res.*, 45(1):131–138, 2012.

[9] B. Abel. Hydrated interfacial ions and electrons. *Annu. Rev. Phys. Chem.*, 64(1):533–552, 2013.

[10] M. P. Coons, Z.-Q. You, and J. M. Herbert. The hydrated electron at the surface of neat liquid water appears to be indistinguishable from the bulk species. *J. Am. Chem. Soc.*, 138(34):10879–10886, 2016.

[11] N. Getoff. Fundamental biological importance of solvated electrons in humans. *Horm. Mol. Biol. Clin. Invest.*, 16(3):125–128, 2013.

[12] M. Dameris. Climate change and atmospheric chemistry: How will the stratospheric ozone layer develop? *Angew. Chem. Int. Edit.*, 49(44):8092–8102, 2010.

[13] J. C. Farman, B. G. Gardiner, and J. D. Shanklin. Large losses of total ozone in antarctica reveal seasonal ClO_x/NO_x interaction. *Nature*, 315:207–210, 1985.

[14] D. G. Loyola, R. M. Coldewey-Egbers, M. Dameris, H. Garny, A. Stenke, M. Van Roozendael, C. Lerot, D. Balis, and M. Koukouli. Global long-term monitoring of the ozone layer - a prerequisite for predictions. *Int. J. Remote Sens.*, 30(15-16):4295–4318, 2009.

[15] S. Solomon. Stratospheric ozone depletion: A review of concepts and history. *Rev. Geophys.*, 37(3):275–316, 1999.

[16] C. George, M. Ammann, B. D'Anna, D. J. Donaldson, and S. A. Nizkorodov. Heterogeneous photochemistry in the atmosphere. *Chem. Rev.*, 115(10):4218–4258, 2015.

[17] I. J. George and J. P. D. Abbatt. Heterogeneous oxidation of atmospheric aerosol particles by gas-phase radicals. *Nat. Chem.*, 2(9):713–722, 2010.

[18] Q.-B. Lu and L. Sanche. Effects of cosmic rays on atmospheric chlorofluorocarbon dissociation and ozone depletion. *Phys. Rev. Lett.*, 87(7):078501 (4), 2001.

[19] Q.-B. Lu and T. E. Madey. Giant enhancement of electron-induced dissociation of chlorofluorocarbons coadsorbed with water or ammonia ices: Implications for atmospheric ozone depletion. *J. Chem. Phys.*, 111(7):2861–2864, 1999.

[20] N. S. Holmes and J. R. Sodeau. A study of the interaction between halomethanes and water-ice. *J. Phys. Chem. A*, 103(24):4673–4679, 1999.

[21] A. Borodin, O. Höfft, U. Kahnert, V. Kempter, S. Krischok, and M. O. Abou-Helal. The interface between benzenes (C_6H_6;C_6H_5Cl;2-C_6H_4OHCl) and amorphous solid water studied with metastable impact electron spectroscopy and ultraviolet photoelectron spectroscopy (HeI and II). *J. Chem. Phys.*, 120(11):5407, 2004.

[22] C.-L. Huang, J.-C. Jiang, A. M. Mebel, Y. T. Lee, and C.-K. Ni. Photodissociation dynamics of fluorobenzene. *J. Am. Chem. Soc.*, 125(32):9814–9820, 2003.

[23] G.-J. Wang, R.-S. Zhu, H. Zhang, K.-L. Han, G.-Z. He, and N.-Q. Lou. Photodissociation of chlorobenzene at 266 nm. *Chem. Phys. Lett.*, 288(2-4):429–432, 1998.

[24] B. Tang, R. Zhu, Y. Tang, L. Ji, and B. Zhang. Photodissociation of bromobenzene at 267 and 234 nm: experimental and theoretical investigation of the photodissociation mechanism. *Chem. Phys. Lett.*, 381(5-6):617–622, 2003.

[25] P. Y. Cheng, D. Zhong, and A. H. Zewail. Kinetic-energy, femtosecond resolved reaction dynamics. modes of dissociation (in iodobenzene) from time-velocity correlations. *Chem. Phys. Lett.*, 237(5-6):399–405, 1995.

[26] H. J. Hwang and M. A. El-Sayed. Photodissociation dynamics of iodobenzene by state-selective photofragment translational spectroscopy. *J. Photochem. Photobiol. A Chem.*, 102(1):13–20, 1996.

[27] H. J. Hwang and M. A. El-Sayed. Determination of the rapid energy redistribution rate in a transition state; using molecular rotation as a clock and translational energy release as an energy monitor: The photodissociation of iodobenzene. *J. Chem. Phys.*, 96(1):856–858, 1992.

[28] C.-Y. Wu, Y.-J. Wu, and Y.-P. Lee. Molecular elimination in photolysis of fluorobenzene at 193 nm: Internal energy of hf determined with time-resolved fourier-transform spectroscopy. *J. Chem. Phys.*, 121(18):8792–8799, 2004.

[29] S.-H. Lee, C.-Y. Wu, S.-K. Yang, and Y.-P. Lee. Photodissociation dynamics of fluorobenzene (C_6H_5F) at 157 and 193 nm: Branching ratios and distributions of kinetic energy. *J. Chem. Phys.*, 125(14):144301 (7), 2006.

[30] S. A. Vázquez and E. Martínez-Núñez. Translational energy distributions in the photodissociation of fluorobenzene. *Chem. Phys.*, 349(1-3):219–225, 2008.

[31] M. N. R. Ashfold, G. A. King, D. Murdock, M. G. D. Nix, T. A. A. Oliver, and A. G. Sage. $\pi\sigma^*$ excited states in molecular photochemistry. *Phys. Chem. Chem. Phys.*, 12(6):1218–1238, 2010.

[32] A. G. Sage, T. A. A. Oliver, D. Murdock, M. B. Crow, G. A. D. Ritchie, J. N. Harvey, and M. N. R. Ashfold. $n\sigma^*$ and $\pi\sigma^*$ excited states in aryl halide photochemistry: a comprehensive study of the uv photodissociation dynamics of iodobenzene. *Phys. Chem. Chem. Phys.*, 13(18):8075–8093, 2011.

[33] T. Ichimura, Y. Mori, H. Shinohara, and N. Nishi. Photofragmentation of chlorobenzene: translational energy distribution of the recoiling cl fragment. *Chem. Phys.*, 189(1):117–125, 1994.

[34] A. L. Sobolewski and W. Domcke. Conical intersections induced by repulsive $^1\pi\sigma^*$ states in planar organic molecules: malonaldehyde, pyrrole and chlorobenzene as photochemical model systems. *Chem. Phys.*, 259(2-3):181–191, 2000.

[35] E. R. Miller, G. D. Muirhead, and E. T. Jensen. Mechanisms for the near-uv photodissociation of CH_3I on D_2O/Cu(110). *J. Chem. Phys.*, 138(8):084702 (10), 2013.

[36] E. T. Jensen. Excitation and quenching mechanisms in the near-uv photodissociation of CH_3Br and CH_3Cl adsorbed on D_2O or CH_3OH on Cu(110). *Phys. Chem. Chem. Phys.*, 17(14):9173–9185, 2015.

[37] V. Poterya, J. Kočišek, J. Lengyel, P. Svrčková, A. Pysanenko, D. Hollas, P. Slavíček, and M. Fárník. Clustering and photochemistry of freon CF_2Cl_2 on argon and ice nanoparticles. *J. Phys. Chem. A*, 118(26):4740–4749, 2014.

[38] O. Ingólfsson, F. Weik, and E. Illenberger. The reactivity of slow electrons with molecules at different degrees of aggregation: gas phase, clusters and condensed phase. *Int. J. M. Spe. I. P.*, 155(1-2):1–68, 1996.

[39] J. C. Steelhammer and W. E. Wentworth. Correlation of electron beam and thermal electron attachment studies for some chloro, bromo, iodo aromatic compounds. *J. Chem. Phys.*, 51(5):1802–1814, 1969.

[40] H. Shimamori, T. Sunagawa, Y. Ogawa, and Y. Tatsumi. Low-energy electron attachment to C_6H_5X (X=Cl, Br and I). *Chem. Phys. Lett.*, 232(1):115–120, 1995.

[41] A. Modelli and M. Venuti. Temporary π^* and σ^* anions and dissociative electron attachment in chlorobenzene and related molecules. *J. Phys. Chem. A*, 105(24):5836–5841, 2001.

[42] W.-L. Feng and S. X. Tian. Ab initio molecular dynamics simulation study of dissociative electron attachment to $C_6H_5(CH_2)_nCl$ (n = 0,1,2,3,4). *Int. J. M. S.*, 399-400:40–43, 2016.

[43] A. Modelli, M. Venuti, and László Szepes. Intramolecular electron transfer in heterosubstituted benzene derivatives as probed by dissociative electron attachment. *J. Am. Chem. Soc.*, 124(28):8498–8504, 2002.

[44] L. G. Christophorou, R. N. Compton, G. S. Hurst, and P. W. Reinhardt. Dissociative electron capture by benzene derivatives. *J. Chem. Phys.*, 45(2):536–547, 1966.

[45] K. L. Stricklett, S. C. Chu, and P. D. Burrow. Dissociative attachment in vinyl and allyl chloride, chlorobenzene and benzyl chloride. *Chem. Phys. Lett.*, 131(3):279–284, 1986.

[46] P. Ayotte, J. Gamache, A. D. Bass, I. I. Fabrikant, and L. Sanche. Absolute cross sections for dissociative electron attachment to condensed CH_3Cl and CH_3Br: Effects of potential energy curve crossing and capture probability. *J. Chem. Phys.*, 106(2):749–760, 1997.

[47] Q.-B. Lu and L. Sanche. Enhancements in dissociative electron attachment to CF_4, chlorofluorocarbons and hydrochlorofluorocarbons adsorbed on H_2O ice. *J. Chem. Phys.*, 120(5):2434–2438, 2004.

[48] C. C. Perry, N. S. Faradzhev, D. H. Fairbrother, and T. E. Madey. Electron-driven chemistry of halogenated compounds in condensed phases: Effects of solvent matrices on reaction dynamics and kinetics. *Int. Rev. Phys. Chem.*, 23(2):289–340, 2004.

[49] C. C. Perry, G. M. Wolfe, A. J. Wagner, J. Torres, N. S. Faradzhev, T. E. Madey, and D. H. Fairbrother. Chemical reactions in CF_2Cl_2/water (ice) films induced by x-ray radiation. *J. Phys. Chem. B*, 107(46):12740–12751, 2003.

[50] I. Kemeny. *Electron Transfer Dynamics in Halobenzenes at Ice and Metal Interfaces*. (phd) dissertation, Universität Duisburg-Essen, 2017.

[51] I. V. Hertel, C. Hüglin, C. Nitsch, and C. P. Schulz. Photoionization of $Na(NH_3)_n$ and $Na(H_2O)_n$ clusters: A step towards the liquid phase? *Phys. Rev. Lett.*, 67(13):1767–1770, 1991.

[52] T. Vondrak, J. M. C. Plane, and S. R. Meech. Influence of submonolayer sodium adsorption on the photoemission of the Cu(111)/water ice surface. *J. Chem. Phys.*, 125(22):224702 (8), 2006.

[53] V. Balzani, G. Bergamini, and P. Ceroni. Light: A very peculiar reactant and product. *Angew. Chem. Int. Edit.*, 54(39):11320–11337, 2015.

[54] R. Benassi, C. Bertarini, and F. Taddei. The dissociative nature of the radical anion of benzyl chloride. a theoretical mo ab initio approach. *Chem. Phys. Lett.*, 257(5-6):633–638, 1996.

[55] C. Fontanesi, P. Baraldi, and M. Marcaccio. On the dissociation dynamics of the benzyl chloride radical anion. an ab initio dynamic reaction coordinate analysis study. *J. Mol. Struct.*, 548(1-3):13–20, 2001.

[56] G. B. Griffin, R. M. Young, O. T. Ehrler, and D. M. Neumark. Electronic relaxation dynamics in large anionic water clusters: $(H_2O)_n^-$ and $(D_2O)_n^-$ (n=25-200). *J. Chem. Phys.*, 131(19):194302 (9), 2009.

[57] B. C. Garrett et al. Role of water in electron-initiated processes and radical chemistry: Issues and scientific advances. *Chem. Rev.*, 105(1):355–389, 2005.

[58] C. Bertram. *Reaktionen durch heiße und solvatisierte Elektronen bei kryogenen Temperaturen*. (phd) dissertation, Ruhr-Universität Bochum, 2017.

[59] V. F. Petrenko and R. W. Whitworth. *Physics of Ice*, volume 1. Oxford University Press, Oxford, 2006.

[60] D. Pan, L.-M. Liu, G. A. Tribello, B. Slater, A. Michaelides, and E. Wang. Surface energy and surface proton order of the ice I_h basal and prism surfaces. *J. Phys. Cond. Mat.*, 22(7):074209 (11), 2010.

[61] M. Bockstedte, A. Michl, M. Kolb, M. Mehlhorn, and K. Morgenstern. Incomplete bilayer termination of the ice (0001) surface. *J. Phys. Chem. C*, 120(2):1097–1109, 2016.

[62] R. Onaka and T. Takahashi. Vacuum uv absorption spectra of liquid water and ice. *J. Phys. Soc. Jap.*, 24(3):548–550, 1968.

[63] T. Shibaguchi, H. Onuki, and R. Onaka. Electronic structures of water and ice. *J. Phys. Soc. Jap.*, 42(1):152–158, 1977.

[64] P. Hahn, W. G. Schmidt, H. Seino, M. Preuss, F. Bechstedt, and J. Bernholc. Optical absorption of water: Coulomb effects versus hydrogen bonding. *Phys. Rev. Lett.*, 94(3):037404 (4), 2005.

[65] J. Vinson, J. J. Kas, F. D. Vila, J. J. Rehr, and E. L. Shirley. Theoretical optical and x-ray spectra of liquid and solid H_2O. *Phys. Rev. B*, 85(4):045101 (6), 2012.

[66] A. Modelli. Electron attachment and intramolecular electron transfer in unsaturated chloroderivatives. *Phys. Chem. Chem. Phys.*, 5(14):2923–2930, 2003.

[67] V. A. Ukraintsev, T. J. Long, T. Gowl, and I. Harrison. Photoinduced dissociative electron attachment of CH_3Br on $Pt(111)$: The role of the local work function. *J. Chem. Phys.*, 96(12):9114–9121, 1992.

[68] C. Gahl, U. Bovensiepen, C. Frischkorn, K. Morgenstern, K.-H. Rieder, and M. Wolf. Ultrafast electron solvation dynamics in $D_2O/Cu(111)$: influence of coverage and structure. *Surf. Sci.*, 532:108–112, 2003.

[69] M. Born and V. Fock. Beweis des adiabatensatzes. *Z. Phys.*, 51(3):165–180, 1928.

[70] P. Hohenberg and W. Kohn. Inhomogeneous electron gas. *Phys. Rev. B*, 136(3):864–871, 1964.

[71] J. W. Strutt 3rd baron Rayleigh. *The theory of sound*, volume 1. The Macmillan Company, London, England, 1877.

[72] W. Ritz. Über eine neue methode zur lösung gewisser variationsprobleme der mathematischen physik. *J. Reine Angew. Math.*, 135:1–61, 1909.

[73] W. Kohn and L. J. Sham. Self-consistent equations including exchange and correlation effects. *Phys. Rev. A*, 140(4):1133–1138, 1965.

[74] R. M. Dreizler and E. K. U. Gross. *Density Functional Theory: An Approach to the Quantum Many-Body Problem*. Springer Verlag, Berlin / Heidelberg / New York, 1990.

[75] J. P. Perdew and A. Zunger. Self-interaction correction to density-functional approximations for many-electron systems. *Phys. Rev. B*, 23(10):5048–5079, 1981.

[76] A. Michl. Ab initio theory of admolecule structures at ice surfaces and the solvated electron. *Diploma Thesis*, 2011.

[77] G. Floquet. Sur les équations différentielles linéaires à coefficients périodiques. *ASENS*, 12(2):47–88, 1883.

[78] F. Bloch. Über die quantenmechanik der elektronen in kristallgittern. *Z. Phys.*, 52(7):555–600, 1929.

[79] J. C. Phillips. Energy-band interpolation scheme based on a pseudopotential. *Phys. Rev.*, 112(3):685–695, 1958.

[80] M. L. Cohen and V. Heine. *Solid State Physics*, volume 24 of *Solid State Physics*, chapter The Fitting of Pseudopotentials to Experimental Data and Their Subsequent Application, pages 37–248. Elsevier B.V., 1970.

[81] M. T. Yin and M. L. Cohen. Theory of ab initio pseudopotential calculations. *Phys. Rev. B*, 25(12):7403–7412, 1982.

[82] M. C. Payne, M. P. Teter, D. C. Allan, T. A. Arias, and J. D. Joannopoulos. Iterative minimization techniques for ab initio total-energy calculations: molecular dynamics and conjugate gradients. *Rev. Mod. Phys.*, 64(4):1045–1097, 1992.

[83] N. Troullier and J. L. Martins. Efficient pseudopotentials for plane-wave calculations. *Phys. Rev. B*, 43(3):1993–2006, 1991.

[84] A. M. Rappe, K. M. Rabe, E. Kaxiras, and J. D. Joannopoulos. Optimized pseudopotentials. *Phys. Rev. B*, 41(2R):1227–1230, 1990.

[85] D. Vanderbilt. Soft self-consistent pseudopotentials in a generalized eigenvalue formalism. *Phys. Rev. B*, 41(11R):7892–7895, 1990.

[86] K. Laasonen, R. Car, C. Lee, and D. Vanderbilt. Implementation of ultrasoft pseudopotentials in ab initio molecular dynamics. *Phys. Rev. B*, 43(8R):6796–6799, 1991.

[87] P. E. Blöchl. Projector augmented-wave method. *Phys. Rev. B*, 50(24):17953–17979, 1994.

[88] G. Kresse and D. Joubert. From ultrasoft pseudopotentials to the projector augmented-wave method. *Phys. Rev. B*, 59(3):1758–1775, 1999.

[89] J. C. Slater. Wave functions in a periodic potential. *Phys. Rev.*, 51(10):846–851, 1937.

[90] P. M. Marcus. Variational methods in the computation of energy bands. *Int. J. Q. Chem.*, 1(S1):567–588, 1967.

[91] O. K. Andersen. Linear methods in band theory. *Phys. Rev. B*, 12(8):3060–3083, 1975.

[92] M. Shishkin and G. Kresse. Implementation and performance of the frequency-dependent gw method within the paw framework. *Phys. Rev. B*, 74(3):035101 (13), 2006.

[93] G. Kresse and J. Furthmüller. Efficient iterative schemes for ab initio total-energy calculations using a plane-wave basis set. *Phys. Rev. B*, 54(16):11169–11186, 1996.

[94] J. P. Perdew and W. Yue. Accurate and simple density functional for the electronic exchange energy: Generalized gradient approximation. *Phys. Rev. B*, 33(12R):8800–8802, 1986.

[95] J. P. Perdew, K. Burke, and M. Ernzerhof. Generalized gradient approximation made simple. *Phys. Rev. Lett.*, 77(18):3865–3868, 1996.

[96] R. Eisenschitz and F. London. Über das verhältnis der van der waalsschen kräfte zu den homöopolaren bindungskräften. *Z. Phys.*, 60(7):491–527, 1930.

[97] F. London. Zur theorie und systematik der molekularkräfte. *Z. Phys.*, 63(3):245–279, 1930.

[98] F. London. Über einige eigenschaften und anwendungen der molekularkräfte. *Z. Phys. Chem. B*, 11:222–251, 1930.

[99] S. Grimme. Accurate description of van der waals complexes by density functional theory including empirical corrections. *J. Comput. Chem.*, 25(12):1463–1473, 2004.

[100] S. Grimme. Semiempirical gga-type density functional constructed with a long-range dispersion correction. *J. Comput. Chem.*, 27(15):1787–1799, 2006.

[101] T. Kerber, M. Sierka, and J. Sauer. Application of semiempirical long-range dispersion corrections to periodic systems in density functional theory. *J. Comput. Chem.*, 29(13):2088–2097, 2008.

[102] T. Bučko, J. Hafner, S. Lebègue, and J. G. Ángyán. Improved description of the structure of molecular and layered crystals: Ab initio dft calculations with van der waals corrections. *J. Phys. Chem. A*, 114(43):11814–11824, 2010.

[103] D. M. Ceperley and B. J. Alder. Ground state of the electron gas by a stochastic method. *Phys. Rev. Lett.*, 45(7):566–569, 1980.

[104] D. R. Hamann. H_2O hydrogen bonding in density-functional theory. *Phys. Rev. B*, 55(16R):10157–10160, 1997.

[105] S. Casassa, M. Calatayud, K. Doll, C. Minot, and C. Pisani. Proton ordered cubic and hexagonal periodic models of ordinary ice. *Chem. Phys. Lett.*, 409(1-3):110–117, 2005.

[106] J. P. Perdew, K. Burke, and M. Ernzerhof. Rationale for mixing exact exchange with density functional approximations. *J. Chem. Phys.*, 105(22):9982–9985, 1996.

[107] J. Heyd, G. E. Scuseria, and M. Ernzerhof. Hybrid functionals based on a screened coulomb potential. *J. Chem. Phys.*, 118(18):8203–8215, 2003.

[108] J. Heyd, G. E. Scuseria, and M. Ernzerhof. Erratum: "hybrid functionals based on a screened coulomb potential" [j. chem. phys. 118, 8207 (2003)]. *J. Chem. Phys.*, 124(21):219906 (1), 2006.

[109] V. Fock. Näherungsmethode zur lösung des quantenmechanischen mehrkörperproblems. *Z. Phys.*, 61(1-2):126–148, 1930.

[110] D. R. Hartree and W. Hartree. Self-consistent field, with exchange, for beryllium. *Proc. Roy. Soc. A*, 150(869):9–33, 1935.

[111] C. C. J. Roothaan. New developments in molecular orbital theory. *Rev. Mod. Phys.*, 23(2):69–89, 1951.

[112] G. G. Hall and J. Lennard-Jones. The molecular orbital theory of chemical valency viii. a method of calculating ionization potentials. *Proc. Roy. Soc. A*, 205(1083):541–552, 1951.

[113] P.-O. Löwdin. On the non-orthogonality problem connected with the use of atomic wave functions in the theory of molecules and crystals. *J. Phys. Chem.*, 18(3):365–375, 1950.

[114] R. Orlando, R. Dovesi, C. Roetti, and V. R. Saunders. *Ab initio* hartree-fock calculations for periodic compounds: application to semiconductors. *J. Phys. Cond. Mat.*, 2(38):7769–7789, 1990.

[115] C. Pisani, R. Dovesi, and C. Roetti. *Hartree-Fock Ab Initio Treatment of Crystalline Systems*, volume 48 of *Lecture Notes in Chemistry*. Springer-Verlag, Berlin, Germany, 1988.

[116] F. Jensen. *Introduction to Computational Chemistry*, volume 2. John Wiley & Sons, Ltd., The Atrium, Southern Gate, Chichester, West Sussex PO19 8SQ, England, 2007.

[117] S. G. Abdu, M. Y. Onimisi, and N. Musa. Computation of the first and second ionization energies of the first ten elements of the periodic table using a modified hartree-fock approximation code. *Am. J. Cond. Mat. Phys.*, 4(3):51–56, 2014.

[118] W. Nolting. *Grundkurs: Theoretische Physik 7. Viel-Teilchen-Theorie*, volume 3 of *Grundkurs: Theoretische Physik*. Zimmermann-Neufang Ulmen, Antoniusstraße 9, D-56766 Ulmen, 1995.

[119] M. Gell-Mann and K. A. Brueckner. Correlation energy of an electron gas at high density. *Phys. Rev.*, 106(2):364–368, 1957.

[120] M. Bockstedte. *Diffusion der Gallium-Leerstelle in Gallium-Arsenid*. (phd) dissertation, Friedrich-Alexander-Universität Erlangen-Nürnberg, 1999.

[121] A. García, C. Elsässer, J. Zhu, S. G. Louie, and M. L. Cohen. Use of gradient-corrected functionals in total-energy calculations for solids. *Phys. Rev. B*, 46(15R):9829–9832, 1992.

[122] G. Ortiz. Gradient-corrected pseudopotential calculations in semiconductors. *Phys. Rev. B*, 45(19):11328–11331, 1992.

[123] M. Fuchs, M. Bockstedte, E. Pehlke, and M. Scheffler. Pseudopotential study of binding properties of solids within generalized gradient approximations: The role of core-valence exchange correlation. *Phys. Rev. B*, 57(4):2134–2145, 1998.

[124] W. J. Carr, Jr. Energy, specific heat, and magnetic properties of the low-density electron gas. *Phys. Rev.*, 122(5):1437–1446, 1961.

[125] K. Sawada. Correlation energy of an electron gas at high density. *Phys. Rev.*, 106(2):372–383, 1957.

[126] K. Sawada, K. A. Brueckner, N. Fukuda, and R. Brout. Correlation energy of an electron gas at high density: Plasma oscillations. *Phys. Rev.*, 108(3):507–514, 1957.

[127] D. Ceperley. Ground state of the fermion one-component plasma: A monte carlo study in two and three dimensions. *Phys. Rev. B*, 18(7):3126–3138, 1978.

[128] S. Misawa. Ferromagnetism of an electron gas. *Phys. Rev.*, 140(5A):A1645–A1648, 1965.

[129] U. von Barth and L. Hedin. A local exchange-correlation potential for the spin polarized case: I. *J. Phys. C: Solid State Physics*, 5(13):1629–1642, 1972.

[130] S. G. Louie and M. S. Hybertsen. Theory of quasiparticle energies: Band gaps and excitation spectra in solids. *Int. J. Q. Chem.*, 32(S21):31–44, 1987.

[131] C. S. Wang, B. M. Klein, and H. Krakauer. Theory of magnetic and structural ordering in iron. *Phys. Rev. Lett.*, 54(16):1852–1855, 1985.

[132] N. Moll, M. Bockstedte, M. Fuchs, E. Pehlke, and M. Scheffler. Application of generalized gradient approximations: The diamond-β-tin phase transition in si and ge. *Phys. Rev. B*, 52(4):2550–2556, 1995.

[133] D. R. Hamann. Generalized gradient theory for silica phase transitions. *Phys. Rev. Lett.*, 76(4):660–663, 1996.

[134] J. P. Perdew. Accurate density functional for the energy: Real-space cutoff of the gradient expansion for the exchange hole. *Phys. Rev. Lett.*, 55(16):1665–1668, 1985.

[135] D. C. Langreth and M. J. Mehl. Beyond the local-density approximation in calculations of ground-state electronic properties. *Phys. Rev. B*, 28(4):1809–1834, 1983.

[136] D. C. Langreth and M. J. Mehl. Easily implementable nonlocal exchange-correlation energy functional. *Phys. Rev. Lett.*, 47(6):446–450, 1981.

[137] J. P. Perdew. *Electronic structure of solids '91*, chapter BEYOND THE LOCAL DENSITY APPROXIMATION, pages 11–20. Electronic structure of solids. Akademie Verlag, Berlin, 1991.

[138] J. Heyd, J. E. Peralta, G. E. Scuseria, and R. L. Martin. Energy band gaps and lattice parameters evaluated with the heyd-scuseria-ernzerhof screened hybrid functional. *J. Chem. Phys.*, 123(17):174101 (8), 2005.

[139] M. Shishkin and G. Kresse. Self-consistent gw calculations for semiconductors and insulators. *Phys. Rev. B*, 75(23):235102 (9), 2007.

[140] F. Tran and P. Blaha. Accurate band gaps of semiconductors and insulators with a semilocal exchange-correlation potential. *Phys. Rev. Lett.*, 102(22):226401 (4), 2009.

[141] T. C. Leung, C. T. Chan, and B. N. Harmon. Ground-state properties of fe, co, ni, and their monoxides: Results of the generalized gradient approximation. *Phys. Rev. B*, 44(7):2923–2927, 1991.

[142] S. Tomić and N. M. Harrison. Electronic structure of iii-v's semiconductors from b3lyp and pbeo functionals. In M. Caldas and N. Studart, editors, *29th International conference on the physics of semiconductors*, volume 1199 of *AIP Conference Proceedings*, pages 65–66. AIP, 2010.

[143] X. Wu, E. J. Walter, A. M. Rappe, R. Car, and A. Selloni. Hybrid density functional calculations of the band gap of $ga_xin_{1-x}n$. *Phys. Rev. B*, 80(11):115201 (5), 2009.

[144] D. Fritsch, B. J. Morgan, and A. Walsh. Self-consistent hybrid functional calculations: Implications for structural, electronic, and optical properties of oxide semiconductors. *Nano. Res. Lett.*, 12(1):19 (7), 2017.

[145] M. Shishkin, G. Kresse, F. Fuchs, J. Furthmüller, and F. Bechstedt. Quasiparticle band structure based on a generalized kohn-sham scheme. *Phys. Rev. B*, 76(11):115109 (8), 2007.

[146] M. K. Y. Chan and G. Ceder. Efficient band gap prediction for solids. *Phys. Rev. Lett.*, 105(19):196403 (4), 2010.

[147] T. M. Henderson, J. Paier, and G. E. Scuseria. Accurate treatment of solids with the hse screened hybrid. *Phys. Stat. Sol.*, 248(4):767, 2011.

[148] F. D. Murnaghan. The compressibility of media under extreme pressures. *Proc. Nat. Acad. Sci.*, 30(9):244–247, 1944.

[149] P. Pulay. Ab initio calculation of force constants and equilibrium geometries in polyatomic molecules. i. theory. *Mol. Phys.*, 17(2):197–204, 1969.

[150] R. P. Feynman. Forces in molecules. *Phys. Rev.*, 56(4):340–343, 1939.

[151] M. Scheffler, J. P. Vigneron, and G. B. Bachelet. Total-energy gradients and lattice distortions at point defects in semiconductors. *Phys. Rev. B*, 31(10):6541–6551, 1985.

[152] P. Pulay. Convergence acceleration of iterative sequences. the case of scf iteration. *Chem. Phys. Lett.*, 73(2):393–398, 1980.

[153] W. H. Press, S. A. Teukolsky, W. T. Vetterling, and B. P. Flannery. *Numerical Recipes. The Art of Scientific Computing*, volume 1. Cambridge

University Press, Shaftesbury Road CB2 8BS, Cambridge, United Kingdom, 1986.

[154] G. P. Francis and M. C. Payne. Finite basis set corrections to total energy pseudopotential calculations. *J. Phys. Cond. Mat.*, 2(19):4395–4404, 1990.

[155] M. Shishkin, G. Kresse, and M. Marsman. Accurate quasiparticle spectra from self-consistent gw calculations with vertex corrections. *Phys. Rev. Lett.*, 99(24):246403 (4), 2007.

[156] W. G. Aulbur, L. Jönsson, and J. W. Wilkins. *Solid State Physics*, volume 54 of *Solid State Physics*, chapter Quasiparticle calculations in solids, pages 1–218. Academic Press, A Harcourt Science and Technology Company 525 B Street, Suite 1900, San Diego, CA 92101-4495, USA, 2000.

[157] L. Hedin. New method for calculating the one-particle green's function with application to the electron-gas problem. *Phys. Rev.*, 139(3A):796–823, 1965.

[158] F. Aryasetiawan and O. Gunnarsson. The gw method. *Rep. Prog. Phys.*, 61(3):237–312, 1998.

[159] G. Onida, L. Reining, and A. Rubio. Electronic excitations: density-functional versus many-body green's-function approaches. *Rev. Mod. Phys.*, 74(2):601–659, 2002.

[160] G. Strinati. Application of the green's functions method to the study of the optical properties of semiconductors. *Riv. Nuovo Cimento*, 11(12):1–86, 1988.

[161] M. Rohlfing and S. G. Louie. Electron-hole excitations and optical spectra from first principles. *Phys. Rev. B*, 62(8):4927–4944, 2000.

[162] S. Albrecht, L. Reining, R. Del Sole, and G. Onida. Excitonic effects in the optical properties. *Phys. Stat. Sol. A*, 170(2):189–197, 1998.

[163] S. Albrecht, L. Reining, R. Del Sole, and G. Onida. *Ab Initio* calculation of excitonic effects in the optical spectra of semiconductors. *Phys. Rev. Lett.*, 80(20):4510–4513, 1998.

[164] A. L. Fetter and J. D. Walecka. *QUANTUM THEORY OF MANY-PARTICLE SYSTEMS*. INTERNATIONAL SERIES IN PURE AND APPLIED PHYSICS. McGraw-Hill, Inc., America, 1971.

[165] L. X. Benedict, E. L. Shirley, and R. B. Bohn. Optical absorption of insulators and the electron-hole interaction: An *Ab Initio* calculation. *Phys. Rev. Lett.*, 80(20):4514–4517, 1998.

[166] M. Rohlfing, P. Krüger, and J. Pollmann. Efficient scheme for gw quasiparticle band-structure calculations with applications to bulk Si and to the Si(001)-(2x1) surface. *Phys. Rev. B*, 52(3):1905–1917, 1995.

[167] M. Rohlfing, P. Krüger, and J. Pollmann. Quasiparticle band structure of CdS. *Phys. Rev. Lett.*, 75(19):3489–3492, 1995.

[168] J. v. Neumann and E. Wigner. Über das verhalten von eigenwerten bei adiabatischen prozessen. *Phys. Z.*, 30:467–470, 1929.

[169] L. D. Landau and E. M. Lifschitz. *LEHRBUCH DER THEORETISCHEN PHYSIK III: QUANTENMECHANIK*, volume 2 of *LEHRBUCH DER THEORETISCHEN PHYSIK*. Akademie-Verlag, Berlin, Germany, 1965.

[170] H. A. Jahn and E. Teller. Stability of polyatomic molecules in degenerate electronic states - i—orbital degeneracy. *Proc. Roy. Soc. A*, 161(905):220–235, 1937.

[171] D. R. Yarkony. Current issues in nonadiabatic chemistry. *J. Phys. Chem.*, 100(48):18612–18628, 1996.

[172] R. Renner. Zur theorie der wechselwirkung zwischen elektronen- und kernbewegung bei dreiatomigen, stabförmigen molekülen. *Phys. Z.*, 92:172–193, 1934.

[173] D. R. Yarkony. Diabolical conical intersections. *Rev. Mod. Phys.*, 68(4):985–1013, 1996.

[174] G. Herzberg and H. C. Longuet-Higgins. Intersection of potential energy surfaces in polyatomic molecules. *Discuss. Faraday Soc.*, 35:77–82, 1963.

[175] M. V. Berry. Quantal phase factors accompanying adiabatic changes. *Proc. Roy. Soc. A*, 392(1802):45–57, 1984.

[176] J. v. Neumann and E. Wigner. Über merkwürdige diskrete eigenwerte. *Phys. Z.*, 30:465–467, 1929.

[177] S. Xantheas, S. T. Elbert, and K. Ruedenberg. An intersection seam between the ground state of ozone and an excited state of like symmetry. *J. Chem. Phys.*, 93(10):7519–7521, 1990.

[178] M. R. Manaa and D. R. Yarkony. On the noncrossing rule in polyatomic systems: Determination of a seam of actual surface crossings relevant to the quenching of $H_2(B^1\Sigma_u^+)$ by helium. *J. Chem. Phys.*, 93(6):4473–4474, 1990.

[179] A. L. Sobolewski, C. Woywod, and W. Domcke. *Ab initio* investigation of potential-energy surfaces involved in the photophysics of benzene and pyrazine. *J. Chem. Phys.*, 98(7):5627–5641, 1993.

[180] C. Woywod, M. Stengle, W. Domcke, H. Flöthmann, and R. Schinke. Photodissociation of ozone in the chappuis band. i. electronic structure calculations. *J. Chem. Phys.*, 107(18):7282–7295, 1997.

[181] D. Simah, B. Hartke, and H.-J. Werner. Photodissociation dynamics of H_2S on new coupled *ab initio* potential energy surfaces. *J. Chem. Phys.*, 111(10):4523–4534, 1999.

[182] H. Köppel, W. Domcke, and L. S. Cederbaum. *Advances in Chemical Physics*, volume LVII of *Adv. Chem. Phys.*, chapter 2: MULTIMODE MOLECULAR DYNAMICS BEYOND THE BORN-OPPENHEIMER APPROXIMATION, pages 59–246. John Wiley & Sons, New York Chichester Brisbane Toronto Singapore, 1984.

[183] C. A. Mead and D. G. Truhlar. Conditions for the definition of a strictly diabatic electronic basis for molecular systems. *J. Chem. Phys.*, 77(12):6090–6098, 1982.

[184] W. Domcke and D. R. Yarkony. Role of conical intersections in molecular spectroscopy and photoinduced chemical dynamics. *Annu. Rev. Phys. Chem.*, 63(1):325–352, 2012.

[185] M. Mehlhorn and K. Morgenstern. Faceting during the transformation of amorphous to crystalline ice. *Phys. Rev. Lett.*, 99(24):246101 (4), 2007.

[186] A. Michaelides, J. Carrasco, B. Santra, and J. Klimeš. To wet or not to wet? dispersion forces tip the balance for water ice on metals. *Phys. Rev. Lett.*, 106(2):026101 (4), 2011.

[187] N. H. Fletcher. Reconstruction of ice crystal surfaces at low temperatures. *Philos. Mag. B*, 66(1):109–115, 1992.

[188] D. Pan, A. Michaelides, B. Slater, L.-M. Liu, G. A. Tribello, and E. Wang. Surface energy and surface proton order of ice I_h. *Phys. Rev. Lett.*, 101(15):155703 (4), 2008.

[189] V. Buch, H. Groenzin, I. Li, M. J. Shultz, and E. Tosatti. Proton order in the ice crystal surface. *PNAS*, 105(16):5969–5974, 2008.

[190] M. T. Suter, P. U. Andersson, and J. B. C. Pettersson. Surface properties of water ice at 150-191 k studied by elastic helium scattering. *J. Chem. Phys.*, 125(17):174704 (6), 2006.

[191] X. Wei, P. B. Miranda, C. Zhang, and Y. R. Shen. Sum-frequency spectroscopic studies of ice interfaces. *Phys. Rev. B*, 66(8):085401 (13), 2002.

[192] A. Glebov, A. P. Graham, A. Menzel, J. P. Toennies, and P. Senet. A helium atom scattering study of the structure and phonon dynamics of the ice surface. *J. Chem. Phys.*, 112(24):11011–11022, 2000.

[193] H. Groenzin, I. Li, V. Buch, and M. J. Shultz. The single-crystal, basal face of ice I_h investigated with sum frequency generation. *J. Chem. Phys.*, 127(21):214502 (8), 2007.

[194] K. Siegbahn. Electron spectroscopy - an outlook. *J. Electron Spectrosc. Relat. Phenom.*, 5(1):3–97, 1974.

[195] K. Kobayashi. Optical spectra and electronic structure of ice. *J. Phys. Chem.*, 87(21):4317–4321, 1983.

[196] N. H. Fletcher. Reconstruction of ice crystal surfaces at low temperatures. *Philos. Mag. B*, 66(1):109–115, 1992.

[197] J. D. Bernal and R. H. Fowler. A theory of water and ionic solution, with particular reference to hydrogen and hydroxl ions. *J. Chem. Phys.*, 1(8):515–548, 1933.

[198] M. Watkins, D. Pan, E. G. Wang, A. Michaelides, J. VandeVondele, and B. Slater. Large variation of vacancy formation energies in the surface of crystalline ice. *Nat. Mater.*, 10:794–798, 2011.

[199] M. Watkins, J. VandeVondele, and B. Slater. Point defects at the ice (0001) surface. *PNAS*, 107(28):12429–12434, 2010.

[200] T. Kobayashi. A simple general tendency in photoelectron angular distributions of some monosubstituted benzenes. *Phys. Lett. A*, 69(2):105–108, 1978.

[201] A. W. Potts, M. L. Lyus, E. P. F. Lee, and G. H. Fattahallah. High resolution ultraviolet photoelectron spectra of C_6H_5X and $p-C_6H_4X_2$ where X = Cl, Br or I. *J. Chem. Soc. Faraday Trans. II*, 76(0):556–570, 1980.

[202] K. Imura, N. Kishimoto, and K. Ohno. Two-dimensional penning ionization electron spectroscopy of monohalogenobenzenes by $He^*(2^3S)$: C_6H_5X(X = F, Cl, Br, I). *J. Phys. Chem. A*, 105(17):4189–4199, 2001.

[203] M. H. Palmer, T. Ridley, S. V. Hoffmann, N. C. Jones, M. Coreno, M. de Simone, C. Grazioli, T. Zhang, M. Biczysko, A. Baiardi, and K. Peterson. Interpretation of the photoelectron, ultraviolet, and vacuum ultraviolet photoabsorption spectra of bromobenzene by ab initio configuration interaction and dft computations. *J. Chem. Phys.*, 143(16):164303 (18), 2015.

[204] M. H. Palmer, T. Ridley, S. V. Hoffmann, N. C. Jones, M. Coreno, M. de Simone, C. Grazioli, T. Zhang, M. Biczysko, A. Baiardi, and K. A. Peterson. Combined theoretical and experimental study of the valence, rydberg, and ionic states of chlorobenzene. *J. Chem. Phys.*, 144(12):124302 (21), 2016.

[205] M. H. Palmer, T. Ridley, S. V. Hoffmann, N. C. Jones, M. Coreno, M. de Simone, C. Grazioli, T. Zhang, M. Biczysko, A. Baiardi, and K. A. Peterson. Combined theoretical and experimental study of the valence, rydberg and ionic states of fluorobenzene. *J. Chem. Phys.*, 144(20):204305 (20), 2016.

[206] J. K. Olthoff, J. A. Tossell, and J. H. Moore. Electron attachment by haloalkenes and halobenzenes. *J. Chem. Phys.*, 83(11):5627–5634, 1985.

[207] P. D. Burrow, A. Modelli, and K. D. Jordan. Temporary anion states of the chlorobenzenes. *Chem. Phys. Lett.*, 132(4-5):441–447, 1986.

[208] A. Modelli and P. D. Burrow. Electron transmission study of the temporary anion states of substituted pyridines. *J. Electron Spectrosc. Relat. Phenom.*, 32(3):263–276, 1983.

[209] A. Modelli. Empty level structure and dissociative electron attachment cross section in (bromoalkyl)benzenes. *J. Phys. Chem. A*, 109(28):6193–6199, 2005.

[210] D. D. Clarke and C. A. Coulson. The dissociative breakdown of negative ions. *J. Chem. Soc. A*, (0):169–172, 1969.

[211] J. Milhaud. Dissociative electron attachment to monohalogenated benzenes. *Chem. Phys. Lett.*, 118(2):167–173, 1985.

[212] H.-P. Fenzlaff and E. Illenberger. Low energy electron impact on benzene and the fluorobenzenes. formation and dissociation of negative ions. *Int. J. M. Spe. I. P.*, 59(2):185–202, 1984.

[213] N. L. Asfandiarov, V. S. Fal'ko, A. I. Fokin, O. G. Khvostenko, G. S. Lomakin, V. G. Lukin, and E. P. Nafikova. Frozen shell approximation violation in negative ion formation from halogenated benzenes via dissociative attachment. *Rapid Commun. Mass Sp.*, 14(4):274–279, 2000.

[214] R. Dressler, M. Allan, and E. Haselbach. Symmetry control in bond cleavage processes. dissociative electron attachment to unsaturated halocarbons. *Chimia*, 39(12):385, 1985.

[215] ed. J. R. Rumble. *CRC Handbook of Chemistry and Physics*, volume 98. CRC Press/Taylor & Francis, Boca Raton, Florida, USA, 2017.

[216] D. W. Chandler and P. L. Houston. Two-dimensional imaging of state-selected photodissociation products detected by multiphoton ionization. *J. Chem. Phys.*, 87(2):1445–1447, 1987.

[217] N. H. Abel. Auflösung einer mechanischen aufgabe. *J. Reine Angew. Math.*, 1:153–157, 1826.

[218] A. T. J. B. Eppink and D. H. Parker. Velocity map imaging of ions and electrons using electrostatic lenses: Application in photoelectron and photofragment ion imaging of molecular oxygen. *Rev. Sci. Instrum.*, 68(9):3477–3484, 1997.

[219] V. Butcher, M. L. Costa, J. M. Dyke, A. R. Ellis, and A. Morris. A study of the phenyl radical by vacuum ultraviolet photoelectron spectroscopy. *Chem. Phys.*, 115(2):261–267, 1987.

[220] Y.-J. Liu, P. Persson, and S. Lunell. Theoretical study of the fast photodissociation channels of the monohalobenzenes. *J. Phys. Chem. A*, 108(12):2339–2345, 2004.

[221] T. Mondal and S. Mahapatra. Photophysics of fluorinated benzene. i. quantum chemistry. *J. Phys. Chem.*, 133(8):084304 (12), 2010.

[222] T. Mondal and S. Mahapatra. Photophysics of fluorinated benzene. ii. quantum dynamics. *J. Phys. Chem.*, 133(8):084305 (13), 2010.

[223] M. H. Palmer, T. Ridley, S. V. Hoffmann, N. C. Jones, M. Coreno, M. de Simone, C. Grazioli, M. Biczysko, A. Baiardi, and P. Limão-Vieira. Interpretation of the vacuum ultraviolet photoabsorption spectrum of

iodobenzene by *ab initio* computations. *J. Chem. Phys.*, 142(13):134302 (13), 2015.

[224] M. Mehlhorn. *Dynamik von CO und D_2O auf Cu(111): Laserinduzierte und thermisch induzierte Prozesse*. (phd) dissertation, Freie Universität Berlin, 2005.

[225] M. Mehlhorn, H. Gawronski, L. Nedelmann, A. Grujic, and K. Morgenstern. An instrument to investigate femtochemistry on metal surfaces in real space. *Rev. Sci. Instrum.*, 78(3):033905 (7), 2007.

[226] M. Mehlhorn and K. Morgenstern. Height analysis of amorphous and crystalline ice structures on Cu(111) in scanning tunneling microscopy. *New J. Phys.*, 11(9):093015 (13), 2009.

[227] J. Stähler, M. Mehlhorn, U. Bovensiepen, M. Meyer, D. O. Kusmierek, K. Morgenstern, and M. Wolf. Impact of ice structure on ultrafast electron dynamics in D_2O clusters on Cu(111). *Phys. Rev. Lett.*, 98(20):206105 (4), 2007.

[228] J. Stähler, J.-C. Deinert, D. Wegkamp, S. Hagen, and M. Wolf. Real-time measurement of the vertical binding energy during the birth of a solvated electron. *J. Am. Chem. Soc.*, 137(10):3520–3524, 2015.

[229] J. Stähler and C. Bertram. private communication.

[230] M. Bockstedte. private communication.

[231] F. Baletto, C. Cavazzoni, and S. Scandolo. Surface trapped excess electrons on ice. *Phys. Rev. Lett.*, 95(17):176801 (4), 2005.

[232] S.-C. Heidorn, K. Lucht, C. Bertram, and K. Morgenstern. Preparation-dependent orientation of crystalline ice islands on Ag(111). *J. Phys. Chem. B*, 122(2):479–484, 2017.

[233] T. Komeda, Y. Kim, M. Kawai, B. N. J. Persson, and H. Ueba. Lateral hopping of molecules induced by excitation of internal vibration mode. *Science*, 295(5562):2055–2058, 2002.

[234] S. B. King, D. Wegkamp, C. Richter, M. Wolf, and J. Stähler. Trapped electrons at the amorphous solid water/vacuum interface as possible reactants in a water splitting reaction. *J. Phys. Chem. C*, 121(13):7379–7386, 2017.

[235] S. Ryu, J. Chang, H. Kwon, and S. K. Kim. Dynamics of solvated electron transfer in thin ice film leading to a large enhancement in photodissociation of $CFCl_3$. *J. Am. Chem. Soc.*, 128(11):3500–3501, 2006.

[236] C. Gahl, U. Bovensiepen, C. Frischkorn, and M. Wolf. Ultrafast dynamics of electron localization and solvation in ice layers on Cu(111). *Phys. Rev. Lett.*, 89(10):107402 (4), 2002.

[237] I. Takei and N. Maeno. Dielectric low-frequency dispersion and crossover phenomena of HCl-doped ice. *J. Phys. Chem. B*, 101(32):6234–6236, 1997.

[238] K. Röttger, A. Endriss, J. Ihringer, S. Doyle, and W. F. Kuhs. Lattice constants and thermal expansion of H_2O and D_2O ice I_h between 10 and 265k. *Acta Cryst. B*, 50(6):644–648, 1994.

[239] K. Röttger, A. Endriss, J. Ihringer, S. Doyle, and W. F. Kuhs. Lattice constants and thermal expansion of H_2O and D_2O ice I_h between 10 and 265k. addendum. *Acta Cryst. B*, 68(1):91, 2012.

[240] C. M. B. Line and R. W. Whitworth. A high resolution neutron powder diffraction study of D_2O ice XI. *J. Chem. Phys.*, 104(24):10008–10013, 1996.

[241] E. Whalley. The difference in the intermolecular forces of H_2O and D_2O. *Trans. Faraday Soc.*, 53(0):1578–1585, 1957.

[242] E. Whalley. *Dynamics, thermodynamics and special systems*, volume 3 of *The hydrogen bond: Recent Developments in Theory and Experiments*, chapter The hydrogen bond in ice, pages 1425–1470. North-Holland Publishing Company (Amsterdam), American Elsevier Publishing Company (New York), North-Holland, Amsterdam, 1976.

[243] C. A. Knight. The contact angle of water on ice. *J. Col. Int. Sc.*, 25(2):280–284, 1967.

[244] W. M. Ketcham and P. V. Hobbs. An experimental determination of the surface energies of ice. *Philos. Mag.*, 19(162):1161–1173, 1969.

[245] C. A. Knight. Experiments on the contact angle of water on ice. *Philos. Mag.*, 23(181):153–165, 1971.

[246] S. C. Hardy. A grain boundary groove measurement of the surface tension between ice and water. *Philos. Mag.*, 35(2):471–484, 1977.

[247] C. J. van Oss, R. F. Giese, R. Wentzek, J. Norris, and E. M. Chuvilin. Surface tension parameters of ice obtained from contact angle data and from positive and negative particle adhesion to advancing freezing fronts. *J. Adh. Sc. Tec.*, 6(4):503–516, 1992.

[248] M. Elbaum, S. G. Lipson, and J. G. Dask. Optical study of surface melting on ice. *J. Cry. Gr.*, 129(3-4):491–505, 1993.

[249] G. Portalone, G. Schultz, A. Domenicano, and I. Hargittai. Molecular structure and ring distortions of fluorobenzene: an electron diffraction study, and a comparison with other experimental and ab initio mo results. *J. Mol. Struct.*, 118(1-2):53–61, 1984.

[250] N. P. Penionzhkevich, N. I. Sadova, and L. V. Vilkov. An electron diffraction study of the structure of the molecules of chlorobenzene in the gaseous phase. *J. Struct. Chem.*, 20(3):446–448, 1979.

[251] A. Almenningen, J. Brunvoll, M. V. Popik, S. V. Sokolkov, L. V. Vilkov, and S. Samdal. The molecular structure of gaseous monobromobenzene. *J. Mol. Struct.*, 127(1-2):85–94, 1985.

[252] J. Brunvoll, S. Sandal, H. Thomassen, L. V. Vilkov, and H. V. Volden. The molecular structure of iodobenzene and p-iodonitrobenzene in the gaseous state. *Acta Chem. Scand.*, 44:23–30, 1990.

List of Figures

Nowadays industrially produced chlorofluorocarbons (CFCs) substantially modify the global climate, since their emission leads to environmentally hazardous ozone depleting reactions. Beforehand photoexcited low-energy electrons must attach dissociatively (DEA) to the CFCs on catalytically active icy grains in the terrestrial atmosphere.

This is the first systematic ab-initio study providing a comprehensive picture of activation and course of these intermediate chemical reactions via analysing prototypical adsorbed molecules (phenyl halogenides) and ice surface structures.

A characteristic scenario for the microscopic mechanisms and the relevant electronic structures is found employing GW and underlying plane wave periodic supercell DFT calculations. Insight into direct neutral photodissociation is given by subsequent BSE calculations. The theoretical results are entirely consistent with the observations, made e.g. via STM or 2PPE experiments, and contribute significantly to their explanation.

Apart from that nascent solvated electrons at the ice surface are of fundamental interest, since they can induce reactions of adsorbates in a wide range of energy and time scales. The results evidence a connection between electron solvation and reorientations of ice surface molecules.

ISBN 978-3-96147-295-6

9 783961 472956

FAU UNIVERSITY PRESS 2020